A THEORETICAL STUDY OF OPTICAL DETECTION METHODS FOR ULTRACOLD ATOMS IN OPTICAL LATTICES

by

Francisco Cordobes Aguilar

Department of Physics
Royal Holloway, University of London

This thesis is submitted for the degree of
Doctor of Philosophy

December 2013

I, Francisco Cordobes Aguilar, hereby declare that this thesis and the work presented in it is entirely my own. Where I have consulted the work of others, this is always clearly stated.

Signed: ....

Date: ....

Contents

List of Symbols

$\bar{\Delta\mathbf{k}}$	Projection of the change of momentum of the light upon scattering $\Delta\mathbf{k}$ [Eq. (4.11)] on the xy plane.
$\chi^{ij}(\mathbf{q},\mathbf{q}';\omega)$	Time-ordered susceptibility [Eq. (3.19)].
$\mathbb{S}(\Delta\mathbf{k},\omega)$	Scattered light spectrum [Eq. (4.38)].
$\mathcal{S}^{g_3g_4}_{g_2g_1}(\mathbf{q},\mathbf{q}')$	Static response function [Eq. (3.25)].
$\mathcal{S}^{g_3g_4}_{g_2g_1}(\mathbf{q},\mathbf{q}';\omega)$	Dynamic response function [Eq. (3.26)].
$\mathfrak{u}^*_{\bar{\Delta\mathbf{k}}}\mathfrak{u}_{\bar{\Delta\mathbf{k}}}$	Diffraction pattern of a 2D square array of $N_s \times N_s$ diffracting apertures [See Eqs.(4.36) and (4.25)].
$\boldsymbol{\chi}^{ij}(\utilde{\mathbf{q}},\omega)$	Time-ordered susceptibility, matrix form [Eq. (3.31)].
$\boldsymbol{\mathcal{S}}^{g_3g_4}_{g_2g_1}(\utilde{\mathbf{q}})$	Static response function, matrix form [Eq. (5.9)].
$\boldsymbol{\mathcal{S}}^{g_3g_4}_{g_2g_1}(\utilde{\mathbf{q}},\omega)$	Dynamic response function, matrix form [see Eq. (5.9)].
$\rho_{\mathbf{0}}$	Condensate density in the Bose-Hubbard model [Eq. (8.32)].
$\utilde{\mathbf{q}}$	Reduced Brillouin Zone vector [See Fig. 3.2].
$\hat{\mathbf{\Psi}}^{\dagger}_{\utilde{\mathbf{k}},g}$	Nambu spinor [Eq. (3.11)].
$\zeta(m)$	Fraction of inelastically scattered photons collected by the lens [Eq. (6.7)].
s	Depth of the optical lattice
$S^{g_3g_4}_{g_2g_1}(\bar{\Delta\mathbf{k}})$	Static structure factor [Eq. (4.29)].
$S^{g_3g_4}_{g_2g_1}(\Delta\mathbf{k},\omega)$	Dynamic structure factor [Eq.(4.29)].
AFM	Antiferromagnetism
BEC	Bose-Einstein Condensation
MFT	Mean-field theory
MI	Mott insulator
NA	Numerical aperture.

QMC	Quantum Monte Carlo
RPA	Random-phase approximation
SF	Superfluid
$\Delta\mathbf{k}$	Change of the wavevector of light upon scattering [Eq. (4.11)].
$I(\Delta\mathbf{k})$	Scattered light intensity [Section 4.2].
κ	Ratio between the probe light wavenumber k and the effective lattice light wavenumber k_{l} [Eq. (4.16)].
$\mathbf{\Lambda}_{g'g}$	Polarisation vector of the scattered electric field [Eq. (4.12)].
$\mathsf{M}_{g_2g_1}^{g_3g_4}$	Polarisation tensor of the scattered light [Eq. (4.20)].
$f_{\mathbf{i}n,\mathbf{j}m}(\Delta\mathbf{k})$	Spatial overlap between wavefunctions in an optical lattice [Eq. (4.21)].

Abstract

This thesis presents a theoretical analysis of light scattered from atoms trapped in optical lattices. The work presented here focuses on the case in which atoms trapped in an optical lattice are described by a Hubbard model.

It is shown that the scattered light can be used to probe the ground state correlations and excitations of the system. Both scattered intensity and scattered spectrum are shown to contain relevant information. Scattered intensity is shown to carry information about the magnetic ordering and correlation functions in the system. Scattered spectrum sheds light on the excitations of the system and can be used to study single-particle and collective excitations.

In the case studied here the behaviour of fermionic atoms in an optical lattice is well described by the repulsive half-filled Fermi-Hubbard model. Within the random phase approximation the well known analytic expressions for the system correlations are rederived for the antiferromagnetic ground state. These expressions are input in the light scattering formulae and the scattered intensity and spectrum are evaluated numerically.

As a particular example the experimentally relevant case of ^{40}K is studied. This is done using the level structure that is used routinely in experiments to realise the Fermi-Hubbard model in optical lattices. The scattered light and spectrum experiments are analysed theoretically. It is shown that within a certain experimental range the scattered light intensity offers a direct probe of the antiferromagnetic order parameter. Different experimental parameters and configurations are studied thoroughly and a set of quasi-optimised experimental parameter values is prescribed. The number of necessary experimental realisations to obtain such accuracy is also calculated and shown to be a realistic figure.

Lastly, the same formalism is applied to the Bose-Hubbard model. It is simulated using a worm-type algorithm and the computed correlations are used to evaluate the scattered intensity.

Chapter 1

Introduction and motivation

1.1 Introduction

Since the experimental discovery of Bose-Einstein condensation (BEC) [8], the field of ultracold atomic physics has exploded with activity. This has only been possible due to the great advances in experimental atomic physics achieved over the last three decades[*]. Of the many applications that ultracold atoms may have, this thesis focuses around the creation of analogue quantum simulators in Feynman's sense [37, 36]. This idea is conceptually simple, but very powerful. Simulating quantum mechanical systems is, in principle, straightforward, eg., it only involves diagonalising a matrix. In practice, though, the growth of the size of the Hilbert space makes this an impossible task. With clever algorithms, this problem can be overcome numerically, specially in the low dimensional cases, and for bosonic systems. However, Monte Carlo methods [93], based on the random sampling of the partition function of the systems, do not work very well for fermionic systems. In this case, the algorithms suffer from the so called *sign problem* [119] and the Monte Carlo approach suffers from a critical slow down that also affects frustrated systems. Feynman's idea was based on the observation that nature is already solving those equations. Thus, one way of solving a quantum mechanical problem is to find a quantum mechanical system that is described by the same Hamiltonian and that is very tunable. Using such an experimental system, solving the original problem amounts to preparing the system in a known initial state, letting it evolve to a final state, and then observing its final state. However, this prescription does not make it an easier problem;

---

[*] A very pedagogical account of the basic experimental details can be found in [56, 57].

it only shifts the difficulties from theorists to experimentalists. The great success of the field is in great part due to the very clever and ingenious experimental setups that have been developed.

With the aim of creating analogue quantum simulators, experiments in ultracold atoms have opened a new way to study strongly-correlated physics in a clean and tunable environment [14]. This allows to experimentally realise some previously thought experiments. For example, studying how the BEC transition occurs for a trapped interacting gas, and more importantly, how it behaves when the interaction is switched off towards the non-interacting case. This has been demonstrated in a very elegant experiment reported in [113].

The race to quantum simulation using optical lattices was started by the theoretical proposal by Jaksch et al. [50] to experimentally realise the Bose-Hubbard model [39]. This model was experimentally realised by Greiner et al. [43]. In this experiment, the system was shown to undergo a transition from a superfluid state to a Mott insulator. These two different phases are characterised by the large number of on-site fluctuations in the first, and the lack of these in the latter, due to being energetically constrained. The Bose-Hubbard model can be solved using QMC, this allows for *ab-initio* quantum simulations of the system taking into account all the experimental parameters [116, 54, 72, 111, 123]. Before quantum simulators can be used to study new physics away form the well known regimes, they have to be validated against known systems [116, 54]. The first steps towards experimentally mapping out the phase diagram of the Bose-Hubbard model have been demonstrated [111, 53]. The experimental efforts go hand in hand with the results of numerical simulations [101, 130, 72].

The fermionic equivalent, the Fermi-Hubbard model, is the original model that John Hubbard [48][†] derived to describe strongly correlated electronic systems in real materials. Optical lattices have opened the possibility of exploring Fermionic physics too [33]. The Fermi-Hubbard model has also been experimentally realised on optical lattices [58], and the Mott insulator regime has been also achieved [54, 107]. Cooling the system down to temperatures for which magnetic correlations take over is a current milestone. Specific cooling schemes targeting this regime have been devised [75], and artificial AFM patterns have been demonstrated in 2D optical lattices [122]. In a recently reported

---

[†] Its exact solution is only known in one [69], and infinite dimensions [81].

experiment from ETH's Quantum Optics group [41], the spin correlations between nearest neighbours were measured for a single-band Hubbard model in a dimerised and an anisotropic cubic lattices. This experiment uses the same level structure that we study in this thesis.

1.2 Motivation

The key result in this thesis is to prove that light can be used as a probe for atoms in optical lattices. This is important, as, contrary to what happens in condensed matter, where there is a myriad of different probes that can be used to characterise the behaviour of a given compound, probes for cold atoms are less numerous and not so easily implemented as in condensed matter. For ultracold atoms in an optical lattice, some possible probes are time-of-flight expansion measurements [42, 43] which map the momentum distribution of the atoms in the lattice or noise-correlations [19], which could be used to detect AFM ordering.

Light scattering from atoms in optical lattices as a probe has been previously studied both theoretically and experimentally. The role of off-resonant light is analogous to that of x-ray or neutron diffraction [112] from crystalline structures. This provides a different route to probing atoms in optical lattices. The crystalline structure leads to Bragg diffraction, which reveals information about the crystalline structure of the system. Moreover, the present background outside the diffraction peaks carries information about the system. Far-field imaging provides a probe for strongly-correlated atoms in optical lattice which is sensitive to correlations, excitations and temperature. Ruostekoski et al. [104] showed that scattered light intensity can be used as a thermometer for single-species non-interacting fermionic gas in an optical lattice. Thermal effects on light scattering off Bose gases in optical lattices have been studied in one [78, 102], two [31], and three dimensions [63]. Douglas and Burnett [31] have used similar methods to the ones used in this thesis to study the two-dimensional Bose-Fermi Hubbard model, at both sides of the transition, within the superfluid regime and in the deep Mott insulator regime. Light scattering can also be used as a probe of magnetic order parameter [29, 124, 75]. This problem is dealt with in Section 5.2.

In this thesis, the necessary formalism to use light as probe for atoms in optical lattices is presented. The formalism is then applied to the Fermi-Hubbard model, which is well known, and light is shown to be an accurate probe. This is important because in cold-atoms, most of the existing probes in condensed matter physics are not available. This is also applied to compute the scattered light intensity from the Bose-Hubbard model.

1.3 Outline

This thesis consists of this introductory chapter, seven main chapters, a conclusions chapter and an appendix. The starting point is Chapter 2, in which optical lattices are introduced, along with the proof that the Hubbard model can be realised in optical lattices. In Chapter 3, the spin-density wave mean-field theory (MFT) for the Hubbard model at half-filling in the square lattice is presented, Sec. 3.2. First, the connection between theory and experiments is made via linear response theory in Sec. 3.2.1. The computation of the susceptibilities for the MFT is presented in Sec. 3.2.1. This is followed by a description of how they are used as the basis for computing the Random Phase Approximation (RPA) susceptibilities, Sec. 3.3.

Once the physical system and the model have been introduced, in Chapter 4, the necessary formalism for optical diagnostics is introduced. The remaining chapters are based on the material presented in this chapter. The methods described in this chapter are used in later chapters for probing atoms in optical lattices using off-resonance scattered light. In particular, how to compute the scattered intensity is shown in Sec. 4.2, and the scattered spectrum in Sec. 4.3. In those sections, the elastic and the intraband inelastic components of the scattered light are formulated in terms of the response functions of the probed system. The interband components of the light are studied in Sec. 4.4.

Chapter 5 is where all the theory developed in the preceding chapters is particularised to study ^{40}K in a two dimensional optical lattice. The properties of this particular atom are recalled in Sec. 5.1, along with the details of the scattered intensity from such an experiment. In Chapter 4, the scattered light is shown to be separable in three different components: elastic, and intraband and interband inelastic components. The analysis in Chapter 5 first focuses on the elastic component of the scattered light in Sec. 5.2. In this section, apart from analysing the scattered light off the spin-density wave state presented in Chapter 3, a phenomenological approach to finite temperatures is shown. Using an Ising model, the case when the temperature is above the transition to the AFM state and no ordering exists in the system is dealt with. In Sec. 5.3, the inelastic component of the intraband scattered intensity is analysed. There, both MFT and RPA results are compared at zero temperature. Also in this section, qualitative arguments are presented, based on the MFT calculation, to describe how finite temperatures may affect the scattered light . The section finishes with the analysis of the interband scattered light in Sec. 5.4.

The experimental detection of the results presented in the thesis is analysed in Chapter 6. The effects of the different parameters on the measured signal under realistic experimental conditions are analysed. In particular, the choice of the lens NA and its location along with the possibility of blocking some parts of the scattered light to improve the signal can affect the results of the experiments. This is described in Sec. 6.1. Next, Sec. 6.2 presents estimates for the number of experimental realisations necessary for detecting changes in the staggered magnetisation or temperature in the system with a given relative accuracy. In this section, changes in the lattice depth and probing laser wavelength are shown to modify the signal in a particular manner. This is studied in order to improve the detection accuracy by means of scattered light. The chapter finishes with Section 6.3, in which the possibility of distinguishing the different transitions by using polarisers is explored. The scattered spectrum is studied in Chapter 7. We study both the detection of single-particle and collective excitations. We show that in principle they could both be observed separately.

Chapter 8 departs from the preceding chapters, at least statistically. This chapter deals with the Bose-Hubbard model, which has also been realised in optical lattices. In particular, the aim of this chapter is to explore the possibilities of light scattering as a probe for bosonic systems. In order to do so, two different ways of computing the properties of the systems are used. First, the Bogoliubov approximation is introduced and the correlations in the superfluid phase are computed. Second, the results obtained from Quantum Monte Carlo simulations are presented and compared with the Bogoliubov approximation. The rest of the chapter deals with the problem of scattered light intensity from bosonic atoms in an optical lattice. The angular distribution of the scattered light for changing temperature, and when other parameters in the system vary are studied.

The last chapter, Chapter 9, presents a summary of the results and future prospects.

In Appendix A, the calculational details necessary to understand the RPA calculation are presented. In particular, Feynman diagrams are used to compute the MFT zero temperature susceptibility, and then give details of the derivation of the RPA results.

Chapter 2

Cold atoms in optical lattices

All the experimental situations studied in this thesis are based on the trapping and cooling of neutral atoms in optical lattices. In this chapter, the tools of atomic physics involved in the experiments studied here are introduced. In particular, optical lattices and the effective models used to describe the behaviour of trapped atoms are presented in detail.

2.1 Trapping of neutral atoms

In experiments, ultracold neutral atoms are trapped in a confined region of space by using a combination of magnetic and electric fields. Here, a possible experimental scheme to cool atoms down to the ultracold regime is described. This approach, of course, is only one of the many different possible techniques developed in the last 20 years. It is beyond the scope of this thesis to give a detailed review of cooling and trapping techniques. Thus, only a phenomenological description of a possible set-up is described.

Typically, the experimental set-up is composed of a set of high-vacuum chambers and one or two optical tables covered with lenses, mirrors, cavities, lasers and other active optical components [66, 55, 56]. The atom source is heated in an oven and atoms at high temperatures escape through an opening in one of the walls of the oven. The atoms go into a Zeeman slower [90, 80]. This apparatus is a large cylindrical tube, with a position dependent number of turns coiled around it. These coils generate a magnetic field inside the cylinder which is designed so that atoms levels are shifted due to the Zeeman effect [17]. A laser is shone along the symmetry axis of the cylinder and in the opposite direction. The atomic levels are shifted slightly below an atomic resonance. Doppler cooling happens when an atom absorbs a photon and decays back to its ground state, re-emitting a photon in a random direction. The atom will absorb many photons in the laser direction and re-emit them in a random direction, thus slowing it down [89]. From such high temperature, hundreds of degrees Kelvin, Doppler cooling in the Zeeman slower cools them down to below 1K [89].

At this temperatures, atoms can then be trapped inside a magneto-optical trap (MOT), which cools down to the Doppler limit[*] [44]. Once the lowest temperature possible has been achieved in a MOT, a dipole trap is overlapped and subsequently the MOT is turned off. Dipole traps work by confining cold atoms with laser light due to the induced dipole force [44, 14]. Optical lattices are a particular case of dipole traps.

Optical lattices are generated by making two counterpropagating laser beams interfere in each direction. This generates the periodic electric field felt by the atoms as a periodic potential. Laser beam profiles have a waist, hence, on top of this periodic potential there is a second component which, at the centre, is approximately harmonic. In this thesis, this potential is ignored[†]. This simplifies the calculations greatly. In experiments, the harmonic trap breaks translation invariance. As a result of the existence of the trap, inhomogeneities appear in the experimental samples at the edges and the filling (site-occupancy) is not uniform [107, 22, 123, 72, 24, 95, 14, 33].

Optical lattices offer the possibility of varying the dimensionality of the system. This is achieved by increasing the confinement strength (laser intensity) in one or two dimensions. This way, 1D, 2D and 3D lattices can be created. At the centre of the trap, which is where experiments happen, a typical 2D potential with a lattice spacing a can be written as

$$V_0(x,y,z) = s_x E_R \sin^2\left(\frac{\pi x}{a}\right) + s_y E_R \sin^2\left(\frac{\pi y}{a}\right) + \frac{1}{2} m\omega_z z^2 \tag{2.1}$$

A two-dimensional lattice is described with $s_x = s_y = s$. The lattice depth s is directly (inversely) proportional to the laser intensity (detuning between the atomic transition frequency and the laser frequency) [44]. This configuration is similar to the one used in experiments with a disk-like lattice [110]. The confinement in the z direction is harmonic

---

[*] Laser cooling techniques are beyond the scope of this thesis. A clear and pedagogical introduction to these techniques can be found in the textbook by Metcalf and Van Der Straten [80].

[†] Homogeneous box trapping potential for ultracold bosonic atoms have been recently demonstrated experimentally [40]. This experiment did not include an optical lattice, but the authors claim that their methods are extensible to degenerate Fermi gases and 3D optical lattices [40].

with a frequency ω_z, hence, particle movement along this direction is not allowed. The lattice depth has been written in terms of the atomic recoil energy

$$E_R = \frac{(\hbar k_\text{l})^2}{2m} \tag{2.2}$$

which is the energy that an atom of mass m at rest would gain when recoiling after absorbing a lattice photon. $\hbar$ is Planck's reduced constant. k_l is the effective lattice wavevector

$$k_\text{l} = \frac{\pi}{a} = \frac{2\pi}{\lambda_\text{l}}. \tag{2.3}$$

λ_l is the wavelength laser beam used for generating the lattice. From the previous equation, it is clear that $a = \lambda_\text{l}/2$. This constraint can be relaxed in accordion-type lattices where the lattice spacing can be considerably increased [67, 125, 1].

2.2 Effective Hamiltonian description

At such low energies, atoms can be considered as single particles. For neutral atoms, particle statistics are solely determined by the number of neutrons in their nucleus. The atom can be described as a fermion if this number is odd or as a boson if it is even. Neutral atoms in optical lattices are trapped in different hyperfine states. If optical lattices are to be seen as quantum simulators for condensed matter models, the relation between physical entities in both systems has to be clarified. In optical lattices, the lattice takes the role of the periodic lattice in the solid, whereas the role of the electrons is taken by the atoms. Usually, only those electrons in the outer shells are included in the Hamiltonian used to describe a solid. In this chapter, the focus in on the fermionic case[‡]. Hence, their behaviour is analogous to that of electrons. At ultracold temperatures, the trapped atoms in two different hyperfine states are denoted as

$$|\downarrow\rangle = |F_g, m_g = -F_g\rangle, \quad |\uparrow\rangle = |F_g, m_g = -F_g + 1\rangle, \tag{2.4}$$

where F_g is the total angular momentum of the atom and m_g is its projection in the z direction.

[‡] Particle statistics are not relevant at this point. A similar derivation can be done for particles which obey bosonic statistics [50].

g-atoms of mass m in an optical lattice can be described in terms of the field operators $\Psi_g^\dagger(\mathbf{r})$. Following [50], the Hamiltonian for such a system can be written as

$$\begin{aligned}\mathcal{H}_a = &\sum_{g=\uparrow,\downarrow} \int d\mathbf{r} \Psi_g^\dagger(\mathbf{r}) \left(-\frac{\hbar^2}{2m}\nabla^2 + V_0(\mathbf{r}) - \mu \right) \Psi_g(\mathbf{r}) \\ &+ \frac{1}{2}\frac{4\pi a_s \hbar^2}{m} \int d\mathbf{r} \Psi_\uparrow^\dagger(\mathbf{r})\Psi_\downarrow^\dagger(\mathbf{r})\Psi_\uparrow(\mathbf{r})\Psi_\downarrow(\mathbf{r}).\end{aligned} \tag{2.5}$$

The field operator $\Psi_g^\dagger(\mathbf{r})$ $[\Psi_g(\mathbf{r})]$ is the operator that describes the creation [destruction] of an atom in a hyperfine state $g =\uparrow,\downarrow$ at position $\mathbf{r}$. $\frac{-\hbar}{2m}\nabla^2$ is the kinetic energy operator and μ is the chemical potential. The last term is the interaction term. For ultracold atoms in optical lattices the interaction is modelled using a short-range pseudopotential with s-wave scattering length a_s which can be modified via Feshbach resonances [26]. In Eq. (2.5) matter fields can be expanded in terms of the complete set of Wannier real functions $w_{n,j}(\mathbf{r}) = w_n(\mathbf{r} - \mathbf{r}_j)$ representing a localised state at site j and band n [59, 9]

$$\hat{\Psi}_g(\mathbf{r}) = \sum_n \sum_{\mathbf{j}} w_{n,\mathbf{j}}(\mathbf{r}) \hat{c}_{n\mathbf{j}g}. \tag{2.6}$$

Here, as usual, $\hat{c}_{n\mathbf{j}g}^\dagger(\hat{c}_{n\mathbf{j}g})$ is the fermionic creation (destruction) operator in direct space representation for a particle of species g at site $\mathbf{j}$ in band n.

To derive an effective Hamiltonian the parameters are assumed to be in a regime such that $U, T >$ bandgap and the higher bands are unpopulated. Under such assumptions, only the lower band, $n = 0$, needs to be taken into account.

If the lattice depth is large enough, a series expansion of the potential shows that it can be approximated in the site origin as a harmonic oscillator. The Wannier functions can be estimated using the ground state wavefunction of a quantum harmonic oscillator with frequencies

$$\omega_x = \omega_y = \frac{2\sqrt{s}E_R}{\hbar}. \tag{2.7}$$

Hence, the Wannier function for the ground state is taken to be

$$w_{0,0}(\mathbf{r}) = \prod_{i=x,y,z} \frac{1}{(\pi l_i^2)^{1/4}} \exp\left(-\frac{r_i^2}{2l_i^2} \right), \tag{2.8}$$

where

$$l_i = (\hbar/m\omega_i)^{1/2}, \quad i = x, y, z \tag{2.9}$$

is the oscillator length.

Within this approximation the overlap between the wavefunctions of neighbouring sites is only significant for nearest neighbours. Any other overlap is neglected. Under such circumstances, the Hamiltonian reduces to the Hubbard model Hamiltonian and can be written as [50]

$$\mathcal{H} = -J \sum_{g=\uparrow,\downarrow} \sum_{\langle \mathbf{j}_1 \mathbf{j}_2 \rangle} \left(\hat{c}^\dagger_{\mathbf{j}_1 g} \hat{c}_{\mathbf{j}_2 g} + h.c. \right) + U \sum_{\mathbf{j}} \hat{n}_{\mathbf{j}\uparrow} \hat{n}_{\mathbf{j}\downarrow} - \mu \sum_{g=\uparrow,\downarrow} \sum_{\mathbf{j}} \hat{n}_{\mathbf{j}g}. \tag{2.10}$$

$\hat{n}_{\mathbf{j}g} = \hat{c}^\dagger_{\mathbf{j}g} \hat{c}_{\mathbf{j}g}$ is the number operator. In this model J is the *hopping parameter* which as denoted by $\langle \mathbf{j}_1 \mathbf{j}_2 \rangle$ is only between nearest neighbours. U is the on-site interaction strength. μ is the chemical potential. This model is studied in Chapter 3 at half-filling in the fermionic case and in Chapter 8 in the bosonic single-species case.

The lattice parameters can in principle be computed from their defining expressions

$$U_{\mathbf{j}} = U = \frac{4\pi a_s \hbar^2}{m} \int d\mathbf{r} |w_{0,\mathbf{j}}(\mathbf{r})|^4 \tag{2.11}$$

$$J_{\mathbf{ij}} = J = -\int d\mathbf{r} w^*_{0,\mathbf{i}}(\mathbf{r}) \left(\frac{-\hbar^2}{2m} \nabla^2 + V_0(\mathbf{r}) \right) w_{0,\mathbf{j}}(\mathbf{r}), \tag{2.12}$$

where $\mathbf{j}$ is a nearest neighbour of $\mathbf{i}$. Using Eq. (2.8) to evaluate Eq. (2.11) we obtain the following expression for the Hubbard model on-site interaction U

$$U = k_l a_s \sqrt{\frac{\hbar^3 \omega_x \omega_y \omega_z}{\pi E_R}} = 2 k_l a_s \sqrt{\frac{\hbar E_R s \omega_z}{\pi}} \ . \tag{2.13}$$

Equations (2.11), (2.13) are a good approximation for the on-site interaction. This is not the case for Eq. (2.12). To estimate the hopping amplitude in an optical lattice, the 1D Mathieu equation can be used. A typical tight-binding dispersion relation has the form $\epsilon_q = 4J \sin^2\left(\frac{qa}{2}\right) = 4J \sin^2\left(\frac{q\pi}{2k_l}\right)$, and it is related to the lowest energy bandwidth of the system by $\Delta E = 4J$ [88]. For deep lattices where $s \gg 1$ the lowest bandwidth of the system can be estimated by using an asymptotic series expansion for the difference between the first and second eigenvalues [30, 82, 68]. In the limit $s \gg E_r$ this results in

$$J = \frac{4}{\sqrt{\pi}} E_R (s)^{3/4} \exp\left[-2\sqrt{s}\right] \ . \tag{2.14}$$

It is clear from Eqs. (2.13) and (2.14) that the model parameters can be modified by changing the laser intensity and the magnetic fields present in the experiment.

Chapter 3

Hubbard model

The one band Hubbard model, Eq. (2.10), was invented with the goal of describing magnetic phenomena, especially ferromagnetism in Fe, Co and Ni [34]. It is also believed to describe the physics of High-T_c superconductivity away from half-filling [13, 47]. For the purpose of this thesis, it is the work of Jaksch et al. [50] that leads to the Hubbard model. It was shown in Chapter 2 that atoms trapped in an optical lattice can be described by a Hubbard Hamiltonian, Eq. (2.10). The aim of this thesis is to study scattered light as a probe for atomic correlations. In order to do this, in this chapter, the fermionic one band Hubbard model [48] is studied at half-filling (i.e., on average, there is only one atom per lattice site). At half-filling, it is well known that the one band Hubbard model ground state is an antiferromagnet (AFM), see for example [10]. Starting from an AFM ground state assumption the mean-field theory approximation (MFT) is solved. Quantum fluctuations play a very important role. Its effects are not accounted for in the MFT calculation which only describes single-particle excitations [18]. Here, the effects of quantum fluctuations are accounted for using a random phase approximation (RPA) calculation for the zero temperature susceptibilities originally presented for the first time by Schrieffer et al. in [109]. This approximation also describes collective modes. In the large U limit, it is also able to describe the low-energy behaviour expected from the Heisenberg model [109, 27].

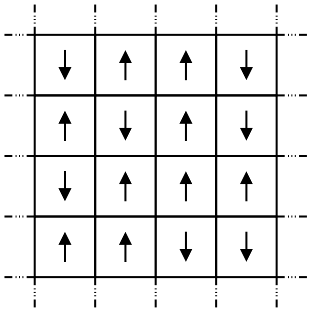

Figure 3.1: Cartoon diagram to illustrate the nature of the insulating phase in the $J/U \to 0$ limit.

3.1 Phenomenology of the model

The Hubbard model of Eq. (2.10) is a tight binding model [9, 34]. As a tight-binding model, it considers atoms/electrons hopping in a discrete lattice. In particular, the Hamiltonian only includes two processes: hopping of particles from one site to any nearest neighbour site with a hopping amplitude J; and an on-site contact interaction, repulsive in our case, with a strength U. The Fermi-Hubbard Hamiltonian of Eq. (2.10) is recalled here for completeness,

$$\mathcal{H} = -J \sum_{g=\uparrow,\downarrow} \sum_{\langle \mathbf{j}_1\mathbf{j}_2\rangle} \left(\hat{c}^\dagger_{\mathbf{j}_1 g} \hat{c}_{\mathbf{j}_2 g} + h.c. \right) + U \sum_{\mathbf{j}} \hat{n}_{\mathbf{j}\uparrow} \hat{n}_{\mathbf{j}\downarrow} - \mu \sum_{g=\uparrow,\downarrow} \sum_{\mathbf{j}} \hat{n}_{\mathbf{j}g}. \tag{3.1}$$

In this thesis, only the repulsive case is studied. The attractive case, $U > 0$, is unitarily equivalent. Every Hamiltonian $\mathcal{H}$ with two-body interaction plus an analytic function of number operators $\hat{F}\left[\{\hat{n}_{\mathbf{j}\sigma}\}\right]$ [*]is unitarily equivalent to $-\mathcal{H} + 2\hat{F}$ (see, for example, [120]). This implies that the spectrum of the Hamiltonian obtained by changing the sign of $\hat{F}$ is obtained also by multiplying the spectrum by minus one. Far from being a mathematical curiosity of the model, this property maps the different phases of the repulsive model via a unitary transformation to those of the attractive one. This means that experimentally, either case could be simulated and then, conclusions for the case with opposite sign of the interaction strength can be drawn [46].

In a square lattice, it is well known there is long-range order in the half-filled Hubbard model [34, 15]. At weak-coupling, the origin of the long-range AFM order is due to a Fermi surface instability [34]. In the strong-coupling regime, the system is in a Mott

---

[*] That is just a straightforward generalisation of the Hubbard model which takes the form:

$$\mathcal{H}_{\text{Hubbard}} = -J \sum_{\sigma_1\sigma_2} \sum_{\langle \mathbf{j}_1\mathbf{j}_2\rangle} \left(\hat{c}^\dagger_{\mathbf{j}_1\sigma_1} \hat{c}_{\mathbf{j}_2\sigma_2} + h.c. \right) + \hat{F}\left[\{\hat{n}_{\mathbf{j}\sigma}\}\right],$$

where $\hat{F}\left[\{\hat{n}_{\mathbf{j}\sigma}\}\right]$ is the mentioned analytical function of the number operators that in the Hubbard case is the U interaction term.

insulator state [15]. The properties of this phase are interaction induced as it is energetically expensive to have a doubly occupied site [34, 49]. At integer-fillings[†], the interaction induced correlations result in a localisation of the atoms at each lattice site and a suppression of the on-site fluctuations of the total atom number. The Mott-Hubbard insulator appears at temperatures below U, and it appears as a result of a crossover. Just below the onset of the crossover, on-site relative atom fluctuations are energetically not so expensive and mixing of the different spin states is possible. As temperature is lowered down, the regime determined by the Néel temperature ($T \sim 4J^4/U$) is achieved. In this new regime, AFM ordering starts to develop and true long-range order only appears at $T = 0$ [79]. In the square lattice, due to its bipartite nature, the system takes a checkerboard-like pattern as illustrated in Fig. 3.1. This state is characterised by having precisely one atom per site with one spin species being only surrounded by opposite spins. At half-filling, this is the ground state of the system in the classical limit, obtained by minimising the energy. On top of this localised phase and at very low temperatures, quantum fluctuations allow for virtual hoppings. Using second order perturbation theory it can be shown in a heuristic way that there is a spin exchange interaction of the order $\sim 4J^2/U$ between atoms in neighbouring sites. This exchange defines the Néel temperature. It is below such temperatures that the system can be described as a spin Heisenberg model [74]. This result can be proved in a more rigorous way by projecting the Hubbard model into the subspace of singly occupied states at large values of U/J [10].

As described by the Mermin-Wager theorem [79], in an infinite lattice in 2D quantum fluctuations destroy long-range AFM order except at zero temperature. Thus, there is no true long-range order in the Hubbard model at finite temperatures. This is not much of a problem, for in optical lattices, system sizes are on the order of hundreds of atoms. A typical 2D optical lattice will have around 100×100 atoms. At low enough temperatures, the antiferromagnetic correlation length grows exponentially and for temperatures low enough quasi-long range order exists, see Sect.3.2. Hence, for the purposes of describing AFM ordering in an optical lattice, quasi-long range order will be indistinguishable from true long-range order as long as the correlation length of the system is larger than the system size.

In an optical lattice, the presence of the harmonic trap complicates the picture de-

---

[†] I.e., when on average there is an integer number of atoms at each site.

scribed in the previous paragraphs. Due to the existence of the harmonic trap, inhomogeneity will prevail [54, 107]. The results of this thesis only describe the behaviour at the centre of the trap, as the effects of the harmonic trap are ignored.

3.2 Finite temperature mean field theory

As has been explained in the previous section, in this thesis, the 2D Hubbard model at half-filling on a square lattice is used to describe atoms in an optical lattice. Besides, the calculations are done as if there is true long-range order in the system. In such scenario, some more approximations are needed to obtain a tractable form of the problem at hand. This section introduces the *spin density wave* mean field theory (MFT) approximation, which is taken as the starting point of the analysis presented here. It can be introduced by considering the Mott state with antiferromagnetic order. The antiferromagnetic order is introduced by imposing a *staggered* magnetisation along the direction of the z axis. This is done via the expectation value of the spin operator in $\hat{S}_z$. The spin density wave approach taken here is a **broken symmetry** one. By imposing a doubling of the lattice size (the super lattice), translation symmetry is broken. This results in the halving of the Brillouin zone. The spin density wave can be written as a condition on the expectation value of the projection of the spin over the z direction. This defines the order parameter m

$$m = \frac{1}{2} e^{i\mathbf{Q}\cdot\mathbf{r}_j} \left\langle \hat{S}^z_{\mathbf{j}} \right\rangle, \tag{3.2}$$

where the spin operator in real space is defined as $\hat{S}^z_j = \hat{c}^\dagger_{\mathbf{j}\uparrow}\hat{c}_{\mathbf{j}\uparrow} - \hat{c}^\dagger_{\mathbf{j}\downarrow}\hat{c}_{\mathbf{j}\downarrow}$ and the nesting vector is

$$\mathbf{Q} = (\pi/a, \pi/a). \tag{3.3}$$

This corresponds to the following assumption on the form of the expectation value of the number operator for each spin

$$\langle \hat{n}_{\mathbf{j},g} \rangle = f_g + m\eta(g) e^{i\mathbf{Q}\cdot\mathbf{j}}. \tag{3.4}$$

f_g is the *filling factor* for species g; at half-filling $f_g = 1/2$. The factor $\eta(g)$ is defined as

$$\eta(g) = \begin{cases} 1 & \text{for} \quad g = \uparrow \\ -1 & \text{for} \quad g = \downarrow \end{cases}. \tag{3.5}$$

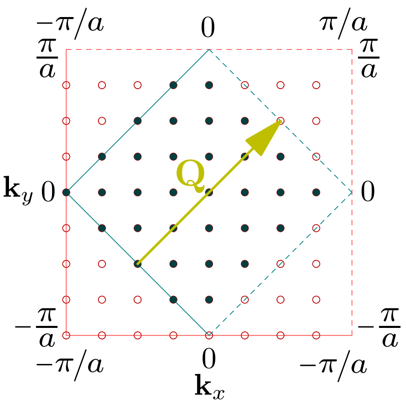

Figure 3.2: Illustration of Brillouin zone (red square) and reduced Brillouin zone (inner blue square) in a finite size system for $N_s = 8$. The filled squares represent filled momentum states in the Fermi sea at half-filling. This partition of the Brillouin zone to obtain the Reduced Brillouin zone is not unique.

The square lattice is *bipartite*, that is, the lattice can be split into two interlaced lattices. Each site of the lattice is surrounded by sites that belong to the other lattice. In the Néel state, each spin of the lattice will have opposite spins as nearest neighbours, see Fig. 3.1. This allows for the lattice to be represented in terms of a magnetic super-cell with a size double that of the original lattice unit cell. Thus, as illustrated in Fig. 3.2, the Brillouin zone is halved. To accommodate the same number of states, a second band appears. This reduced Brillouin zone (RBZ) is bound by $k_x \pm k_y = \pi/a$. The filled circles denote the quasi-momentum states that belong to it. Note that only half the edges are inside the RBZ. The ordering vector $\mathbf{Q}$ always links a quasi-momentum inside the RBZ with one outside (and vice-versa).

Thus, the MFT theory is an effective two-band model as will be shown in the next section. Magnetic ordering opens a gap which results in the splitting of the two effective bands.

Mean field Hamiltonian

The basic idea behind the mean field assumption is that the system does not fluctuate much from the expected value, and thus the *fluctuating term* $\langle\langle \hat n_{\mathbf{j},g}\rangle - \hat n_{\mathbf{j},g}\rangle$ is small. The assumption made about the *form* of the expected value of the number operator, Eq. (3.4), is to be used in the Hubbard Hamiltonian of Eq. (3.1). In order to do this, the following trivial expression is used: $\hat n_{\mathbf{j}g} = \langle \hat n_{\mathbf{j}g}\rangle + (\hat n_{\mathbf{j}g} - \langle \hat n_{\mathbf{j}g}\rangle)$. Thus, the interaction term in Eq. (3.1) can be rewritten as

$$U\sum_{\mathbf{j}} \hat n_{\mathbf{j}\uparrow}\hat n_{\mathbf{j}\downarrow} \approx U\sum_{\mathbf{j}}(\hat n_{\mathbf{j}\uparrow}\langle \hat n_{\mathbf{j}\downarrow}\rangle + \hat n_{\mathbf{j}\downarrow}\langle \hat n_{\mathbf{j}\uparrow}\rangle - \langle \hat n_{\mathbf{j}\uparrow}\rangle\langle \hat n_{\mathbf{j}\downarrow}\rangle).$$

This decouples Eq. (3.1) and the non-trivially soluble part now has a tractable form. At this point, it is convenient to work in momentum space. To transform from real space to momentum space, periodic boundary conditions are imposed and a lattice with N_s atoms per direction is assumed. With these premises,

$$\hat{c}_{\mathbf{j}g} = \frac{1}{N_s}\sum_{\mathbf{k}} e^{i\mathbf{k}\cdot\mathbf{j}}\hat{c}_{\mathbf{k}g}. \tag{3.6}$$

The summation over momenta is over the whole Brillouin zone: $(k_x, k_y) = \frac{2\pi}{N_s a}(j_x, j_y)$ where $-N_s/2 \leq j_{x,y} \leq N_s/2 - 1$. After using Eq. (3.6), the fermion operator $\hat{c}_{\mathbf{k}g}$, defined over the whole Brillouin zone splits into two operators $\hat{c}_{\underset{\sim}{\mathbf{k}}g}$ and $\hat{c}_{\underset{\sim}{\mathbf{k}}+\mathbf{Q}g}$, with $\underset{\sim}{\mathbf{k}}$ denoting a vector defined only for the RBZ. Some algebra later, the mean field Hamiltonian can be written as

$$\begin{aligned}\mathcal{H} = C + \sum_{g=\uparrow,\downarrow}\sum_{\underset{\sim}{\mathbf{k}}}^{\text{RBZ}}\Bigg\{ &\left(\frac{nU}{2} + \epsilon_{\underset{\sim}{\mathbf{k}}} - \mu\right)\hat{c}^{\dagger}_{\underset{\sim}{\mathbf{k}},g}\hat{c}_{\underset{\sim}{\mathbf{k}},g} + \left(\frac{nU}{2} + \epsilon_{\underset{\sim}{\mathbf{k}}+\mathbf{Q}} - \mu\right)\hat{c}^{\dagger}_{\underset{\sim}{\mathbf{k}}+\mathbf{Q},g}\hat{c}_{\underset{\sim}{\mathbf{k}}+\mathbf{Q},g} \\ &- mU\eta(g)\left(\hat{c}^{\dagger}_{\underset{\sim}{\mathbf{k}},g}\hat{c}_{\underset{\sim}{\mathbf{k}}+\mathbf{Q},g} + \hat{c}^{\dagger}_{\underset{\sim}{\mathbf{k}}+\mathbf{Q},g}\hat{c}_{\underset{\sim}{\mathbf{k}},g}\right)\Bigg\}\end{aligned} \tag{3.7}$$

with a single particle dispersion relation given by $\epsilon_{\mathbf{k}} = -2J(\cos k_x a + \cos k_y a)$ and a constant $C \equiv UN_s^2(m^2 - 1/4)$. The dispersion relation satisfies the *perfect nesting condition*, $\epsilon_{\mathbf{k}+\mathbf{Q}} = -\epsilon_{\mathbf{k}}$. At half-filling $n = 1$ and $\mu = U/2$ and these two terms cancel each other. Defining the order parameter (also called gap parameter)

$$\Delta_g = \eta(g)\Delta\ , \qquad \Delta = mU. \tag{3.8}$$

The Hamiltonian in Eq. (3.7) is block diagonal in a spin symmetric form and it can be written as a 2×2 matrix with a sum over the spin degree of freedom

$$\mathcal{H} = C + \sum_{g=\uparrow,\downarrow}\sum_{\underset{\sim}{\mathbf{k}}}^{\text{RBZ}}\begin{pmatrix}\hat{c}^{\dagger}_{\underset{\sim}{\mathbf{k}},g} & \hat{c}^{\dagger}_{\underset{\sim}{\mathbf{k}}+\mathbf{Q},g}\end{pmatrix}\begin{pmatrix}\epsilon_{\underset{\sim}{\mathbf{k}}} & -\Delta_g \\ -\Delta_g & \epsilon_{\underset{\sim}{\mathbf{k}}+\mathbf{Q}}\end{pmatrix}\begin{pmatrix}\hat{c}_{\underset{\sim}{\mathbf{k}},g} \\ \hat{c}_{\underset{\sim}{\mathbf{k}}+\mathbf{Q},g}\end{pmatrix} = C + \sum_{g=\uparrow,\downarrow}\sum_{\underset{\sim}{\mathbf{k}}}^{\text{RBZ}}\hat{\boldsymbol{\Psi}}^{\dagger}_{\underset{\sim}{\mathbf{k}},g}\boldsymbol{\mathcal{H}}_{\underset{\sim}{\mathbf{k}}g}\hat{\boldsymbol{\Psi}}_{\underset{\sim}{\mathbf{k}},g} \tag{3.9}$$

where the Hamiltonian has been rewritten in matrix notation as

$$\boldsymbol{\mathcal{H}}_{\underset{\sim}{\mathbf{k}},g} = \begin{pmatrix}\epsilon_{\underset{\sim}{\mathbf{k}}} & -\Delta_g \\ -\Delta_g & \epsilon_{\underset{\sim}{\mathbf{k}}+\mathbf{Q}}\end{pmatrix} \tag{3.10}$$

and where the AFM equivalent of the *Nambu spinors* used in the theory of superconductivity [108] has been introduced. It is defined as

$$\hat{\boldsymbol{\Psi}}^{\dagger}_{\underset{\sim}{\mathbf{k}},g} = \begin{pmatrix}\hat{c}^{\dagger}_{\underset{\sim}{\mathbf{k}},g} & \hat{c}^{\dagger}_{\underset{\sim}{\mathbf{k}}+\mathbf{Q},g}\end{pmatrix}, \quad \hat{\boldsymbol{\Psi}}_{\underset{\sim}{\mathbf{k}},g} = \begin{pmatrix}\hat{c}_{\underset{\sim}{\mathbf{k}},g} \\ \hat{c}_{\underset{\sim}{\mathbf{k}}+\mathbf{Q},g}\end{pmatrix} \tag{3.11}$$

In this form of the Hamiltonian, it can be diagonalised by means of a Bogoliubov transformation. It is in this step that the two effective bands appear due to the transformation from the full original Brillouin zone with the first half being $\hat{c}_{\underset{\sim}{\mathbf{k}},g}$ and the second being $\hat{c}_{\underset{\sim}{\mathbf{k}}+\mathbf{Q},g}$, to the reduced BZ where the first band is $\hat{c}_{1\underset{\sim}{\mathbf{k}},g}$, and second, $\hat{c}_{2\underset{\sim}{\mathbf{k}},g}$ (see Fig. 3.2). Diagonalisation of the Hamiltonian is achieved by means of the well known SDW Bogoliubov transformation $\boldsymbol{P}_{\underset{\sim}{\mathbf{k}},g}$ [109, 27]. This transformation has to be unitary, and it has to preserve the commutation relations. It transforms from the split BZ representation $\hat{c}_{\underset{\sim}{\mathbf{k}},g}$ and $\hat{c}_{\underset{\sim}{\mathbf{k}}+\mathbf{Q},g}$ to the two effective bands representation[‡] $\hat{c}_{1\underset{\sim}{\mathbf{k}},g}$ and $\hat{c}_{2\underset{\sim}{\mathbf{k}},g}$.

$$\hat{\boldsymbol{\Psi}}_{\underset{\sim}{\mathbf{k}},g} = \begin{pmatrix} \hat{c}_{\underset{\sim}{\mathbf{k}},g} \\ \hat{c}_{\underset{\sim}{\mathbf{k}}+\mathbf{Q},g} \end{pmatrix} = \boldsymbol{P}_{\underset{\sim}{\mathbf{k}},g} \hat{\boldsymbol{\Psi}}'_{\underset{\sim}{\mathbf{k}},g} = \begin{pmatrix} v_{\underset{\sim}{\mathbf{k}},g} & u_{\underset{\sim}{\mathbf{k}},g} \\ -\eta(g) u_{\underset{\sim}{\mathbf{k}},g} & \eta(g) v_{\underset{\sim}{\mathbf{k}},g} \end{pmatrix} \begin{pmatrix} \hat{c}_{1\underset{\sim}{\mathbf{k}},g} \\ \hat{c}_{2\underset{\sim}{\mathbf{k}},g} \end{pmatrix}. \tag{3.13}$$

$v_{\mathbf{k},g}$ and $u_{\mathbf{k},g}$ are carefully chosen to conserve the commutation relations. This condition holds if $v^2_{\mathbf{k},g} + u^2_{\mathbf{k},g} = 1$. The solution is

$$v_{\mathbf{k},g} = \sqrt{\frac{1}{2}\left(1 - \frac{\epsilon_{\mathbf{k}}}{E_{\mathbf{k}g}}\right)}, \quad u_{\mathbf{k},g} = \sqrt{\frac{1}{2}\left(1 + \frac{\epsilon_{\mathbf{k}}}{E_{\mathbf{k}g}}\right)}, \tag{3.14}$$

$$E_{\mathbf{k}g} = \sqrt{\Delta_g^2 + \epsilon_{\mathbf{k}}^2} = \sqrt{\Delta^2 + \epsilon_{\mathbf{k}}^2} \equiv E_{\mathbf{k}}. \tag{3.15}$$

The last equation follows from the definition of the gap parameter $\Delta_g = \eta(g)\Delta$ [see Eq. (3.5)]. In the new basis, the diagonalised Hamiltonian can be simply written as

$$\boldsymbol{\mathcal{H}} = C + \sum_{g=\uparrow,\downarrow} \sum_{\underset{\sim}{\mathbf{k}}}^{\text{RBZ}} \begin{pmatrix} \hat{c}^{\dagger}_{1\underset{\sim}{\mathbf{k}},g} & \hat{c}^{\dagger}_{2\underset{\sim}{\mathbf{k}},g} \end{pmatrix} \begin{pmatrix} -E_{\underset{\sim}{\mathbf{k}}g} & 0 \\ 0 & +E_{\underset{\sim}{\mathbf{k}}g} \end{pmatrix} \begin{pmatrix} \hat{c}_{1\underset{\sim}{\mathbf{k}},g} \\ \hat{c}_{2\underset{\sim}{\mathbf{k}},g} \end{pmatrix}. \tag{3.16}$$

From this, it follows that at zero temperature and at half-filling, the first band (with negative energies) is full and the second band (with positive energies) is empty. Exciting a particle from the lower to the upper band has an energy cost of ≈ $2E_{\underset{\sim}{\mathbf{q}}g}$, which is the only type of excitation described in the model. At large values of U/J, the kinetic energy term can be neglected and the energy gap can be written as ≈ 2Δ.

[‡] The transformation matrix is unitary, that is $\boldsymbol{P}^{-1}_{\underset{\sim}{\mathbf{k}},g} = (\boldsymbol{P}^{T}_{\underset{\sim}{\mathbf{k}},g})^*$. Hence, the change of base is obtained by taking into account that the Hamiltonian is really a scalar quantity and thus, it must be invariant when changing the basis for the matrices and vectors

$$\hat{\boldsymbol{\Psi}}^{\dagger}_{\underset{\sim}{\mathbf{k}},g} \boldsymbol{\mathcal{H}}_{\underset{\sim}{\mathbf{k}}g} \hat{\boldsymbol{\Psi}}_{\underset{\sim}{\mathbf{k}},g} = \hat{\boldsymbol{\Psi}}^{\dagger}_{\underset{\sim}{\mathbf{k}},g} \boldsymbol{P}_{\underset{\sim}{\mathbf{k}},g} \boldsymbol{P}^{-1}_{\underset{\sim}{\mathbf{k}},g} \boldsymbol{\mathcal{H}}_{\underset{\sim}{\mathbf{k}}g} \boldsymbol{P}_{\underset{\sim}{\mathbf{k}},g} \boldsymbol{P}^{-1}_{\underset{\sim}{\mathbf{k}},g} \hat{\boldsymbol{\Psi}}_{\underset{\sim}{\mathbf{k}},g} = \hat{\boldsymbol{\Psi}}'^{\dagger}_{\underset{\sim}{\mathbf{k}},g} \boldsymbol{\mathcal{H}}'_{\underset{\sim}{\mathbf{k}}g} \hat{\boldsymbol{\Psi}}'_{\underset{\sim}{\mathbf{k}},g}.$$

The diagonal Hamiltonian is given by

$$\boldsymbol{\mathcal{H}}'_{\underset{\sim}{\mathbf{k}},g} = \boldsymbol{P}^{-1}_{\underset{\sim}{\mathbf{k}},g} \boldsymbol{\mathcal{H}}_{\underset{\sim}{\mathbf{k}},g} \boldsymbol{P}_{\underset{\sim}{\mathbf{k}},g}. \tag{3.12}$$

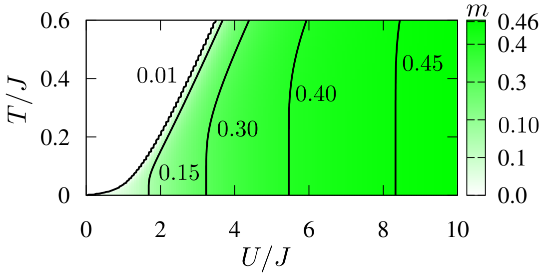

Figure 3.3: Diagram showing the (U, T) dependence of the staggered magnetisation, m, obtained by solving Eq. (3.17) in a lattice with $N_s = 40$ (total number of lattice sites $= N_s^2$). The colour shading encodes the value of m.

Mean field approximation gap equation

Once the system is in diagonal form, using Eq. (3.13), the mean field solution of Eq. (3.16) can be used in the expectation value of the spin operator $\hat{S}^z_{\mathbf{j}}$ of Eq. (3.2). This results in a self-consistency equation for the *order parameter* m, which can be solved numerically. The resulting *gap equation* at finite temperatures is

$$1 = \frac{1}{N_s^2} \sum_{\underset{\sim}{\mathbf{k}'}}^{\text{RBZ}} \frac{U}{E_{\underset{\sim}{\mathbf{k}'}}} \tanh\left(\frac{E_{\underset{\sim}{\mathbf{k}'}}}{2k_B T}\right) \tag{3.17}$$

Where $E_{\mathbf{k}} = \sqrt{\Delta^2 + \epsilon^2_{\mathbf{k}}}$ and k_B is Boltzmann's constant. At half-filling and $T = 0$ with an on-site interaction $U \gg J$ the solution can be shown to be $m = 1/2$. The value of staggered magnetisation is shown in the (U, T) space in Fig. 3.3.

The critical temperature that is obtained from solving this equation, $T_{C,\text{MFT}}$, is not valid for a large range of U values but only makes physical sense for the *weak interacting regime*, $U \lesssim 4J$ where it predicts an exponentially small order parameter. For large values of U, the transition temperature obtained from Eq. (3.17) grows linearly with U, and it is known from strong coupling theories that this is not the real physical behaviour. Using a strong coupling expansion, the half-filled Hubbard model can be projected onto a Heisenberg model where charge dynamics are frozen due to the high energy cost, of the order of U, that it has for an electron to hop from a lattice site to another. Spin dynamics through a super-exchange effective interaction are the only possible phenomena in that scenario [74]. From the Heisenberg model it is known that in 3D, T_C is inversely proportional to U, as $T_C \propto 4J^2/U$. On top of that, working with a two dimensional system fluctuations prevent any kind of long-range order except at $T = 0$ [79]. In two dimensions, long range AFM order only exists at $T = 0$. At a finite but low temperature,

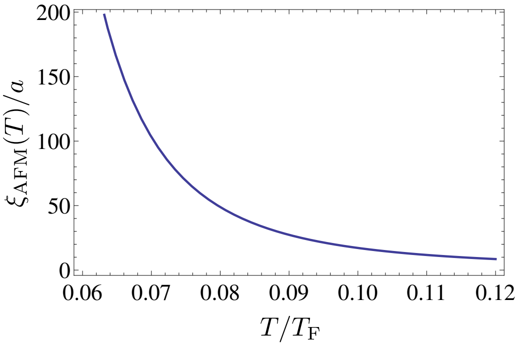

Figure 3.4: Temperature dependence of correlation length in the Heisenberg AFM for temperatures above the transition.

the precursors of long range order exist. They exist below the crossover temperature T_X. This crossover temperature is physically related to the antiferromagnetic correlation length ξ_{AFM}. Below $T_{C,\mathrm{MFT}}$ and above T_X, $\xi_{\mathrm{AFM}} \sim a$. The onset of AFM ordering is signalled by an exponential growth in ξ_{AFM}. That is, T_X is the maximum temperature at which the AFM correlation length ξ_{AFM} [15] has an exponential dependence. Below T_X, the AFM correlation length can then be written as [74]

$$\xi_{\mathrm{AFM}}(T) \sim \frac{c_s}{k_B T} e^{2\pi\rho_s/k_B T} \approx c_0 a \exp\left(\frac{2\pi b_0 J_{\mathrm{H}}}{k_B T}\right) \tag{3.18}$$

Where ρ_s is the zero temperature spin stiffness and c_s is the spin-wave velocity[§]. In the second approximation, a functional form fitted from Monte Carlo data is shown. The coefficients are $c_0 \sim 0.26$, $b_0 \sim 0.2$ [25, 74]. The Heisenberg model coupling $J_{\mathrm{H}} = 4J^2/U$ has been introduced and a is the lattice spacing. The temperature dependence of the correlation length in Eq. (3.18) is shown in Fig. 3.4. At weak-coupling, this crossover temperature coincides with the critical temperature computed from Eq. (3.17), but in the strong-coupling regime, it behaves as $T_X \approx T_C \sim 4J^2/U$ (see, for example, [73]). This behaviour can be described using a non-linear sigma model approach to model the crossover from weak to strong coupling regimes, see [15, 16]. Fig. 3.5 shows a schematic phase diagram for the Hubbard model in 2D at half-filling based on Fig. 2 of [15].

[§] Spin stiffness is defined through [27] $\chi^{xx}(\underset{\sim}{\mathbf{q}} \approx \mathbf{Q}, \omega = 0) = \frac{N_0^2}{\rho_s (q-Q)^2}$.The spin-wave velocity is defined as $c_s^2 = \rho_s/\chi_\perp$ [27], with $\chi_\perp$ defined as [27] $\chi_\perp = \chi^{xx}(\underset{\sim}{\mathbf{q}} = 0, \omega = 0)$. The susceptibility χ^{xx} is computed according to the methods presented in Section 3.2.1. In particular Eqs. (3.19) and (3.21).

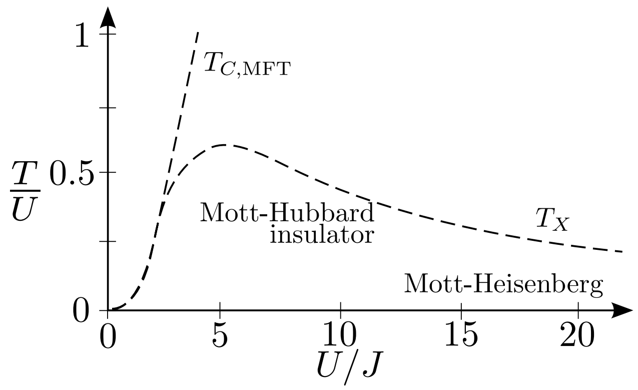

Figure 3.5: Schematic phase diagram of the 2D Hubbard model at half-filling (based on Fig. 2 from [15]). $T_{C,\mathrm{MFT}}$ is the critical temperature computed from the gap equation, Eq. (3.17). T_X is the actual temperature at which the crossover happens.

3.2.1 Susceptibilities

One of the key results in this thesis is the explicit connection made between the physical observables of scattered light intensity and spectrum (written in terms of static and dynamic response functions) and the susceptibilities calculated from the Hubbard model. First, the different expressions that connect the response functions and the model susceptibilities are introduced. This is followed by the susceptibilities computed first in the mean field theory and the susceptibilities computed within the RPA.

The Fourier transform in time of the susceptibility function is defined as

$$\chi^{ij}(\mathbf{q},\mathbf{q}';\omega) = \int dt \left[\frac{i}{2N_s^2}\left\langle \mathcal{T}\hat{O}^i_{\mathbf{q}}(0)\hat{O}^j_{-\mathbf{q}'}(t)\right\rangle\right] e^{i\omega t}, \tag{3.19}$$

where $\mathcal{T}$ represents the time ordered product, and $\hat{O}^i_{\mathbf{q}}(t)$ can be $\hat{\rho}_{\mathbf{q}}(t)$ or $\hat{S}^i_{\mathbf{q}}(t)$. where operators $\hat{O}^i_{\mathbf{q}}$ can be any of the spin operators (following the convention used by Schrieffer et al. [109])

$$\hat{S}^z_{\mathbf{q}} = \sum_{\mathbf{k}} \hat{c}^\dagger_{\mathbf{k}+\mathbf{q},\uparrow}\hat{c}_{\mathbf{k},\uparrow} - \hat{c}^\dagger_{\mathbf{k}+\mathbf{q},\downarrow}\hat{c}_{\mathbf{k},\downarrow}, \tag{3.20}$$

$$\hat{S}^x_{\mathbf{q}} = \sum_{\mathbf{k}} \hat{c}^\dagger_{\mathbf{k}+\mathbf{q},\uparrow}\hat{c}_{\mathbf{k},\downarrow} + \hat{c}^\dagger_{\mathbf{k}+\mathbf{q},\downarrow}\hat{c}_{\mathbf{k},\uparrow}, \tag{3.21}$$

$$\hat{S}^y_{\mathbf{q}} = -i\sum_{\mathbf{k}} \hat{c}^\dagger_{\mathbf{k}+\mathbf{q},\uparrow}\hat{c}_{\mathbf{k},\downarrow} - \hat{c}^\dagger_{\mathbf{k}+\mathbf{q},\downarrow}\hat{c}_{\mathbf{k},\uparrow}, \tag{3.22}$$

$$\hat{S}^+_{\mathbf{q}} = \frac{1}{\sqrt{2}}\left(\hat{S}^x_{\mathbf{q}} + i\hat{S}^y_{\mathbf{q}}\right) = \sqrt{2}\sum_{\mathbf{k}} \hat{c}^\dagger_{\mathbf{k}+\mathbf{q}\uparrow}\hat{c}_{\mathbf{k}\downarrow}, \qquad \hat{S}^-_{\mathbf{q}} = \left(\hat{S}^+_{-\mathbf{q}}\right)^\dagger \tag{3.23}$$

or the total density operator

$$\hat{\rho}_{\mathbf{q}} = \sum_g \hat{\rho}_{\mathbf{q}g} = \sum_{\mathbf{k},g} \hat{c}^\dagger_{\mathbf{k}+\mathbf{q},g}\hat{c}_{\mathbf{k},g}. \tag{3.24}$$

In Sections 4.2 and 4.3 the observable scattered intensity and scattered spectrum are shown to be directly computable in terms of the *response functions*. The *static response function* is defined as

$$\mathcal{S}^{g_3g_4}_{g_2g_1}(\mathbf{q},\mathbf{q}') \equiv \frac{1}{N_s^4}\sum_{\mathbf{k},\mathbf{k}'}\left\langle \hat{c}^{\dagger}_{\mathbf{k}+\mathbf{q}g_4}\hat{c}_{\mathbf{k}g_3}\hat{c}^{\dagger}_{\mathbf{k}'-\mathbf{q}'g_2}\hat{c}_{\mathbf{k}'g_1}\right\rangle_c . \tag{3.25}$$

The subscript c denotes a connected correlation function. The definition in Eq. (3.25) has more indices than that of Eq. (3.19) because they are needed to formulate the general formalism for scattering off atoms trapped in optical lattices. Every symbol with two superscripts ij can be written as a linear combination of a symbol with four indices and vice-versa [see Eqs. (5.10), (5.11) and (5.12)]. The dynamic equivalent of Eq. (3.25), the *dynamic response function* is defined as

$$\mathcal{S}^{g_3g_4}_{g_2g_1}(\mathbf{q},\mathbf{q}';\omega) = \frac{1}{N_s^4}\sum_{\mathbf{k},\mathbf{k}'}\int dte^{i\omega t}\left\langle \hat{c}^{\dagger}_{\mathbf{k}+\mathbf{q}g_4}(0)\hat{c}_{\mathbf{k}g_3}(0)\hat{c}^{\dagger}_{\mathbf{k}'-\mathbf{q}'g_2}(t)\hat{c}_{\mathbf{k}'g_1}(t)\right\rangle_c . \tag{3.26}$$

The *static response function* can be computed by integrating the dynamic response function over ω,

$$\mathcal{S}^{g_3g_4}_{g_2g_1}(\mathbf{q},\mathbf{q}') = \hbar\int\limits_0^{\infty} d\omega\mathcal{S}^{g_3g_4}_{g_2g_1}(\mathbf{q},\mathbf{q}',\omega). \tag{3.27}$$

The connection between time-ordered susceptibilities and physically observable response functions is made using linear response theory [35]. This formalism allows to connect time-ordered correlation functions to the response functions needed for scattered intensity and spectrum. At temperature $T = 0$, the dynamic response function $\mathcal{S}^{ij}(\mathbf{q},\mathbf{q}';\omega)$ is related to the retarded susceptibility $\chi^{ij\,R}$ via

$$\mathcal{S}^{ij}(\mathbf{q},\mathbf{q}';\omega) = \frac{-2}{\pi N_s^2}\mathrm{Im}\left[\chi^{ij\,R}(\mathbf{q},\mathbf{q}';\omega)\right], \tag{3.28}$$

and at finite $T = 1/k_B\beta$:

$$\mathcal{S}^{ij}(\mathbf{q},\mathbf{q}';\omega) = \frac{-2}{\pi(1-e^{-\beta\omega})N_s^2}\mathrm{Im}\left[\chi^{ij\,R}(\mathbf{q},\mathbf{q}';\omega)\right], \tag{3.29}$$

where the indices $i, j = \rho, z, +, -$. The factor of 2 in Eq. (3.28) is there to compensate for the unconventional factor of 2 in Eq. (3.19). $\chi^{ij\,R}$ is the *retarded susceptibility*. Retarded correlation functions are needed because the intensity and the spectrum are physical observables. The connection between *time-ordered* susceptibilities and retarded susceptibilities is made via analytical continuation, resulting in [35]

$$\begin{aligned}\mathrm{Re}[\chi^{ij}(\mathbf{q},\mathbf{q}';\omega)] =& \mathrm{Re}[\chi^{ijR}(\mathbf{q},\mathbf{q}';\omega)]\\ \mathrm{Im}[\chi^{ij}(\mathbf{q},\mathbf{q}';\omega)] =& \mathrm{sgn}(\omega)\mathrm{Im}[\chi^{ijR}(\mathbf{q},\mathbf{q}';\omega)].\end{aligned} \tag{3.30}$$

In the following section, all the computed susceptibilities are time-ordered correlations functions or their time Fourier transform. The related retarded functions are obtained numerically using Eqs. (3.28) and (3.30).

Mean field susceptibilities at zero temperature

When computing the scattered light off atoms in an optical lattice, only three types of susceptibilities will be needed. The density (charge), longitudinal, and transverse spin susceptibilities. In this section the results presented are for a two dimensional Hubbard model in a square lattice at half-filling and at zero temperature for a system in an anti-ferromagnetic ground state computed within the mean field approximation. At $T = 0$, the first band is full and the second one is empty. Thus, the only processes allowed are those that start with an atom in the lower band and end up with it in the upper one. This Pauli blocking effect is not present at finite temperature and the susceptibilities have many more terms which account for the other intraband scattering processes. The zero temperature results were first presented by Schrieffer et al. in [109].

The broken symmetry in the system is manifest in the matrix version of the Hamiltonian, Eq. (3.9). This matricial structure also carries over to the susceptibilities which take the following form,

$$\boldsymbol{\chi}^{ij}(\underset{\sim}{\mathbf{q}}, \omega) = \begin{pmatrix} \chi^{ij}(\underset{\sim}{\mathbf{q}}, \underset{\sim}{\mathbf{q}}; \omega) & \chi^{ij}(\underset{\sim}{\mathbf{q}}, \underset{\sim}{\mathbf{q}} + \mathbf{Q}; \omega) \\ \chi^{ij}(\underset{\sim}{\mathbf{q}} + \mathbf{Q}, \underset{\sim}{\mathbf{q}}; \omega) & \chi^{ij}(\underset{\sim}{\mathbf{q}} + \mathbf{Q}, \underset{\sim}{\mathbf{q}} + \mathbf{Q}; \omega) \end{pmatrix}. \tag{3.31}$$

Because periodic boundary conditions are imposed in the solution of the Hamiltonian [Eqs. (3.6) and (3.7)], only diagonal terms are present in Eq. (3.19). I.e., only terms where $\mathbf{q} = \mathbf{q}'$. In the *sdw* case treated here, this condition is modified to $\underset{\sim}{\mathbf{q}} = \underset{\sim}{\mathbf{q}}'$ or $\underset{\sim}{\mathbf{q}} = \underset{\sim}{\mathbf{q}}' + \mathbf{Q}$. With the momenta $\underset{\sim}{\mathbf{q}}$ belonging to the RBZ, only the four possible combinations in Eq. (3.31) are present. Using Eqs. (3.13), (3.19) and (3.24), the charge susceptibility within the MFT takes the following matricial form,

$$\boldsymbol{\chi}^{\rho\rho}_{(0)}(\underset{\sim}{\mathbf{q}}, \omega) = \begin{pmatrix} \chi^{\rho\rho}_{(0)}(\underset{\sim}{\mathbf{q}}, \underset{\sim}{\mathbf{q}}; \omega) & 0 \\ 0 & \chi^{\rho\rho}_{(0)}(\underset{\sim}{\mathbf{q}} + \mathbf{Q}, \underset{\sim}{\mathbf{q}} + \mathbf{Q}; \omega) \end{pmatrix}. \tag{3.32}$$

In Eq. (3.32) the off-diagonal terms are zero because the sum over spins in Eq. (3.24) combined with the factor $\eta(g)$ [Eq. (3.5)] cancels the term. The diagonal component can be written as

$$\chi^{\rho\rho}_{(0)}(\tilde{\mathbf{q}},\tilde{\mathbf{q}};\omega) = -\frac{1}{2N_s^2}\sum_{\mathbf{k}}^{\mathrm{RBZ}}\left(1-\frac{\epsilon_{\mathbf{k}}\epsilon_{\mathbf{k}+\tilde{\mathbf{q}}}+\Delta^2}{E_{\mathbf{k}}E_{\mathbf{k}+\tilde{\mathbf{q}}}}\right)\left(\frac{1}{\hbar\omega-E_{\mathbf{k}}-E_{\mathbf{k}+\tilde{\mathbf{q}}}+i\delta}\right.$$
$$\left.+\frac{1}{-\hbar\omega-E_{\mathbf{k}}-E_{\mathbf{k}+\tilde{\mathbf{q}}}+i\delta}\right). \tag{3.33}$$

Here, $\tilde{\mathbf{q}}$ represents a vector that belongs to the full BZ. In the language of the RBZ this means that, in both sides of the equation, $\tilde{\mathbf{q}}$ can be equal to $\underset{\sim}{\mathbf{q}}$ or $\underset{\sim}{\mathbf{q}}+\mathbf{Q}$. At the MFT level, the longitudinal spin susceptibility coincides with the charge susceptibility of Eq. (3.33)

$$\boldsymbol{\chi}^{zz}_{(0)}(\underset{\sim}{\mathbf{q}},\omega) = \boldsymbol{\chi}^{\rho\rho}_{(0)}(\underset{\sim}{\mathbf{q}},\omega). \tag{3.34}$$

In the next section, it will be shown that, going beyond MFT to the RPA approximation, the charge and longitudinal spin susceptibility differ [Eqs. (3.45) and (3.46) and Fig. 3.7(b)].

The transverse spin susceptibility is not diagonal; it has the full matrix structure of Eq. (3.31). This means that apart from the diagonal terms, the off-diagonal terms which link $\underset{\sim}{\mathbf{q}}$ with $\underset{\sim}{\mathbf{q}}+\mathbf{Q}$ are also non-zero. In matrix form it is

$$\boldsymbol{\chi}^{+-}_{(0)}(\underset{\sim}{\mathbf{q}},\omega) = \begin{pmatrix} \chi^{+-}_{(0)}(\underset{\sim}{\mathbf{q}},\underset{\sim}{\mathbf{q}};\omega) & \chi^{+-}_{(0)}(\underset{\sim}{\mathbf{q}},\underset{\sim}{\mathbf{q}}+\mathbf{Q};\omega) \\ \chi^{+-}_{(0)}(\underset{\sim}{\mathbf{q}}+\mathbf{Q},\underset{\sim}{\mathbf{q}};\omega) & \chi^{+-}_{(0)}(\underset{\sim}{\mathbf{q}}+\mathbf{Q},\underset{\sim}{\mathbf{q}}+\mathbf{Q};\omega) \end{pmatrix}. \tag{3.35}$$

The matrix elements are

$$\chi^{+-}_{(0)}(\tilde{\mathbf{q}},\tilde{\mathbf{q}};\omega) = -\frac{1}{2N_s^2}\sum_{\mathbf{k}}^{\mathrm{RBZ}}\left(1-\frac{\epsilon_{\mathbf{k}}\epsilon_{\mathbf{k}+\tilde{\mathbf{q}}}-\Delta^2}{E_{\mathbf{k}}E_{\mathbf{k}+\tilde{\mathbf{q}}}}\right)\left(\frac{1}{\hbar\omega-E_{\mathbf{k}}-E_{\mathbf{k}+\tilde{\mathbf{q}}}+i\delta}\right.$$
$$\left.+\frac{1}{-\hbar\omega-E_{\mathbf{k}}-E_{\mathbf{k}+\tilde{\mathbf{q}}}+i\delta}\right), \tag{3.36}$$

$$\chi^{+-}_{(0)}(\tilde{\mathbf{q}},\tilde{\mathbf{q}}+\mathbf{Q};\omega) = -\frac{1}{2N_s^2}\sum_{\mathbf{k}}^{\mathrm{RBZ}}\frac{\Delta(E_{\mathbf{k}}+E_{\mathbf{k}+\tilde{\mathbf{q}}})}{E_{\mathbf{k}}E_{\mathbf{k}+\tilde{\mathbf{q}}}}\left(\frac{1}{\hbar\omega-E_{\mathbf{k}}-E_{\mathbf{k}+\tilde{\mathbf{q}}}+i\delta}\right.$$
$$\left.-\frac{1}{-\hbar\omega-E_{\mathbf{k}}-E_{\mathbf{k}+\tilde{\mathbf{q}}}+i\delta}\right). \tag{3.37}$$

Here as in Eq. (3.33), $\tilde{\mathbf{q}}$ represents a vector that belongs to the full BZ. The transverse spin susceptibility is different from the longitudinal one because the spin isotropy is not conserved within the MFT approximation [Eq. (3.2)].

The term $i\delta$ in the denominator in Eqs. (3.33), (3.36) and (3.37) is an infinitesimal which results from integrating over time to do the Fourier transform in Eq. (3.19). If the computations were to be done only at the MFT level, these expressions could be simplified by means of Dirac's formula [129],

$$\frac{1}{x'-x\mp i\delta}=\mathcal{P}\frac{1}{x'-x\pm i\delta}\pm i\pi\delta(x'-x). \tag{3.38}$$

Here, $\mathcal{P}$ represents the Cauchy principal value and $\delta(x)$ is Dirac's delta function [128]. Scattered light is a physical observable, and according to Eq. (3.28), observables are related to the imaginary part of the retarded susceptibility [see Eq. (3.30)]. Using Eq. (3.38), the imaginary part of Eq. (3.36) can be written as

$$\begin{aligned}\mathrm{Im}[\chi^{+-}_{(0)}(\tilde{\mathbf{q}},\tilde{\mathbf{q}};\omega)]=\frac{\pi}{2N_s^2}\sum_{\mathbf{k}}^{\mathrm{RBZ}}\left(1-\frac{\epsilon_{\mathbf{k}}\epsilon_{\mathbf{k}+\tilde{\mathbf{q}}}-\Delta^2}{E_{\mathbf{k}}E_{\mathbf{k}+\tilde{\mathbf{q}}}}\right)&\left[\delta(\hbar\omega-E_{\mathbf{k}}-E_{\mathbf{k}+\tilde{\mathbf{q}}})\right.\\&\left.-\delta(\hbar\omega+E_{\mathbf{k}}+E_{\mathbf{k}+\tilde{\mathbf{q}}})\right].\end{aligned} \tag{3.39}$$

At $T=0$, only positive frequencies are allowed because a negative frequency component is equivalent to an energy loss for the system, which, if the system is in its ground state, is not possible [91]. For $\omega>0$, the imaginary part of the time-ordered product susceptibility in Eq. (3.39) is equivalent to that of the retarded one [35]. From Eq. (3.39) it is clear that in the MFT approximation the only terms that contribute to the susceptibility appear at $\hbar\omega=-E_{\mathbf{k}}-E_{\mathbf{k}+\tilde{\mathbf{q}}}$, which are clearly only due to the excitations of the single-particles in the system. In this thesis, the MFT susceptibilities are fed into the RPA ones, presented in the following section. Eq. (3.39) is not very convenient for numerical computations. For the results presented in Chapters 5, 6 and 7, the infinitesimal δ is given a finite value equal to the frequency resolution [$\delta=0.07J$]. With a finite δ, the Dirac delta peak takes the form of a Lorentzian curve with a width related to the finite value of δ [see Fig. 3.6(a)]. Denoting by Γ the finite value assigned to δ, the numerical susceptibility can be written as

$$\begin{aligned}\mathrm{Im}[\chi^{+-}_{(0)}(\tilde{\mathbf{q}},\tilde{\mathbf{q}};\omega)]\approx&\frac{1}{2N_s^2}\sum_{\mathbf{k}}^{\mathrm{RBZ}}\left(1-\frac{\epsilon_{\mathbf{k}}\epsilon_{\mathbf{k}+\tilde{\mathbf{q}}}-\Delta^2}{E_{\mathbf{k}}E_{\mathbf{k}+\tilde{\mathbf{q}}}}\right)\left[\frac{\Gamma}{(\hbar\omega-E_{\mathbf{k}}-E_{\mathbf{k}+\tilde{\mathbf{q}}})^2+\Gamma^2}\right.\\&\left.-\frac{\Gamma}{(\hbar\omega+E_{\mathbf{k}}+E_{\mathbf{k}+\tilde{\mathbf{q}}})^2+\Gamma^2}\right]\\=&\sum_{\mathbf{k}}^{\mathrm{RBZ}}\mathrm{Im}\left[\chi^{+-(\mathbf{k})}_{(0)}(\tilde{\mathbf{q}},\tilde{\mathbf{q}};\omega)\right].\end{aligned} \tag{3.40}$$

This expression illustrates how the imaginary part of the MFT susceptibilities are numerically computed. In the RPA case, the complex-valued time-ordered susceptibilities are computed with a finite value for δ. To do this computation, the complex-valued MFT expressions are fed to the RPA expressions [see below, Eqs. (3.45), (3.46) and (3.47)], and the imaginary part is taken at the last step to obtain the observable magnitude.

3.2.2 Mean-field susceptibilities at finite temperature

In this section the finite temperature MFT static structure factors [Eq. (4.29)] necessary to compute the inelastic component of the scattered light [Eq. (4.28)] is presented. This calculation can be evaluated using the imaginary time Matsubara formalism, but it is more straightforward to evaluate the correlation functions directly in the MFT from the Hamiltonian (3.16). Only the connected correlation function in Eq. (4.29) needs to be evaluated. Starting with the original fermions belonging to the full Brillouin Zone, these are transformed into the two-effective-bands fermions defined in the RBZ via the Bogoliubov transformation Eq. (3.13). Given the quadratic form of the diagonal MFT Hamiltonian obtained after performing the Bogoliubov transformation [Eq. (3.16)], the correlation functions can be simplified easily. All the terms have the following form: $\left\langle \hat{c}^{\dagger}_{\alpha_4\mathbf{k}+\mathbf{q},g_4}\hat{c}_{\alpha_3\mathbf{k},g_3}\hat{c}^{\dagger}_{\alpha_2\mathbf{k}'-\mathbf{q}',g_2}\hat{c}_{\alpha_1\mathbf{k}',g_1}\right\rangle_c$. Applying Wick's theorem [71], it is clear that

$$\left\langle \hat{c}^{\dagger}_{\alpha_4\mathbf{k}+\mathbf{q},g_4}\hat{c}_{\alpha_3\mathbf{k},g_3}\hat{c}^{\dagger}_{\alpha_2\mathbf{k}'-\mathbf{q}',g_2}\hat{c}_{\alpha_1\mathbf{k}',g_1}\right\rangle_c = \left\langle \overbrace{\hat{c}^{\dagger}_{\alpha_4\mathbf{k}+\mathbf{q},g_4}\overbrace{\hat{c}_{\alpha_3\mathbf{k},g_3}\hat{c}^{\dagger}_{\alpha_2\mathbf{k}'-\mathbf{q}',g_2}}\hat{c}_{\alpha_1\mathbf{k}',g_1}}\right\rangle_c \tag{3.41}$$

I.e., the expectation value is zero unless the effective band index ($\alpha_i,\ \ i=1,\ldots,4$), the spin index ($g_i$), and the momenta all coincide for the two contractions. For each contraction, $\left\langle \hat{c}^{\dagger}_{\alpha\mathbf{k},g}\hat{c}_{\alpha\mathbf{k},g}\right\rangle = n_{\alpha\mathbf{k}g}$, where $n_{1\mathbf{k}g} = f(E_{\mathbf{k}g})$ and $n_{2\mathbf{k}g} = 1 - f(E_{\mathbf{k}g})$, and $f(E) = [\exp(E/k_BT)+1]^{-1}$ is the Fermi-Dirac distribution. Collecting all the factors, the MFT static structure factor [see Eq. (4.29)] is given by

$$S^{g_3g_4}_{g_2g_1}(\Delta\mathbf{k}) = \delta_{g_4,g_1}\delta_{g_2,g_3}\frac{1}{N_s^4}\sum_{\alpha,\beta=1,2}\sum_{\mathbf{q}\mathbf{q}'}^{RBZ} g^{g_4g_2}_{\alpha,\beta}(\bar{\Delta}\mathbf{k},\mathbf{q},\mathbf{q}')n_{\alpha\mathbf{q}g_4}\left(1-n_{\beta\mathbf{q}'g_2}\right)\ , \tag{3.42}$$

where

$$\begin{aligned}
g^{g_4g_2}_{\alpha,\beta}(\Delta\mathbf{k},\mathbf{q},\mathbf{q}') =& \frac{1}{2}\mathfrak{u}^{*}_{\bar{\Delta}\mathbf{k}-\mathbf{q}}\mathfrak{u}_{\bar{\Delta}\mathbf{k}-\mathbf{q}'}\left[1+\frac{\Delta_{g_4}\Delta_{g_2}+\epsilon_{\mathbf{q}}\epsilon_{\mathbf{q}'}}{(-1)^{\alpha+\beta}E_{\mathbf{q}}E_{\mathbf{q}'}}\right]\\
&+\mathfrak{u}^{*}_{\bar{\Delta}\mathbf{k}-\mathbf{q}+\mathbf{Q}}\mathfrak{u}_{\bar{\Delta}\mathbf{k}-\mathbf{q}'}\left[\frac{\Delta_{g_4}}{(-1)^{\alpha+1}E_{\mathbf{q}}}+\frac{\Delta_{g_2}}{(-1)^{\beta+1}E_{\mathbf{q}'}}\right]\\
&+\frac{1}{2}\mathfrak{u}^{*}_{\bar{\Delta}\mathbf{k}-\mathbf{q}+\mathbf{Q}}\mathfrak{u}_{\bar{\Delta}\mathbf{k}-\mathbf{q}'+\mathbf{Q}}\left[1+\frac{\Delta_{g_4}\Delta_{g_2}-\epsilon_{\mathbf{q}}\epsilon_{\mathbf{q}'}}{(-1)^{\alpha+\beta}E_{\mathbf{q}}E_{\mathbf{q}'}}\right]\ ,
\end{aligned} \tag{3.43}$$

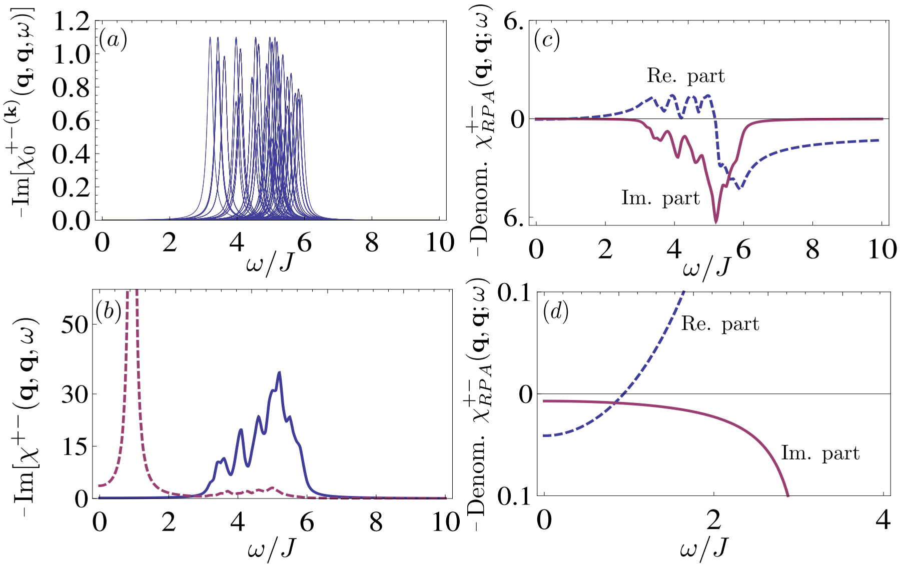

Figure 3.6: Comparison between the transverse spin susceptibility in the MFT and RPA approximation; for $U = 5J$, $\mathbf{q} = (\pi/a, 0)$ and with a finite frequency resolution given by $\delta = 0.1J$. (a) Individual contributions of each term $\chi_0^{+-(\mathbf{k})}(\mathbf{q},\mathbf{q};\omega)$ [Eq. (3.40)] for a small lattice with $N_s = 20$. Each term contributes with a Lorentzian shaped peak at $\hbar\omega = -E_{\mathbf{k}} - E_{\mathbf{k+q}}$. (b) shows the imaginary part of the MFT (solid) and RPA (dashed) susceptibility. (c) shows the imaginary (solid) and real (dashed) parts of the denominator (Denom.) in the RPA case $\chi^{+-}_{\mathrm{RPA}}(\mathbf{q},\mathbf{q};\omega)$. (d) zooms into both quantities close to zero energy and shows the zero-crossing in the real part.

and α and β are the effective band indices. The factor $\mathfrak{u}_{\mathbf{k}}$ denotes a sum plane waves over the lattice [See Eq. (4.25)]. The the product of Fermi distribution functions $[n_{\alpha\mathbf{q}g_4}\,(1 - n_{\beta\mathbf{q}'g_2})]$ results in Fermi blocking. This is the Pauli principle in action, i.e., only one fermion can occupy a given state. At low temperatures, the lower effective band is full and the upper effective band is empty; hence, the only scattering process allowed is for a particle in the lower effective band to be scattered to a state in the upper effective band. Thus, in the $T = 0$ limit, the terms of the form $n_{\alpha\mathbf{q}g_4}\,(1 - n_{\beta\mathbf{q}'g_2})$ only contribute for the pair $(\alpha,\beta) = (1,2)$. Contributions from all the other terms increases with temperature. Taking the limit $U \to 0$, the non-interacting case is recovered, as expected [¶].

3.3 RPA susceptibilities

The results of the previous section are mean field results, therefore they do not include the effect of quantum fluctuations. As exemplified in Eqs. (3.39), and (3.40), all they can show is the effect of single-particle excitations. To take into account quantum fluctuations in the treatment presented here, it is necessary to recall the solution of Dyson's equation in the Random Phase Approximation(RPA) for the susceptibilities, first derived in [109]. The basic idea behind the RPA is the fact that certain terms in the perturbation expansion (or Feynman diagrams) can be summed to infinite order because they *factorise* in a mathematical structure equivalent to a geometric series [77]. This remarkable property allows for obtaining an approximation to the susceptibility which, hopefully, captures the collective behaviour of the system. The collective behaviour will take the form of new poles in the correlation functions. In the case studied here, the charge $\boldsymbol{\chi}^{\rho\rho}_{\mathrm{RPA}}(\underset{\sim}{\mathbf{q}},\omega)$ [Eq. (3.45) and Fig. 3.7(b)] and longitudinal spin $\boldsymbol{\chi}^{zz}_{\mathrm{RPA}}(\underset{\sim}{\mathbf{q}},\omega)$ [Eq.(3.46) and Fig. 3.7(b)] susceptibilities do not contain any bosonic gapless modes. On the other hand, the transverse spin $\boldsymbol{\chi}^{+-}_{\mathrm{RPA}}(\underset{\sim}{\mathbf{q}},\omega)$ describes a collective mode [Eq. (3.47) and Fig. 3.7(a)].

The *factorisation* of the perturbative series can be illustrated by writing down the perturbation expansion for the density-density correlation in the bubble approximation. That is, considering contributions only from terms like the one in Eq. (3.32). The perturbation expansion then takes the following form

$$\begin{aligned}
\boldsymbol{\chi}^{\rho\rho}_{\mathrm{RPA}}(\underset{\sim}{\mathbf{q}},\omega) =&\boldsymbol{\chi}^{\rho\rho}_{(0)}(\underset{\sim}{\mathbf{q}},\omega) - \boldsymbol{\chi}^{\rho\rho}_{(0)}(\underset{\sim}{\mathbf{q}},\omega)U\boldsymbol{\chi}^{\rho\rho}_{(0)}(\underset{\sim}{\mathbf{q}},\omega) + \boldsymbol{\chi}^{\rho\rho}_{(0)}(\underset{\sim}{\mathbf{q}},\omega)U\boldsymbol{\chi}^{\rho\rho}_{(0)}(\underset{\sim}{\mathbf{q}},\omega)U\boldsymbol{\chi}^{\rho\rho}_{(0)}(\underset{\sim}{\mathbf{q}},\omega) + \ldots \\
=&\boldsymbol{\chi}^{\rho\rho}_{(0)}(\underset{\sim}{\mathbf{q}},\omega) - \boldsymbol{\chi}^{\rho\rho}_{(0)}(\underset{\sim}{\mathbf{q}},\omega)U\left[\boldsymbol{\chi}^{\rho\rho}_{(0)}(\underset{\sim}{\mathbf{q}},\omega) - \boldsymbol{\chi}^{\rho\rho}_{(0)}(\underset{\sim}{\mathbf{q}},\omega)U\boldsymbol{\chi}^{\rho\rho}_{(0)}(\underset{\sim}{\mathbf{q}},\omega) + \ldots\right] \\
=&\boldsymbol{\chi}^{\rho\rho}_{(0)}(\underset{\sim}{\mathbf{q}},\omega) - \boldsymbol{\chi}^{\rho\rho}_{(0)}(\underset{\sim}{\mathbf{q}},\omega)U\boldsymbol{\chi}^{\rho\rho}_{\mathrm{RPA}}(\underset{\sim}{\mathbf{q}},\omega).
\end{aligned} \tag{3.44}$$

It can be solved by inversion. This is how the RPA density-density susceptibility is obtained. The result is

$$\boldsymbol{\chi}^{\rho\rho}_{\mathrm{RPA}}(\underset{\sim}{\mathbf{q}},\omega) = \boldsymbol{\chi}^{\rho\rho}_{(0)}(\underset{\sim}{\mathbf{q}},\omega)\left[\mathbf{1} + U\boldsymbol{\chi}^{\rho\rho}_{(0)}(\underset{\sim}{\mathbf{q}},\omega)\right]^{-1} \tag{3.45}$$

[¶] Care must be taken when making $U \rightarrow 0$ as due to the special properties of the lattice and band structure the Fermi surface coincides with the reduced Brillouin zone and the Bogoliubov transformations is singular in the Fermi surface. Apart from that, the Bogoliubov transformation reduces to a particle hole transformation. In the Fermi surface given that in the non interacting limit there is no gap in the band structure at that point there is a degeneracy between both bands and thus the Bogoliubov quasi-particles are mixed states of particle-hole.

The longitudinal spin susceptibility coincides with the density only at the MFT level. If the whole RPA series is written down for this case, the factor $\eta(g)$ [Eq. (3.5)] in the definition of $\hat{S}^z_{\mathbf{q}}$ in Eq. (3.20), introduces a sign change in terms with an even number of interaction vertices (see Appendix A for the details) and the RPA susceptibility is different

$$\boldsymbol{\chi}^{zz}_{\mathrm{RPA}}(\utilde{\mathbf{q}},\omega) = \boldsymbol{\chi}^{zz}_{(0)}(\utilde{\mathbf{q}},\omega)\left[\mathbf{1} - U\boldsymbol{\chi}^{zz}_{(0)}(\utilde{\mathbf{q}},\omega)\right]^{-1}. \tag{3.46}$$

The transverse spin susceptibility is more interesting. In this case, the matricial susceptibility is not diagonal. This results in mixing of momenta, which in turn, is responsible for the appearance of the collective modes. It can be written in the same manner as for the charge and longitudinal spin as

$$\boldsymbol{\chi}^{+-}_{\mathrm{RPA}}(\utilde{\mathbf{q}},\omega) = \boldsymbol{\chi}^{+-}_{(0)}(\utilde{\mathbf{q}},\omega)\left[\mathbf{1} - U\boldsymbol{\chi}^{+-}_{(0)}(\utilde{\mathbf{q}},\omega)\right]^{-1} \tag{3.47}$$

The diagonal term in the RPA matrix has a complicated explicit form given by [27]

$$\chi^{+-}_{\mathrm{RPA}}(\tilde{\mathbf{q}},\tilde{\mathbf{q}};\omega) = \frac{\chi^{+-}_{(0)}(\tilde{\mathbf{q}},\tilde{\mathbf{q}};\omega)[1 - U\chi^{+-}_{(0)}(\tilde{\mathbf{q}}+\mathbf{Q},\tilde{\mathbf{q}}+\mathbf{Q};\omega)] + U[\chi^{+-}_{(0)}(\tilde{\mathbf{q}},\tilde{\mathbf{q}}+\mathbf{Q};\omega)]^2}{[1 - U\chi^{+-}_{(0)}(\tilde{\mathbf{q}},\tilde{\mathbf{q}};\omega)][1 - U\chi^{+-}_{(0)}(\tilde{\mathbf{q}}+\mathbf{Q},\tilde{\mathbf{q}}+\mathbf{Q};\omega)] - U^2[\chi^{+-}_{(0)}(\tilde{\mathbf{q}},\tilde{\mathbf{q}}+\mathbf{Q};\omega)]^2}. \tag{3.48}$$

The resulting expression for the off-diagonal term is also complicated. It is

$$\chi^{+-}_{\mathrm{RPA}}(\tilde{\mathbf{q}},\tilde{\mathbf{q}}+\mathbf{Q};\omega) = \frac{\chi^{+-}_{(0)}(\tilde{\mathbf{q}},\tilde{\mathbf{q}}+\mathbf{Q};\omega)}{[1 - U\chi^{+-}_{(0)}(\tilde{\mathbf{q}},\tilde{\mathbf{q}};\omega)][1 - U\chi^{+-}_{(0)}(\tilde{\mathbf{q}}+\mathbf{Q},\tilde{\mathbf{q}}+\mathbf{Q};\omega)] - U^2[\chi^{+-}_{(0)}(\tilde{\mathbf{q}},\tilde{\mathbf{q}}+\mathbf{Q};\omega)]^2}. \tag{3.49}$$

The RPA transverse spin susceptibility has the same form as Eqs. (3.45) and (3.46) but the physics described by it contain a new type of excitation, a magnon. Or in other words, the transverse spin susceptibility describes collective modes. The appearance of new poles can be seen in Figs. 3.6(c), and (d), where the real (dashed line) and imaginary (solid line) parts of the denominator of Eq. (3.48) are shown separately. In Fig. 3.6(d), it can be seen how both imaginary and real parts of the denominator approach zero but only the real part crosses it. That is the mathematical origin of the collective mode. The imaginary, observable, part of both MFT and RPA transverse spin susceptibilities is shown in Fig. 3.6(b) to illustrate how the RPA renormalises the single particle excitations and includes collective modes in the description.

It has been mentioned earlier in this chapter that the Hubbard model at half-filling maps onto the Heisenberg model for large values of U [74]. The transverse spin susceptibilities have been shown to reduce analytically to those of the Heisenberg model

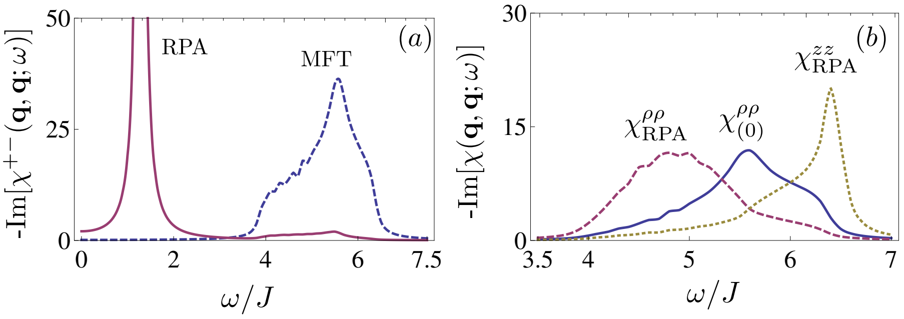

Figure 3.7: Imaginary part of the MFT and RPA density, longitudinal spin and transverse spin susceptibilities. This figure has the same parameters as in Fig. 3.6 in a 40×40 lattice. (a) Imaginary part of the transverse spin susceptibility for MFT (dashed) [Eq. (3.36)] and RPA (solid) [Eq. (3.48)]. (b) RPA density (dashed) [Eq. (3.45)] and longitudinal spin (dotted) [Eq. (3.46)] susceptibilities. For MFT (solid) both susceptibilities coincide, see Eqs. (3.33) and (3.34). At the RPA level, the charge and longitudinal spin susceptibilities are renormalised but they no longer coincide.

in the large U limit [27]. The Heisenberg model *gapless* excitation is present in the RPA calculation [27]. These excitations, *magnons*, have a dispersion relation of the following form

$$\hbar\omega_{\mathbf{q}} = 2J_{\mathrm{H}}\sqrt{1-\gamma_{\mathbf{q}}^2}\,, \tag{3.50}$$

with $\gamma_{\mathbf{q}} = (\cos q_x a + \cos q_y a)/2$. The effective coupling constant is J_H, and it can be calculated from the Hubbard model parameters as

$$J_{\mathrm{H}} = \frac{4J^2}{U}. \tag{3.51}$$

It is shown in Section 7.4 that this dispersion relation can, in principle, be directly observed experimentally, albeit it poses a very difficult technical challenge[‖].

RPA correction to the AFM order parameter

Quantum fluctuations also affect the AFM order parameter m. In the Heisenberg model, quantum fluctuations suppress the order parameter m by about 40% [74]. Schrieffer et al. [109] have computed corrections within the RPA to the order parameter m numerically for the half-filled Hubbard model. The RPA-corrected m_{RPA} can be calculated from a polynomial fit to the curve shown in Fig. 3.8. The data shown in this figure has been

---

[‖] In chapters 5 - 7, the particular case of ^{40}K trapped in an optical lattice is studied. With the parameters used in these chapters [See Section 5.1] the hopping amplitude J [Eq. (2.14)] corresponds to frequencies on the order of 5 to 20 Hz. Illuminating with a laser beam with a frequency of ≈ 3.91 THz, the necessary relative frequency resolution to observe the structure of the collective mode is of the order of less than 10^{-14}.

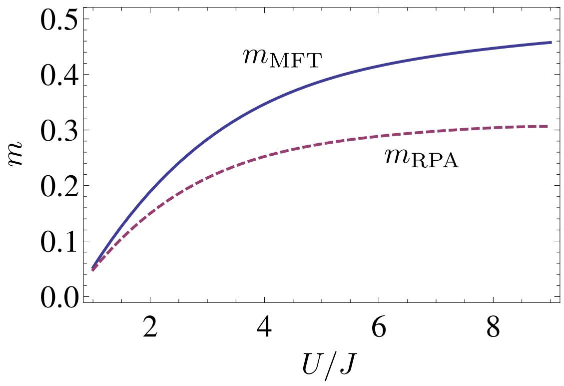

Figure 3.8: Renormalised order parameter compared to the mean-field theory order parameter. This data has been extracted from Schrieffer et al.'s Fig. 7 in [109].

extracted from Fig. 7 in [109]. The polynomial used to compute $m_{\rm RPA}$ in this thesis is

$$m_{\rm RPA} = b_0 + b_1 U/J - b_2(U/J)^2 + b_3(U/J)^3 - b_4(U/J)^4. \tag{3.52}$$

Here, the approximate values of the coefficients are $b_0 \simeq -0.11$, $b_1 \simeq 0.19$, $b_2 \simeq 0.035$, $b_3 \simeq 0.0031$ and $b_4 \simeq 1.1 \times 10^{-4}$.

Chapter 4

Optical diagnostics

In this chapter, the necessary formalism to do optical diagnostics is presented. In particular, the problem of light scattering off atoms in an optical lattice is analysed in detail. The focus is on the regime where light is tuned far from the atomic transition resonance. It will be shown how the atomic correlations can be mapped onto the fluctuations of the scattered light [52]. Light scattering is shown to be a powerful tool for diagnostics of the many-body state of atoms in an optical lattice.

4.1 Derivation of the scattered electric field

This section introduces the problem of matter interacting with light in the quantum regime. The formalism presented here follows the work of Javanainen and Ruostekoski [51]. In principle, the problem consists of writing down the Hamiltonian for light, matter, and an interaction term. With this starting point, a set of coupled equations of motion for the matter and light fields are derived and the initial problem is reduced to solving the derived equations.

The physical operators describing atoms in optical lattices were introduced in Chapter 2. In particular, Eq. (2.4), connects the $|\downarrow\rangle$ and $|\uparrow\rangle$ states of the model to the atomic hyperfine states. Here, the set of internal-states of the atoms is considered, which includes excited states. Thus, the states are split into two categories: ground g, and excited states e. The atomic states are denoted by $\{|F_g m_g\rangle, |F_e m_e\rangle\}_{g,e}$. Respectively, F_g or F_e is the angular momentum of the ground or the excited state, and m_g or m_e is its z component. To simplify the notation in the subscripts, m_g and m_e will be denoted respectively by g and e.

Light is described by the electric field operator $\hat{E}(\mathbf{r},t)$. This operator is decomposed into a positive and a negative frequency component, respectively denoted as $\hat{E}^{+}(\mathbf{r},t)$, and $\hat{E}^{-}(\mathbf{r},t)$. These two operators are adjoint to each other:

$$\hat{E}^{-}(\mathbf{r},t) = \left[\hat{E}^{+}(\mathbf{r},t)\right]^{\dagger}. \tag{4.1}$$

The electric field can be written in the plane wave representation. In this representation, $\hat{a}_{\mathbf{q}}$ is the annihilation operator for a photon with wave vector $\mathbf{q}$ and mode frequency $\nu_{\mathbf{q}}$. The electric field transverse polarisation is given by $\hat{\mathbf{e}}_{\mathbf{q}}$. In this representation, the positive frequency component is

$$\hat{E}^{+}(\mathbf{r},t) = \sum_{\mathbf{q}} \xi_{\mathbf{q}} \hat{\mathbf{e}}_{\mathbf{q}} \hat{a}_{\mathbf{q}}(t) e^{i\mathbf{q}\cdot\mathbf{r}}, \quad \xi_{\mathbf{q}} = \sqrt{\frac{\hbar\nu_{\mathbf{q}}}{2\epsilon_0 V}}. \tag{4.2}$$

Here, V is the quantisation volume and ϵ_0 is the vacuum permittivity.

For the purposes of the problem at hand, light-matter interaction is considered only at the dipole level. The dipole approximation is the lowest order approximation for the interaction between matter and light, but it is enough for the formalism presented in this thesis, as it is also the one with a highest probability amplitude. The dipole approximation neglects the spatial variation of the radiation field across the atom [17]. Moreover, the rotating-wave approximation is made. This is a standard approximation in quantum optics [28, 11, 23]; it throws away the rapidly oscillating terms under the assumption that they oscillate with such a high frequency that the atom only *sees* the average null contribution of the fast term. The RWA keeps only those terms in which a photon is absorbed and an atom is excited, and the reverse process. These two terms account for transitions between the ground and the excited state, and vice-versa. Processes involving simultaneous emission and excitation of an atom are neglected. With these approximation, the interaction term can be written in terms of the atomic transition dipole matrix elements between the ground state m_g and the excited state m_e. These terms have the following form:

$$\mathbf{d}_{eg} = (\mathbf{d}_{ge})^{*} = \langle F_e m_e | \mathbf{d} | F_g m_g \rangle = \mathfrak{D} \sum_{g} \langle F_g 1; F_e m_e | F_g m_g 1 g \rangle \, \hat{\mathbf{e}}_g^{*}. \tag{4.3}$$

The summation on the right-hand side of Eq. (4.3) runs over the circular polarisation vectors. These three vectors correspond to $g = -1, 0, 1$, and their explicit expression is

$$\hat{\mathbf{e}}_{+} = -\frac{1}{\sqrt{2}}\left(\hat{\mathbf{e}}_x + i\hat{\mathbf{e}}_y\right), \hat{\mathbf{e}}_0 = \hat{\mathbf{e}}_z, \hat{\mathbf{e}}_{-} = \frac{1}{\sqrt{2}}\left(\hat{\mathbf{e}}_x - i\hat{\mathbf{e}}_y\right). \tag{4.4}$$

Here, $\hat{\mathbf{e}}_i$ are the cartesian unit vectors ($i = x, y, z$). In Eq. (4.3), $\langle F_g 1; F_e m_e | F_g m_g 1 g\rangle$ denotes the corresponding Clebsch-Gordan coefficient [17], and

$$\mathfrak{D} = \left(\frac{6\pi\hbar\epsilon_0\gamma}{k^3}\right)^{1/2} \tag{4.5}$$

is the reduced dipole matrix element. The latter is related to the Weisskopf-Wigner radiative resonance linewidth γ by

$$\gamma = \frac{\mathfrak{D}^2 k^3}{6\pi\hbar\epsilon_0}. \tag{4.6}$$

The collision terms in the excited state, and those between atoms in the ground state and the excited state are ignored. As atoms only move a fraction of its wavelength during its lifetime, the centre of mass motion of the excited state can be ignored [51]. After all the previous provisos, the Hamiltonian that describes the scattering of light from atoms in an optical lattice can be written as [51]

$$\begin{aligned}\mathcal{H} =& \mathcal{H}_a + \int d\mathbf{r} \sum_e \Psi^\dagger_{F_e m_e}(\mathbf{r},t)\left[\frac{-\hbar^2}{2m}\nabla^2 + V_e(\mathbf{r}) - \mu + \omega_0\right]\Psi_{F_e m_e}(\mathbf{r},t)\\ &- \int d\mathbf{r}\sum_{g,e}\left[\mathbf{d}^*_{ge}\cdot\hat{E}^-(\mathbf{r},t)\Psi^\dagger_{F_g m_g}(\mathbf{r},t)\Psi_{F_e m_e}(\mathbf{r},t) + \mathbf{d}_{eg}\cdot\hat{E}^+(\mathbf{r},t)\Psi^\dagger_{F_e m_e}(\mathbf{r},t)\Psi_{F_g m_g}(\mathbf{r},t)\right]\\ &+ \hbar\sum_{\mathbf{q}'}\omega_{\mathbf{q}'}\hat{a}^\dagger_{\mathbf{q}'}(t)\hat{a}_{\mathbf{q}'}(t).\end{aligned} \tag{4.7}$$

Where $\mathcal{H}_a$ represents the Hamiltonian of the ground-state. A particular example of which is given in Eq. (2.5), which shows the Hamiltonian for a two-species system in an optical lattice. In Eq. (4.7), μ is the chemical potential. The second term in the first line represents the Hamiltonian of the excited state. $V_e(\mathbf{r})$ is the trapping potential felt by the atoms in the excited state[*]. The interaction between light and matter is described by the terms in the second line. The term in the third line is the Hamiltonian for free photons.

In order to obtain a tractable set of equations of motion from the Hamiltonian of Eq. (4.7), the light electric field $\hat{E}(\mathbf{r},t)$ is assumed to have a frequency Ω nearly resonant with the atomic transition ω_0 [51]. The equations of motion for the fields are obtained from Eq. (4.7) and Heisenberg's equation of motion[†]. As computed directly from

---

[*] The trapping potential felt by atoms in the excited state, with angular momentum F_e, does not necessarily have the same shape than that of the ground state atoms F_g [44].

[†] Heisenberg's equation of motion for a quantum operator $\hat{O}$ is [105]

$$\frac{d\hat{O}}{dt} = \frac{i}{\hbar}\left[\mathcal{H}, \hat{O}\right]$$

Eq. (4.7), these are coupled equations which cannot be solved in a direct manner. Off-resonance scattering of light can be studied analytically by considering that the incoming light is a monochromatic plane wave with frequency Ω_{in}. The incident light is assumed to propagate in a direction perpendicular to the lattice, that is, in the z direction as illustrated in Fig. 4.1. The positive frequency component of the incident electric field $\mathbf{E}^{+}_{\text{in}}$ can be written as

$$\mathbf{E}^{+}_{\text{in}}(\mathbf{r},t) = \frac{1}{2}\xi\hat{\mathbf{e}}_{\text{in}}e^{i\mathbf{k}_1\cdot\mathbf{r}-i\Omega_{\text{in}}t}, \tag{4.8}$$

where $\hat{\mathbf{e}}_{\text{in}}$ and $\mathbf{k}_1 = k\hat{\mathbf{e}}_z$ ($k = \Omega_{\text{in}}/c$) are, respectively, the polarisation and wavevector of the incoming light. Because the incoming light is assumed to be monochromatic, the equation of motion for the excited state can be solved adiabatically[‡]. This allows for writing down the excited state field operator in terms of the incoming light and the ground state field operators. The resulting expression for the scattered electric field only depends on the ground state field operators. In fact, the scattered electric field is proportional to the transition amplitude of atoms between the initial and final hyperfine electronic ground states g and g' [51],

$$\mathbf{E}^{+}_{\text{sc}}(\mathbf{r},t) = C\sum_{g'g}\mathbf{\Lambda}_{g'g}\int d^3r' e^{-\mathrm{i}\Delta\mathbf{k}\cdot\mathbf{r}'}\hat{\Psi}^{\dagger}_{g'}(\mathbf{r}',t)\hat{\Psi}_{g}(\mathbf{r}',t). \tag{4.9}$$

Thus, the problem has been reduced to solving the ground state Hamiltonian for the atoms, for example Eq. (2.5). The effects of light on the ground state can be regarded as secondary as long as the intensity of the incoming light is low. The assumption is also made that atoms do not experience multiple scattering of light and that QED effects are negligible [51].

In Eq. (4.9), the field is evaluated at $\mathbf{r}$ in the far radiation zone with the origin located inside the atomic sample. Thus, $|\mathbf{r}-\mathbf{r}'| \simeq r - \hat{\mathbf{n}}\cdot\mathbf{r}'$ with

$$\hat{\mathbf{n}} = \frac{(\mathbf{r}-\mathbf{r}')}{|\mathbf{r}-\mathbf{r}'|}, \tag{4.10}$$

The integral in Eq. (4.9) is over all the radiating atomic dipole sources at the positions $\mathbf{r}'$. The field is scattered in the direction $\mathbf{k}_2$ and the change of the wavevector of light upon scattering is, see Fig. 4.1,

$$\Delta\mathbf{k} = \mathbf{k}_2 - \mathbf{k}_1 = k(\hat{\mathbf{n}} - \hat{\mathbf{e}}_z) = k\left(\sin\theta\sin\phi, \sin\theta\cos\phi, \cos\theta - 1\right). \tag{4.11}$$

[‡] This boils down to the assumption $d/dt\left(e^{i\Omega t}\Psi_e(\mathbf{r},t)\right) \approx 0$.

Equation (4.9) encodes the relevant information about the level structure and its effects in the vector $\mathbf{\Lambda}_{g'g}$. It is defined as

$$\mathbf{\Lambda}_{g'g} = \frac{1}{\mathfrak{D}^2} \sum_e \hat{\mathbf{n}} \times (\hat{\mathbf{n}} \times \mathbf{d}^*_{g'e})(\hat{\mathbf{e}}_{\text{in}} \cdot \mathbf{d}_{eg}). \tag{4.12}$$

The atomic transition dipole matrix elements, $\mathbf{d}_{ge}$, between the ground state g and the excited state e are defined in Eq. (4.3). The prefactor C in Eq. (4.9) is

$$C = \frac{3\xi e^{ikr}\gamma}{4\delta kr}, \quad \delta \equiv \Omega_{\text{in}} - \omega_0. \tag{4.13}$$

δ denotes the detuning of the incident light frequency Ω_{in} from the atomic resonance frequency ω_0. From Eq. (4.9), it is clear that the polarisation of the scattered electric field is

$$\hat{\epsilon}_{g'g} = \frac{\mathbf{\Lambda}_{g'g}}{|\mathbf{\Lambda}_{g'g}|}. \tag{4.14}$$

It is worth mentioning that even though the excited state has been eliminated from the calculation of the electric field, it is not being neglected. It is present in the description of the scattered light in the polarisation factor. The scattered light polarised in a direction parallel to the polarisation vector of one of the scattered transitions can be computed projecting the scattered electric field along that direction. This is done dotting the given field with that particular polarisation

$$\mathbf{\Lambda}_{g'g} \to \mathbf{\Lambda}_{g'g}|_{\hat{\epsilon}_{g_1g_2}} = \mathbf{\Lambda}_{g'g} \cdot \hat{\epsilon}_{g_1g_2}\hat{\epsilon}_{g_1g_2} \tag{4.15}$$

Before going into the scattered intensity, the relation between the optical lattice laser and the probing laser has to be clarified. The frequency of the lasers used for creating an optical lattice is off-resonance from the atomic transition as this diminishes the atomic losses, see Chapter 2. Using active optical components, the lattice spacing can be modulated as in, for example, the case with accordion lattices where the lattice spacing is different from the one determined by the laser frequency [67, 125, 1]. In this thesis, the ratio κ between the probe light wavenumber k and the effective lattice light wavenumber k_{l} [Eq. 2.3] is varied. Thus, κ is defined as

$$k = \kappa\, k_{\text{l}} = \kappa \frac{\pi}{a}. \tag{4.16}$$

The parameter κ determines the range of momenta probed by the scattered light [see Eqs. (4.11) and (4.28)].

4.2 Scattered intensity

In the previous section, the scattered electric field was shown to depend on the ground-state of the atoms [Eq. (4.9)]. These fields can be detected by measuring the intensity or their spectrum [see Sec. 4.3]. This section concentrates on the intensity of the scattered light. If the scattered electric fields are known, the intensity is given by[§] [104]

$$I = 2\epsilon_0 c \left\langle \mathbf{E}^-_{\text{sc}}(\mathbf{r},t)\mathbf{E}^+_{\text{sc}}(\mathbf{r},t) \right\rangle . \tag{4.17}$$

Here, c denotes the speed of light in vacuum. To obtain the intensity in terms of the atomic correlation functions, the electric field amplitudes from Eq. (4.9) are substituted in Eq. (4.17). This is done along with the assumption that the atoms only populate the lowest energy band. In a similar fashion as was done in Chapter 2, the atom field operators are expanded in terms of the Wannier functions [Eq. (2.6)]. Here, $\hat{c}_{\mathbf{j}ng}$ is the annihilation operator for the atoms in the electronic ground state g in the n-th band and at the lattice site $\mathbf{j} = (j_x, j_y)$. By expanding the field operators making use of Wannier functions the intensity can be written as:

$$I(\Delta\mathbf{k}) = B \sum_{\substack{g_1,g_2\\ g_3,g_4}} \mathsf{M}^{g_3 g_4}_{g_2 g_1} \left(\sum_{\substack{\mathbf{j}_1,\mathbf{j}_2\\ \mathbf{j}_3,\mathbf{j}_4}} \sum_{\substack{n_1,n_2\\ n_4,n_4}} f^*_{\mathbf{j}_4 n_4,\mathbf{j}_3 n_3} f_{\mathbf{j}n_1,\mathbf{j}n_2} \left\langle \hat{c}^\dagger_{\mathbf{j}_4 n_4 g_4} \hat{c}_{\mathbf{j}_3 n_3 g_3} \hat{c}^\dagger_{\mathbf{j}_2 n_2 g_2} \hat{c}_{\mathbf{j}_1 n_1 g_1} \right\rangle \right). \tag{4.18}$$

In Eq. (4.18), the following factors have been defined

$$B \equiv I_{\text{in}} \left(\frac{3\gamma}{2\delta k r} \right)^2 , \quad I_{\text{in}} = \frac{1}{2}\epsilon_0 c \xi^2 . \tag{4.19}$$

I_{in} denotes the intensity of the incoming light. $\mathsf{M}^{g_3 g_4}_{g_2 g_1}$ encodes all the information on the level structure of the system and the polarisation of the probing light. These factors are defined as

$$\mathsf{M}^{g_3 g_4}_{g_2 g_1} = \mathbf{\Lambda}^*_{g_3 g_4} \mathbf{\Lambda}_{g_2 g_1} . \tag{4.20}$$

The spatial overlap between wavefunctions is denoted by $f_{\mathbf{i}n,\mathbf{j}m}$. The explicit definition of this factor is

$$f_{\mathbf{i}n,\mathbf{j}m}(\Delta\mathbf{k}) = \int d\mathbf{r} w^*_m(\mathbf{r} - \mathbf{r}_j) w_n(\mathbf{r} - \mathbf{r}_i) e^{-i\Delta\mathbf{k}\cdot\mathbf{r}} . \tag{4.21}$$

[§] Eq. (4.17) is a special case from the most general formula for the quantum intensity operator, as in formula (5.98) of [70]

$$I(\mathbf{r}) = \left\langle \hat{\mathbf{I}}(\mathbf{r}t) \right\rangle = \frac{\left\langle \hat{\mathbf{E}}^-(\mathbf{r}t) \times \hat{\mathbf{B}}^+(\mathbf{r}t) - \hat{\mathbf{B}}^-(\mathbf{r}t) \times \hat{\mathbf{E}}^+(\mathbf{r}t) \right\rangle}{\mu_0}$$

where as should be $\hat{\mathbf{E}}$ and $\hat{\mathbf{B}}$ represent the electric and magnetic field operator respectively. In the particular case of polarised incoming light beam it reduces to Eq. (4.17).

This follows the notation introduced by Douglas and Burnett [31]. Equation (4.18) is completely general, i.e., it includes both type of processes: those between atoms in the lowest band, and scattering events to higher bands [¶]. When the temperature is low enough, higher bands are unpopulated. In this regime, scattering to higher bands carries no information about the atomic correlations and can be studied separately. This is considered in Sec. 4.4. Even though when no information can be extracted from such processes, they cannot be ignored altogether as they contribute to the atom losses and heating effects. From this point onwards, and for the following section [Section 4.3], only processes within the lowest band [$n = 0$] are considered.

In the tight-binding regime, the spatial overlap between different sites in Eq. (4.18) is negligible. Mathematically, this corresponds to $f_{\mathbf{i}0,\mathbf{j}0}(\Delta\mathbf{k}) \approx \delta_{\mathbf{ij}} f_{\mathbf{i}0,\mathbf{i}0}(\Delta\mathbf{k})$, where $\delta_{\mathbf{ij}}$ is a Kronecker delta in lattice space. If the lattice potential does not depend, at least approximately, on the particular ground state level g, the Debye-Waller factor $\alpha_{\Delta\mathbf{k}}$ is the Fourier transform of the lattice site density. An analytical expression for this factor can be evaluated by means of the harmonic approximation to the Wannier functions introduced in Eq. (2.8),

$$\alpha_{\Delta\mathbf{k}} = |f_{\mathbf{i}0,\mathbf{i}0}(\Delta\mathbf{k})|^2 = \left|\int d^3\mathbf{r} e^{-i\Delta\mathbf{k}\cdot\mathbf{r}} |w_0(\mathbf{r})|^2\right|^2 = \prod_{i=x,y,z} \exp\left[-\frac{(\Delta k_i)^2 l_i^2}{2}\right]. \tag{4.22}$$

The oscillator length l_i is defined by Eq. (2.9). Hence, the scattered light intensity is [104]

$$I(\Delta\mathbf{k}) = \alpha_{\Delta\mathbf{k}} B \sum_{\substack{g_1,g_2\\g_3,g_4}} \mathsf{M}^{g_3 g_4}_{g_2 g_1} \sum_{\mathbf{i},\mathbf{j}} e^{i\Delta\mathbf{k}\cdot(\mathbf{r}_i - \mathbf{r}_j)} \left\langle \hat{c}^{\dagger}_{\mathbf{i}g_4} \hat{c}_{\mathbf{i}g_3} \hat{c}^{\dagger}_{\mathbf{j}g_2} \hat{c}_{\mathbf{j}g_1} \right\rangle. \tag{4.23}$$

The scattered intensity from the sample is dependent on the atomic correlations and the light serves only as a way of looking at those. The expression for the scattered intensity intensity expression [Eq. (4.23)] can be written in a more condensed matter theorist-friendly way. Using Eq. (3.6) to transform to momentum space representation results in

$$I(\Delta\mathbf{k}) = B\alpha_{\Delta\mathbf{k}} \sum_{\substack{g_1,g_2\\g_3,g_4}} \mathsf{M}^{g_3 g_4}_{g_2 g_1} \left(\frac{1}{N_s^4} \sum_{\mathbf{q},\mathbf{q}'} \mathfrak{u}^{*}_{\bar{\Delta}\mathbf{k}-\mathbf{q}} \mathfrak{u}_{\bar{\Delta}\mathbf{k}-\mathbf{q}'} \sum_{\mathbf{k},\mathbf{k}'} \left\langle \hat{c}^{\dagger}_{\mathbf{k}+\mathbf{q}g_4} \hat{c}_{\mathbf{k}g_3} \hat{c}^{\dagger}_{\mathbf{k}'-\mathbf{q}'g_2} \hat{c}_{\mathbf{k}'g_1} \right\rangle \right). \tag{4.24}$$

The sum of the plane waves over the lattice is denoted as

$$\mathfrak{u}_{\mathbf{k}} \equiv \sum_{\mathbf{j}} e^{-i\mathbf{k}\cdot\mathbf{r}_j}. \tag{4.25}$$

[¶] An equivalent expression to Eq. (4.23) where the effect of higher bands in the scattered light is taken was first presented in [31].

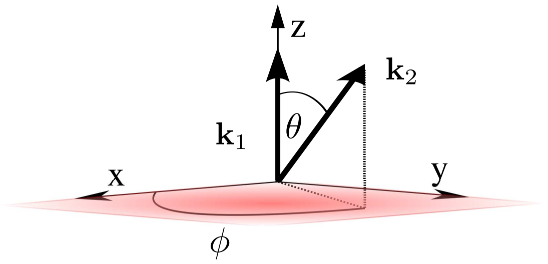

Figure 4.1: Schematic illustration of the light scattering set-up. The atoms are confined in the optical lattice close to the xy plane. The incident light field with the wavevector $\mathbf{k}_1$ propagates perpendicular to lattice in the positive z direction. The wavevector of the scattered light is denoted by $\mathbf{k}_2$ with the scattering direction determined by the coordinates θ and ϕ

The expectation values in Eq. (4.24) split into two possible categories, *connected* and *disconnected correlation functions*[‖](see, for example, Ch. 13.4 of [20]). All the $\mathbf{q} = \mathbf{q}' = 0$ terms in Eq. (4.24) correspond to the disconnected case; physically, disconnected correlations describe processes in which the initial and final states are the same. Consequently, connected correlations functions (indicated by the subscript c) correspond to processes where the initial and final states are different.

Evaluating the expected value in Eq. (4.24), the different contributions can be classified in terms of the elastic and inelastic components[**]. Thus, the scattered light can be separated in terms of the elastically and inelastically scattered light intensities $I_{\mathrm{e}}(\Delta\mathbf{k})$ and $I_{\mathrm{i}}(\Delta\mathbf{k})$, respectively,

$$I(\Delta\mathbf{k}) = I_{\mathrm{e}}(\Delta\mathbf{k}) + I_{\mathrm{i}}(\Delta\mathbf{k}) \tag{4.26}$$

$$I_{\mathrm{e}}(\Delta\mathbf{k}) = B\alpha_{\Delta\mathbf{k}} \left| \sum_g \mathbf{\Lambda}^*_{gg} \langle \hat{\rho}_{\bar{\Delta\mathbf{k}}g} \rangle \right|^2 = B\alpha_{\Delta\mathbf{k}} \sum_{g_1 g_3} \mathsf{M}^{g_3 g_3}_{g_1 g_1} \langle \hat{\rho}_{\bar{\Delta\mathbf{k}}g_3} \rangle \langle \hat{\rho}_{-\bar{\Delta\mathbf{k}}g_1} \rangle, \tag{4.27}$$

$$I_{\mathrm{i}}(\Delta\mathbf{k}) = B\alpha_{\Delta\mathbf{k}} \sum_{\substack{g_1, g_2\\ g_3, g_4}} \mathsf{M}^{g_3 g_4}_{g_2 g_1} S^{g_3 g_4}_{g_2 g_1}(\bar{\Delta\mathbf{k}}). \tag{4.28}$$

$\bar{\Delta\mathbf{k}}$ denotes the change of wave vector of light on the xy plane [$\Delta\mathbf{k}$ is defined in Eq. (4.11)]. The density operator $\hat{\rho}_{\mathbf{k}g}$ for the spin state g is given by Eq. (3.24), and the *static structure*

[‖] This separation can be understood in terms of Wick contractions [71]. Consider the time dependent version of the correlation in Eq. (4.24)

$$\begin{aligned}\left\langle \mathcal{T} \hat{c}^\dagger_{\mathbf{k}+\mathbf{q}g_4}(t_4) \hat{c}_{\mathbf{k}g_3}(t_3) \hat{c}^\dagger_{\mathbf{k}'-\mathbf{q}'g_2}(t_2) \hat{c}_{\mathbf{k}'g_1}(t_1) \right\rangle = &\left\langle \mathcal{T} \wick{\c1{\hat{c}^\dagger_{\mathbf{k}+\mathbf{q}g_4}(t_4)} \c1{\hat{c}_{\mathbf{k}g_3}(t_3)} \c2{\hat{c}^\dagger_{\mathbf{k}'-\mathbf{q}'g_2}(t_2)} \c2{\hat{c}_{\mathbf{k}'g_1}(t_1)}} \right\rangle \\ &+ \left\langle \mathcal{T} \wick{\c1{\hat{c}^\dagger_{\mathbf{k}+\mathbf{q}g_4}(t_4)} \c2{\hat{c}_{\mathbf{k}g_3}(t_3)} \c2{\hat{c}^\dagger_{\mathbf{k}'-\mathbf{q}'g_2}(t_2)} \c1{\hat{c}_{\mathbf{k}'g_1}(t_1)}} \right\rangle\end{aligned}$$

Here $\mathcal{T}$ denotes a time-ordered product [71]. The first term can be written as the product of two independent expectated values. In general, the second term links the involved momenta, which means that there is a momenta exchange. See also Section 4.3.1.

[**] See Section 4.3.1

factor is defined as

$$S^{g_3g_4}_{g_2g_1}(\bar{\Delta}\mathbf{k}) \equiv \frac{1}{N_s^4}\sum_{\mathbf{q},\mathbf{q}'\neq 0} \mathrm{u}^*_{\bar{\Delta}\mathbf{k}-\mathbf{q}}\mathrm{u}_{\bar{\Delta}\mathbf{k}-\mathbf{q}'}\sum_{\mathbf{k},\mathbf{k}'}\left\langle \hat{c}^\dagger_{\mathbf{k}+\mathbf{q}g_4}\hat{c}_{\mathbf{k}g_3}\hat{c}^\dagger_{\mathbf{k}'-\mathbf{q}'g_2}\hat{c}_{\mathbf{k}'g_1}\right\rangle_c. \tag{4.29}$$

The effect of the finite size of the lattice, due to the finite number of atoms in an optical lattice, is included in Eq. (4.29) via the $\mathrm{u}_\mathbf{k}$ factors. The real experimental system is not translationally invariant. In this thesis, as was explicitly done in Chapter 3, the system is approximated by an translationally invariant system. For a large lattice, the $\mathrm{u}_\mathbf{k}$ factors can be approximated by a delta function

$$\mathrm{u}_\mathbf{k} \to N_s^2\delta_{\mathbf{k},0} \tag{4.30}$$

and the static structure factor simplifies to

$$S^{g_3g_4}_{g_2g_1}(\bar{\Delta}\mathbf{k}) \simeq \sum_{\mathbf{k},\mathbf{k}'}\left\langle \hat{c}^\dagger_{\mathbf{k}+\bar{\Delta}\mathbf{k}g_4}\hat{c}_{\mathbf{k}g_3}\hat{c}^\dagger_{\mathbf{k}'-\bar{\Delta}\mathbf{k}g_2}\hat{c}_{\mathbf{k}'g_1}\right\rangle_c. \tag{4.31}$$

For a 40×40 lattice, using Eq. (4.31) in Eq. (4.28) leads to changes in the integrated inelastically scattered light intensity which are less than 2%. In Section 3.2.1, the static response function was introduced. This function is directly related to the correlations in the system. If the atomic gas trapped in an optical lattice, which is inhomogeneous, is approximated by the homogeneous and translationally invariant system, then the correlations are computed and result in diagonal response functions. The scattered light scattering [Eq. (4.28) can be written in terms of this functions as

$$I_\mathrm{i}(\Delta\mathbf{k}) \simeq B\alpha_{\Delta\mathbf{k}}\sum_{\mathbf{q}\neq 0}|\mathrm{u}_{\bar{\Delta}\mathbf{k}-\mathbf{q}}|^2\sum_{\substack{g_1,g_2\\g_3,g_4}}\mathsf{M}^{g_3g_4}_{g_2g_1}\mathcal{S}^{g_3g_4}_{g_2g_1}(\mathbf{q},\mathbf{q}). \tag{4.32}$$

This approximation still includes some finite-size effects. These finite-size effects are described by the diffraction pattern $|\mathrm{u}_{\bar{\Delta}\mathbf{k}-\mathbf{q}}|^2$.

In this section, the scattered light intensity has been shown to convey information about the atomic correlations function in the lattice. The crystal-like structure of the lattice is put to manifest in the diffraction pattern generated by the $|\mathrm{u}_{\bar{\Delta}\mathbf{k}-\mathbf{q}}|^2$ factors, and in overall envelope due to the Debye-Waller factor [Eq. (4.22)]. On the other hand, the level structure and the polarisation of the probe light is encoded in the $\mathsf{M}^{g_3g_4}_{g_2g_1}$.

4.2.1 Elastic component of the scattered light: single species atomic gas

In order to clarify the elastic component of the scattered light, the case of a uniformly filled lattice with a single-species is analysed here [104]. In this case, there is no broken translation symmetry and there is no interference nor magnetic ordering peaks. If there is a single-species g with a uniform f_g, the expectation value of the density operator is

$$\left\langle \hat{\rho}_{\bar{\Delta}\mathbf{k}g} \right\rangle = \mathfrak{u}_{\bar{\Delta}\mathbf{k}} f_g. \tag{4.33}$$

The atomic filling factor f_g is defined as the number of atoms of species g divided by the number of lattices sites,

$$f_g = \frac{N_g}{N_s^2}. \tag{4.34}$$

The change of light momentum $\bar{\Delta}\mathbf{k}$ is defined in Eq. (4.11). Using Eq. (4.33) into Eq. (4.27), the elastic component of the scattered light is

$$I_{\mathrm{e}}(\Delta\mathbf{k}) = B\alpha_{\Delta\mathbf{k}} |\mathfrak{u}_{\bar{\Delta}\mathbf{k}}|^2 \mathsf{M}^{gg}_{gg} \left| f_g \right|^2. \tag{4.35}$$

In the previous expression, there are three different factors: the Debye-Waller factor [Eq. (4.22)], the M^{gg}_{gg}-tensor [Eq. (4.20)], and the Bragg diffraction pattern of the lattice $|\mathfrak{u}_{\bar{\Delta}\mathbf{k}}|^2$. In the specific case of a 2D square lattice, this factor is the diffraction pattern resulting from a 2D square array of $N_s \times N_s$ diffracting apertures

$$|\mathfrak{u}_{\bar{\Delta}\mathbf{k}}|^2 = \prod_{\alpha=x,y} \frac{\sin^2\left(\frac{N_s \bar{\Delta}\mathbf{k}_\alpha a}{2}\right)}{\sin^2\left(\frac{\bar{\Delta}\mathbf{k}_\alpha a}{2}\right)}. \tag{4.36}$$

In Eqs. (4.35) and (4.36) and in the rest of this thesis, $\bar{\Delta}\mathbf{k}$ is projection of the change of momentum of the light upon scattering $\Delta\mathbf{k}$ [Eq. (4.11)] on the xy plane. It is clear from Eqs. (4.35) and (4.36) that in the uniformly filled single-species case[††], the elastic component of the scattered light carries no information about the correlations of the particles. All it contains is information about the filling (the maximum height of the diffraction peak in the forward direction is proportional to N_s^4, and is weighted by the square of the atomic filling factor f_g). Any other information to be extracted from the system about its correlations has to be obtained from analysing the intraband inelastic component of the scattered light [Eq. (4.28)]. Given the lattice-size scaling of the elastic diffraction pattern, blocking it before the detection of the light improves the detection of the inelastic component considerably [104]. This is analysed in detail in Sections 5.2 and 6.1.1.

For the elastic component of the single-species uniformly filled optical lattice, the effect of the Debye-Waller factor is negligible. It modulates the scattered light, but it

---

[††] This is also true when there are multiple-species all with uniform filling.

only affects it away from the forward direction. As shown above, the elastic component is a diffraction pattern which is to be blocked.

If translation symmetry is broken, the picture presented above no longer holds. In particular, in the AFM state studied in Sec. 3.2, it was shown that the bipartite nature of the AFM pattern breaks translation symmetry. This translates into a halving of the BZ which doubles its periodicity. If this is the case, as analysed in Section 5.2, the broken symmetry has an observable effect in the diffraction pattern. The new emerging peaks are a signature of the AFM ordering in the system. This effect was first analysed in Ref. [29] for the 3D Heisenberg model.

4.3 Scattered spectrum

In the previous Section, the relation between the scattered light intensity with the equal time atomic correlations [Eqs. (4.26)-(4.28)] was presented. This Section is devoted to the spectrum of the scattered light. It is shown how it conveys information about the excitation spectrum of the atoms in the lattice. The scattered light spectrum is obtained as the Fourier transform of the two-time correlation function of the scattered electric field [51]

$$\mathbb{S}(\Delta\mathbf{k},\omega) = A\int dt e^{i\omega t}\left\langle \mathbf{E}^{-}(\mathbf{r},0)\mathbf{E}^{+}(\mathbf{r},t)\right\rangle . \tag{4.37}$$

Here, A denotes a normalisation factor. Thus, the scattered spectrum can be written in terms of the two-time correlation functions of the atoms in the optical lattice. In the same fashion as was done with the intensity in the previous section, the spectrum can be separated into an elastic and inelastic component resulting in

$$\mathbb{S}(\Delta\mathbf{k},\omega) =\mathbb{S}_{\mathrm{e}}(\Delta\mathbf{k},\omega) + \mathbb{S}_{\mathrm{i}}(\Delta\mathbf{k},\omega), \tag{4.38}$$

$$\mathbb{S}_{\mathrm{e}}(\Delta\mathbf{k},\omega) =A'\alpha_{\Delta\mathbf{k}}\delta(\omega)\left|\sum_{g}\mathbf{\Lambda}_{gg}\left\langle\hat{\rho}_{-\bar{\Delta\mathbf{k}}g}\right\rangle\right|^{2}, \tag{4.39}$$

$$\mathbb{S}_{\mathrm{i}}(\Delta\mathbf{k},\omega) =A'\alpha_{\Delta\mathbf{k}}\sum_{\substack{g_1,g_2\\g_3,g_4}}\mathsf{M}_{g_2g_1}^{g_3g_4}S_{g_2g_1}^{g_3g_4}(\Delta\mathbf{k},\omega). \tag{4.40}$$

where $A'\equiv AB/(2\epsilon_0 c)$. The dynamical structure factor, which is analogous to the static case of Eq. (4.29), has been introduced in the last equation. It is defined as

$$S^{g_3g_4}_{g_2g_1}(\Delta\mathbf{k},\omega) = \frac{1}{N_s^4}\sum_{\mathbf{q},\mathbf{q}'\neq 0}\mathfrak{u}^*_{\bar{\Delta}\mathbf{k}-\mathbf{q}}\mathfrak{u}_{\bar{\Delta}\mathbf{k}-\mathbf{q}'}\sum_{\mathbf{k},\mathbf{k}'}\int dte^{i\omega t}\left\langle \hat{c}^\dagger_{\mathbf{k}+\mathbf{q}g_4}(0)\hat{c}_{\mathbf{k}g_3}(0)\hat{c}^\dagger_{\mathbf{k}'-\mathbf{q}'g_2}(t)\hat{c}_{\mathbf{k}'g_1}(t)\right\rangle_c . \tag{4.41}$$

The elastic component corresponds to a peak at $\omega = 0$. The subscript c indicates the connected diagrams for which $\omega \neq 0$. Non-negative frequencies corresponds to the excitations of the system [see Chapter 7]. Eq. (4.40) is approximated in a similar fashion to Eq. (4.32)

$$\mathbb{S}_{\mathrm{i}}(\Delta\mathbf{k},\omega) \simeq \alpha_{\Delta\mathbf{k}}A'\sum_{\mathbf{q}\neq 0}\left|\mathfrak{u}^*_{\bar{\Delta}\mathbf{k}-\mathbf{q}}\right|^2\sum_{\substack{g_1,g_2\\g_3,g_4}}\mathsf{M}^{g_3g_4}_{g_2g_1}\mathcal{S}^{g_3g_4}_{g_2g_1}(\mathbf{q},\mathbf{q};\omega). \tag{4.42}$$

4.3.1 Remark on the separation between the elastic and inelastic components of the scattered light

In Sections 4.2 and 4.3, the scattered light was separated into two components: the *elastic*, which encompasses processes in which there is no transfer of energy or momentum between the light and the system, and the *inelastic*, which contains any other possible process. The separation can be clarified by writing down a spectral decomposition of the dynamic response function [Eq. (3.26)]. This results in [91]

$$\begin{aligned}\mathcal{S}^{g_3g_4}_{g_2g_1}(\mathbf{q},\mathbf{q}',\omega) = \frac{1}{ZN_s^4}\sum_{m,n}\sum_{\mathbf{k},\mathbf{k}'}&e^{\beta E_m}\delta(\omega-(E_m-E_n)/\hbar))\times\\ &\times\left\langle m|\hat{c}^\dagger_{\mathbf{k}+\mathbf{q}g_4}\hat{c}_{\mathbf{k}g_3}|n\right\rangle\left\langle n|\hat{c}^\dagger_{\mathbf{k}'-\mathbf{q}'g_2}\hat{c}_{\mathbf{k}'g_1}|m\right\rangle .\end{aligned} \tag{4.43}$$

Here, Z is the grand canonical partition function [91]. In Eq. (4.43), for a non-degenerate system, the probability amplitudes that represent an elastic process are those for which $m = n$. For $m \neq n$ there is an energy transfer. For a non-degenerate system, only those transitions with $\omega = 0$ will be part of the elastic component. It is easy to see that this reasoning is still valid for the degenerate case. It can be shown by *lifting* the degeneracy, by adding another subindex to the energies $E_{m,\gamma}$, and repeating the same reasoning as for the non-degenerate system. Then, given that $E_m = E_{m,\gamma}\forall\gamma$, $\omega = 0$ is the elastic component of the scattered light, as stated earlier. From this, it follows that the elastic components of the scattered light results from the four operator expectation values that factor as $\left\langle\hat{c}^\dagger_{\mathbf{k}+\mathbf{q}g_4}\hat{c}_{\mathbf{k}g_3}\right\rangle\left\langle\hat{c}^\dagger_{\mathbf{k}'+\mathbf{q}'g_2}\hat{c}_{\mathbf{k}'g_1}\right\rangle$. Taking this into the following constraints follow: $g_4 = g_3$ and $g_2 = g_1$. In general, the only possible value for $\mathbf{q}$ and $\mathbf{q}'$ is $\mathbf{0}$[‡‡]. Hence, the

---

[‡‡] In the particular case of an AFM ground state in the 2D half-filled Hubbard model, the doubling of the BZ results in $\mathbf{Q}$ [Eq. (3.3)] being equivalent to $\mathbf{0}$.

scattered light can be written in terms of two different contributions

$$\mathbb{S}(\Delta\mathbf{k},\omega)=\mathbb{S}_{\mathrm{e}}(\omega=0,\Delta\mathbf{k})+\mathbb{S}_{\mathrm{i}}(\omega>0,\Delta\mathbf{k}), \tag{4.44}$$

and analogously for the intensity

$$I(\Delta\mathbf{k})=I_{\mathrm{e}}(\Delta\mathbf{k})+I_{\mathrm{i}}(\Delta\mathbf{k}) \tag{4.45}$$

Where I_{e} and I_{i} stand for elastic and intraband inelastic scattering respectively. It is worth mentioning that Eq. (4.44) is only valid at $T=0$, as for finite temperature there are contributions with negative frequencies to the scattered light.

4.4 Estimating the losses due to scattering to higher bands

As it was pointed out in [31], Eq. 4.23 is not the whole story. Inelastically scattered light has another component, scattering to higher bands, that has not been taken into account in Sections 4.2 and 4.3. This component plays a non-negligible role in the destruction of the system during the experiment. In [31], Douglas and Burnett derived an expression to compute the contributions for to the scattered light in a single-species case. Here, the general expression for the full multi-species case is presented. Starting with Eq. (4.18) and focusing only on the sum over lattice sites and bands, following [31], the terms that represent lost atoms due to scattering to higher bands can be written as

$$(*)=\sum_{\mathbf{j},m\neq 0} f^{*}_{\mathbf{j}_4 0,\mathbf{j}_3 m} f_{\mathbf{j}_1 0,\mathbf{j}_2 m}\left\langle \hat{c}^{\dagger}_{\mathbf{j}_4 0 g_4}\hat{c}_{\mathbf{j}_3 m g_3}\hat{c}^{\dagger}_{\mathbf{j}_2 m g_2}\hat{c}_{\mathbf{j}_1 0 g_1}\right\rangle. \tag{4.46}$$

The previous expression can be simplified, thus eliminating any dependencies on the higher bands. This is achieved via the following closure relation for the Wannier functions:

$$\sum_{\mathbf{j}m} f^{*}_{\mathbf{j}_4 0,\mathbf{j}m} f_{\mathbf{j}_1 0,\mathbf{j}m}=\delta_{\mathbf{j}_1\mathbf{j}_2}. \tag{4.47}$$

Which leads to

$$(*)=\delta_{g_4 g_1}\delta_{g_3 g_2}N\left[1-\alpha_{\Delta\mathbf{k}}\right]. \tag{4.48}$$

Apart from the Kronecker delta function for the spin species, this expression is the same as Eq. (16) of [31]. N is the total number of atoms in the lattice. As long as the assumption about unpopulated higher bands is valid, this result remains valid for both statistics, fermionic and bosonic. An accompanying expression for Eq. (4.23) can be written now. The losses due to the scattering to higher bands as can be estimated from

$$I_{\mathrm{hb}}(\Delta\mathbf{k}) = BN\left[1-\alpha_{\Delta\mathbf{k}}\right]\sum_{g,g'}\mathsf{M}^{g'g}_{g'g}. \tag{4.49}$$

The losses to higher bands are independent of the state of the system but its only a function of the probing laser frequency, intensity, and the optical lattice depth.

4.5 Summary of the results presented in this chapter

This chapter presents the general equations that describe the scattered light intensity [Eqs. (4.26)-(4.28) and Eq. (4.49)] and scattered light spectrum [Eqs. (4.38)-(4.40)]. The scattered light can be separated into two components: the elastic component and the inelastic. The elastic component has been shown to be formed of those processes where there is no change in momentum. In the case in which the initial state of the lattice is that of unpopulated higher bands, the inelastic component of the scattered light can be furthermore separated into two components: intraband processes [Eqs.(4.28) and (4.40)] and interband processes [Eq. (4.49)]. The intraband scattering processes serve as a probe of the correlations between the atoms, whereas the interband processes are only important due to the finite size of the lattice because of their influence on the heating effect of the scattering of light[§§].

Equation (4.28) clearly shows how to connect the experimental signal with calculations and how results from condensed matter physics can be directly used to study their analogous realisation in optical lattices. When the harmonic trapping can be neglected, Eq. (4.28) simplifies to Eq. (4.35).

[§§] This is analysed in great detail in Chapter 6.

Chapter 5

Scattered light intensity from a two-dimensional optical lattice of ^{40}K

All the previous developments form the basis to formulate a particular problem and solve it in a straightforward way. It can be simply stated as: *what is the optical response of* ^{40}K *atoms loaded in an optical lattice if they are in an antiferromagnetic phase (sdw one)?* This is the first of three chapters in which the many-body physics of Chapter 3 is joined with the optical diagnostics of Chapter 4 to analyse light scattering as a probe for ultracold atoms in optical lattices. The study presented in this Chapter and in the following two [Chapters 6 and 7] concentrates in modelling a particular experiment. Here, results on the scattered light intensity off a 2D optical lattice loaded with ^{40}K in the half-filled Hubbard model regime at very low temperatures are presented.

5.1 Two-species atomic gas of ^{40}K

This part of the thesis [Chapters 5, 6 and 7] focuses on applying the formalism presented in Chapter 4 to the fermionic atom ^{40}K. This isotope has been used in the realisation of a Mott insulator in optical lattices [54, 107], but other atoms are available and different level states could be used. The available level structure of ^{40}K is shown in Fig. 5.1. The correspondence between ground and excited states and the hyperfine states for atoms trapped in the lattice is given by:

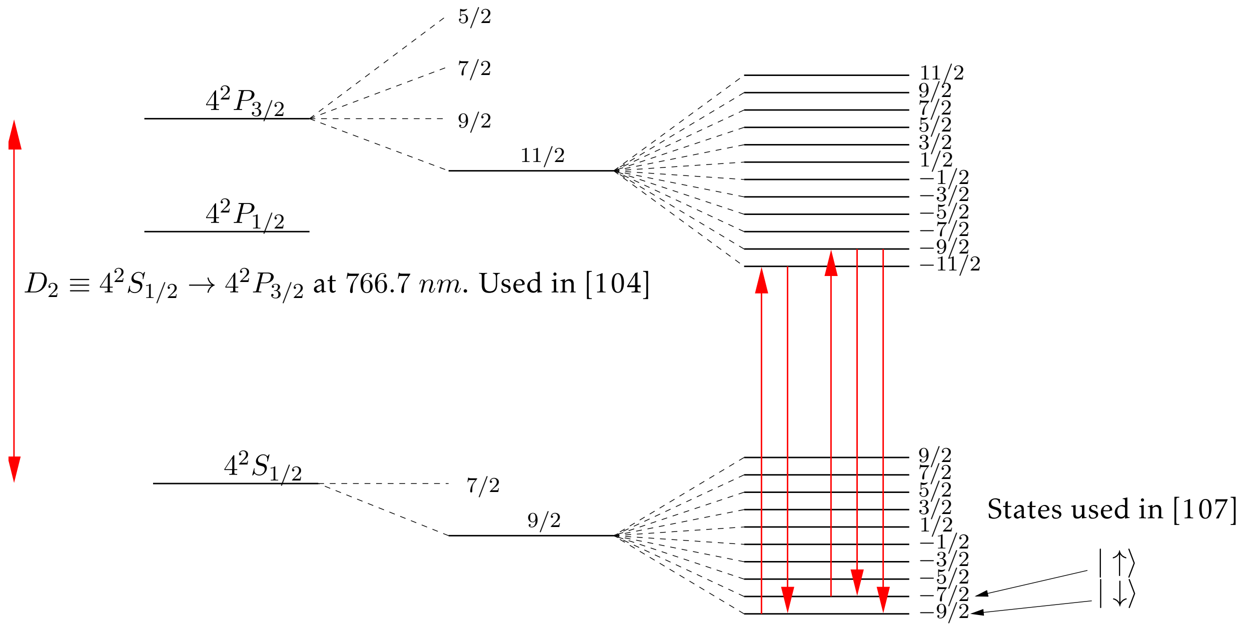

Figure 5.1: Hyperfine spectra of the first three levels of ^{40}K. Arbitrary scale.

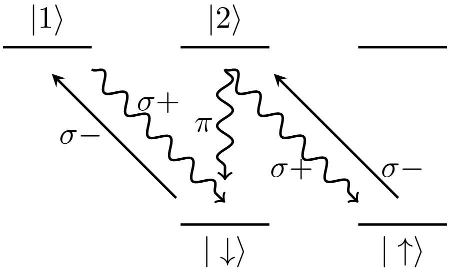

Figure 5.2: Transitions induced with σ^- illumination in the particular case of ^{40}K that is studied in this thesis. There are two different transitions: cycling transitions ($|\uparrow\rangle \overset{\sigma^-}{\rightarrow} |2\rangle \overset{\sigma^+}{\rightarrow} |\uparrow\rangle$ and $|\downarrow\rangle \overset{\sigma^-}{\rightarrow} |1\rangle \overset{\sigma^+}{\rightarrow} |\downarrow\rangle$) and a spin flipping transition ($|\uparrow\rangle \overset{\sigma^-}{\rightarrow} |2\rangle \overset{\pi}{\rightarrow} |\downarrow\rangle$). These have different polarisation tensors, and hence, a different geometrical factor, which, given that each transition is associated with a physically different susceptibility, is good when it comes to distinguishing them, as one has only to measure in different directions.

$$|1\rangle = |F_e, m_e = -F_e\rangle, \qquad |2\rangle = |F_e, m_e = -F_e + 1\rangle \tag{5.1}$$

$$|\uparrow\rangle = |F_g, m_g = -F_g + 1\rangle, \qquad |\downarrow\rangle = |F_g, m_g = -F_g\rangle \tag{5.2}$$

Where $F_e = F_g + 1$. The setup studied here is illustrated in Fig. 5.3. The presence of a periodic array of atoms gives rise to a diffraction pattern highly peaked at the origin. This peak hides the less intense inelastically scattered photons that convey information about the correlations of the system. Hence, the main peak is blocked to improve the signal-to-noise ratio. For the analysis presented here, the probing light has been chosen to be a σ^- polarised beam. With this beam, the two ground states are coupled to the electronically excited states. Figure 5.2 shows the specific transitions considered here which correspond to the following ground states

$$\begin{aligned} |\downarrow\rangle =& |4S_{1/2}, F_g = 9/2, m_F = -9/2\rangle, \\ |\uparrow\rangle =& |4S_{1/2}, F_g = 9/2, m_F = -7/2\rangle. \end{aligned} \tag{5.3}$$

σ^- light excites the atoms to the following states

$$\begin{aligned} |1\rangle =& |4P_{3/2}, F_e = 11/2, m_F = -11/2\rangle, \\ |2\rangle =& |4P_{3/2}, F_e = 11/2, m_F = -9/2\rangle. \end{aligned} \tag{5.4}$$

The non-zero polarisation tensors $\mathsf{M}^{g_3 g_4}_{g_2 g_1}$ [Eq. (4.20)] are those that describe the transitions shown in Fig. 5.2. Using Eq. (4.20) with the levels given of Eqs. (5.3) and (5.4) results in

$$\begin{aligned} \mathsf{M}^{\downarrow\downarrow}_{\downarrow\downarrow} =& \frac{1}{4}\left(3 + \cos 2\theta\right), & \mathsf{M}^{\uparrow\uparrow}_{\downarrow\downarrow} =& \mathsf{M}^{\downarrow\downarrow}_{\uparrow\uparrow} = \frac{9}{44}\left(3 + \cos 2\theta\right), \\ \mathsf{M}^{\uparrow\uparrow}_{\uparrow\uparrow} =& \frac{81}{484}\left(3 + \cos 2\theta\right), & \mathsf{M}^{\downarrow\uparrow}_{\downarrow\uparrow} =& \frac{18}{121}\sin^2\theta. \end{aligned} \tag{5.5}$$

There are two types of transitions: a *cycling transition*, which excites to a level and then decays back to the original ground state level, and a *spin-flipping transition*, which excites an $|\uparrow\rangle$ state into $|2\rangle$, and then decays to $|\downarrow\rangle$. The different transitions are related to different susceptibilities [Eq. (5.14)]. This is advantageous from the experimental point of view as each different transition has a different polarisation [See Fig. 5.2 and Eq. (5.5)]. As a result, there exists a partial geometrical separation of the different contributions, which can be investigated by changing the position of the lens. This can be exploited to extract information from the system by measuring the scattered light at different angles. Here, this possibility is explored by means of the different configurations illustrated in Fig. 5.3. Three different possibilities are studied: a configuration where the lens is directly on top of the magnetic Bragg peak [Fig. 5.3(a)], a configuration where the lens is placed in the forward direction [Fig. 5.3](b), and a configuration where the lens is placed in the perpendicular direction [Fig. 5.3(c)].

Unless otherwise stated, all the results shown in this chapter have been computed with a lattice of linear size $N_s = 40$. When considering the possible optical lattice configurations, two lattice heights have been studied: $7.8E_R$ and $25E_R$. In the direction perpendicular to the lattice, the trap frequency has been chosen as $\omega_z = 10\sqrt{2}E_R/\hbar$. For ^{40}K, experimentally realistic [54, 107, 41] values for the parameters have been assumed. The incoming light wavelength is taken to be $\lambda = 766.5$nm, its intensity is chosen as $I_{\text{in}} = 5W/m^2$, and it is assumed to be detuned from the atomic resonance[*] $\delta = 20\gamma$ [Eq. (4.13)]. This yields in Eq. (4.19) $Br^2 \approx 1615$ photons/s. The ratio between the lattice spacing and the wavelength of the incident light is varied by changing κ [Eq. (4.16)]. Three different values of this parameter are studied: $\kappa = 0.66$, 1.05 and 1.5. All these correspond to subwavelength lattice spacing, but the additional magnetic peak due to period doubling may only be observed for $\kappa = 1.5 > \sqrt{2}$.

In the previous chapter, the scattered light intensity was shown to be separable into three different contributions,

$$I = I_{\text{e}} + I_{\text{i}} + I_{\text{hb}}. \tag{5.6}$$

Here, each of these different contributions is analysed separately. Given that the only non-zero contributions to the scattered intensity are determined by Eq. (5.5) [Fig. 5.2] the explicit expressions for the elastic and interband components are

$$\frac{I_{\text{e}}(\Delta\mathbf{k})}{\alpha_{\Delta\mathbf{k}}B} = \left(\sqrt{\mathsf{M}^{\downarrow\downarrow}_{\downarrow\downarrow}}\left\langle\hat{\rho}_{\bar{\Delta}\mathbf{k}\downarrow}\right\rangle + \sqrt{\mathsf{M}^{\uparrow\uparrow}_{\uparrow\uparrow}}\left\langle\hat{\rho}_{\bar{\Delta}\mathbf{k}\uparrow}\right\rangle\right)^2, \tag{5.7}$$

$$I_{\text{hb}}(\Delta\mathbf{k}) = BN_s^2\left(1 - \alpha_{\Delta\mathbf{k}}\right)\left(\mathsf{M}^{\uparrow\uparrow}_{\uparrow\uparrow} + \mathsf{M}^{\downarrow\downarrow}_{\downarrow\downarrow} + \mathsf{M}^{\downarrow\uparrow}_{\downarrow\uparrow}\right). \tag{5.8}$$

The explicit expression for Debye-Waller factor $\alpha_{\Delta\mathbf{k}}$ is given in Eq. (4.22), and the coefficient B is defined in Eq. (4.19). In Eq. (5.7), the Fourier transform of the density operator is defined in Eq. (5.17).

The intraband inelastic component of the scattered intensity $I_{\text{i}}(\Delta\mathbf{k})$ has a more cumbersome expression. When the susceptibilities for the Hubbard model were introduced in Chapter 3, the broken translation invariance was accommodated by writing the susceptibilities as 2×2 matrices [Eqs. (3.45), (3.46) and (3.47) Eq. (3.31)]. Hence, here the formalism presented in Chapter 4 has to be adapted to the matricial notation. In particular, Eq. (4.32) is written with a matricial equivalent of the static response function

---

[*] In the particular case of ^{40}K, the frequency separation between the $|4P_{3/2}, F_e = 11/2\rangle$ and $|4P_{3/2}, F_e = 9/2\rangle$ is $\approx$ 44.1 MHz[115], see also Fig. 5.1. The natural linewidth of the D_2 line in ^{40}K is 6.035(11) MHz [115] with a wavelength of $\lambda_{D_2} = 767.7021$ nm [65]. This can also excite atoms to the $|4P_{3/2}, F_e = 9/2\rangle$ although these processes are not considered in this thesis. To include them, extra terms would have to be included and those terms would differ from the ones considered because the factor B, defined in Eq. (4.19), depends on the detuning and it is different for the $|4P_{3/2}, F_e = 9/2\rangle$ states. This can be minimized by tuning away from this frequency.

[Eq. (3.25)]. This is a 2×2 matrix which has an analogous definition to that of the matricial susceptibility [Eq. (3.31)]. It is defined as

$$\boldsymbol{\mathcal{S}}^{g_3g_4}_{g_2g_1}(\underset{\sim}{\mathbf{q}}) = \begin{pmatrix} \mathcal{S}^{g_3g_4}_{g_2g_1}(\underset{\sim}{\mathbf{q}},\underset{\sim}{\mathbf{q}}) & \mathcal{S}^{g_3g_4}_{g_2g_1}(\underset{\sim}{\mathbf{q}},\underset{\sim}{\mathbf{q}}+\mathbf{Q}) \\ \mathcal{S}^{g_3g_4}_{g_2g_1}(\underset{\sim}{\mathbf{q}}+\mathbf{Q},\underset{\sim}{\mathbf{q}}) & \mathcal{S}^{g_3g_4}_{g_2g_1}(\underset{\sim}{\mathbf{q}}+\mathbf{Q},\underset{\sim}{\mathbf{q}}+\mathbf{Q}) \end{pmatrix}. \tag{5.9}$$

As defined in the previous equation, the static response function has four indices which correspond to the species of each operator in its definition. The results presented in Section 3.2.1 [Eqs. (3.32), (3.34), and (3.35)], and in Section 3.3 [Eqs. (3.45), (3.46), and (3.47)] are for the charge, longitudinal spin and transverse spin susceptibilities, respectively. The susceptibilities are time-ordered correlation functions which can be used to compute the dynamical response functions via Eqs. (3.30) and (3.28). The static response function is obtained by integrating the dynamic response function over frequencies [Eq. (3.27)]. Using the definition of those operators [Eqs. (3.24), (3.23) and (3.20)], it is trivial to relate the operator defined response function to the quadruply indexed ones. Explicitly, this results in

$$\boldsymbol{\mathcal{S}}^{\rho\rho}(\mathbf{q}) = \boldsymbol{\mathcal{S}}^{\uparrow\uparrow}_{\uparrow\uparrow}(\mathbf{q}) + \boldsymbol{\mathcal{S}}^{\downarrow\downarrow}_{\downarrow\downarrow}(\mathbf{q}) + \boldsymbol{\mathcal{S}}^{\uparrow\uparrow}_{\downarrow\downarrow}(\mathbf{q}) + \boldsymbol{\mathcal{S}}^{\downarrow\downarrow}_{\uparrow\uparrow}(\mathbf{q}), \tag{5.10}$$

$$\boldsymbol{\mathcal{S}}^{zz}(\mathbf{q}) = \boldsymbol{\mathcal{S}}^{\uparrow\uparrow}_{\uparrow\uparrow}(\mathbf{q}) + \boldsymbol{\mathcal{S}}^{\downarrow\downarrow}_{\downarrow\downarrow}(\mathbf{q}) - \boldsymbol{\mathcal{S}}^{\uparrow\uparrow}_{\downarrow\downarrow}(\mathbf{q}) - \boldsymbol{\mathcal{S}}^{\downarrow\downarrow}_{\uparrow\uparrow}(\mathbf{q}), \tag{5.11}$$

$$\boldsymbol{\mathcal{S}}^{+-}(\mathbf{q}) = 2\boldsymbol{\mathcal{S}}^{\downarrow\uparrow}_{\downarrow\uparrow}(\mathbf{q}). \tag{5.12}$$

The diffraction factors $u_{\mathbf{q}}$ defined in Eq. (4.25) can also be accommodated into the RBZ structure by defining

$$\boldsymbol{u}_{\mathbf{k}} = \begin{pmatrix} u_{\mathbf{k}} \\ u_{\mathbf{k}+\mathbf{Q}} \end{pmatrix}, \qquad \mathbf{k} \in \text{RBZ}. \tag{5.13}$$

After the previous notational digression, the explicit form of the intraband scattered light intensity [Eq. (4.32)] for a 2D atomic gas of ^{40}K in the half-filled Hubbard regime is

$$\begin{aligned} I_i(\Delta\mathbf{k}) = \alpha_{\Delta\mathbf{k}} B \Bigg\{ & \left(\mathsf{M}^{\downarrow\downarrow}_{\downarrow\downarrow} + \mathsf{M}^{\uparrow\uparrow}_{\uparrow\uparrow}\right) \sum_{\mathbf{q}\neq 0}^{\text{RBZ}} \boldsymbol{u}^{\dagger}_{\bar{\Delta}\mathbf{k}-\mathbf{q}} \frac{1}{4} \left[\boldsymbol{\mathcal{S}}^{\rho\rho}(\mathbf{q}) + \boldsymbol{\mathcal{S}}^{zz}(\mathbf{q})\right] \boldsymbol{u}_{\bar{\Delta}\mathbf{k}-\mathbf{q}} \\ & + \left(\mathsf{M}^{\downarrow\downarrow}_{\uparrow\uparrow} + \mathsf{M}^{\uparrow\uparrow}_{\downarrow\downarrow}\right) \sum_{\mathbf{q}\neq 0}^{\text{RBZ}} \boldsymbol{u}^{\dagger}_{\bar{\Delta}\mathbf{k}-\mathbf{q}} \frac{1}{4} \left[\boldsymbol{\mathcal{S}}^{\rho\rho}(\mathbf{q}) - \boldsymbol{\mathcal{S}}^{zz}(\mathbf{q})\right] \boldsymbol{u}_{\bar{\Delta}\mathbf{k}-\mathbf{q}} \\ & + \mathsf{M}^{\downarrow\uparrow}_{\downarrow\uparrow} \sum_{\mathbf{q}\neq 0}^{\text{RBZ}} \boldsymbol{u}^{\dagger}_{\bar{\Delta}\mathbf{k}-\mathbf{q}} \frac{1}{2} \boldsymbol{\mathcal{S}}^{+-}(\mathbf{q}) \boldsymbol{u}_{\bar{\Delta}\mathbf{k}-\mathbf{q}} \Bigg\}. \end{aligned} \tag{5.14}$$

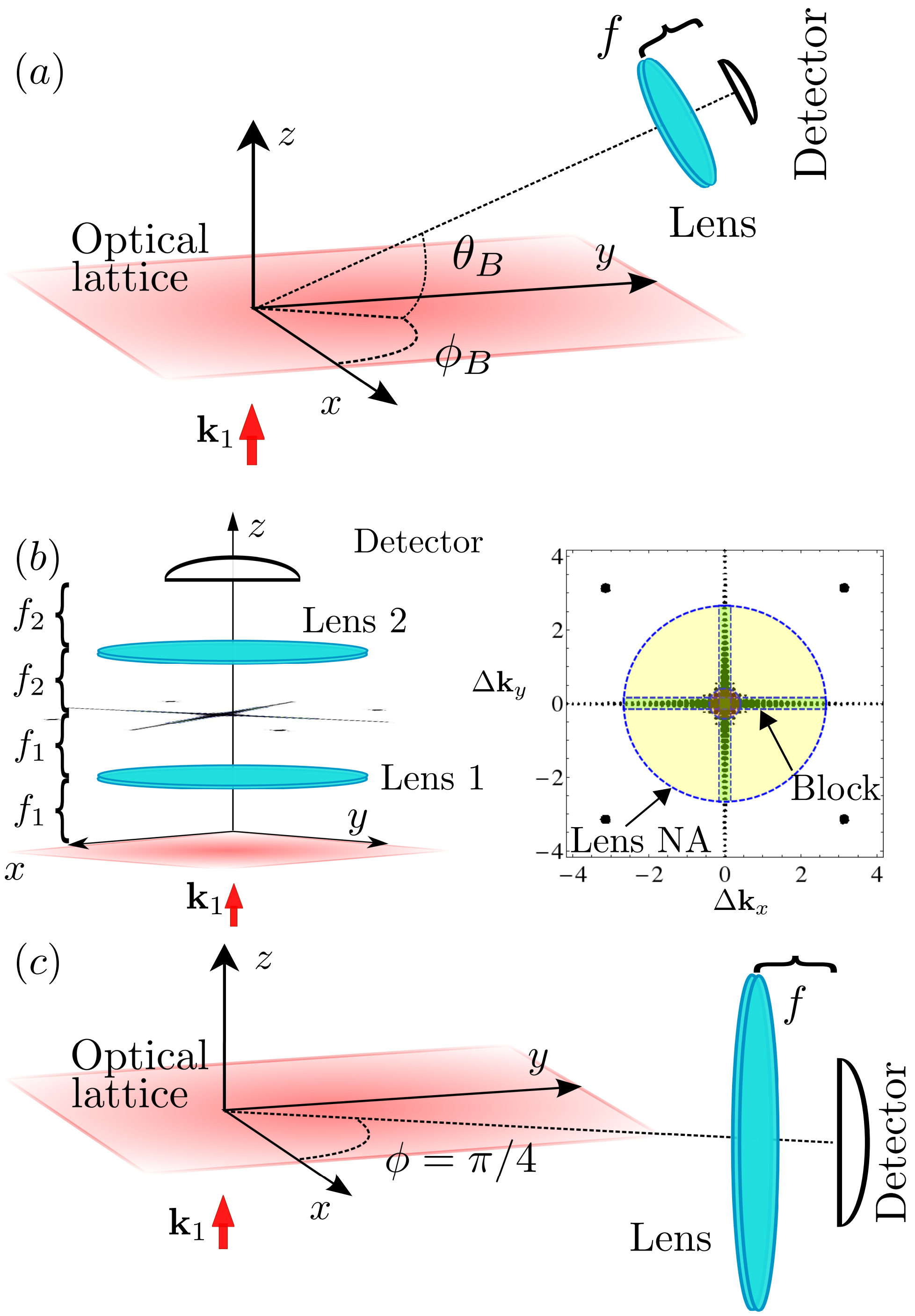

Figure 5.3: Schematic illustration of the experimental configurations to detect AFM ordering of fermionic atoms in an optical lattice. The atoms are confined in the 2D optical lattice close to the $z = 0$ plane and the incident light propagates towards the positive z direction. In (a), the elastically scattered light corresponding to the emerging additional Bragg peak generated by the AFM ordering is collected by a small lens. In (b), the setup is closely related to that of Ref. [104]. The two lenses have focal lengths f_1 and f_2. The light scattered in the near-forward direction is first collected by lens 1. In the focal plane the scattered light is selectively stopped by a block in order to suppress the intensity of the elastically scattered light at the detector. The shape and the size of the block can be optimised for different measurements of collective excitations or of temperature. In (c) the scattered light is collected near the perpendicular scattering direction of $\theta = \pi/2$, to measure transverse spin correlations.

5.2 Elastic scattering

This section focuses on the elastic component of the scattered light [Eq.(5.14)]. Contrary to the uniformly filled case [Section. 4.2.1], in the half-filled Hubbard model, the elastic component of the scattered light contains a great deal of information about the state of the system. In order to analyse this effect in detail, the explicit values of the M-tensor listed in Eq. (5.5) can be substituted into Eq. (5.14) to obtain an explicit expression. The elastic component of the scattered light can then be written as

$$I_{\mathrm{e}}(\Delta\mathbf{k}) = \alpha_{\Delta\mathbf{k}} B \frac{1}{4}\left(3+\cos 2\theta\right)\left(\left\langle \hat{\rho}_{\bar{\Delta}\mathbf{k}\downarrow}\right\rangle + \frac{9}{11}\left\langle \hat{\rho}_{\bar{\Delta}\mathbf{k}\uparrow}\right\rangle\right)^{2} \,. \tag{5.15}$$

Eq. (5.15) has two different contributions. Each term $\langle\hat{\rho}_{\Delta\mathbf{k}g}\rangle$ represents the Fourier transform of the expectation value of the density operator for spin species g. These terms are weighted by a different factor. In particular, the factor of $9/11$ in front of the $|\uparrow\rangle$ term originates in the Clebsh-Gordan coefficient. It is due to the dipole matrix transition elements of the transitions associated with that particular hyperfine state [Fig. 5.2]. This does not happen in solids but only for atoms trapped in a hyperfine state on an optical lattice. This equation, though, is not physically transparent, meaning that it does not show how the magnetisation of the system affects the elastic scattered light. The magnetic ordering appears when the equivalent of Eq. (4.33) is written for the half-filled Hubbard Hamiltonian. The doubling of the unit cell is included in the MFT assumption, second summand on the right-hand side of Eq. (3.4)]. Hence, the expectation value of the density operator for the sdw case is

$$\left\langle \hat{\rho}_{\bar{\Delta}\mathbf{k}g}\right\rangle = \sum_{\mathbf{j}} e^{i\bar{\Delta}\mathbf{k}\cdot\mathbf{r}_{\mathbf{j}}}\hat{n}_{\mathbf{j}g} = \sum_{\mathbf{j}} e^{i\bar{\Delta}\mathbf{k}\cdot\mathbf{r}_{\mathbf{j}}}\left(f_g + m\eta(g)e^{i\mathbf{Q}\cdot\mathbf{r}_{\mathbf{j}}}\right) \tag{5.16}$$

$$= \mathfrak{u}_{\bar{\Delta}\mathbf{k}}\, f_g + \mathfrak{u}_{\bar{\Delta}\mathbf{k}+\mathbf{Q}}\, m\,\eta(g) \,, \tag{5.17}$$

where $f_g = 1/2$ is the atomic filling factor of species g at half-filling and $\eta(g)$ is defined in Eq. (3.5). Comparing Eq. (5.17) to Eq. (4.33), there is a new term proportional to the AFM order parameter m [Eq. (3.2)]. This term is centred around the ordering vector $\mathbf{Q}$ [Eq. (3.3)]. Within the MFT approximation, the order parameter m is obtained self-consistently as a solution of Eq. (3.17). The T and U dependence of the MFT order parameter is shown in Fig. 3.3. As discussed in Section 3.3, quantum fluctuations are not accounted for in the MFT order parameter. If quantum fluctuations are taken into account, the AFM order parameter is renormalised as shown in Fig. 3.8. The RPA corrections to the order parameter m [Sec. 3.3] can result in a suppression by up to a factor of $\sim 40\%$ for large U [109]. Thus, the RPA-corrected values for m are used in this thesis [109]. A fully explicit expression for the elastic component is obtained by using Eq. (5.17) into Eq. (5.15)

$$I_{\mathrm{e}}(\Delta \mathbf{k}) = B\alpha_{\Delta \mathbf{k}} \frac{(3+\cos 2\theta)}{4} \left[\frac{400}{121} f_g^2 \left| \mathrm{u}_{\bar{\Delta \mathbf{k}}} \right|^2 + \frac{202}{121} m^2 \left| \mathrm{u}_{\bar{\Delta \mathbf{k}}+\mathbf{Q}} \right|^2 - \frac{40}{121} f_g m \mathrm{u}^*_{\bar{\Delta \mathbf{k}}+\mathbf{Q}} \mathrm{u}_{\bar{\Delta \mathbf{k}}} \right] \tag{5.18}$$

It represents the elastic component of the scattered light from atoms in an optical lattice. The diffraction factor $|\mathrm{u}_{\mathbf{k}}|^2$ is defined in Eq. (4.36). The diffraction is due to the presence of a periodic array of atoms, the density of which gives rise to a diffraction pattern. In Eq. (5.18) there are two diffraction factors: $\mathrm{u}^*_{\mathbf{k}}\mathrm{u}_{\mathbf{k}}$, centered at the origin, and $\mathrm{u}^*_{\mathbf{k}+\mathbf{Q}}\mathrm{u}_{\mathbf{k}+\mathbf{Q}}$, which is proportional to the square of the order parameter m [Eq. (3.2)] and which is *shifted* by the ordering vector $\mathbf{Q}$ [(3.3)]. The origin of this term is due to the doubling of the Brilluoin zone, which happens because there is AFM ordering in the system. The magnetic Bragg peaks are shown in Fig. 5.4. Eq. (5.18) is, in principle, *exact*. That is, it does not depend on the approximation used to describe the ground state of the system. Of course, there is the caveat that even though it is known that the magnetic peak is proportional to the square of the staggered magnetisation, its value is not known exactly and this is constrained by the approximation used to study the ground state. The position of the magnetic peaks depends on the modulus of the change of momentum in the scattered light $\Delta\mathbf{k}$, which, in turn, is dependent on the ratio κ between the wavevectors of the incoming laser light and the lattice [Eq. (4.16)]. Hence, the magnetic Bragg peaks are only observable if $\kappa \geq \sqrt{2}$. The angular position of this peak can be computed as $\theta_{\text{Bragg}} = \arcsin \frac{\sqrt{2}}{\kappa}$ and $\phi_{\text{Bragg}} = \pi/4$. It could, in principle, be measured with a very small lens (eg. NA $= 0.2$) in that direction. Magnetic Bragg peaks were first analysed in optical lattices in [29] and experimentally measured for an artifical density pattern in [122].

The diffraction factor term in Eq. (5.18) $\mathrm{u}^*_{\Delta\mathbf{k}}\mathrm{u}_{\Delta\mathbf{k}}$ gives rise to a diffraction pattern in the forward direction. The intensity of the central peak is proportional to the square of the number of atoms in the lattice [N_s^4]. If the setup is similar to the one described in Fig. 5.3(b) with a lens in the forward direction, it contributes nearly in its entirety to the signal collected by a lens. Hence, in order to study the inelastically scattered light, the elastic one has to be blocked [104]. The cross-term $\mathrm{u}^*_{\mathbf{k}+\mathbf{Q}}\mathrm{u}_{\mathbf{k}}$ can be also explicitly

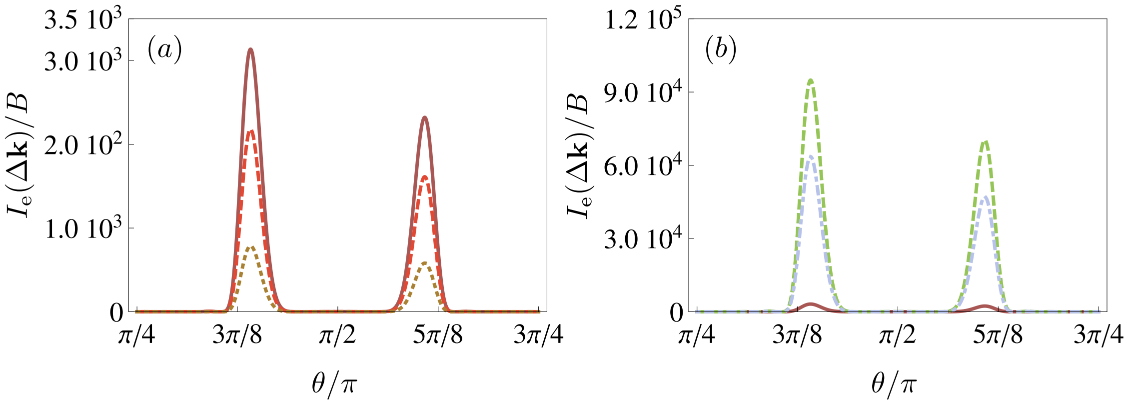

Figure 5.4: Angular distribution of the elastic component of the scattered light intensity along the direction $\phi = \pi/4$. The calculations use the AFM order parameter m computed with RPA corrections. Here the number of sites is 40×40 and the lattice depth $s = 25$. (a) $I_e(\Delta\mathbf{k})$ for different values of m, when both species are detected. Different curves represent $U = 7.3J$ and $m_{\text{RPA}} = 0.3$ (solid), $U = 3.9J$ and $m_{\text{RPA}} = 0.25$ (dashed), $U = 2.0J$ and $m_{\text{RPA}} = 0.15$ (short dashed). (b) compares the results for the total density with the single species detection ($m_{\text{RPA}} = 0.3$). Curves from top to bottom: $I_e^{\downarrow}(\Delta\mathbf{k})$ (dashed), $I_e^{\uparrow}(\Delta\mathbf{k})$ (dash-dotted), and $I_e(\Delta\mathbf{k})$ (solid). The magnetic Bragg peak is observable since $\kappa = 1.5 > \sqrt{2}$. Note that the highest peak in (a) corresponds to the smallest one in (b).

computed. It results in

$$\mathfrak{u}^*_{\mathbf{k}+\mathbf{Q}}\mathfrak{u}_{\mathbf{k}} = \mathfrak{u}^*_{\mathbf{k}}\mathfrak{u}_{\mathbf{k}+\mathbf{Q}} = \prod_{\alpha=x,y} \frac{\sin^2\left(\frac{N\bar{\mathbf{k}}_\alpha a}{2}\right)}{\sin\left(\frac{\bar{\mathbf{k}}_\alpha a}{2}\right)\cos\left(\frac{\bar{\mathbf{k}}_\alpha a}{2}\right)}. \tag{5.19}$$

The contributions from this term are negligible and it dissapears in the continuum limit.

5.2.1 Single-species magnetic Bragg scattering

A different way of looking at the magnetic peak would be by ramping up the lattice, eg., freezing the hopping between atoms and then eliminating one of the hyperfine states. In this case, the magnitude of the magnetic Bragg peaks is enhanced, as there is no interference. This is shown in Fig. 5.4(a). The explicit expression for, eg., the case where the $|\uparrow\rangle$ atoms have been removed is

$$I_e^{\downarrow}(\Delta\mathbf{k}) = \alpha_{\Delta\mathbf{k}} B\frac{(3+\cos 2\theta)}{4}\left\langle \hat{\rho}_{\bar{\Delta\mathbf{k}}\downarrow}\right\rangle^2 = \frac{(3+\cos 2\theta)}{4}\left(\frac{\mathfrak{u}_{\bar{\Delta\mathbf{k}}}}{2} - \mathfrak{u}_{\bar{\Delta\mathbf{k}}+\mathbf{Q}}m\right)^2.$$

The destructive intereference in the elastic component of the scattered light [Eq. (5.18)] supressed the intensity of the magnetic Bragg peak. Fig. 5.4(a) shows the separate contribution of each spin species to the elastic intensity, and the sum of these contributions. Without spin-specific detection, the total signal is very weak because of destructive interference between the scattered light from the two species. In fact, there is a contribution only because the dipole transition matrix elements are slightly different between the two species, see Eq. (5.15), and the difference in magnitude between Fig. 5.4(a) and 5.4(b). According to Eqs. (5.15) and (5.17), the intensity of the magnetic Bragg peak is weaker with both species in the lattice by a factor of $(2/11)^2$. If these matrix elements were the same, then spin-independent imaging would only probe the total density and would not reveal the antiferromagnetic pattern.

If one of the species is removed from the lattice, Eq. (5.20) illustrates the changes in the elastic component. Naturally, the inelastic components also differ from the case when both species are present in the lattice. In Chapter 6, the sensistivity of the single-species magnetic Bragg scattering as a probe of magnetic ordering in an optical lattice is studied. To study the single-species in the lattice case, the intraband inelastic scattering is

$$I_i^{\downarrow}(\Delta\mathbf{k}) = \alpha_{\Delta\mathbf{k}} B \mathsf{M}^{\downarrow\downarrow}_{\downarrow\downarrow} \sum_{\mathbf{q}\neq 0}^{\text{RBZ}} \boldsymbol{u}^{\dagger}_{\bar{\Delta}\mathbf{k}-\mathbf{q}} \frac{1}{4} \left[\boldsymbol{\mathcal{S}}^{\rho\rho}(\mathbf{q}) + \boldsymbol{\mathcal{S}}^{zz}(\mathbf{q})\right] \boldsymbol{u}_{\bar{\Delta}\mathbf{k}-\mathbf{q}}, \tag{5.20}$$

and the interband inelastic scattering reduces to

$$I_{\text{hb}}(\Delta\mathbf{k}) = B N_s^2 \left(1 - \alpha_{\Delta\mathbf{k}}\right) \mathsf{M}^{\downarrow\downarrow}_{\downarrow\downarrow} \tag{5.21}$$

5.2.2 Bragg diffraction in the presence of short-range order

In the previous section and in the following chapters, the calculation assumes the existence of long-range order. This is a meaningful assumption for low enough temperatures. However, achieving such low temperatures in an optical lattice is a very challenging problem. Hence, it is more likely that the first experiments to achieve low enough temperatures[†] will observe short-range order, as described in Section 3.2. I.e., AFM correlations will appear for temperatures close to the crossover temperature, and the correlation length $\xi_{\text{AFM}}(T)$ will depend exponentially on temperature[‡].

In the sdw MFT calculation [Sec. 3.2], the order parameter m is homogeneous throughout the sample. At finite temperatures, spins are correlated only up to a distance of the order of the correlation length. Hence, the sample is formed by a series of domains of size $\sim \xi_{\text{AFM}}$ which leads to a inhomogeneous order parameter $m_{\mathbf{j}}$. As a first approach to the problem, and only in a qualitative manner, one way to study the effect of short-range

---

[†] A possible scheme to cool down a two-component fermionic gas to the Néel state, in a cubic lattice, is proposed in [75].

[‡] For the Heisenberg model, the correlation length is given by Eq. (3.18).

order in an AFM is by studying the Ising model (See, for example, [86, 76]). A site-dependent version of the order parameter [Eq (3.2)] can be written for the Ising model

$$m_{\mathbf{j}} = m_{\mathrm{RPA}}\sigma_{\mathbf{j}}. \tag{5.22}$$

The amplitude of the order parameter is fixed to the $T = 0$ magnetisation value m_{RPA}. $\sigma_{\mathbf{i}}$ represents classical spins, the possible values of which are $+1$ and -1. This approach is purely phenomenological. Hence, the approach taken here to model the effect of short-range order in scattered light is as follows: for a given temperature T, spin configurations are sampled using Monte Carlo Wolff algorithm [126, 60], and the scattered light is computed using Eq. (5.32). The effective correlation length ξ_{Ising} corresponding to the temperature T is estimated using Eq. (5.28). Note that contrary to the Hubbard or Heisenberg models, the critical temperature of the Ising model is finite. To account for the fact that the Hubbard and Heisenberg model critical temperatures are zero in two dimensions, only temperatures above the transitions are considered in this section.

Ising Model in the square lattice

The 2D Ising model consists of a system of classical spins $\sigma_{\mathbf{i}}$, positioned at lattice site **i** in a square lattice. The Hamiltonian can be written as [86, 76]

$$\frac{H}{k_B T} = -\frac{J_{\mathrm{Ising}}}{k_B T}\sum_{\langle \mathbf{i},\mathbf{j}\rangle}\sigma_{\mathbf{i}}\sigma_{\mathbf{j}} = -K\sum_{\langle \mathbf{i},\mathbf{j}\rangle}\sigma_{\mathbf{i}}\sigma_{\mathbf{j}}. \tag{5.23}$$

k_B is Boltzmann constant and T is the temperature of the system. $\langle \mathbf{i},\mathbf{j}\rangle$ denotes nearest neighbours, and J_{Ising} is the coupling strength. For $J_{\mathrm{Ising}} < 0$, the ground state of the system at $T = 0$ is an AFM Neél state. For $J_{\mathrm{Ising}} > 0$, the ground state of the system at $T = 0$ is a ferromagnet with all the spins aligned in the same direction. This direction is either *up* or *down*, and in the absence of an external field, it is random. The ferromagnetic model and the AFM model can be mapped into one another by the following transformation:

$$\sigma_{\mathbf{i}} \to (-1)^{i_x + i_y}\tilde{\sigma}_{\mathbf{i}}. \tag{5.24}$$

The Ising model can be solved analytically in 2D [85]. The transition temperature for the infinite system in a square lattice is [86]

$$K_c(\infty) = \frac{1}{2}\sinh^{-1} 1 = \frac{1}{2}\ln\left(\sqrt{2}+1\right) \simeq 0.4407. \tag{5.25}$$

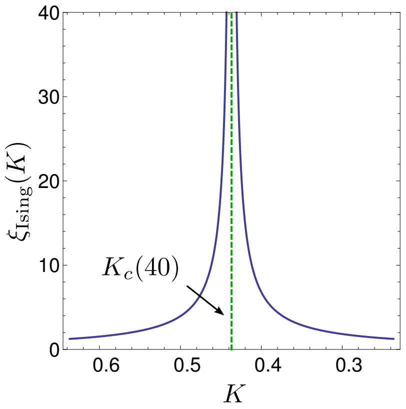

Figure 5.5: Temperature dependence of the correlation length for the 2D Ising model given by Eqs. (5.28) and (5.29).

The results presented here are for a lattice of linear size $N_s = 40$, and finite-size effects shift the transition point from $K_c(\infty)$ to the finite-size critical point $K_c(N_s)$. The finite-size critical temperature can be estimated from the the infinite system using the finite-size scaling arguments of [38], along with the numerical fit to the finite-size scaling hypothesis from [64]. The finite-size shifted value of the critical temperature can be estimated as

$$K_c(N_s) \approx \frac{N_s K_c(\infty)}{N_s - \alpha}. \tag{5.26}$$

For a system with periodic boundary conditions $\alpha \approx -0.36$ [64]. Hence,

$$K_c(40) \approx 0.437. \tag{5.27}$$

The correlation length takes the following form for $T > T_c(40)$ ($K_c(40) < K$):

$$\xi_{\text{Ising}}(K) \approx \frac{1}{4[K_c(40) - K]} : \tag{5.28}$$

and, for $T < T_c(40)$ ($K > K_c(40)$)

$$\xi_{\text{Ising}}(K) \approx \frac{1}{4[K - K_c(40)]}. \tag{5.29}$$

Eqs. (5.28) and (5.29) are strictly valid only in the thermodynamic limit[§]. Here, they are being used to estimate the finite-size correlation length. This is done by using the finite-size critical temperature $K_c(40)$ [Eq. (5.27)] instead of the infinite system one. Figure 5.5 illustrates Eqs. (5.28) and (5.29). In the thermodynamic limit, the correlation length diverges as a power law [Eqs. (5.28) and (5.29)]. This divergence occurs on both sides of the transition because deep in the ordered phase, a spin flip does not affect any other surrounding spins. It is only closer to the critical temperature, at which the phase transition

---

[§] With $K_c(\infty)$ instead of $K_c(40)$.

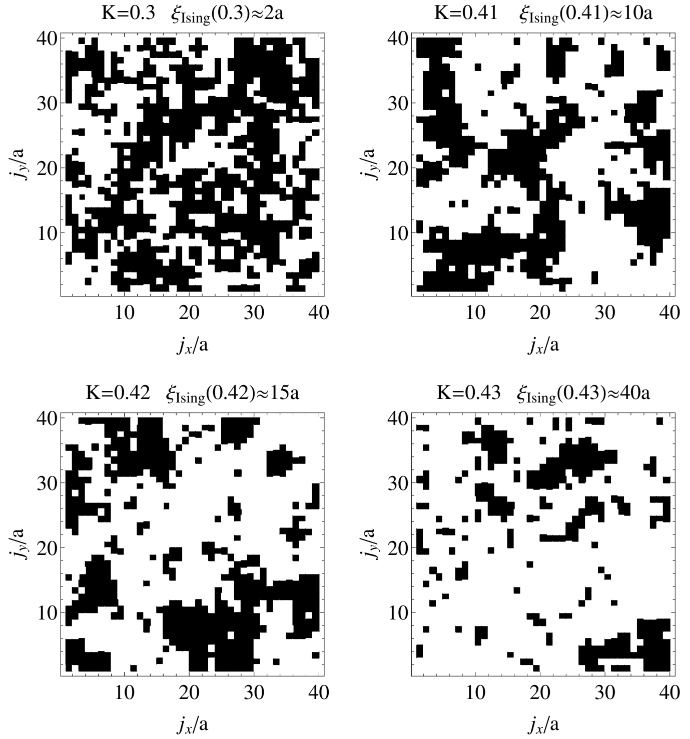

Figure 5.6: Typical configurations of the 2D Ising model for four different temperatures above the transition. The configurations are displayed in the ferromagnetic case because it is easier to spot the different domains in this representation. The indicated correlation length $\xi_{\text{Ising}}(K)$ is estimated from Eq. (5.28).

occurs, that the flip of a single spin can flip the whole system. For a finite-size system, there are no divergences. The transition is identified by finding the maximum of the temperature dependence curve. With increasing system size, this maximum increases its height and shifts its position towards its value in the thermodynamic limit [64]. The fact that the temperature dependence of the correlation length is different for the Heisenberg and the Ising model is not relevant here. The Ising model is used here only as a way of generating spin configurations with a given correlation length.

To compute the scattered light, the Wolff Algorithm [126, 60] was implemented in MATHEMATICA [127]. Using the Wolff Algorithm with 10000 thermalisation steps, and 10000000 Monte Carlo updates per temperature, configurations were generated for the ferromagnetic Ising model. Once the configurations are obtained, the equivalent AFM configuration is obtained via Eq. (5.24). In order to obtain uncorrelated configurations, measurements are only made every 50 Monte Carlo updates. If, during a measurement, the configuration fulfils the constraint imposed, it is saved. It does not fulfil the constraint, it is not saved and another set of 50 Monte Carlo updates is performed. The

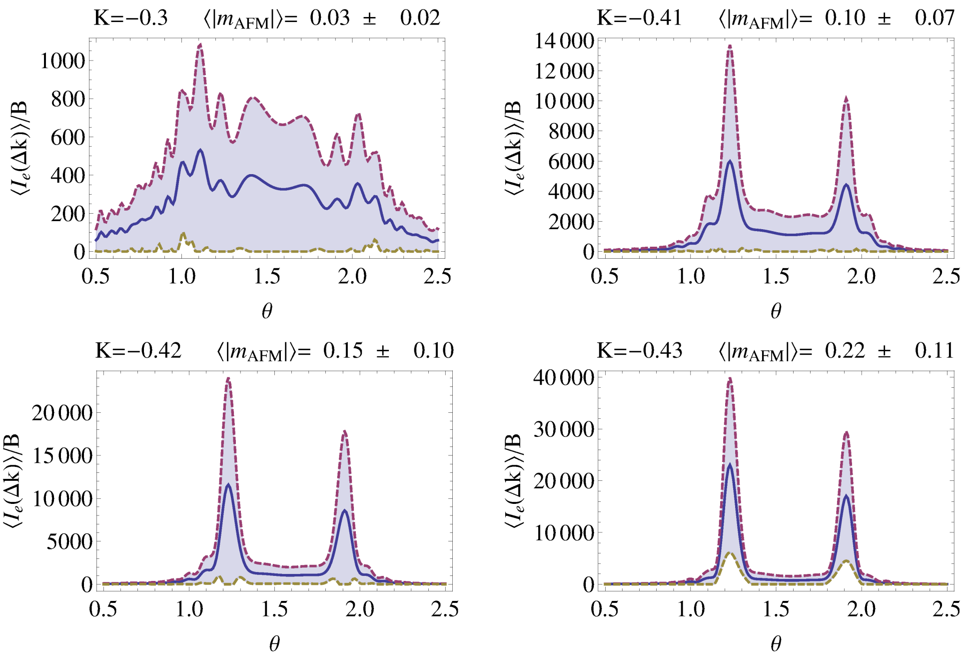

Figure 5.7: Angular distribution of the elastic component of the scattered light from a 2D AFM Ising model. The solid lines represent the average at each temperature value, computed for 100 configurations. The dashed lines denote the average $\pm\sqrt{\text{variance}}$ of the scattered light intensity from all the configurations for each value of θ. Typical configurations are shown in Fig. 5.6. Light fluctuates largely from configuration to configuration. Note that the non-zero average values are for the absolute value. The average values of the order parameter m_{AFM} are smaller than 0.02 for all the temperatures shown.

constraint imposed on the configurations to be saved is that the ferromagnetic Ising order parameter[¶] is smaller, in absolute value, than 0.01. Explicitly,

$$|m_{\text{F}}| = \left|\sum_{\mathbf{i}} \sigma_{\mathbf{i}}\right| < 0.01. \tag{5.30}$$

This constraint ensures that the same number of up and down spins are present[‖]. Figure 5.6 shows some typical configurations generated in this manner for different temperatures. The quoted value for the correlation length is estimated using Eq. (5.28).

Scattered light

The elastically scattered light can be written following Eq. (4.27), but instead of using the *sdw*-state density operator of Eq. (5.16), the Fourier transform of the Ising model

---

[¶] Note that the constraint for the ferromagnetic order parameter applies to the AFM configuration. In the ferromagnetic configuration, this constraint transforms via Eq. (5.24) into the equivalent constraint $|m_{\text{AFM}}| = \left|\sum_{\mathbf{i}} (-1)^{i_x+i_y}\sigma_{\mathbf{i}}\right| < 0.01$.

[‖] In the rest of the thesis, the fermionic Hubbard model is assumed to have an equal number of $|\uparrow\rangle$ and $|\downarrow\rangle$ spins.

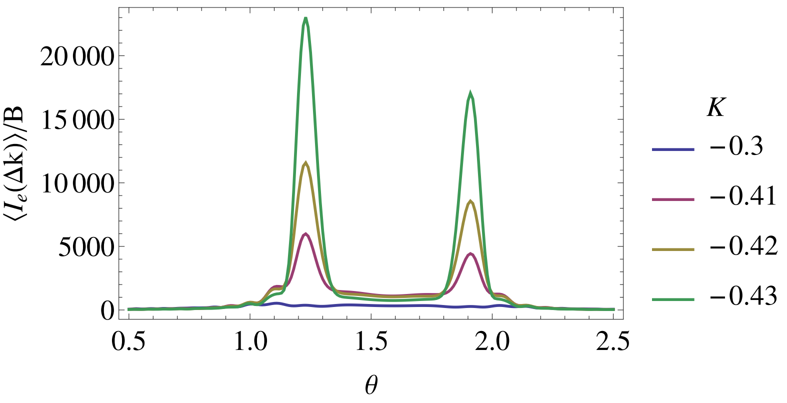

Figure 5.8: Angular distribution of the elastic component of the scattered light from a 2D AFM Ising model. The lines represent the average at each temperature value, computed for 100 configurations. Typical configurations are shown in Fig. 5.6. However, the scattered light fluctuates largely from configuration to configuration as can be seen in Fig. 5.7.

spin configurations is used. To compute the elastic scattering from the Ising model, the first term in the right-hand side of Eq. (5.16) will be ignored. This is because only the magnetic Bragg peak is interesting for this calculation. Also, away from the forward direction, Eq. (5.16) can be written as

$$\left\langle \hat{\rho}_{\bar{\Delta}\mathbf{k}g} \right\rangle \approx \eta(g) m_{\mathrm{RPA}} \sum_{\mathbf{j}} e^{i\bar{\Delta}\mathbf{k}\cdot\mathbf{r}_{\mathbf{j}}} \sigma_{\mathbf{j}}. \tag{5.31}$$

When only one of the species is in the lattice, using Eqs.(4.27) and (5.31), the elastic component of the scattered light off an Ising model can be written as

$$I_{\mathrm{e}}^{\downarrow}(\Delta\mathbf{k}) = B\alpha_{\Delta\mathbf{k}} \mathsf{M}^{\downarrow\downarrow}_{\downarrow\downarrow} m^2_{\mathrm{RPA}} \left| \sum_{\mathbf{j}} e^{i\bar{\Delta}\mathbf{k}\cdot\mathbf{r}_{\mathbf{j}}} \sigma_{\mathbf{j}} \right|^2 , \tag{5.32}$$

Computed in this manner, the scattered light fluctuates largely from configuration to configuration. Here, 100 different configurations are obtained for each temperature, and the average scattered light intensity is computed. For computing the scattered light intensity, the parameters have been given the following values $\kappa = 1.5$ [Eq. (4.16)], and the lattice depth is taken to be $s = 25$. The average, and the average $\pm\sqrt{\text{variance}}$ (dashed lines) for each value of θ of the scattered light are shown for different temperatures in Fig. 5.7. In Fig. 5.7, the quoted non-zero average values are for $|m_{\mathrm{AFM}}|$. The average values of the order parameter m_{AFM} are smaller than 0.02 for all the cases shown. The average grows for temperatures close to the transition [Fig. 5.8], and the magnetic Bragg peaks emerge with growing correlation length. However, the variance of the scattered light [Fig. 5.7] is too large for this technique to be able to extract more information from the system than whether some sort of short-range ordering exists. That is, if the AFM correlation length is $\gtrapprox 10a$, magnetic Bragg peaks will reveal it. Note that below the transition temperature, not shown in the figures, the fluctuations are suppressed and the error bars are significantly smaller.

In summary, it has been shown in this section that even though true long-range order only exists at $T = 0$, due to the finite size of the studied system, at low temperatures, the precursors of long-range order are observable. However, with the limited data used here, it is not possible to discern whether the fluctuations are due to the Physics or the small number of configurations over which the average has been taken. It is important to note that experimentally, the same issue of limited and fluctuating data may arise.

5.3 Inelastic intraband scattering

The previous section analysed the elastic component of light scattering and showed how it contains information about the atomic density in the lattice, which translates into a diffraction pattern of the lattice structure. If the detected signal cannot separate the contributions from the two spin components, extracting information about the AFM ordering is quite hard. On the other hand, when single-species detection is possible, the emerging Braggs peaks can be identified as experimental signatures of AFM ordering. It is also interesting to study the intraband inelastic component [Eq. (5.14)].

The inelastic scattering processes are proportional to the static structure factor $S^{g_3 g_4}_{g_2 g_1}(\Delta\mathbf{k})$ [Eq. (4.29)] which includes all events in which an atom is scattered from a quasimomentum state $\mathbf{q}$ to a different quasimomentum state $\mathbf{q}'$ [Eq. (4.43)]. The atoms absorb recoil kicks from the scattered photons. These events depend on the statistical correlations between the atoms, which generates fluctuating shifts in the diffraction pattern and significant scattered photons outside the diffraction peaks. This process maps the atomic correlations onto the emitted light.

For the two-component ^{40}K gas, the inelastic component of the scattered light is given by Eq. (5.14). There are two different contributions: those in which the spin is conserved, which are proportional to the density and longitudinal spin susceptibilities, and the transition which exchanges the spin[**] (see Fig. 5.2), which is proportional to the transverse spin susceptibility. The angular dependence of those two types of transitions is very dif-

---

[**] That is, the hyperfine state in which the atoms are trapped.

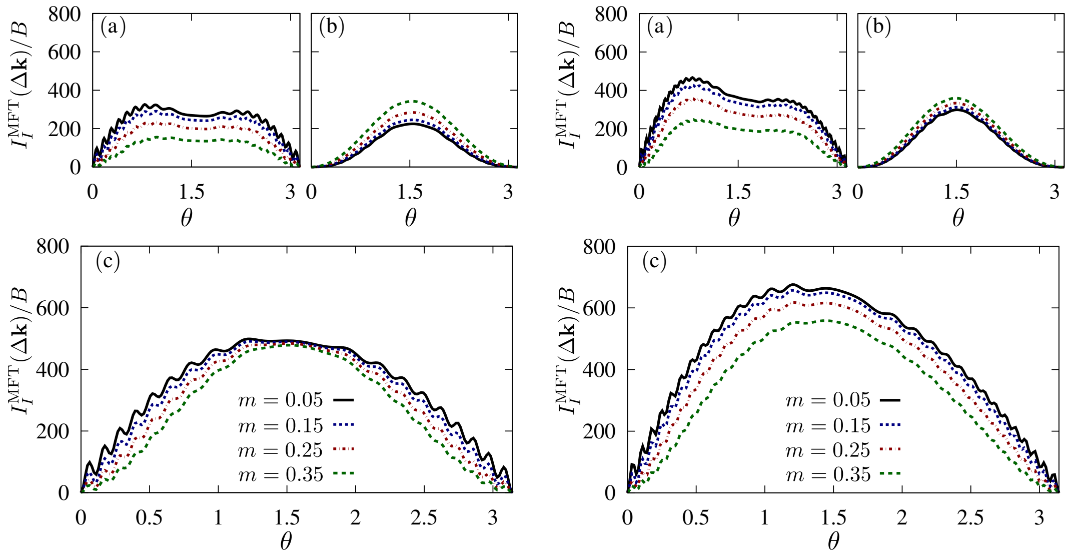

(a) $\kappa = 0.66$

(b) $\kappa = 1.05$

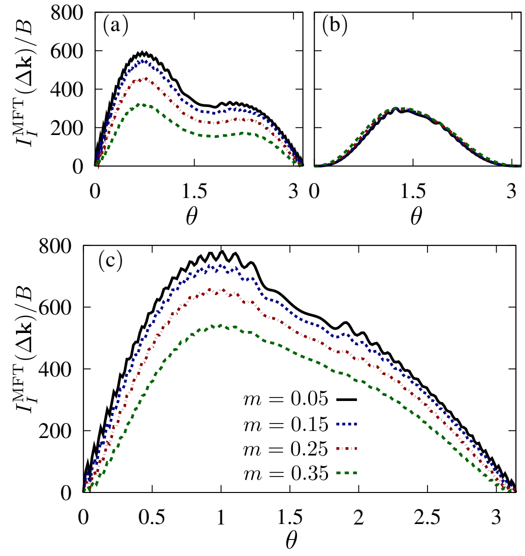

(c) $\kappa = 1.5$

Figure 5.9: Angular distribution of the inelastically scattered light intensity for different values of the interaction strength U at $T = 0$ along the direction $\phi = \pi/4$. The calculations are based on MFT. Here, the number of sites is 40×40. The different figures show a varying ratio between the wavenumber of the probe light to the effective wavenumber of the optical lattice light κ [Eq. (4.16)]. The lattice height is $s = 7$. For each value of κ, the separate intensity contributions are shown for (a) the density and longitudinal spin components; (b) transverse spin component; (c) total scattered light intensity. The scattered intensity decreases with increasing magnetisation because of the changes in the density and longitudinal spin susceptibility.

ferent. In the spin-conserving processes, the resulting emitted photons are generated by the σ^+ transition, which is supressed in the perpendicular direction. In fact, in the forward direction, it is twice as intense as in the perpendicular direction. On the other hand, the spin-exchanging process results in photons scattered via a π transition which is oriented parallel to the forward direction. Hence, the intensity of the scattered light from this component is zero in the forward direction and reaches its maximum in the perpendicular direction ($\theta = \pi/2$).

Within the MFT, the angular distribution of the inlastically scattered light has been computed for different values of the on-site interaction strength U. This corresponds to different values of the staggered magnetisation m [via Eq. (3.17)]. Fig. 5.9 shows the results based on MFT at $T = 0$ for different values of the parameter κ [Eq. (4.16)]. In this case the intensity is obtained using the MFT static structure factor [Eqs. (3.42) and (3.43)] in Eq. (4.28). In Fig. 5.9, the different angular distributions of the two transitions are shown independently along with the angular distribution of the full signal. Being at zero temperature, most of the change occurs in the perpendicular direction, around $\theta \approx \pi/2$ because Pauli blocking highly supresses scattering processes in the forward direction at $T = 0$. In the MFT calculation, the density and longitudinal spin susceptibilities are more sensitive to changes in the on-site interaction strength U than the transverse susceptibility.

A comparison of the intensities resulting from the MFT and RPA calculations is shown in Fig. 5.11. The most significant change occurs around the perpendicular direction. It is in this direction that the polarisation factor of the spin-exchanging transitions, which contains the collective modes, reaches its maximum. Hence, the effect of the collective modes is most notable around this direction. In the forward direction, there is practically no difference between both approximations.

Fig. 5.10 shows how the RPA intensity changes when the on-site interaction U is increased at zero temperature. This affects the zero temperature staggered magnetisation m. The most important contribution to the inelastic scattered light within the RPA approximation comes from the collective modes which are suppresed due to the polarisation factor in the forward direction and not supressed at all in the perpendicular direction.

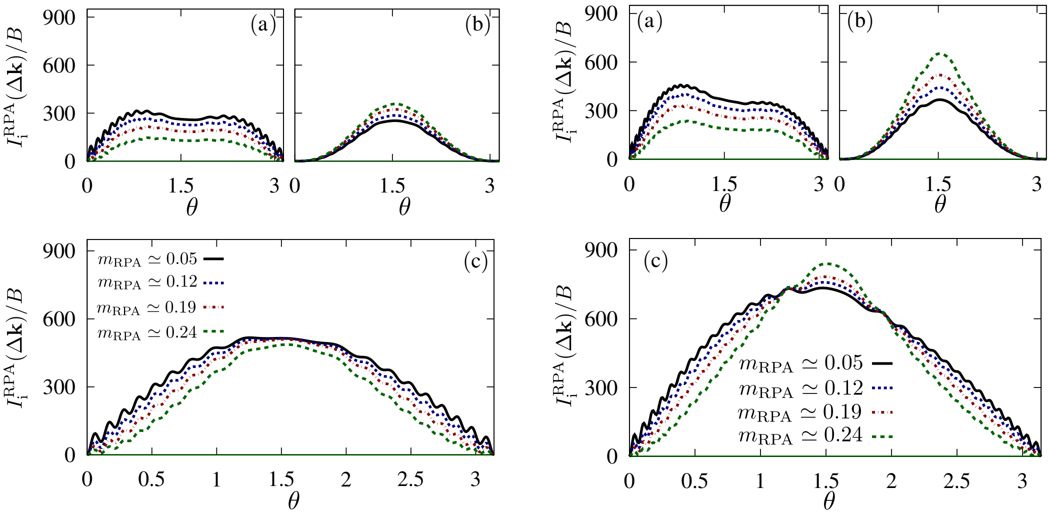

(a) $\kappa = 0.66$

(b) $\kappa = 1.05$

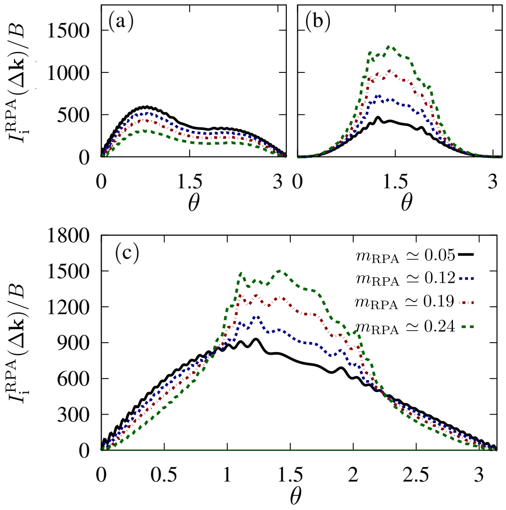

(c) $\kappa = 1.5$

Figure 5.10: Angular distribution of the inelastically scattered light intensity for different values of the interaction strength U at $T = 0$ along the direction $\phi = \pi/4$. The calculations are based on RPA. The different figures show a varying ratio between the wavenumber of the probe light to the effective wavenumber of the optical lattice light κ [Eq. (4.16)]. The lattice height is $s = 25$. For each κ value, the separate intensity contributions are shown for (a) the density and longitudinal spin components; (b) transverse spin component; (c) total scattered light intensity. The scattered intensity increases with increasing magnetisation near the perpendicular direction $\theta \sim \pi/2$ because, due to the collective modes, the transverse spin component dominates the scattered light.

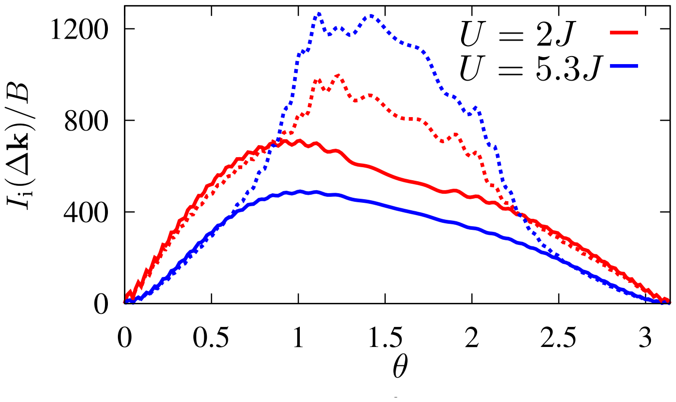

Figure 5.11: Comparison of the angular distribution of the inelastic scattered light intensity based on MFT (solid) and RPA (dashed) at $T = 0$ along the direction $\phi = \pi/4$, with $\kappa = 1.5$. The rest of the parameters are as in Fig. 5.9. The MFT and the RPA results notably differ, owing to the collective modes that significantly modify the transverse spin component. The magnitude of the order parameter [Eq. (3.2)] is $m = 0.19$ ($m_{\text{RPA}} \simeq 0.15$) for $U = 2J$ and $m = 0.4$ ($m_{\text{RPA}} \simeq 0.28$) for $U = 5.3J$.

5.3.1 Temperature dependence within the mean field approximation

Even though the calculation at the mean field level does not capture the collective modes of the AFM state, it can be used to analyse how temperature affects the system. In fact, in the forward direction, this calculation remains qualitatively valid. This can be seen in Fig. 5.11. The MFT is qualitatively valid for describing the scattered light in the forward direction because of the geometrical dependence of the different contributions to Eq. (5.14). The first two terms, which depend on the charge and on the longitudinal spin susceptibility, are responsible for most of the scattering in the forward direction. The third term, proportional to the transverse spin susceptibility, is highly supressed in the forward direction by the polarisation factor. To compute the finite temperature inelastic component of the scattered light, the finite temperature static structure factors presented in Section 3.2.2 [Eq. 3.42] can be used in Equation. (4.28). Figure 5.12 shows the inelastic scattered light for a system with fixed on-site interaction, $U = 5.3J$, and for different temperatures. Increasing temperature supresses the MFT staggered magnetization m, see Eq. (3.17) and Fig. 3.3. At $T = 0$, the scattering processes with small change in momentum are highly supressed, this is the so-called *Fermi blocking*. Fermi-blocking is supressed with increasing temperature, as can be seen in Fig. 5.12. This is because with raising temperature, vacancies appear in the lower effective band, as some of the atoms are excited to the higher effective band and scattering within the lowest band is

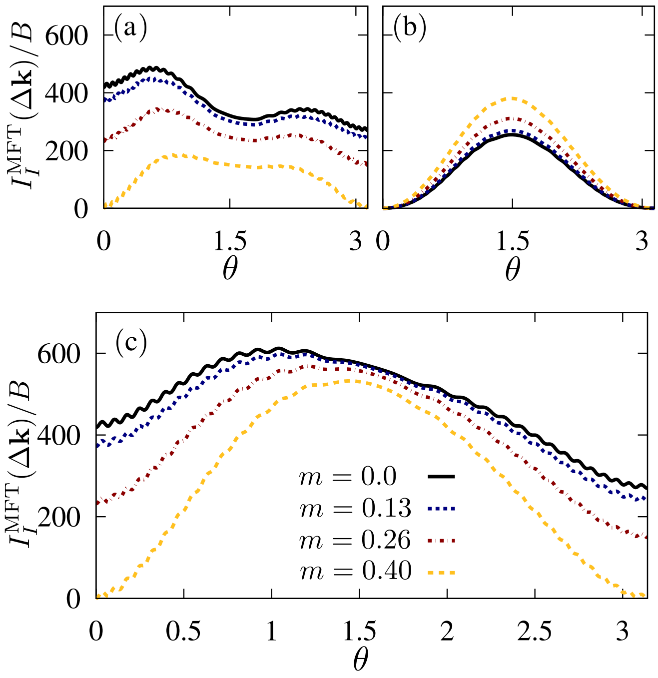

Figure 5.12: Angular distribution of the inelastically scattered light intensity at different temperatures along the direction $\phi = \pi/4$. The calculations are based on MFT. Here the on-site interaction is fixed at $U = 5.3J$. This means that lower T corresponds to higher values of m. The parameters have the same values as in Fig. 5.9. The figure shows the intensity contributions from (a) the density and longitudinal spin components; (b) transverse spin component; (c) total scattered light intensity. An increase in temperature enhances scattering in the near-forward direction.

possible. This behaviour is analogous to the single-component noninteracting fermionic gas [104]. In Fig. 5.12(a) and 5.12(b), the longitudinal and transversal modes are shown separately. At high temperatures or very low on-site interaction (both ways of obtaining a low staggered magnetisation), the longitudinal mode dominates the inelastic scattering. As m increases, the contribution from the transverse mode becomes the more important contribution as magnetic order suppresses the longitudinal correlations. The response is similar when the on-site interaction is increased at zero temperature.

The temperature sensitivity of the signal makes it plausible to use the scattered light for an interacting two-component case[††]. This is studied in Section 6.2.

[††] Thermometry with a single-component noninteracting fermionic gas was proposed by Ruostekoski et al. in [104].

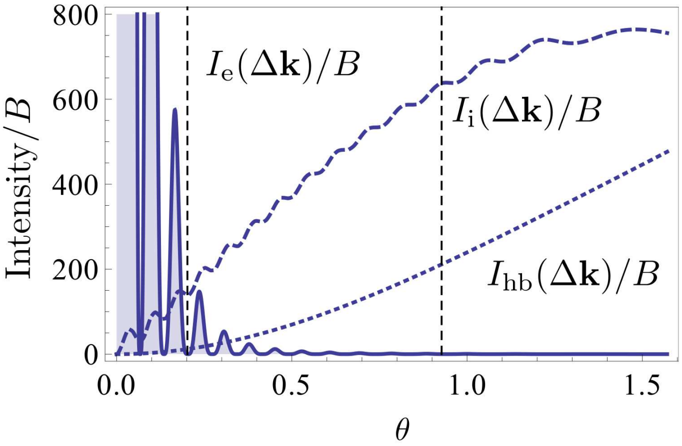

Figure 5.13: Comparison of the angular distribution of the different components of the scattered light intensity at $T = 0$ along the direction $\phi = \pi/4$. Here, the on-site interaction strength is $U = 1.76J$ and the order parameter $m = 0.16$ ($m_\mathrm{RPA} \simeq 0.13$). The parameters used are the same as in Fig. 5.9. The curves in the figure are: MFT elastic component (solid), RPA inelastic intraband component (dashed) and exact inelastic interband component (dotted). From left to right, the dashed vertical lines represent the block (depicted such that it blocks up to the third diffraction peak) and the edge of the lens in the forward direction (NA= 0.8).

5.4 Inelastic losses to higher bands

The signal measured in an experiment consists of the elastic and the inelastic intraband components which for ^{40}K are studied in the previous Sections 5.2 and 5.3. Apart from these two processes, in Section 4.4, atomic scattering to higher bands was taken into account. The frequencies of the scattered photons for the interband components are different to those of the elastic and inelastic intraband. Due to this difference, photons emitted due to an atom being scattered to higher bands can be filtered out of the signal. Hence, the interband scattering only has to be considered to estimate de heating rates of the atoms. For the transitions considered in this chapter, Fig. 5.2, the scattered light intensity corresponding to the interband transitions, Eq. (4.49), can be written as

$$I_\mathrm{hb}(\Delta\mathbf{k}) = BN_s^2\,(1-\alpha_{\Delta\mathbf{k}})\,\frac{192+10\cos 2\theta}{121}\,. \tag{5.33}$$

Figure 5.13 shows the angular distribution of the interband component, as well as the elastic and intraband component. The interband component does not have any dependencies on the atomic correlations. It is entirely determined by the set of available states [Fig. 5.1] and the light used to illuminate the sample [Fig. 5.2]. This component is proportional to $1-\alpha_{\Delta\mathbf{k}}$, where $\alpha_{\Delta\mathbf{k}}$ denotes the Debye-Waller factor [Eq. (4.22)]. This dependence is opposite to that of the intraband inelastic scattering, which is proportional to $\alpha_{\Delta\mathbf{k}}$. Thus, changing the lattice depths has opposite effects for both components of the scattered light. As will be analysed in Chapter 6, it is important to keep atom heating rates to a minimum. Deep lattices result in atoms being more strongly confined, which supresses the losses to higher bands, while at the same time enhancing the inelastic intraband scattering, which carries information on the atomic correlations.

Chapter 6

Experimental considerations

In this chapter, the proposed experimental schemes of Fig. 5.3 are analysed in detail. In [104], the scattered light from a single species gas of non-interacting fermionic atoms trapped in an optical lattice was shown to be a feasible tool for the detection of temperature changes in an optical lattice. In the previous chapters, it was shown that for a two-species interacting gas a similar temperature dependence is observed [Fig. 5.12]. In this chapter, it is shown that for the two-species interacting gas scattered light serves as a probe for temperature and, this is new to the interacting case, AFM ordering in the system. Also in the previous chapter, the effect of varying the on-site interaction/temperature on the scattered light was shown. These results are used in this chapter to estimate the number of experiments that need to be performed to achieve a given temperature/magnetic ordering sensitivity. The analysis in this chapter generalises[*] the analysis of the single-species non-interacting gas presented in [104].

6.1 Detection of scattered light

In the proposed experimental scheme, shown in Fig. 5.3, a 2D optical lattice in the xy plane is assumed. A laser is shone in the z direction [Fig. 4.1], and light is scattered by the atoms in the optical lattice. The scattered light is then collected by a lens, and the collected intensity is measured. The lens can be positioned in different configurations, depending on the magnitude being probed, and/or the experimental availability of space. The latter possibility depends on the particular experimental setup. Experiments with

---

[*] The generalisation includes the effect of the scattering to higher bands, first taken into account by Douglas and Burnett in [31].

ultracold atoms are extremely complex, and the high-vacuum chamber where the atoms are contained is usually surrounded by the different components of the experiment. In this chapter, three different possible configurations are studied. A lens in the forward direction, similar to the setup studied in [104], and two new configurations: a lens in the perpendicular direction [Fig. 5.3(c)], and a lens which is centred around the magnetic Bragg peak [Fig. 5.3(a)]. Theoretically, the light collected by the lens is obtained by integrating the scattered intensity [Eqs.(5.7), (5.8), and (5.14)] over the appropriate angular range corresponding to a given geometry and lens NA. The collected scattered light photon rate by a lens L of numerical aperture NA is denoted by

$$\mathfrak{I}^{\mathrm{L}}_{\alpha,\mathrm{NA}}(m) = \int_{\mathrm{L,NA}} d\Omega I_\alpha(\Delta\mathbf{k}, m). \tag{6.1}$$

Here the subscript α denotes the component. e for elastic [Eq.(5.7)], i for inelastic intraband [Eq. (5.14)], and hb for scattering to higher bands [Eq. (5.8)]. For example, the integration for the lens in the forward direction F [Fig. 5.3(b)] can be written explicitly as:

$$\mathfrak{I}^{\mathrm{F}}_{\alpha,\mathrm{NA}}(m) = \int\limits_0^{2\pi} d\phi \int\limits_0^{\arcsin \mathrm{NA}} \sin\theta d\theta I_\alpha(\Delta\mathbf{k}, m). \tag{6.2}$$

In order to estimate the heating-rates, the total scattered photon rates are also needed. This quantity is denoted by

$$\mathfrak{I}^{\mathrm{Total}}_{\alpha}(m) = \int_{\mathrm{Total}} d\Omega I_\alpha(\Delta\mathbf{k}, m) = \int\limits_0^{2\pi} d\phi \int\limits_0^{\pi} d\theta I_\alpha(\Delta\mathbf{k}, m). \tag{6.3}$$

Elastically scattered photons do not destroy the sample. Hence, the elastic component scattering rate does not pose any time constraint on how long the laser pulses can be. Inelastically scattered light, on the other hand, *heats up* the sample, destroying the ground state. The heating happens due to the exchange of momentum between the photon and the atom, which increases the energy of the system, thus, increasing the temperature of the sample. Inelastic light scattering also affects the system in a second way, as has been already discussed in Secs. 4.4 and 5.4, atoms are excited to higher bands. This process involves an atom being scattered off the lowest band, consequently, the atom is lost from the trap. In optical lattices, the number of trapped atoms is at most of the order of $\sim 100^2$, thus, with a finite number of atoms, loosing a fraction of them rapidly leads to the total destruction of the sample. To avoid this, instead of illuminating with a continuous mode

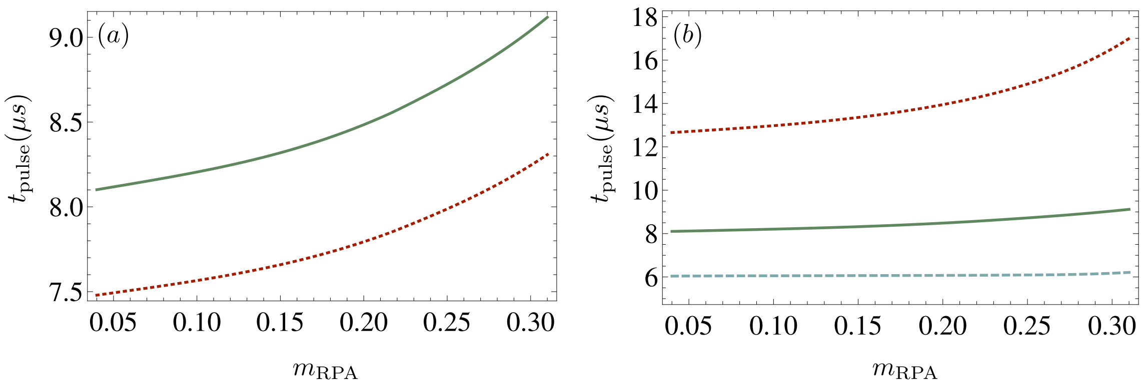

Figure 6.1: Illuminating laser pulse length t_{pulse} [Eq. (6.4)] in units of μs. The calculations are computed with RPA susceptibilities at $T = 0$. (a) shows a fixed value of $\kappa = 1.05$ and compare two different lattice depths $s = 7.8$ (dotted) and $s = 25$ (solid). (b) shows a fixed lattice depth $s = 25$, and compares three different values of the parameter $\kappa = 0.66$ (dotted line), $\kappa = 1.05$ (solid) and $\kappa = 1.5$ (dashed).

laser, the sample has to be illuminated with very short pulses [Fig. 6.1]. However, illuminating during a very short period of time means that the number of scattered photons is not very large. The length of the laser pulses can be estimated by assuming that, as long as only a small percentage W of the atoms are lost in a single experiment, the ground state is not destroyed during the measurement. A pulse length determined by a fixed number W of scattering events can be computed from the following expression

$$t_{\text{pulse}} = \frac{W}{\mathfrak{I}_{\text{i}}^{\text{Total}}(m) + \mathfrak{I}_{\text{hb}}^{\text{Total}}(m)}. \tag{6.4}$$

t_{pulse} only depends on the number of scattering events W, which here is taken to be a 10% of the number of atoms in the sample,

$$W = 0.1 N_s^2. \tag{6.5}$$

In Eq. (6.4), only the total scattering rates [Eq. (6.3)] for inelastic components of the scattered light are taken into account as elastic scattering does not destroy the sample.

A factor to be considered is the size of the lattice N_s^2, and how the different components of the scattered light scale with it. Elastic scattering can be seen from Eqs. (5.18), (4.36) to scale as N_s^4. The losses to higher bands scale proportionally to N_s^2 [Eq. (4.49)]. The inelastically scattered light is, on the other hand, not that clear from the analytic expression but a simple numerical test shows that it is, in fact, also proportional to the number of atoms in the lattice N_s^2.

The time scale of an ultracold atomic experiment is determined by the lifetime of an atom in an optical lattice. The typical lifetime of an atom in an optical lattice ranges from

100ms to 5s [33]. It is important that the hopping lifetime is kept low relative to the atom lifetime. In this manner, atoms will have enough time to reach equilibrium in the lattice. Thus, thermalisation times pose an important constraint when it comes to choosing the experimental parameters. However, one possible way to avoid this constraint is to rapidly change the lattice depth before probing the system. Changing the lattice depth affects the signal mainly through the change in the Wannier factor $\alpha_{\Delta\mathbf{k}}$ [Eq. (2.6)]. It enters the intraband inelastic scattered light as an overall multiplying factor, and the losses to higher bands as a factor of $1 - \alpha_{\Delta\mathbf{k}}$. The effect of changing the lattice depth can be appreciated in Fig. 6.2 where the angle-resolved intraband inelastic intensity [Eq. (5.14)], and the losses to higher bands [Eq. (5.8)] are shown along the $\phi = \pi/4$ direction for different values of the lattice depth. Increasing the lattice depth leads to an increment in the intraband scattering, and a suppression of the the interband component.

Having discussed the different aspects of the experiment that have to be taken into account, what follows, is a prescription for how to choose the best values. To choose a quasi-optimal combination of parameters, one possible way to proceed is as follows: compute the signal in both lenses, and also compute the total number of inelastically scattered photons. This includes both, intraband and interband scattering components. The best result will maximise the number of photons scattered into the lens. In particular, the best detection accuracy is obtained for the set of parameters that maximises the slope of the number of photons scattered into the lens. With the extra constraint that the total number of inelastically scattered photons should remain as low as possible. Due to the different dependence on the Debye-Waller factor $\alpha_{\Delta\mathbf{k}}$ [Fig. 6.2] that the intraband and interband components have, increasing the lattice depth, increases the intraband inelastic scattering, hence, improving the signal, and suppressing the losses to higher bands. Also, this happens in such a way that the overall total number of inelastically scattered photons decreases. This allows for a longer pulse length. When it comes to determining the probing laser, the particular atom and the existence of resonances for it constrain the choice. For the AFM ordering case, choosing a large factor of κ increases the signal, as this means reaching for larger values of momentum and the possibility of probing the susceptibility around $\mathbf{Q} = (\pi, \pi)$. The estimates on the number of experimental realisations support this. For the set of parameters used in this chapter, the number of collected photons per experimental run is at most ~ 20. To determine an optimal value for the lens

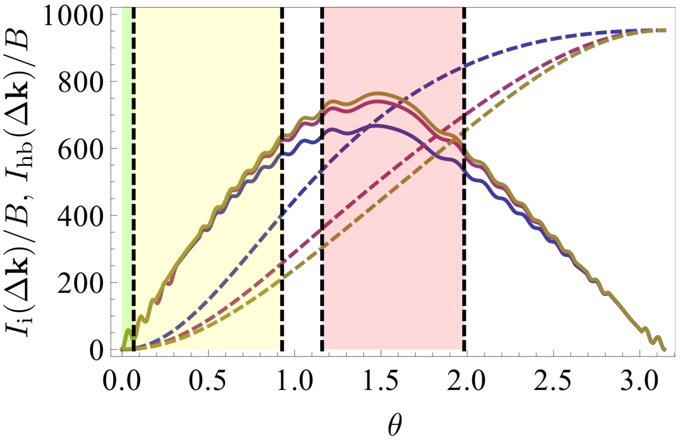

Figure 6.2: Angular distribution of the inelastically scattered light intensity for different lattice depths at $T = 0$ along the direction $\phi = \pi/4$[Eqs. (5.8) and (5.14)]. The calculations are exact for the interband component (dashed) and based on RPA for the intraband component (solid). Here the on-site interaction strength $U = 1.76J$. The rest of the parameters are as in Fig. 5.9. Bottom to top for intraband and vice-versa for the interband, $s = 5, 15, 25$. From left to right we schematically show the positions of the block (green), lens with NA= 0.8 in the forward direction (yellow) and a lens with NA=0.4 in the perpendicular direction (red). Increasing lattice depth enhances the intraband and suppresses the interband scattered light. Such changes are most notable around the perpendicular direction.

NA, the same principles have to be followed. The best results are obtained with the lens NA that maximises the slope of the collected intensity with respect to the magnitude to be determined. For the forward direction, it depends whether temperature or magnetisation is to be determined. The changes in the scattered light are very different for each case. For temperature changes, the major changes occur in the forward direction. Hence, choosing the block properly is more critical than the choosing the numerical aperture of the lens. This is because the main diffraction peak has to be blocked without killing all the inelastic scattering signal.

For determining the magnetisation of a system, at zero temperature at least, the changes happen mostly in the perpendicular direction [Fig. 6.3]. In the forward direction, the changes are not so large. The approach taken here is to block completely the elastic signal, and to use a lens with a very large numerical aperture that captures photons over a large range of scattering angles. In the perpendicular direction, on the other hand, as can be seen on Fig. 6.3, the changes happen around $\theta = \pi/2$. No block is needed in this direction. Any elastically scattered light in this direction depends on the magnetic ordering in the system. However, choosing a lens with a large numerical aperture may

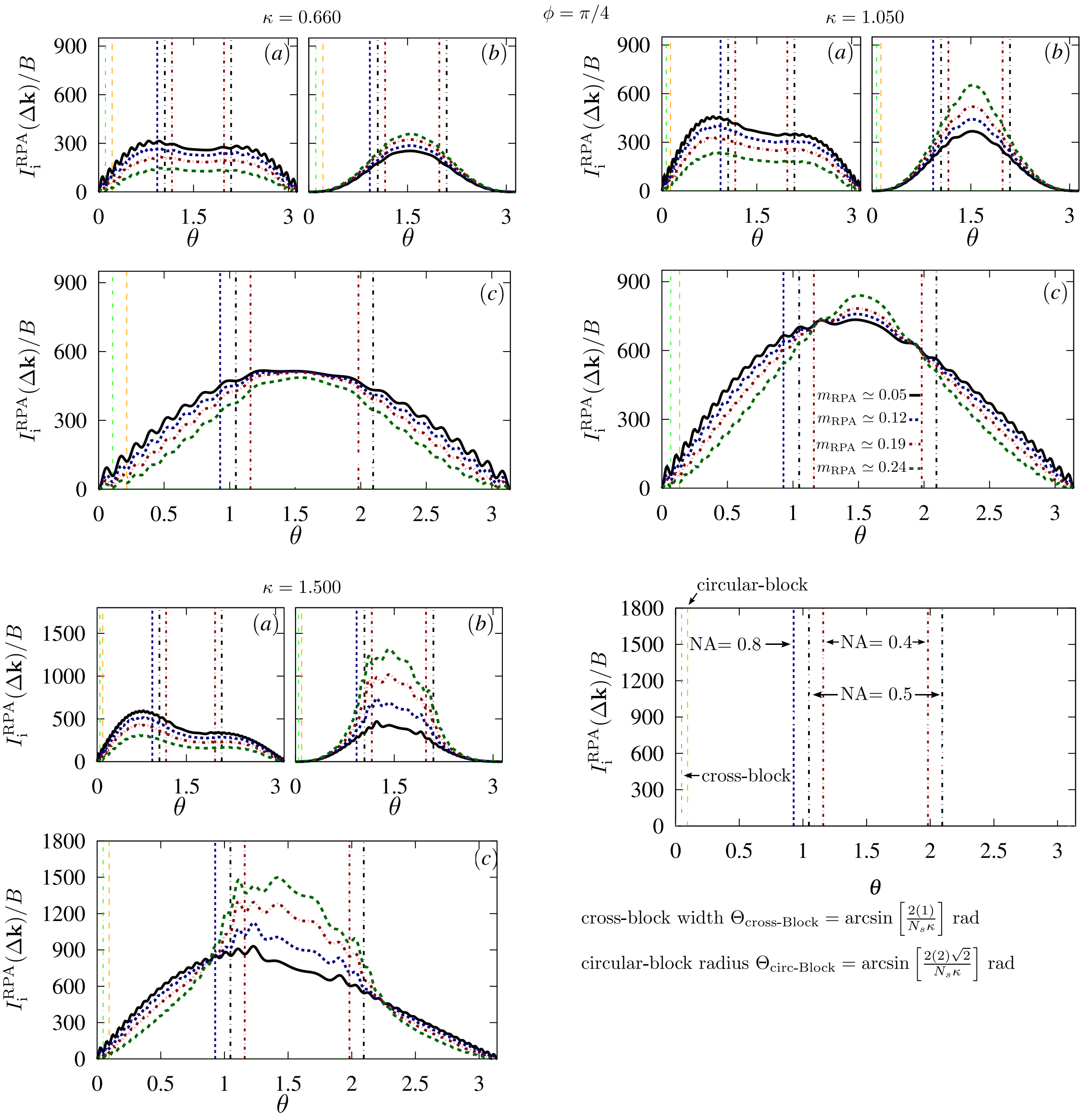

Figure 6.3: Angular distribution of the scattered inelastic light intensity for different values of κ. These figures are the same as in Fig. 5.10. Here, the positions of the lenses and the block are shown schematically.

affect the slope of the intensity as a function of m, as the most significant changes happen around the perpendicular direction. If some filtering is applied, the lens NA may be optimised to the changes in the filtered scattered light.

6.1.1 Block size choice

The angular size of the block can be computed from the analytical expression for the diffraction pattern [Eq. (4.36)] and the expression for the change of light momentum upon scattering $\Delta\mathbf{k}$ [Eq. (4.11)]. In this thesis two types of blocks are considered: a cross

Table 6.1: Parameters of the block used to estimate the measurement accuracy estimates shown in Fig. 6.5.

κ	Cross width (rad)	Circular radius(rad)
0.66	0.08	0.22
1.05	0.05	0.14
1.50	0.03	0.10

shaped and a circular block. Both blocks are shown in Fig. 5.3(b). The cross shaped block removes the scattered light off the diffraction pattern along the x and y axis. The circular block reduces the collected photons from the elastically scattered light by blocking the first two or three peaks along the diagonal. The size of the cross block can be estimated by taking $\phi = 0$ in Eq. (4.11), $\Delta\mathbf{k}_t(\theta, \phi = 0) = \kappa\pi\sin(\theta)$. Looking at the diffraction factor, along the x direction, the first zero of the diffraction peak will be when the argument of the function is equal to π and the nth zero whenever it is equal to $n\pi$.

$$\begin{aligned}\frac{N_s\Delta\mathbf{k}_x(\theta,\phi=0)}{2} =& \frac{N_s\kappa\pi\sin\Theta_{\text{Cross-Block}}}{2} = n\pi \\ \rightarrow \Theta_{\text{Cross-Block}} =& \arcsin\left(\frac{2n}{N_s\kappa}\right).\end{aligned}$$

For a circular block to block up to the n-th zero along $\phi = \pi/4$, its radius is given by:

$$\Theta_{\text{Circ-Block}} = \arcsin\left(\frac{2n}{N_s\kappa\cos\pi/4}\right).$$

6.2 Number of experimental realisations

This section assesses the experimental feasibility of scattered light experiments as a probe. This is important from the practical point of view as the type of measurements proposed here need to be repeated a given number of times and averaged over. The determination of the number of experimental realisations follows the analysis presented by Ruostekoski et al. in [104], and Douglas and Burnett in [31]. For simplicity, it is assumed that the photon detection efficiently is 100%. In a single measurement $N_c(m)$ photons will be collected, and the experiment can be repeated τ times. The average total number of collected photons is

$$\varpi_{m,\tau} = \tau N_c(m) = \tau\left[N_c^i(m) + N_c^e(m)\right]. \tag{6.6}$$

Here, $N_c^i(m) = \zeta(m)W$. W is the fraction of inelastically scattered photons in a single experimental realisation [Eq. (6.5)]. $\zeta(m)$ is the fraction of collected inelastically scattered photons. It can be computed as follows

$$\zeta(m) = \frac{\mathfrak{I}^{\mathrm{L}}_{\mathrm{i,NA}}(m) + \mathfrak{I}^{\mathrm{L}}_{\mathrm{hb,NA}}(m)}{\mathfrak{I}^{\mathrm{Total}}_{\mathrm{i}}(m) + \mathfrak{I}^{\mathrm{Total}}_{\mathrm{hb}}(m)}. \tag{6.7}$$

Using Eq. (6.4), the number of collected photons in a single experimental realisation corresponding to the inelastic component of the scattered light can be written as

$$N^i_c(m) = \zeta(m)W = \left[\mathfrak{I}^{\mathrm{L}}_{\mathrm{i,NA}}(m) + \mathfrak{I}^{\mathrm{L}}_{\mathrm{hb,NA}}(m)\right] t_{\mathrm{pulse}}. \tag{6.8}$$

In an analogous manner, the number of collected photons in a single experimental realisation corresponding to the elastic component is

$$N^e_c(m) = \mathfrak{I}^{\mathrm{L}}_{\mathrm{e,NA}}(m) t_{\mathrm{pulse}} = \frac{\mathfrak{I}^{\mathrm{L}}_{\mathrm{e,NA}}(m)}{\mathfrak{I}^{\mathrm{L}}_{\mathrm{i,NA}}(m) + \mathfrak{I}^{\mathrm{L}}_{\mathrm{hb,NA}}(m)} N^i_c(m). \tag{6.9}$$

The distinction between photons corresponding to the elastic or inelastic component is, of course, merely a theoretical device; photons are indistinguishable. Taking this into account, the total number of collected photons can be rewritten as

$$\begin{aligned} N_c(m) =& N^i_c(m) + N^e_c(m) \\ =& \left(\mathfrak{I}^{\mathrm{L}}_{\mathrm{i,NA}}(m) + \mathfrak{I}^{\mathrm{L}}_{\mathrm{hb,NA}}(m) + \mathfrak{I}^{\mathrm{L}}_{\mathrm{e,NA}}(m)\right) t_{\mathrm{pulse}}. \end{aligned} \tag{6.10}$$

This is a general definition. In this thesis, it is also assumed that the interband scattered component is filtered out off the collected signal. This can be done because of the relation between the scattered light and momentum. The elastic and inelastic intraband component signals originates from low momentum scattering processes, while the higher band scattered photons have a high energy. Hence, a slightly different definition for $\zeta(m)$ where the higher band scattered photons can be filtered out can be used

$$\zeta_f(m) = \frac{\mathfrak{I}^{\mathrm{L}}_{\mathrm{i,NA}}(m)}{\mathfrak{I}^{\mathrm{Total}}_{\mathrm{i}}(m) + \mathfrak{I}^{\mathrm{Total}}_{\mathrm{hb}}(m)}. \tag{6.11}$$

Of course, light still scatters atoms to higher bands and this leads to losses. Hence, the scattering to higher bands has to be taken into account in the denominator of Eq. (6.11). The fluctuations of the number of scattered photons obey Poisson statistics. The aim of this type of experiments is to distinguish two AFM states characterised by two different values of the magnetisation m_1 and m_2 via scattered light. Mathematically, this translates into the question of distinguishing the average of two Poisson distributions with a sample of size τ. Taking m_2 as a reference state, the difference in the average number of

Table 6.2: Specific values of the estimated number of experimental realisations, $\tau(m_{\text{ref}})$ for single species detection [Fig. 6.4(d)] with $\kappa = 1.5$. The two lenses with NA= 0.2 and NA= 0.4 are pointing in the direction of the magnetic Bragg peak [Fig. 5.3(a)] and in the direction perpendicular to the incident field[Fig. 5.3(c)], respectively. These values are for a relative accuracy of 10%. Here m_{ref} is the RPA corrected order parameter (Sec. 3.3).

NA	$\tau(0.08)$	$\tau(0.12)$	$\tau(0.19)$
0.2	210	60	10
0.4	200	50	10

collected photons $\varpi_{m_2,\tau} - \varpi_{m_1,\tau}$ has to be at least of the order of the photon shot-noise $\sqrt{\varpi_{m_2,\tau}}$. Thus, the minimum sample size, that is, the minimum number of experimental realisations to distinguish between the optical signal from two different magnetisation stats m_1 and m_2 is,

$$\tau_{\text{min}} \approx \frac{\varpi_{m_2}}{\left(\varpi_{m_2} - \varpi_{m_1}\right)^2} = \frac{N_c(m_2)}{\left(N_c(m_2) - N_c(m_1)\right)^2}. \tag{6.12}$$

The subscript $_{\text{min}}$ is dropped for the rest of this section. The rest of this section is dedicated to presenting the results for the rate of collected photons, and the estimates for the minimum number of experimental realisations τ needed to distinguish two different AFM states. The changes are calculated with respect to a reference value m_{ref}, and for a given relative accuracy $\Delta m/m_{\text{ref}}$ [Eq. (6.12)]. At $T = 0$, the inelastic scattering is calculated using the RPA susceptibilities. In Figs. 6.4, 6.5 and 6.8 m_{ref} is the RPA corrected order parameter (Sec. 3.3). The elastic component of the scattered light [Eqs. (5.15) and (5.20)] has been computed using the RPA corrected order parameter m_{RPA} (Sec. 3.3). At finite temperature, only MFT results are used. Hence, for the temperature dependent MFT results of Fig. 6.7, m_{ref} is the MFT order parameter obtained from the solution of Eq. (3.2). Except for the scaling analysis of τ with lattice size, all the results in this Section are for a lattice of size 40×40.

First, direct detection of the magnetic Bragg peaks is analysed [Section 5.2]. This can be done in two ways: using a small NA= 0.2 positioned directly on top of the peak [Fig. 5.3(a)], or using a wide lens in the perpendicular direction [Fig. 5.3(c)]. The lens considered here is characterised by NA= 0.4, and with this NA, it captures both magnetic Bragg peaks [Figs 5.4 and 6.3]. As noted in Sec. 5.2, this is only possible when the parameter $\kappa \geq \sqrt{2}$ [Eq. (4.16)]. Figure 6.4(a) and (b) show, respectively, the collected photon rates and the estimated minimum number of necessary experimental realisations. If

Table 6.3: Specific values of the estimated number of experimental realisations, $\tau(m_{\text{ref}})$, for two lattice depths with $\kappa = 1.05$ presented in Fig. 6.5(b). The parameters of the block are given in Table 6.1. Here m_{ref} is the RPA corrected order parameter (Sec. 3.3).

	$\Delta m/m_{\text{ref}} = 10\%$		$\Delta m/m_{\text{ref}} = 20\%$	
s	$\tau(0.12)$	$\tau(0.19)$	$\tau(0.12)$	$\tau(0.19)$
7.8	410	50	90	10
25	390	50	90	10

one of the species, say $|\uparrow\rangle$, is removed from the lattice[†] before the probing laser is shone, no destructive interference occurs, and the magnetic Bragg peak is proportional to $m^2 N_s^4$. As shown in Section 5.2.1, in this case, the elastic component of the collected signal dominates over the inelastic one. This is the best way to determine the order parameter m. Figure 6.4(c) and (d) show the results of such an experiment for the case with a lens in the perpendicular direction of NA= 0.4 [Figs. 5.3(c)] and the setup with a small lens on top of the magnetic Bragg peak with NA= 0.2 [Fig. 5.3(a)]. Compared with the rest of the cases in this section, the number of experimental realisations is dramatically low. In order to compare this configuration with the cases presented below, Table 6.2 shows the estimated τ values [Eq. (6.12)] for some specific cases. Hence, *single-species detection, is the most accurate method for the determination of AFM ordering in optical lattices presented in this thesis.*

Fig. 6.5 shows the results for a setup where light is collected in the forward direction [Fig. 5.3(b)], with a lens of a large numerical aperture, NA= 0.8, computed within the RPA approximation. Fig. 6.5(a) shows the collected photon rates for two lattices with different depths. A shallow one with $s = 7.8E_R$ and a deep one with $s = 25E_R$. It shows quantitatively what was noted in the previous section, intraband inelastic scattering increases with lattice depth. Fig. 6.5(b) shows the estimated minimum number of measurements to achieve a given relative accuracy $\Delta m/m_{\text{ref}}$ computed from Eq. (6.12). Lattice depth turns out not to be relevant for this set of parameters, but it is clear from the figure that very small magnetisations are extremely hard to measure. This is clear from the data in Table 6.3, in which some specific numerical values are shown. Table 6.3 shows the τ for two different accuracies and it illustrates that if the required accuracy is not so high, say 20%, the number of experimental realisations drops significantly.

In Figs. 6.5(c) and (d), the ratio κ [Eq. (4.16)] between the wave-number of probe light

---

[†] This can be done, for example, by transferring the other spin component to a different hyperfine state [122].

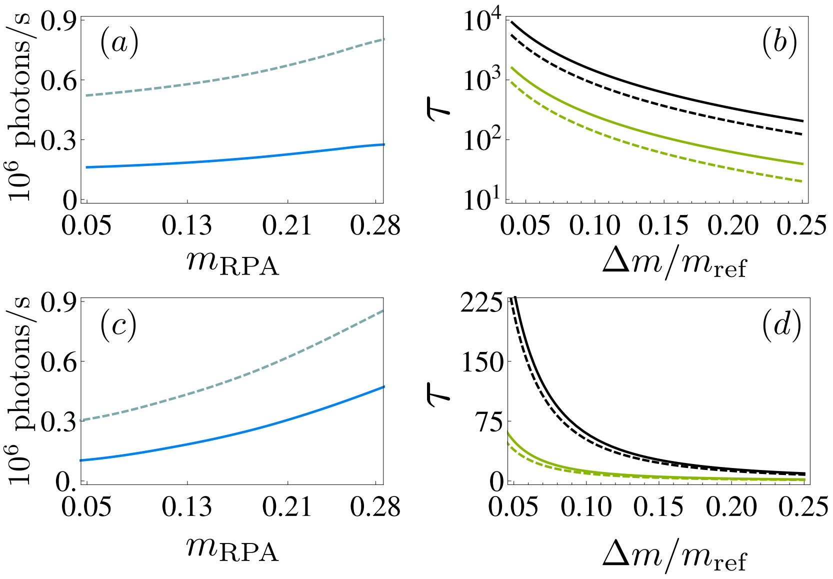

Figure 6.4: Measurement accuracy at $\kappa = 1.5$ when light along the direction of the emerging magnetic Bragg peak is detected. The calculations are based on RPA susceptibilities at $T = 0$ with an RPA corrected order parameter $m_{\rm RPA}$ for the elastic component. The left column shows the collected photon rates vs. the RPA corrected AFM order parameter $m_{\rm RPA}$ and the right column shows the number of experimental realisations τ to achieve a relative accuracy $\Delta m/m_{\rm ref}$. In all the plots (a)-(d), dashed curves correspond to the configuration of a lens with NA= 0.4 pointing in the perpendicular direction [Fig. 5.3(c)], and solid curves are for a small lens with NA= 0.2 pointing in the direction of the emerging magnetic Bragg peak [Fig. 5.3(a)]. Note that the lens in the perpendicular direction also collects the signal from two magnetic Bragg peaks. (a), (b) show the case when both spin species are detected.(c), (d) show the case when only the $|\downarrow\rangle$ atoms are detected. The number of experimental realisations needed for a given accuracy is highly suppressed when only one species is detected. In (b) and (d) we show the τ values for two different reference states: $m_{\rm ref} \simeq 0.12$ in black (top two curves) and $m_{\rm ref} \simeq 0.19$ in green (bottom two curves).

and the lattice light, is varied. In particular, results for $\kappa = 0.66, 1.05, 1.5$ are shown. The scattering rate at the detector increases for larger values of κ. Some specific numerical values for the number of experimental realisations corresponding to Fig. 6.5(c) and (d) are presented in Table 6.4. For small values of $m_{\rm ref}$, τ increases with increasing κ but this is negligible for $m_{\rm ref} \approx 0.19$. This behaviour is because as bigger values of κ increase the inelastic intraband photon rates, most of the scattered light scatters away from the forward direction [Figs 5.10 or 6.3]. For a lens in the forward direction, this translates into shorter pulse lengths [Fig. 6.1], and the increment in collected photon numbers does not compensate this. Hence, for small values of κ, the minimum number of experimental realisations is smaller. If, for example, the block is chosen less carefully, as for the case of a wider cross block that blocks up to the fourth diffraction peak [Second column of

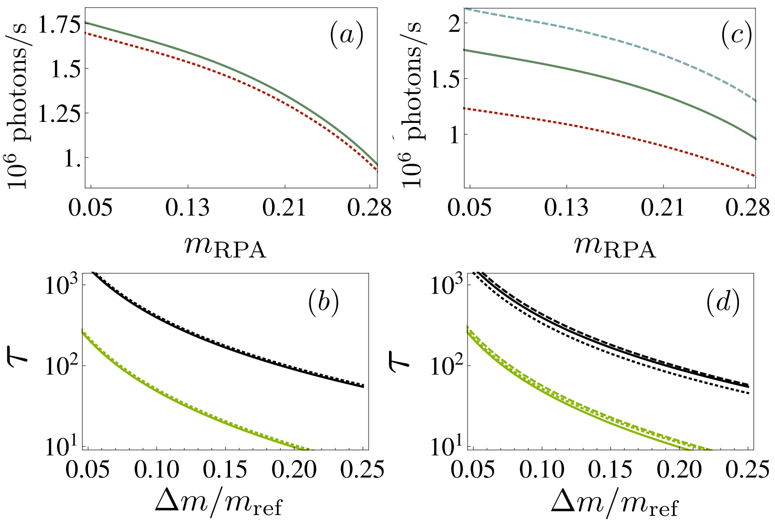

Figure 6.5: $T = 0$ collected photon rates vs. the RPA corrected AFM order parameter $m_{\rm RPA}$ with a lens of NA$= 0.8$ in the forward direction (top row) and the corresponding estimated number of experimental realisations to achieve a relative accuracy $\Delta m/m_{\rm ref}$ (bottom row). The calculations are computed with RPA susceptibilities at $T = 0$ and with an RPA corrected order parameter $m_{\rm RPA}$ for the elastic component. Both (a) and (b), show a fixed value of $\kappa = 1.05$ and compare two different lattice depths $s = 7.8$ (dotted) and $s = 25$ (solid). In (b), the top two curves (in black) are for $m_{\rm ref} \simeq 0.12$ and the bottom two curves (in green) are for $m_{\rm ref} \simeq 0.19$. The top two curves are essentially on top of one another, similarly for the bottom two curves. Both (c) and (d), show a fixed lattice depth $s = 25$ and compare three different values of the parameter $\kappa = 0.66$ (dotted line), $\kappa = 1.05$ (solid) and $\kappa = 1.5$ (dashed). Note that varying κ changes the width of the elastic diffraction peak. Thus, to block out the main elastic diffraction peaks, a different block width is required for each κ value, see Table 6.1. In (d), the top three curves (in black) are for $m_{\rm ref} \simeq 0.12$ and the bottom three curves (in green) are for $m_{\rm ref} \simeq 0.19$. The top three curves are close together, and even more so for the bottom three curves.

Table 6.4: Specific values of the estimated number of experimental realisations, $\tau(m_{\rm ref})$, for the different κ cases presented in Fig. 6.5(d). These values are for a relative accuracy of 10%. The parameters of the block are given in Table 6.1.

κ	$\tau(0.12)$	$\tau(0.19)$
0.66	340	50
1.05	390	50
1.50	440	60

Table. 6.5], the resulting τ estimates increase dramatically. It can be seen in the third and fourth columns of Table 6.5. For this block, the dependence on κ is the opposite of the optimal block case [Tables. 6.1 and 6.4]. In this case, τ decreases with increasing κ [Compare Tables. 6.4 and 6.5]. Using a wide block is not beneficial because it blocks inelastically scattered photons. As a result of this, the collected photon rates, the equivalent to the curves in Fig. 6.5(c), flatten with decreasing κ. This can be seen by comparing Figs. 6.5(a) and 6.6(c).

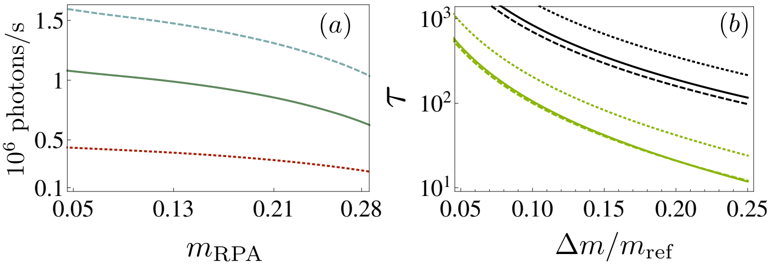

Figure 6.6: $T = 0$ collected photon rates vs. the RPA corrected AFM order parameter m_{RPA} with a lens of NA$= 0.8$ in the forward direction (a) and the corresponding estimated number of experimental realisations to achieve a relative accuracy $\Delta m/m_{\mathrm{ref}}$ (b). This figure show the results for a wide cross block. The width for each κ value is listed in the second column of Table 6.5. The calculations are computed with RPA susceptibilities at $T = 0$ and with an RPA corrected order parameter m_{RPA} for the elastic component. Both (a) and (b), show a fixed lattice depth $s = 25$ and compare three different values of the parameter $\kappa = 0.66$ (dotted line), $\kappa = 1.05$ (solid) and $\kappa = 1.5$ (dashed). In (b), the top three curves (in black) are for $m_{\mathrm{ref}} \simeq 0.12$ and the bottom three curves (in green) are for $m_{\mathrm{ref}} \simeq 0.19$. The bottom two green curves, corresponding to $\kappa = 1.05$ and $\kappa = 1.5$, are very close together.

Table 6.5: Parameters of the wide cross block and estimated number of experimental realisations $\tau(m_{\mathrm{ref}})$. These values are for a relative accuracy of 10%. All other parameter values are as for Table 6.4.

κ	Cross width (rad)	$\tau(0.12)$	$\tau(0.19)$
0.66	0.31	1560	210
1.05	0.19	840	110
1.50	0.13	700	100

As was mentioned before, even though the MFT does not correctly describe collective modes in the system, in the forward direction the behaviour is similar to the RPA due to the geometrical suppression that the spin-exchanging transition has. Thus, the finite temperature mean field theory calculation can be used to explore the use of inelastic light scattering as a temperature probe for interacting Fermi gases. Using a narrow cross-shaped block [with width 0.05 rad], the light can be collected near the forward direction [Fig. 5.3(b)]. Fig. 6.7(a) shows the collected photon rate which, as expected, diminishes with increasing magnetisation. This can be understood by looking at Fig. 5.12. in which it is shown that for decreasing temperature (hence increasing magnetisation) the scattered light in the forward direction decreases due to Pauli-Blocking. Lower T corresponds to stronger magnetisation values, and a smaller number of collected photons, as displayed in Fig. 6.7(a). Fig. 6.7(b) shows that the changes in m due to temperature can be accurately detected. For example, for $m_{\mathrm{ref}} = 0.18$ can be measured with the accuracy of 10% with 100 realisations. This small number of experimental realisations can be understood

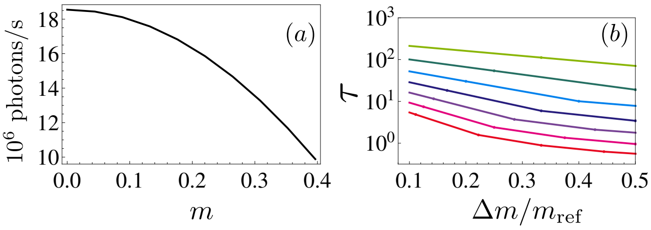

Figure 6.7: Finite temperature plots of (a) collected photon rates vs. the MFT AFM order parameter m with a lens of NA= 0.8 in the forward direction, and (b) the corresponding estimated number of experimental realisations to achieve a relative accuracy $\Delta m/m_{\text{ref}}$. Results are obtained with MFT at finite T with fixed $U = 5.3J$, and with $s = 25$ and $\kappa = 1.05$. The cross block width is 0.05 rad. At fixed U, increasing T leads to decreasing m, and (b) shows from top to bottom (corresponding to lowering T), $m_{\text{ref}} = 0.13, 0.18, 0.22, 0.26, 0.31, 0.35, 0.4$. In (b) the data points are joined with straight lines.

by looking at Fig. 6.7(a) and noticing the relatively large change in the collected photon rate with decreasing temperature. The block parameters affect the number of measured photons, and have a huge impact for lenses with a small NA. For lenses with a larger NA, the size and details of the block change the number of experimental realisations in less than an order of magnitude.

Figure 6.8 considers the lens arrangements of Fig. 5.3(c), in which case the light is collected from the perpendicular direction. The atomic correlations calculated in RPA for the 40×40 lattice. If both the transitions related to the transverse spin correlations as well as the density and the longitudinal spin correlations are measured, the detection accuracy is significantly lower than in the case of forward direction measurements [Figs. 6.8(a), and (b)]. In general, for $\kappa = 1.5$, in the perpendicular direction the scattering rates are higher because of the strong enhancement of spin-exchanging processes [Compare Fig. 5.10(a) to Fig. 5.10(c)]. This is why the τ values are lower for the $\kappa = 1.5$ [dashed line in Figs. 6.8(b),(d)]. Some specific values of τ for this configuration are shown in the first two-columns of Table 6.6. These numbers are significantly higher than the equivalent estimates for τ in the forward direction [Table 6.4]. However, the accuracy improves notably when only the transverse spin correlations are detected [Figs. 6.8(c) and (d)]. Whenever the internal levels are not degenerate, the different scattering processes can be separated owing to the frequency difference of the photons. For instance, for $NA = 0.4$ and $\kappa = 1.5$, the accuracy of 10% for $m_{\text{ref}} = 0.19$ can now be achieved after 50 realisations. By increasing the size of the lens to NA= 0.5, the results can be further improved

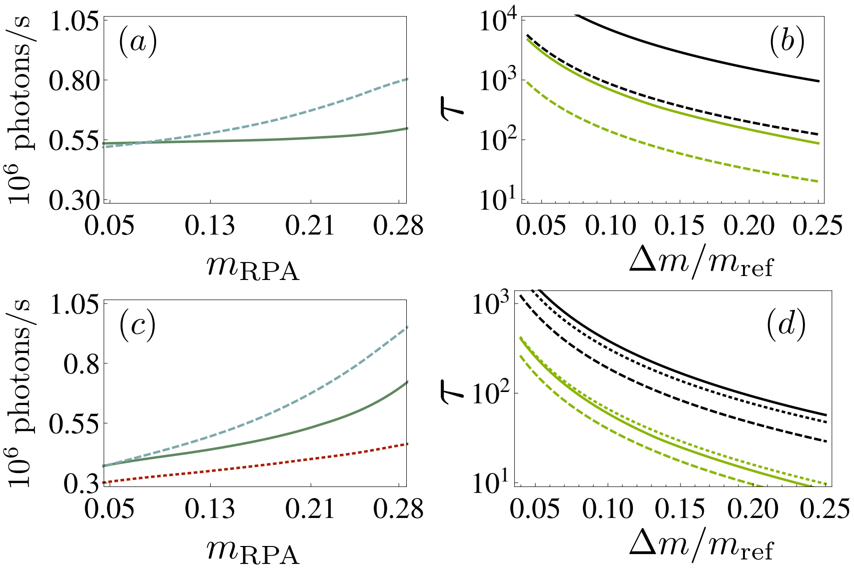

Figure 6.8: Collected photon rates vs. the AFM order parameter m with a lens pointing in the perpendicular direction (left column) and the corresponding estimated number of experimental realisations τ to achieve a relative accuracy $\Delta m/m_{\text{ref}}$ (right column). The calculations are computed with RPA susceptibilities at $T = 0$ and with an RPA corrected order parameter m_{RPA} for the elastic component. (a) and (b) compare the case when all the density and spin components are collected by a lens with NA$= 0.4$, to the case when [(c) and (d)] only the transverse spin component of the scattered light is collected by a lens with NA$= 0.5$. In both (a) and (b), solid lines are for $\kappa = 1.05$ and dashed lines for $\kappa = 1.5$. In (b), the top two curves (in black) are for $m_{\text{ref}} \simeq 0.12$ and bottom two curves (in green) are for $m_{\text{ref}} \simeq 0.19$. Note that the bottom black dashed curve almost overlaps the top green solid curve. In both (c) and (d), dotted lines are for $\kappa = 0.66$, solid lines for $\kappa = 1.05$ and dashed lines for $\kappa = 1.5$. In (d), the top three curves (in black) are for $m_{\text{ref}} \simeq 0.12$ and bottom three curves (in green) are for $m_{\text{ref}} \simeq 0.19$.

Table 6.6: Specific values of the estimated number of experimental realisations, $\tau(m_{\text{ref}})$. The data labelled as Total [left column] corresponds to the case where all components of the intraband scattering are collected [Fig. 6.8(a),(b)]. The data labelled as Transverse corresponds to the case where only the transverse spin component of the scattered light is detected [Fig. 6.8(c),(d)]. These values are for a relative accuracy of 10%.

	Total (NA$= 0.4$)		Transverse (NA$= 0.5$)	
κ	$\tau(0.12)$	$\tau(0.19)$	$\tau(0.12)$	$\tau(0.19)$
0.66			320	70
1.05	6870	680	390	60
1.50	850	140	190	40

to only 40 realisations. This numbers are now comparable to those in the forward direction [Table 6.4]. In Table 6.6 some specific values are listed which illustrate the difference in the results between Figs. 6.8(b) and 6.8(d) can be appreciated.

The previous results are for a lattice with a fixed linear size of $N_s = 40$. It has already been noted that the different components of the scattered light scale with lattice

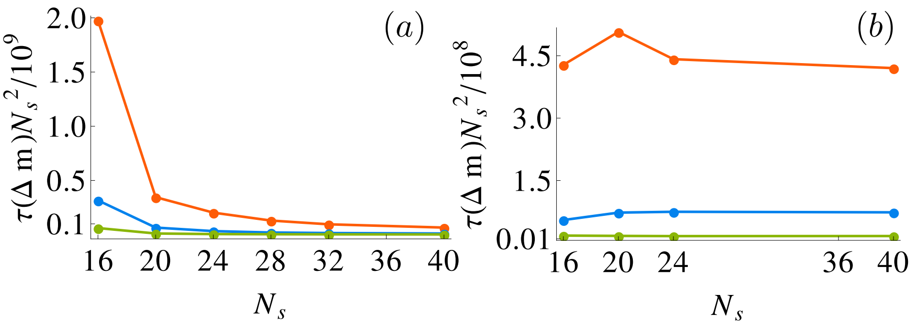

Figure 6.9: Scaling of the number of experimental realisations with the size of the lattice along one direction N_s for different values of $m_{ref} = 0.2, 0.3, 0.4$ (top to bottom) for $\kappa = 1.050$ [Eq. (4.16)]. (a) for a lens in the forward direction [Fig. 5.3(b)], with a numerical aperture of NA $= 0.8$ and a cross-block such that it blocks up to the fourth diffraction peak and (b) for a lens in the perpendicular direction [Fig. 5.3(c)], with a numerical aperture of NA $= 0.4$.

size differently. In particular, the elastic component is proportional to N_s^4 and the intraband inelastic component to N_s^2. An estimate of the way the number of measurements τ scales with lattice size can be made by considering Eq. (6.12). Assuming that the elastic component is completely blocked, it is easy to see that $\tau \propto N_s^{-2}$. Figs. 6.9(a) and (b) illustrate that, for $N_s \geq 16$, τ scales approximately linearly with the lattice size for both, the forward and the perpendicular direction. For smaller systems, the choice of the block size and shape results in larger variations owing to the dependence of the width of the diffraction peak on the lattice size.

To conclude this section, the main results will be summarised. In this section, it has been shown that the detection of AFM ordering by means of the magnetic Bragg peaks is feasible. In particular, if single species detection is possible, this is a very accurate probe. If single species detection is not possible, or the magnetic peaks are not reachable (because of the value of the parameter κ), alternative ways to probe the system have been analysed, and it has been showed that the sensitivity of the inelastic component of the scattered light to changes in the order parameter m are detectable. The minimum number of experimental realisations for such detection has been estimated.

6.3 Distinguishability of transitions by light polarisation

In general, the scattered light corresponding to different transitions are separated in frequency space. The different components could, in principle, be identified by filtering the relevant frequencies. If spectral measurements are not possible, the transitions could still be partially distinguished by the polarisation of the scattered light. In the forward direction, the polarisation of the photons scattered from the spin-flipping transition and the spin-conserving transitions are orthogonal and fully distinguishable. Away from the forward direction, this simple separation is no longer possible.

To study these, it has been assumed that an ideal polariser can be constructed such that it only allows the light component that is parallel to a given transition polarisation vector. The polarisation of the scattered field is given by Eq. (4.14). The effect of having a polariser in front of the detector can be studied by projecting the scattered electric field [Eq. (4.9)] onto the polarisation of the polariser $\hat{\epsilon}_{\mathrm{p}}$. This, modifies the polarisation vector of the scattered field $\boldsymbol{\Lambda}_{g'g}$ [Eq. (4.12)]. The projected electric field has a polarisation given by Eq. (4.15). Using the projected polarisation tensor instead of Eq. (4.20), the corresponding projected dipole matrix elements are

$$\mathsf{M}^{g_3g_4}_{g_2g_1}|_{\hat{\epsilon}_{g'g}} = (\Lambda_{g_3g_4}|_{\hat{\epsilon}_{g'g}})^*\Lambda_{g_2g_1}|_{\hat{\epsilon}_{g'g}}. \tag{6.13}$$

Projecting the scattered fields parallel to the polarisation of the light coming from the equal spin terms results in,

$$\begin{aligned}
\mathsf{M}^{\downarrow\downarrow}_{\downarrow\downarrow}|_{\hat{\epsilon}_{gg}} =& \frac{1}{4}\left(3+\cos 2\theta\right),\\
\mathsf{M}^{\uparrow\uparrow}_{\downarrow\downarrow}|_{\hat{\epsilon}_{gg}} = \mathsf{M}^{\downarrow\downarrow}_{\uparrow\uparrow}|_{\hat{\epsilon}_{gg}} =& \frac{9}{44}\left(3+\cos 2\theta\right),\\
\mathsf{M}^{\uparrow\uparrow}_{\uparrow\uparrow}|_{\hat{\epsilon}_{gg}} =& \frac{81}{484}\left(3+\cos 2\theta\right),\\
\mathsf{M}^{\downarrow\uparrow}_{\downarrow\uparrow}|_{\hat{\epsilon}_{gg}} =& \frac{9\sin^2 2\theta}{121(3+\cos 2\theta)}.
\end{aligned} \tag{6.14}$$

The angular dependence with this projected transitions is shown in Figs. 6.10(d) and (e). Likewise, projecting the scattered fields on the direction of the light scattered from the spin flipping term results in

$$\begin{aligned}
\mathsf{M}^{\downarrow\downarrow}_{\downarrow\downarrow}|_{\hat{\epsilon}_{\uparrow\downarrow}} =& \frac{\cos^2\theta\sin^2\theta}{2},\\
\mathsf{M}^{\uparrow\uparrow}_{\downarrow\downarrow}|_{\hat{\epsilon}_{\uparrow\downarrow}} = \mathsf{M}^{\downarrow\downarrow}_{\uparrow\uparrow}|_{\hat{\epsilon}_{\uparrow\downarrow}} =& \frac{9\cos^2\theta\sin^2\theta}{22},\\
\mathsf{M}^{\uparrow\uparrow}_{\uparrow\uparrow}|_{\hat{\epsilon}_{\uparrow\downarrow}} =& \frac{81}{242}\cos^2\theta\sin^2\theta,\\
\mathsf{M}^{\downarrow\uparrow}_{\downarrow\uparrow}|_{\hat{\epsilon}_{\uparrow\downarrow}} =& \frac{18}{121}\sin^2\theta.
\end{aligned} \tag{6.15}$$

which is shown in Figs. 6.10(e) and (f). Although the separation is not full, by using a polariser the light coming from the other transition can be highly suppressed.

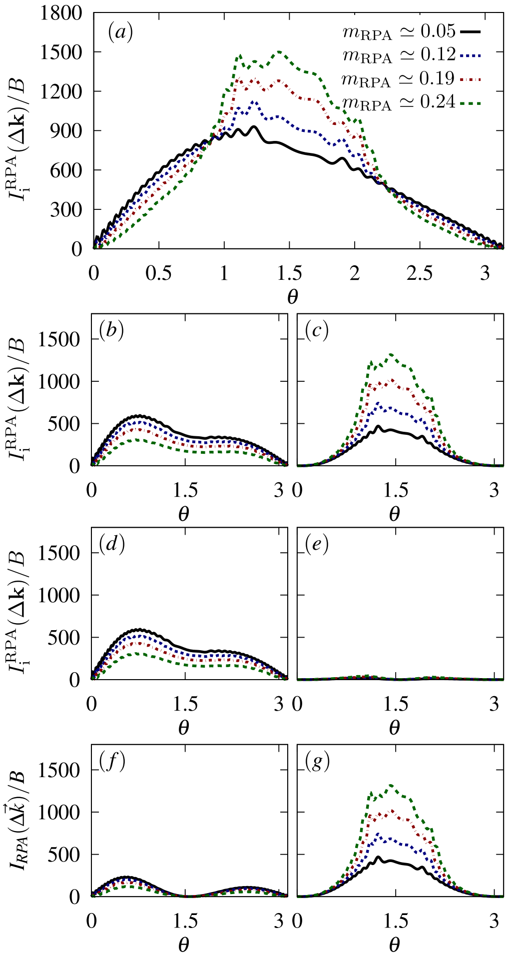

Figure 6.10: Angular distribution of the inelastically scattered light intensity along the direction $\phi = \pi/4$ with and without a polariser. The figure shows different values of the interaction strength U at $T = 0$. The calculations are based on RPA. $\kappa = 1.500$ and the other parameters are as in Fig. 5.9. (a) shows the total scattered light intensity. The left column shows the density and longitudinal spin components and the right column the transverse spin component; (a), (b) and (c) are for the case where no polariser is used. In (d) and (e) the scattered light has been projected on the density-density and longitudinal spin polarisation vector. (f) and (g) are projected onto the polarisation vector the the transverse spin component.

Chapter 7

Scattered light spectrum of ^{40}K in an optical lattice

In the previous chapters, it was shown how the scattered light intensity can be used to probe atoms in an optical lattice. In Chapter 5, it was shown how the elastic component of the scattered light can be used to detect AFM ordering in the system [Sec. 5.2]. It was also shown how the inelastic intraband component of the scattered light maps the atomic correlations into the properties of the emitted light, which results in the inelastic scattering being very sensitive to changes in the order parameter. In Chapter 6, the sensitivity of the scattered intensity to changes in ordering in the atomic correlations was shown to be a feasible tool for experimentally probing the system. All those results are for the experimental situation when energy resolution is not achievable in the scattered light.

In this Chapter, the scattered spectrum is analysed and it is shown that, if energy resolution is available, the atomic correlations can be probed in a very direct manner. In Section 7.1, the scattering formulas are presented for the particular case of a ^{40}K atomic gas. In Section 7.2, a comparison between the physical quantities of interest is presented. In particular, the angle-resolved spectrum [Eq. (7.5)], RPA susceptibilities [Eqs. (3.45), (3.46) and (3.47)], and the angle-integrated spectra [Eq. (7.6)]. The latter corresponds to the measured spectrum over a range of scattering angles using a lens. Section 7.3 deals with the single particle excitations in both the MFT and RPA approximations. In Section 7.4, the collective peak is analysed in the RPA spectrum.

7.1 Spectrum formulae

The necessary formalism for the scattered spectrum was presented in Section 4.3. The elastic component of the scattered spectrum has a simple spectral structure, which consists of only a zero frequency part, by definition [Eq. (4.39) and Section 4.3.1]. The losses to higher bands occur at high frequency (on the order of the band gap) and can be filtered out. As this component contains no information about the correlations in the system, it can be ignored. It is in the inelastic component of the scattered spectrum [Eq. (4.40) or (4.42)] that the properties of the excitations of the system can be directly observed.

The inelastic component of the scattered spectrum can be written in an analogous manner to that of the intensity [Eq. (5.14)]. In order to do this, a 2×2 matricial version of the dynamic response function [Eq. (3.26)] can be defined in an analogous manner to Eq. (5.9):

$$\boldsymbol{\mathcal{S}}^{g_3g_4}_{g_2g_1}(\underset{\sim}{\mathbf{q}},\omega)=\begin{pmatrix}\mathcal{S}^{g_3g_4}_{g_2g_1}(\underset{\sim}{\mathbf{q}},\underset{\sim}{\mathbf{q}};\omega) & \mathcal{S}^{g_3g_4}_{g_2g_1}(\underset{\sim}{\mathbf{q}},\underset{\sim}{\mathbf{q}}+\mathbf{Q};\omega)\\ \mathcal{S}^{g_3g_4}_{g_2g_1}(\underset{\sim}{\mathbf{q}}+\mathbf{Q},\underset{\sim}{\mathbf{q}};\omega) & \mathcal{S}^{g_3g_4}_{g_2g_1}(\underset{\sim}{\mathbf{q}}+\mathbf{Q},\underset{\sim}{\mathbf{q}}+\mathbf{Q};\omega)\end{pmatrix}. \tag{7.1}$$

A frequency-dependent equivalent to Eqs. (5.10), (5.11), and (5.12), allows the density, longitudinal spin and transverse spin dynamic response functions to be written in terms of the quadruply indexed ones of Eq. (7.1). This results in

$$\boldsymbol{\mathcal{S}}^{\rho\rho}(\mathbf{q},\omega)=\boldsymbol{\mathcal{S}}^{\uparrow\uparrow}_{\uparrow\uparrow}(\mathbf{q},\omega)+\boldsymbol{\mathcal{S}}^{\downarrow\downarrow}_{\downarrow\downarrow}(\mathbf{q},\omega)+\boldsymbol{\mathcal{S}}^{\uparrow\uparrow}_{\downarrow\downarrow}(\mathbf{q},\omega)+\boldsymbol{\mathcal{S}}^{\downarrow\downarrow}_{\uparrow\uparrow}(\mathbf{q},\omega) \tag{7.2}$$

$$\boldsymbol{\mathcal{S}}^{zz}(\mathbf{q},\omega)=\boldsymbol{\mathcal{S}}^{\uparrow\uparrow}_{\uparrow\uparrow}(\mathbf{q},\omega)+\boldsymbol{\mathcal{S}}^{\downarrow\downarrow}_{\downarrow\downarrow}(\mathbf{q},\omega)-\boldsymbol{\mathcal{S}}^{\uparrow\uparrow}_{\downarrow\downarrow}(\mathbf{q},\omega)-\boldsymbol{\mathcal{S}}^{\downarrow\downarrow}_{\uparrow\uparrow}(\mathbf{q},\omega), \tag{7.3}$$

$$\boldsymbol{\mathcal{S}}^{+-}(\mathbf{q},\omega)=2\boldsymbol{\mathcal{S}}^{\downarrow\uparrow}_{\downarrow\uparrow}(\mathbf{q},\omega). \tag{7.4}$$

These response functions are related to the susceptibilities of Sections 3.2.1 or 3.3 via Eq. (3.28) for the MFT or RPA cases, respectively. This allows for writing the inelastic component of the scattered light spectrum in a 2D ^{40}K gas in the half-filled Hubbard model as a special case of Eq. (4.42),

$$\begin{aligned}\mathbb{S}_{\mathbf{i}}(\Delta\mathbf{k},\omega)=\alpha_{\Delta\mathbf{k}}B\Bigg\{&\left(\mathsf{M}^{\downarrow\downarrow}_{\downarrow\downarrow}+\mathsf{M}^{\uparrow\uparrow}_{\uparrow\uparrow}\right)\sum_{\mathbf{q}\neq0}^{\text{RBZ}}\boldsymbol{u}^{\dagger}_{\bar{\Delta}\mathbf{k}-\mathbf{q}}\frac{1}{4}\left[\boldsymbol{\mathcal{S}}^{\rho\rho}(\mathbf{q},\omega)+\boldsymbol{\mathcal{S}}^{zz}(\mathbf{q},\omega)\right]\boldsymbol{u}_{\bar{\Delta}\mathbf{k}-\mathbf{q}}\\ &+\left(\mathsf{M}^{\uparrow\uparrow}_{\downarrow\downarrow}+\mathsf{M}^{\downarrow\downarrow}_{\uparrow\uparrow}\right)\sum_{\mathbf{q}\neq0}^{\text{RBZ}}\boldsymbol{u}^{\dagger}_{\bar{\Delta}\mathbf{k}-\mathbf{q}}\frac{1}{4}\left[\boldsymbol{\mathcal{S}}^{\rho\rho}(\mathbf{q},\omega)-\boldsymbol{\mathcal{S}}^{zz}(\mathbf{q},\omega)\right]\boldsymbol{u}_{\bar{\Delta}\mathbf{k}-\mathbf{q}}\\ &+\mathsf{M}^{\downarrow\uparrow}_{\downarrow\uparrow}\sum_{\mathbf{q}\neq0}^{\text{RBZ}}\boldsymbol{u}^{\dagger}_{\bar{\Delta}\mathbf{k}-\mathbf{q}}\frac{1}{2}\boldsymbol{\mathcal{S}}^{+-}(\mathbf{q},\omega)\,\boldsymbol{u}^{\dagger}_{\bar{\Delta}\mathbf{k}-\mathbf{q}}\Bigg\}.\end{aligned} \tag{7.5}$$

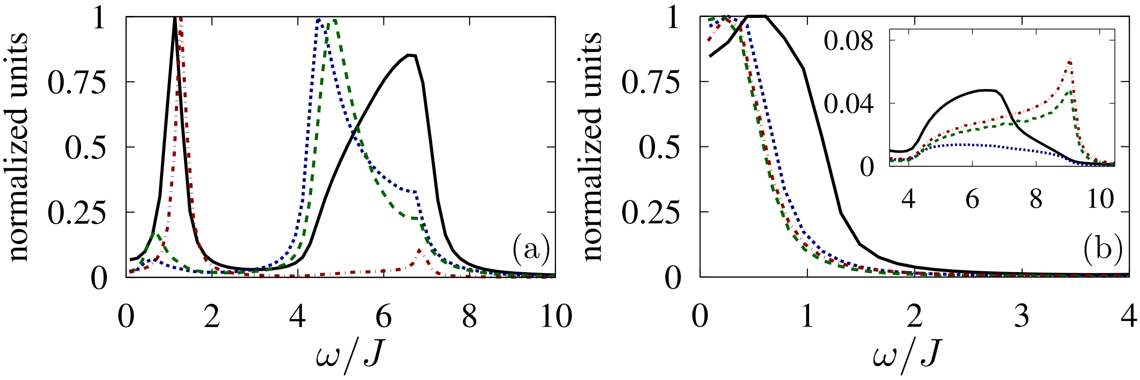

Figure 7.1: Comparison between the RPA susceptibilities, angle-resolved spectrum, and the spectrum collected by a lens over a range of scattering angles. The ratio between the wavenumber of the probe light to the effective wavenumber of the optical lattice light is $\kappa = 1.5$ [Eq. (4.16)] and $U = 5J$. Each line shown has been normalised to its maximum value for comparison. We show $\mathfrak{s}^{\mathrm{L}}_{0.5}(\omega)$ [solid (black)], $\mathfrak{s}^{\mathrm{L}}_{0.1}(\omega)$ [dotted (blue)], $\mathbb{S}(\Delta\mathbf{k}, \omega)$ [dashed (green)] and $\chi(\Delta\mathbf{k}, \Delta\mathbf{k}; \omega)$ [dotdashed (red)]. (a) shows the configuration with a lens in the forward direction [Fig. 5.3(b)]. The angle-resolved quantities, the spectrum $\mathbb{S}(\Delta\mathbf{k}, \omega)$ and total susceptibility $\chi(\Delta\mathbf{k}, \Delta\mathbf{k}; \omega)$ are computed at a wavevector close to the axis of the lens [$\theta \sim 0$, $\phi \sim 0$; $\Delta\mathbf{k}_F(0, 0.01)$]. (b) shows the case for a lens in the perpendicular direction [Fig. 5.3(c)]. $\mathbb{S}(\Delta\mathbf{k}, \omega)$ and $\chi(\Delta\mathbf{k}, \Delta\mathbf{k}; \omega)$ are computed at a wavevector $\Delta\mathbf{k}$ close to the axis of the lens at [$\theta \sim \pi/2, \phi \sim \pi/4$; $\Delta\mathbf{k}_P(\pi/2, \pi/4 \times 1.01)$]. (b) shows the collective mode at low energies and the inset shows the single-particle excitations at energies above the gap.

In Eq. (7.5), the vector diffraction term $\boldsymbol{u}_{\bar{\Delta\mathbf{k}}}$ is defined in Eq. (5.13). $\alpha_{\Delta\mathbf{k}}$ is the Debye-Waller factor defined in Eq. (4.22), and the constant B is defined in Eq. (4.19).

7.2 Comparison between angle-resolved and angle-integrated spectrum

The spectrum contains a great wealth of information about the system, but, staying within the basic approximation, the mean field theory, then, as is typical to this approximation to have single particle excitations, that is the only excitation present. Here, it is shown that when the RPA is used, the collective modes dominate the spectrum, hence rendering the MFT results incomplete.

Ultimately, the interest lies in studying susceptibilities, as that is the way predictions from models can be tested against physical systems more directly. Using a lens with a large numerical aperture (NA), which captures photons from a large range of scattering angles, increases the number of collected photons. Collecting the scattered photons with a lens of a high numerical aperture improves the signal, but it may also *distort* it, modifying the shape of the spectrum. This is because in the spectrum, each $\Delta\mathbf{k}$ [Eq. 4.11] represents a different argument for the structure factor. Thus, using a large NA lens is equivalent to integrating the dynamical structure factor [Eq. (4.41)]. To asses how much information about the spectral structure can be obtained when light is collected by a lens with a given NA, the spectrum is integrated over the corresponding range of scattering angles. This quantity is denoted by

$$\mathfrak{s}^{\mathrm{L}}_{\mathrm{NA}}(\omega) = \int\limits_{\mathrm{L,NA}} d\phi \sin\theta d\theta \, \mathbb{S}(\Delta\mathbf{k}(\theta,\phi),\omega) \, , \tag{7.6}$$

where $\mathrm{L} = \mathrm{F}, \mathrm{P}$ indicates the experimental configuration: F for the lens with a given NA pointing in the forward direction [Fig. 5.3(b)], and P for the perpendicular direction [Fig. 5.3(c)].

To study how different the angle-resolved and angle-integrated spectrum collected by the lens are from the original susceptibility, the angle-integrated spectrum has been computed for two lenses: one with a large NA [$\mathrm{NA} = 0.5$], and another with a small NA [$\mathrm{NA} = 0.1$]. Fig 7.1 compares these quantities with the scattered spectrum $\mathbb{S}(\Delta\mathbf{k},\omega)$ at a point $\Delta\mathbf{k}$ close to the direction of the lens, and the sum of the susceptibilities

$$\chi(\Delta\mathbf{k},\Delta\mathbf{k},\omega) = \chi^{\rho\rho}_{\mathrm{RPA}}(\Delta\mathbf{k},\Delta\mathbf{k},\omega) + \chi^{zz}_{\mathrm{RPA}}(\Delta\mathbf{k},\Delta\mathbf{k},\omega) + \chi^{+-}_{\mathrm{RPA}}(\Delta\mathbf{k},\Delta\mathbf{k},\omega). \tag{7.7}$$

Note that the total susceptibility does not include the polarisation of the light as it does not contains any dipole matrix elements $\mathsf{M}^{g_3g_4}_{g_2g_1}$ [Eq. (4.20)]. In Fig. 7.1(a) the lens is pointing in the forward direction [Fig. 5.3(b)] and in Fig. 7.1(b) it points in the perpendicular direction [Fig. 5.3(c)]. The first noticeable aspect of Fig. 7.1 is that if the scattered light is collected with the small NA lens $\mathfrak{s}^{\mathrm{L}}_{0.1}(\omega)$ [dotted(blue) line], the signal is very close to the scattered spectrum $\mathbb{S}(\Delta\mathbf{k},\omega)$ [dashed(green) line], in both forward and perpendicular directions. Both lenses are able to distinguish between the low-energy collective mode and the high-energy single particle excitations, but the collective mode is broadened by the large lens. These two different contributions are analysed in detail in the next sections. However, compared to the large NA lens, using a small NA lens results in a signal which is smaller by a factor of 200 in the forward direction, and by a factor of 10 in the perpendicular direction. One of the key features of the the scattered light spectrum is clearly visible in Figure 7.1; the position of the lens determines which susceptibilities can be observed. This occurs as a result of the polarisation of the scattered light spectrum

$\mathbb{S}(\Delta\mathbf{k},\omega)$, taken into account by the specific factors $\mathsf{M}^{g_3g_4}_{g_2g_1}$ [Eq. (5.5)] present in Eq. (7.5). From Eq. (5.5), it can be seen that the dipole matrix elements have a geometrical dependence which allows for capturing the different contributions, density and longitudinal spin, and transverse spin, in the different lenses (at different orientations). Thus, the fact that the susceptibilities are probed with a different transition [Fig. 5.2] results in a skewing of the scattered spectrum in certain directions. In particular, in the forward direction, the contributions from the density and longitudinal spin susceptibilities are not suppressed. On the other hand, the collective mode is hardly visible in Fig. 7.1(a). This is because the corresponding polarisation tensor* is $\sim \sin^2\theta$. In the perpendicular direction, the polarisation factor [$\sim 3 + \cos 2\theta$] suppresses the contributions from the density, and the longitudinal spin configuration. In this geometry, the majority of the light is from the spin-exchanging transition. Thus, it is possible to perform a separate measurement of the susceptibilities in the longitudinal and the transverse channel. Hence, one key finding in this chapter is that the position of the lens can be used to select the different susceptibilities. This allows for a separation between the collective modes and the single particle excitations.

7.3 Single particle excitations

Within the MFT, the spectrum is computed from the susceptibilities of Eqs. (3.33), (3.34), for density and longitudinal mode and Eqs. (3.36) and (3.37) for the transverse ones. Fig. 7.2 shows the numerical results at zero temperature for different values of the on-site interaction U, for a lens in the forward direction in (a), and in the perpendicular direction in (b). As mentioned in the previous section, the forward direction captures light scattered mostly from spin-preserving transitions while in the perpendicular direction, the captured light mostly originates in the spin-exchanging transition. This is because of the angular dependence of the respective dipole transition matrix elements coded in the $\mathsf{M}^{g_3g_4}_{g_2g_1}$ tensor of Eq. (5.5). The only spectral features in Fig. (7.2) are the gapped single particle excitations. A simple calculation shows that for $\Delta \gg J$ the gap can be approximated by $2\Delta = 2mU$. Indeed, from the denominators, the frequency term in the susceptibilities [Eqs. (3.33), (3.34), (3.36) and (3.37)], the range over which

---

*The precise value of $\mathsf{M}^{\downarrow\uparrow}_{\downarrow\uparrow}$ is given Eq. (5.5).

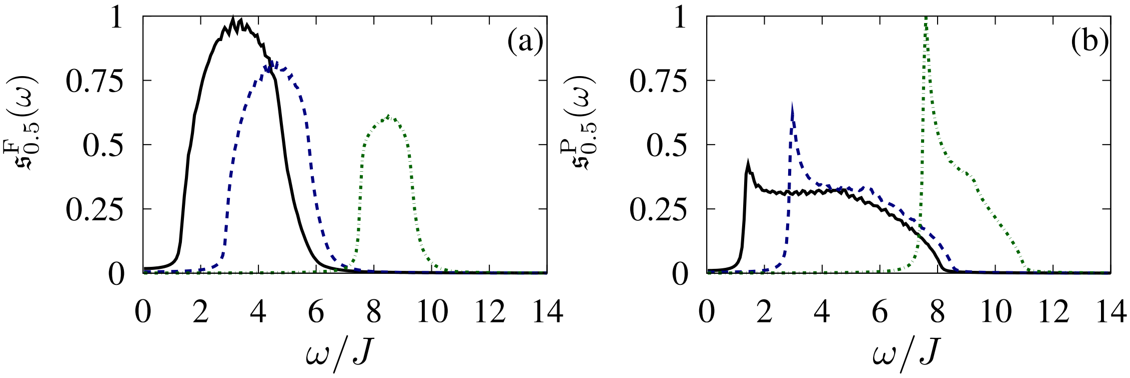

Figure 7.2: MFT spectrum collected by a lens for different values of the on-site interaction strength U at $T = 0$. Here the number of sites is 40×40. The ratio between the wavenumber of the probe light to the effective wavenumber of the optical lattice light $\kappa = 1.500$ [Eq. (4.16)]. The lattice height is $s = 25$. Light is collected with a lens of NA$= 0.5$ pointing in (a) the forward direction; (b) the perpendicular direction. It consists of the different single particle excitations. The energy gap is characteristic of the MFT ground state. The gap has a width of about 2Δ for large values of U. From left to right, black (solid) is $U = 2.6J$, $m = 0.25$, blue (dashed) is $U = 4.01J$, $m = 0.35$, and green (dot-dashed) is $U = 8.33J$, $m = 0.45$. All the curves have been normalised to the maximum of the highest peak in each figure.

single-particle excitations are to be expected can be bounded. Specifically, the spectrum is non-zero only for $2\Delta \leq \omega \leq 2\sqrt{\Delta^2 + 16J^2}$. In Fig. 7.2, the numerical results are for $T = 0$, and for different values of the on-site interaction U. The larger the on-site interaction is, the closest m is to its saturation value of $1/2$ [Eq. (3.17) and Fig. 3.3]. As described in Section 3.2.1 [Eq. (3.40)], the numerical values are computed with a finite value to the infinitesimal imaginary part. In particular, with 200 points in the interval $0 \leq \omega \leq 14J$.

Figure 7.3 shows the scattered light spectrum corresponding to a calculation within the RPA approximation. This is computed from the susceptibilities in Eqs. (3.45), (3.46) and (3.47). To compute these susceptibilities numerically, the MFT susceptibilities of Eqs. (3.33), (3.34), (3.36) and (3.37) are computed using complex arithmetic from expressions equivalent to that of Eq. (3.40)[†]. These are then fed into Eqs. (3.45), (3.46) and (3.47). The observable spectrum is then obtained via Eq. (3.28), taking the imaginary part and multiplying by the necessary numerical factors. It is important to note that due to the way the RPA susceptibilities are calculated, when computing their numerical values, the gap parameter Δ [Eq. (3.8)] is computed from the MFT order parameter m as computed from Eq. (3.17). Using the RPA-corrected order parameter m_{RPA} would be incorrect as m_{RPA} is computed from the RPA susceptibilities and the calculation used here

---

[†] Without taking the imaginary part.

Table 7.1: Height of the single-particle peaks in the scattered spectrum. Comparison between the MFT [Fig. 7.2] and the RPA [Fig. 7.3] calculations. The results are given in the units of Fig. 7.3(a), and Fig. 7.3(b) for the forward and perpendicular directions, respectively.

	Forward direction		Perpendicular direction	
U/J	MFT	RPA	MFT	RPA
2.6	0.70	0.61	0.13	0.07
4.0	0.59	0.48	0.18	0.05
8.3	0.43	0.31	0.29	0.03

is not self-consistent in any way. In this thesis, m_{RPA} is only to compute the elastic component of the scattered light [Sec. 5.2]. As was already discussed in Section 3.3, the RPA approximation renormalises the single-particle excitations. This is illustrated in Figs. 3.6 and 3.7. This is also observable in the scattered spectrum. Comparing Fig. 7.2 and 7.3, it is apparent that the shape of the single-particle excitations changes. The height of the peak in the collected scattered light, which is the factor determining the normalisation of the figures, changes as follows: in the perpendicular direction, the maximum value reached by the RPA spectrum is a factor of ~ 1.4 larger than the MFT. In the perpendicular direction this factor is ~ 3.4. The change from MFT to RPA is larger in the perpendicular direction because of the presence of the collective mode. For comparison, the height of the single-particle peaks in Figs 7.2 and 7.3 are listed in Table 7.1 in the units of Fig. 7.3. The renormalisation in the single-particle peaks in the forward direction is mainly due to the differences between $\boldsymbol{\chi}^{\rho\rho}_{(0)}(\mathbf{q},\omega)$ and $\boldsymbol{\chi}^{\rho\rho}_{\text{RPA}}(\mathbf{q},\omega)$ [Fig. 3.7(b)]. This is because of the nearly total cancellation of the term $\boldsymbol{\mathcal{S}}^{zz}(\mathbf{q},\omega)$ in Eq. (7.5) due to the minus sign in front of the dipole matrix elements $\mathsf{M}^{\downarrow\downarrow}_{\uparrow\uparrow}$, and $\mathsf{M}^{\uparrow\uparrow}_{\downarrow\downarrow}$ [Eq. (5.5)]. Note that in the perpendicular direction, within the MFT, the peak height grows with U; in the RPA calculation, this trend reverses as the single-particle peaks decrease in height for larger values of U.

7.4 Collective modes

The crucial difference between Figs 7.2 and 7.3 is the presence of the collective mode. The collective mode is the sharp peak at low energies in Fig. 7.3. This peak appears in the the RPA transverse spin susceptibility of Eq.(3.47). Thus, going beyond MFT and using RPA changes drastically the spectral response of the system [Compare Figs. 7.2 and 7.3]. The other spectral feature, single-particle excitations, have been analysed in

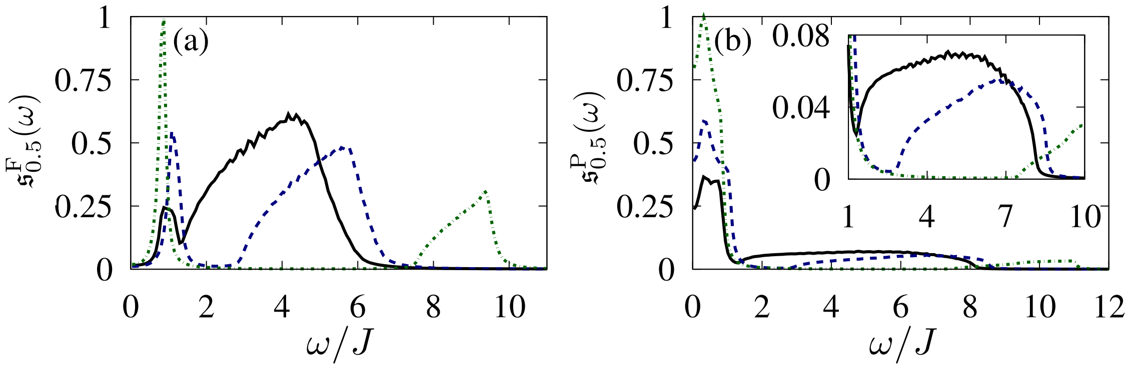

Figure 7.3: RPA spectrum collected by a lens for different values of the on-site interaction strength U at $T = 0$. Here the number of sites is 40×40. The lattice height is $s = 25$ and $\kappa = 1.5$. Light is collected with a lens of NA= 0.5 pointing in (a) the forward direction [Fig. 5.3(b)]; (b) the perpendicular direction [Fig. 5.3(c)]. From left to right, black (solid) is $m_{\mathrm{RPA}} \simeq 0.19$ ($U \approx 2.6J$), blue (dashed) is $m_{\mathrm{RPA}} \simeq 0.25$ ($U \approx 4.0J$), and green (dot-dashed) is $m_{\mathrm{RPA}} \simeq 0.30$ ($U \approx 8.3J$). Inset in (b) shows the renormalised single-particle excitations starting at $\omega \approx U/J$. All the curves have been normalised to the maximum of the $m_{\mathrm{RPA}} \simeq 0.30$ case.

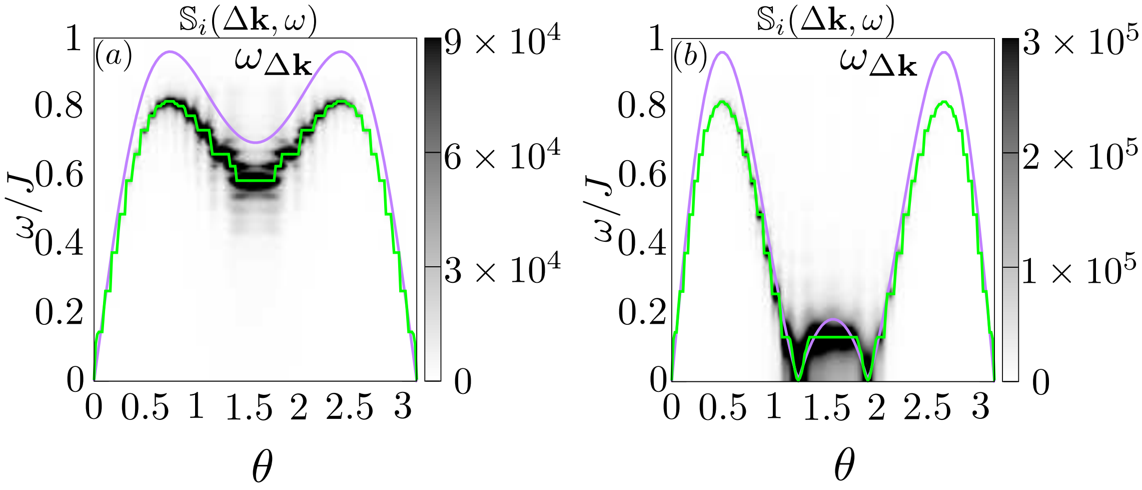

Figure 7.4: RPA scattered spectrum at zero temperature along $\phi = \pi/4$ for $U = 8.3J$ ($m_{\mathrm{RPA}} \simeq 0.30$). This figure only shows the low energy part of the spectrum that includes the collective modes. Single particle excitations occur at much higher energies and are not shown. The grey scale on the left gives the magnitude of the spectrum plotted. (a) shows $\kappa = 1.05$ and (b) $\kappa = 1.5$. $\omega_{\Delta\mathbf{k}}$ (solid line) given by Eq. (3.50) is the spin wave dispersion relation of the Heisenberg model. The green (step-like) line connects the maximum values of the collective mode peak of the RPA spectrum for each θ point evaluated.

the previous section. The major contributions to the spectrum in the RPA come from the spin-exchanging transition, as that is the one related to the transverse spin susceptibility $\chi^{+-}_{\mathrm{RPA}}(\mathbf{q},\omega)$ [see Fig. 5.2]. As described in Chapter 3, in the large U limit, the Hubbard model reduces to an effective Heisenberg Hamiltonian [34, 74]. The fundamental excitations of the Heisenberg model are the so-called magnons [Eq. (3.50)]. Contrary to the single-particle excitation, which correspond to gapped quasi-particle excitations in the system[‡], the collective modes are gapless and obey bosonic statistics. These excitations are present in the RPA calculation [27], and the results from RPA and Heisenberg model coincide for large values of U [$U \gtrapprox 25J$]. Figure 7.4 shows the angle and frequency-resolved scattered light spectrum [Eq. (7.5) along the $\phi = \pi/4$ direction. For comparison, the magnon dispersion relation, computed from the Heisenberg model [Eq. (3.50)], is also shown. As a visual aid, the line connecting the maximum of the spectrum for each θ point is also drawn. The scattered spectrum is very close to the magnon dispersion relation. Figure 7.4 is not a purely theoretical result, such measurement could be realised with a small NA lens, moving it along the θ direction. The reason both lines do not fall on top of each other is because the case shown is for $U = 8.33J$ and $m_{\text{RPA}} = 0.30$. The low-energy component RPA scattered spectrum[§] coincides with the scattered spectrum computed from the Heisenberg model for $U \gtrapprox 25J$.

[‡] This quasi-particles obey fermionic statistics. See Eqs. (3.13), (3.14), (3.14), (3.40) and Fig. 3.6(a).

[§] The Heisenberg model does not describe the Hubbard model single-particle excitations.

Chapter 8

The bosonic Hubbard model

This chapter describes the second part of the thesis. In this chapter, the scattered light intensity from an ultracold gas realisation of the Bose-Hubbard model (BHM) [39, 50] is studied using the Bogoliubov approximation in optical lattices [121, 21] and Quantum Monte Carlo Simulations (QMC).

8.1 Introduction

The bosonic version of the Hubbard model [Eq. (2.10)] was first introduced by Fisher et al. [39]. At $T = 0$, the Bose-Hubbard model [Eq. (8.2), below] has two possible states. It can be a superfluid (SF) or a Mott-insulator (MI). At $J/U = 0$, the Mott-insulator phase has the property of integer filling, i.e., the number of atoms per lattice site are exact integers, and atom fluctuations are highly suppressed. On the other hand, in the $U/J = 0$ limit, the superfluid phase can be described by coherent states where lattice site occupation number fluctuates according to Poissonian statistics [14]. At $T = 0$, the system has a quantum phase transition which in 2D happens at a critical ratio between $J/U|_c \approx 0.06$ [32, 22]. This phase transition can be induced in cold atoms trapped in an optical lattice by changing the depth of the lattice [Eq. (2.14)] [61, 111, 53]. The Bose-Hubbard model has been realised experimentally in 2D optical lattices, and the superfluid to Mott insulator transition has been observed [61, 111, 53]. As mentioned in Chapter 2, when it is realised in optical lattices, the Bose-Hubbard model has an extra term, which describes the harmonic component of the trapping potential due to the beam waist. This inhomogeneity results in a ring-like structure, where the region at the centre of the trap can be in a Mott insulating state that is surrounded by a SF ring [101, 53, 72, 123, 24]. The trapped system can be studied with QMC methods in the same manner as the homogeneous case. However, in this thesis only results for the homogeneous system will be presented. Following [50], the Hamiltonian that describes atoms of mass m in an optical lattice in terms of the field operators can be written as

$$\mathcal{H}_a = \int d\mathbf{r}\Psi^\dagger(\mathbf{r})\left(-\frac{\hbar^2}{2m}\nabla^2 + V_0(\mathbf{r})\right)\Psi(\mathbf{r}) + \frac{1}{2}\frac{4\pi a_s\hbar^2}{m}\int d\mathbf{r}\Psi^\dagger(\mathbf{r})\Psi^\dagger(\mathbf{r})\Psi(\mathbf{r})\Psi(\mathbf{r}). \tag{8.1}$$

From the previous Hamiltonian, and following the same procedure as in Chapter 2, the Bose-Hubbard model can be derived [50]

$$\mathcal{H} = -J\sum_{\langle i,j\rangle}\left(\hat{b}_i^\dagger\hat{b}_j + h.c.\right) + \frac{U}{2}\sum_j \hat{n}_j(\hat{n}_j - 1). \tag{8.2}$$

Here, $\hat{b}_i^\dagger$ creates a boson and $\hat{b}_i$ destroys it at lattice site $i = (i_x, i_y)$ or $i = i_x$ for 2D or 1D lattices respectively. The number of bosons on a particular site can be computed using the number operator $\hat{n}_i = \hat{b}_i^\dagger\hat{b}_i$. The hopping parameter is denoted by J [Eq. (2.14)], and the on-site interaction by U [Eq. (2.13)]. Bosons obey the usual bosonic commutation relations:

$$\left[\hat{b}_i, \hat{b}_j^\dagger\right] = \delta_{ij}. \tag{8.3}$$

8.2 Bogoliubov approximation

In this section, the Bogoliubov approximation is applied to the Bose-Hubbard model in a homogeneous system. The basic premise of the Bogoliubov approximation is the realisation that in the condensed phase the occupation of the single particle ground state, the zero-momentum state, is macroscopically large compared with the rest of the states. In this approximation, the creation operator for the zero-momentum state is written as a combination of a c-number z_i and an operator $\hat{\delta}_i$ which represents the fluctuations around the condensate number and which also obeys Bose-Einstein statistics. This can be explicitly written as

$$\hat{b}_i = z_i + \hat{\delta}_i, \quad \hat{b}_i^\dagger = z_i^* + \hat{\delta}_i^\dagger \tag{8.4}$$

This approximation is valid whenever the hopping amplitude J is large compared to the on-site interaction U, and small enough for the single-band approximation to be valid.

The behaviour of the c-numbers z_i can be described by means of a set of coupled non-linear Schrodinger equations, Gross-Pitaevskii (GP), which can be written as [6, 7]

$$i\hbar\partial_t z_i = U|z_i|^2 z_i - J\sum_{j/\langle i,j\rangle} z_j \tag{8.5}$$

where, $j/\langle i,j\rangle$, denotes j *such that* j is a nearest-neighbour of i. This is the starting equation used in [21] and [100] to study superfluidity in optical lattices. The time dependence of the original bosonic operator, written in terms of the c-number plus the fluctuating part $\hat{\delta}_i$, can be written as [21]:

$$\hat{b}_i = (z_i + \hat{\delta}_i)\exp\left(-i\frac{\varsigma t}{\hbar}\right). \tag{8.6}$$

Using Eq. (8.6) in Eq. (8.5) along with their respective complex conjugates, a system of coupled non-linear equations for z_i is obtained. Assuming a homogeneous system, the Bogoliubov approximation translates into $z_i = z_j = \sqrt{\rho_{\mathbf{0}}}$. Here, $\rho_{\mathbf{0}} = N_{\mathbf{0}}/N_s^d$ is the condensate density, and $N_{\mathbf{0}}$ is the total number of atoms in the condensate in a lattice with N_s^d sites. N denotes the total number of atoms in the lattice, and the nearest-neighbours number is z. The parameter ς is given by

$$\varsigma = U\rho_{\mathbf{0}} - 4J. \tag{8.7}$$

Note that if the calculation is done in the Grand Canonical ensemble [121], ς is the equivalent magnitude to the chemical potential. Hence, Eq. (8.7) can be used as a first order approximation at low T to the equivalent chemical potential that given U and J would lead to a condensate density $\rho_{\mathbf{0}}$. Also note that the factor of 4 multiplying J in Eq. (8.7) is inherent to the square lattice. In general, J is multiplied by the number of nearest neighbours. The time dependence of the fluctuating part $\hat{\delta}_i$ is given by the Bogoliubov equation [21, 100]

$$i\hbar\partial_t\hat{\delta}_i = (2\rho_{\mathbf{0}}U - \varsigma)\hat{\delta}_i - J\sum_{j/\langle i,j\rangle}\hat{\delta}_j + \rho_{\mathbf{0}}U\hat{\delta}_i^{\dagger}. \tag{8.8}$$

Equation (8.8) and its hermitian conjugate can be solved by expanding the fluctuating fields in terms of a set of quasi-particles [121]:

$$\hat{\delta}_i = \frac{1}{\sqrt{N_s^d}}\sum_{\mathbf{q}\neq\mathbf{0}}\left(u_{\mathbf{q}}\hat{\alpha}_{\mathbf{q}}e^{i(\mathbf{q}\cdot\mathbf{r}_i - \omega_{\mathbf{q}}t)} - v_{\mathbf{q}}^{*}\hat{\alpha}_{\mathbf{q}}^{\dagger}e^{-i(\mathbf{q}\cdot\mathbf{r}_i - \omega_{\mathbf{q}}t)}\right) \tag{8.9}$$

where $\mathbf{r}_i = a(i_x, i_y)$ or $\mathbf{r}_i = a i_x$ in 2D or 1D respectively and a is the lattice spacing. The sum in Eq. (8.9) is over the Brillouin zone except the origin, which is taken into account by the c-number z_i. Specifically

$$\begin{aligned} a\mathbf{q} =& \left(\frac{2\pi}{N_s} i_x, \frac{2\pi}{N_s} i_y\right) \\ (i_x, i_y) \in& \{(i_x, i_y) : i_l = (0, \ldots, N_s - 1)\, l = x, y\} - \{(0,0)\}. \end{aligned}$$

or in other words, a usual summation over the Brillouin zone is done, but the point at the origin $\mathbf{q} = (0,0)$ is excluded. The quasi-particle obey bosonic statistics:

$$\left[\hat{\alpha}_{\mathbf{q}}, \hat{\alpha}^{\dagger}_{\mathbf{q}'}\right] = \delta_{\mathbf{q}\mathbf{q}'}. \tag{8.10}$$

For the transformation in Eq. (8.9) to respect the bosonic commutation relation, the functions $u_{\mathbf{q}}$ and $v_{\mathbf{q}}$ have to be constrained by

$$|u_{\mathbf{q}}| - |v_{\mathbf{q}}|^2 = 1. \tag{8.11}$$

The quasi particle thermal expectation value at a temperature T is given by a Bose-Einstein distribution function:

$$\left\langle \hat{\alpha}^{\dagger}_{\mathbf{q}} \hat{\alpha}_{\mathbf{q}'} \right\rangle = n_{\mathbf{q}} = \frac{\delta_{\mathbf{q}\mathbf{q}'}}{e^{\beta\hbar\omega_{\mathbf{q}}} - 1} \tag{8.12}$$

where $\beta = 1/k_B T$ and k_B is Boltzmann constant. Using Eq. (8.9) and its hermitian conjugate into Eq. (8.8) and its hermitian conjugate, the following set of equations is obtained:

$$\hbar\omega_{\mathbf{q}} u_{\mathbf{q}} = \left[\rho_{\mathbf{0}} U + 4J \sum_{l=1}^{d} \sin^2\left(\frac{q_l a}{2}\right)\right] u_{\mathbf{q}} - \rho_{\mathbf{0}} U v_{\mathbf{q}} \tag{8.13}$$

$$-\hbar\omega_{\mathbf{q}} v_{\mathbf{q}} = \left[\rho_{\mathbf{0}} U + 4J \sum_{l=1}^{d} \sin^2\left(\frac{q_l a}{2}\right)\right] v_{\mathbf{q}} - \rho_{\mathbf{0}} U u_{\mathbf{q}}. \tag{8.14}$$

Squaring and subtracting these two equations, the quasi-particle spectrum can be obtained with the aid of Eq. (8.11):

$$\begin{aligned} \hbar\omega_{\mathbf{q}} =& \sqrt{4J \sum_{l=1}^{d} \sin^2\left(\frac{q_l a}{2}\right)} \sqrt{2\rho_{\mathbf{0}} U + 4J \sum_{l=1}^{d} \sin^2\left(\frac{q_l a}{2}\right)} \\ =& \sqrt{\epsilon_{\mathbf{q}}} \sqrt{2\rho_{\mathbf{0}} U + \epsilon_{\mathbf{q}}}. \end{aligned} \tag{8.15}$$

The bare particle dispersion relation as now denoted by

$$\epsilon_{\mathbf{q}} = 4J \sum_{l=1}^{d} \sin^2\left(\frac{q_l a}{2}\right). \tag{8.16}$$

To solve for u_q and v_q, square, say, Eq. (8.13), and write $|v_q|^2 = |u_q|^2 - 1$, Eq. (8.11). After some simplifications, these results in

$$|u_q|^2 = \frac{1}{2}\left(\frac{\epsilon_{\mathbf{q}} + \rho_{\mathbf{0}} U}{\hbar\omega_{\mathbf{q}}} + 1\right). \tag{8.17}$$

And, using Eq. (8.11) again,

$$|v_q|^2 = \frac{1}{2}\left(\frac{\epsilon_{\mathbf{q}} + \rho_{\mathbf{0}} U}{\hbar\omega_{\mathbf{q}}} - 1\right). \tag{8.18}$$

Thus, the diagonalisation problem for the system with periodic boundary conditions is solved.

8.2.1 Total number of atoms

In the previous section, the Bose-Hubbard Hamiltonian of Eq. (8.2) has been solved using the Bogoliubov approximation. This section is dedicated to computing some properties of the system. The first magnitude that will be computed is the the total density at a site

$$\langle \hat{n}_i \rangle = \left\langle \hat{b}_i^\dagger \hat{b}_i \right\rangle = n. \tag{8.19}$$

Using Eqs. (8.4), (8.9), (8.12) and taking into account that expectation values of odd number of operators vanish, in particular $\left\langle \hat{\delta}_i \right\rangle = 0$ and $\left\langle \hat{\delta}_i^\dagger \right\rangle = 0$, Eq. (8.19) can be written as

$$\left\langle \hat{b}_i^\dagger \hat{b}_j \right\rangle = \rho_{\mathbf{0}} + \frac{1}{N_s^d} \sum_{\mathbf{q}\neq\mathbf{0}} \left[e^{-i\mathbf{q}\cdot(\mathbf{r}_i - \mathbf{r}_j)} u_{\mathbf{q}}^2 n_{\mathbf{q}} + e^{i\mathbf{q}\cdot(\mathbf{r}_i - \mathbf{r}_j)} v_{\mathbf{q}}^2 \left(n_{\mathbf{q}} + 1\right) \right]. \tag{8.20}$$

The total density is given by taking $i = j$ in Eq. (8.20),

$$n = \rho_{\mathbf{0}} + \frac{1}{N_s^d} \sum_{\mathbf{q}\neq\mathbf{0}} \left[u_{\mathbf{q}}^2 n_{\mathbf{q}} + v_{\mathbf{q}}^2 \left(n_{\mathbf{q}} + 1\right) \right]. \tag{8.21}$$

Using Eq. (8.21), the density of atoms in the ground state $\rho_{\mathbf{0}}$ can be computed once the total density n, and the temperature T are fixed . The solution for $\rho_{\mathbf{0}}$ is obtained numerically with a recursive scheme. Numerical solutions of Eq. (8.21) are shown in Fig. 8.1 for zero temperature and two different values for the total density. Within the Bogoliubov approximation, the condensate density $\rho_{\mathbf{0}}$ decreases with increasing the on-site interaction U. However, it always remain finite, never reaching zero, which would signal a phase transition. Hence, the Bogoliubov approximation can only describe the superfluid phase of the Bose-Hubbard model.

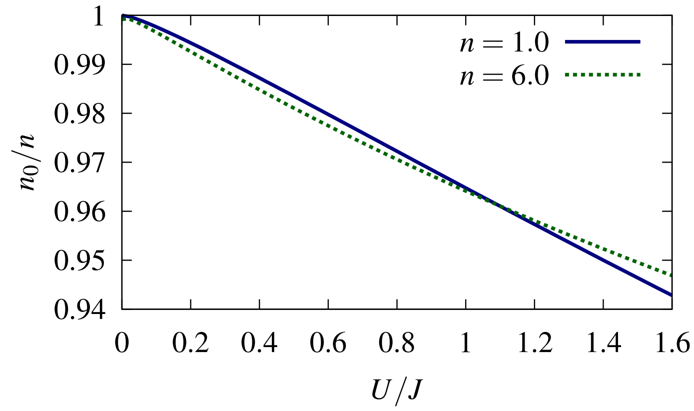

Figure 8.1: U dependence of the condensate density ρ_0 at zero temperature. ρ_0 is obtained as a solution of Eq. (8.21), for lattice of linear finite size $N_s = 32$, and two different values for the total density.

8.2.2 Density-density correlation function

In this chapter, the goal is to use off-resonance light scattering to do optical diagnostics about the state of the system [104]. For the single-species bosonic case, the scattered intensity is characterised by the density-density correlations of the system [104, 31]. The density-density correlation functions can be separated into a connected and a disconnected correlation function. These, see Chapter 4, contribute to the inelastic and elastic components of the scattered light, respectively. Thus, the density-density correlations can be written as

$$\begin{aligned} \langle \hat{n}_i \hat{n}_j \rangle &= \left\langle \hat{b}_i^\dagger \hat{b}_i \hat{b}_j^\dagger \hat{b}_j \right\rangle \\ &= \overbrace{\left\langle \hat{b}_i^\dagger \hat{b}_i \right\rangle \left\langle \hat{b}_j^\dagger \hat{b}_j \right\rangle}^{\text{elastic}} + \underbrace{\left\langle \hat{b}_i^\dagger \hat{b}_i \hat{b}_j^\dagger \hat{b}_j \right\rangle - \left\langle \hat{b}_i^\dagger \hat{b}_i \right\rangle \left\langle \hat{b}_j^\dagger \hat{b}_j \right\rangle}_{\text{inelastic}} \qquad (8.22) \\ &= \left\langle \hat{b}_i^\dagger \hat{b}_i \hat{b}_j^\dagger \hat{b}_j \right\rangle_d + \left\langle \hat{b}_i^\dagger \hat{b}_i \hat{b}_j^\dagger \hat{b}_j \right\rangle_c \qquad (8.23) \end{aligned}$$

The correlation function has been split in two terms: *elastic* and *inelastic*. The total result is independent of the way the correlations are written, but as was shown in Chapters 4 and 5, it is convenient to separate the different contributions. The elastic component is nothing else but the square of the total density. It can be computed squaring Eq. (8.21),

$$\begin{aligned} \left\langle \hat{b}_i^\dagger \hat{b}_i \hat{b}_j^\dagger \hat{b}_j \right\rangle_d &= \left\langle \hat{b}_i^\dagger \hat{b}_i \right\rangle \left\langle \hat{b}_j^\dagger \hat{b}_j \right\rangle = \langle \hat{n}_i \rangle \langle \hat{n}_j \rangle \\ &= n^2 \qquad (8.24) \end{aligned}$$

Using Eqs. (8.4), (8.9), (8.12) the connected term can be calculated in the same way as the density.

$$\begin{aligned}\left\langle \hat{b}_i^\dagger \hat{b}_i \hat{b}_j^\dagger \hat{b}_j \right\rangle_c =& \left\langle \hat{b}_i^\dagger \hat{b}_i \hat{b}_j^\dagger \hat{b}_j \right\rangle - \left\langle \hat{b}_i^\dagger \hat{b}_i \right\rangle \left\langle \hat{b}_j^\dagger \hat{b}_j \right\rangle \\ =& z_i^* z_j^* \left\langle \hat{\delta}_i \hat{\delta}_j \right\rangle + z_i z_j \left\langle \hat{\delta}_i^\dagger \hat{\delta}_j^\dagger \right\rangle + z_i^* z_j \left\langle \hat{\delta}_i \hat{\delta}_j^\dagger \right\rangle + z_i z_j^* \left\langle \hat{\delta}_i^\dagger \hat{\delta}_j \right\rangle \\ &+ \left\langle \hat{\delta}_i^\dagger \hat{\delta}_i \hat{\delta}_j^\dagger \hat{\delta}_j \right\rangle - \left\langle \hat{\delta}_i^\dagger \hat{\delta}_i \right\rangle \left\langle \hat{\delta}_j^\dagger \hat{\delta}_j \right\rangle \end{aligned} \tag{8.25}$$

Listing term by term we obtain:

$$z_i^* z_j^* \left\langle \hat{\delta}_i \hat{\delta}_j \right\rangle = -\frac{z_i^* z_j^*}{N_s^d} \sum_{\mathbf{q}\neq\mathbf{0}} u_{\mathbf{q}} v_{\mathbf{q}}^* \left[e^{-i\mathbf{q}\cdot(\mathbf{r}_i-\mathbf{r}_j)} n_{\mathbf{q}} + e^{i\mathbf{q}\cdot(\mathbf{r}_i-\mathbf{r}_j)} (1+n_{\mathbf{q}}) \right] \tag{8.26}$$

$$z_i z_j \left\langle \hat{\delta}_i^\dagger \hat{\delta}_j^\dagger \right\rangle = -\frac{z_i z_j}{N_s^d} \sum_{\mathbf{q}\neq\mathbf{0}} v_{\mathbf{q}} u_{\mathbf{q}}^* \left[e^{-i\mathbf{q}\cdot(\mathbf{r}_i-\mathbf{r}_j)} n_{\mathbf{q}} + e^{i\mathbf{q}\cdot(\mathbf{r}_i-\mathbf{r}_j)} (1+n_{\mathbf{q}}) \right] \tag{8.27}$$

$$z_i^* z_j \left\langle \hat{\delta}_i \hat{\delta}_j^\dagger \right\rangle = \frac{z_i^* z_j}{N_s^d} \sum_{\mathbf{q}\neq\mathbf{0}} \left[|v_{\mathbf{q}}|^2 e^{-i\mathbf{q}\cdot(\mathbf{r}_i-\mathbf{r}_j)} n_{\mathbf{q}} + |u_{\mathbf{q}}| e^{i\mathbf{q}\cdot(\mathbf{r}_i-\mathbf{r}_j)} (1+n_{\mathbf{q}}) \right] \tag{8.28}$$

$$z_i z_j^* \left\langle \hat{\delta}_i \hat{\delta}_j^\dagger \right\rangle = \frac{z_i z_j^*}{N_s^d} \sum_{\mathbf{q}\neq\mathbf{0}} \left[|u_{\mathbf{q}}|^2 e^{-i\mathbf{q}\cdot(\mathbf{r}_i-\mathbf{r}_j)} n_{\mathbf{q}} + |v_{\mathbf{q}}| e^{i\mathbf{q}\cdot(\mathbf{r}_i-\mathbf{r}_j)} (1+n_{\mathbf{q}}) \right] \tag{8.29}$$

Furthermore, taking $z_i, u_{\mathbf{q}}, v_{\mathbf{q}} \in$ Reals, and using the fact that the system is homogeneous, $z_i = z_j = \sqrt{\rho_{\mathbf{0}}}$, Eqs. (8.26) -(8.29) can be combined to rewrite an explicit expression for the connected correlations Eq. (8.25)

$$\begin{aligned}\left\langle \hat{b}_i^\dagger \hat{b}_i \hat{b}_j^\dagger \hat{b}_j \right\rangle_c =& \frac{\rho_{\mathbf{0}}}{N_s^d} \sum_{\mathbf{q}\neq\mathbf{0}} (u_{\mathbf{q}} - v_{\mathbf{q}})^2 \left[e^{-i\mathbf{q}\cdot(\mathbf{r}_i-\mathbf{r}_j)} n_{\mathbf{q}} + e^{-i\mathbf{q}\cdot(\mathbf{r}_i-\mathbf{r}_j)} (1+n_{\mathbf{q}}) \right] \\ &+ \frac{1}{N_s^{2d}} \sum_{\mathbf{q},\mathbf{q}'\neq\mathbf{0}} \Big\{ \left(u_{\mathbf{q}} u_{\mathbf{q}'} + v_{\mathbf{q}} v_{\mathbf{q}'} \right)^2 n_{\mathbf{q}} (1+n_{\mathbf{q}'}) e^{-i(\mathbf{q}-\mathbf{q}')\cdot(\mathbf{r}_i-\mathbf{r}_j)} \\ &+ \frac{\left(u_{\mathbf{q}} v_{\mathbf{q}'} + v_{\mathbf{q}} u_{\mathbf{q}'} \right)^2}{2} \left[n_{\mathbf{q}} n_{\mathbf{q}'} e^{-i(\mathbf{q}+\mathbf{q}')\cdot(\mathbf{r}_i-\mathbf{r}_j)} + (1+n_{\mathbf{q}})(1+n_{\mathbf{q}'}) e^{i(\mathbf{q}+\mathbf{q}')\cdot(\mathbf{r}_i-\mathbf{r}_j)} \right] \Big\} \end{aligned} \tag{8.30}$$

8.3 The Quantum Monte Carlo approach

The QMC results presented here have been obtained using the codes distributed in the ALPS suite [12, 2, 83]. In particular, all the results presented in this thesis have been computed with the directed loop algorithm in the SSE representation [4, 106, 96].

Quantum Monte Carlo is based on the observation that the partition function and the physical observables in a quantum system can be written in terms of integrals over all

Table 8.1: Input parameters for the Quantum Monte Carlo simulations.

	Number of thermalisation steps
N_s	Linear lattice size
T	Temperature
U	On-site interaction strength
J	Hopping parameter
μ	Chemical potential
NMax	Maximum number of bosons per state

configurations (in terms of the partition function Z). These integrals are multidimensional, and computing a numerical value with regular grid methods or even with naive random sampling approaches is impossible in the first case, and highly inefficient in the second one. Very clever tricks and algorithms have been developed in the last few years, starting with Wang-Landau sampling [114] and the cluster updates ideas, which have led to the current *state-of-the-art* algorithms for simulating the Bose-Hubbard model: the *worm* algorithm and its variants [99, 98, 117, 94], and the *stochastic series expansions* algorithm [4, 106, 96].

8.3.1 QMC parameters

In the QMC simulations presented in this chapter, the system is simulated in the Grand canonical ensemble. The system is defined by the Hamiltonian [Eq. (8.2)], and a set of input parameters. The input parameters for the QMC code are listed in Table 8.1. The physical quantities have been already described above. The other two parameters: the number of thermalisation steps and NMax are specific to Monte Carlo simulations. A Monte Carlo, specifically a Markov Chain Monte Carlo simulation uses a pseudo random number generator to sample the probability distribution or the partition function of the system in this case. Numerically, it is necessary to discard the initial set of states obtained because the system takes a certain amount of steps to achieve a steady state [60, 114]. In a Monte Carlo simulation, the simulation is initialised from a random state, and the thermalisation steps are performed. Once the thermalisation run is finished, the estimators for the measured quantities are set to zero and the simulation starts. Measurements will be done until the finalisation condition is met. This condition can be either a fixed number of Monte Carlo steps after thermalisation, a convergence test on the error bars of the estimated quantities, or the simulation can be run until a given relative accuracy is achieved. The resulting system configuration between two consecutive Monte Carlo steps are correlated. Either these correlations have to be taken into account when computing the error bars, or measurements are to be performed skipping a number of Monte Carlo steps [118]. The number of Monte Carlo steps to be skipped between measurements is of the order of the autocorrelation time for the estimated magnitude [118, 5]. The ALPS code [3] takes care of the previous steps. Only a number of thermalisation steps has to be supplied as an input parameters. After the thermalisation has been carried out, the simulations are run until the density, energy, and density-density correlations have achieved convergence [Table 8.1].

The other unfamiliar parameter, NMax, represents the maximum number of bosons allowed in a state, the optimal value of this parameters can be estimated from the following argument. In the Mott state, at low temperature the fluctuations are negligible, and in principle, this parameter could be set to just slightly above the total density. In the superfluid state, on the other hand, the wave-functions can be approximated by a *coherent state*, with fluctuations that can be described according to a Poisson distribution. For a given total density[*], one way to make sure that this parameter is in the correct regime is by plotting the Poisson distribution for the total density and checking that the tail is not cut-off.

8.3.2 QMC applied to the Bose-Hubbard model

QMC methods have been applied intensively to the simulation of the 2D Bose-Hubbard model in optical lattices [22, 123, 72, 24, 95]. The QMC results presented have been computed using the ALPS collaboration codes. In particular, the implementation of the directed loop algorithm in the SSE representation [4, 106, 96]. Every QMC run has been allowed a fixed number of Monte Carlo steps for thermalisation. This number was fixed to 50000. After thermalisation, the simulation was run until the error bars for the average total density, the energy and the density-density correlations have converged. The QMC codes use the input parameters listed in Table 8.1 and produces the output quantities listed in Table 8.2.

---

[*] The total density can be roughly estimated, at least at low temperatures, using the Bogoliubov approximation [Eq. (8.7)].

Table 8.2: Output parameters for the Quantum Monte Carlo simulations.

$n = \frac{1}{L^2}\sum_{\mathbf{i}} \langle \hat{n}_{\mathbf{i}} \rangle$	Average total density at a site
$\langle \hat{n}_{\mathbf{i}} \rangle$	Local density
$\langle \hat{n}_{\mathbf{0}} \hat{n}_{\mathbf{j}} \rangle$	Full density-density correlations functions
$\left\langle \hat{b}^{\dagger}_{\mathbf{0}} \hat{b}_{\mathbf{i}} \right\rangle$	Green's function
ρ_s	Superfluid density [97]

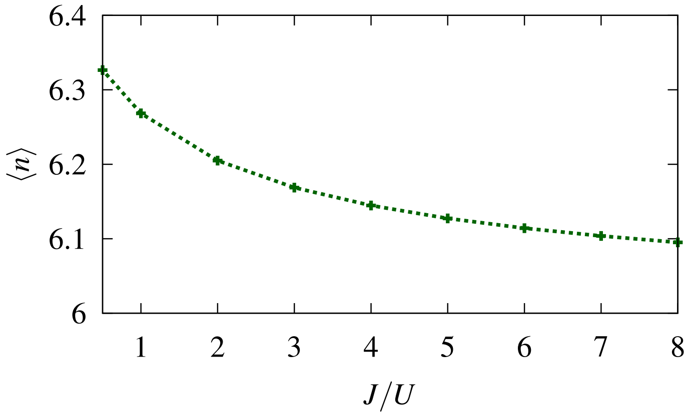

Figure 8.2: Average density when varying the hopping parameter. This is computed with the ALPS QMC libraries for a 2D Bose-Hubbard model in a square lattice with $N_s = 16$,$U = 1$, $T = 0.05U$, μ given by Eq. (8.31), and NMax= 20. Data points are joined with straight lines.

8.3.3 Small system in the Bogoliubov regime

In the following section, the Bogoliubov approximation of Section 8.2 is compared with the QMC results for a small lattice of linear size of $N_s = 16$ at low temperatures [$T = 0.05U$]. Figure 8.2 shows the total density computed from QMC for a lattice with 16×16 sites, and $T = 0.05U$. The chemical potential has been estimated using Eq. (8.7) and taking into account that if the Bogoliubov calculation is done in the Grand canonical ensemble, ς is the equivalent magnitude to the chemical potential [121]. To achieve an on-site density of around 6, the value of the chemical potential has been estimated from

$$\mu = 6U - 4J. \tag{8.31}$$

The resulting total density from this set of parameters is shown in Fig. 8.2. It can be seen that Eq. (8.31) approaches the *target* value for the total density, 6, for large values of J/U. This is to be expected as the origin of Eq. (8.7) and (8.31) is in the Bogoliubov approximation, which is only a good approximation in the large J/U regime. The bosonic Green's function can be calculated in the QMC simulation [Table 8.2]. This can be used to estimate the condensate density from the QMC simulation. This is done by taking

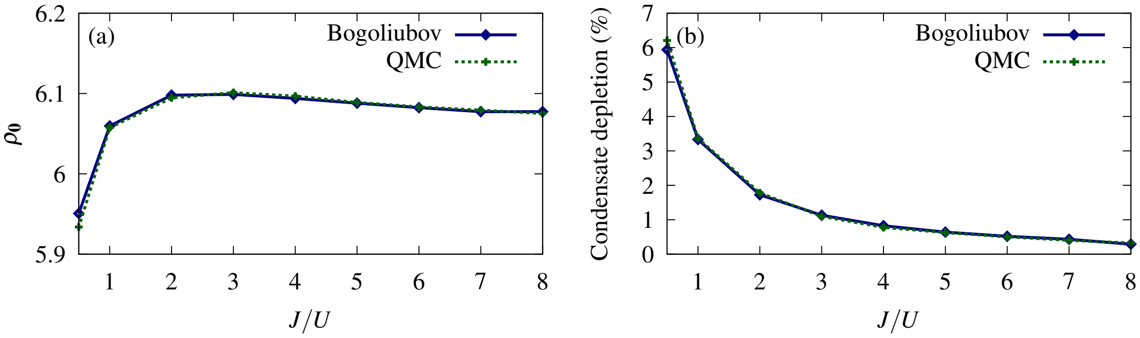

Figure 8.3: Comparison between the Bogoliubov approximation and Quantum Monte Carlo for a 2D Bose-Hubbard model in a square lattice with $N_s = 16$, $U = 1$, $T = 0.05U$, and NMax$= 20$. Note that the total density, shown in Fig. 8.2, is not constant. This total density is used in the Bogoliubov approximation to compute the condensate density $\rho_{\mathbf{0}}$ self-consistently from Eq. (8.21). (a) Condensate density, and (b) condensate depletion [Eq. (8.33)]. The QMC condensate density is computed using Eq. (8.32). The bump in (a) is due to the fact that the total density is not constant for the data points shown.

the Fourier transform of $\left\langle \hat{b}_{\mathbf{i}}^{\dagger}\hat{b}_{\mathbf{j}}\right\rangle$. By definition, the condensate density corresponds to the value of this Fourier transform at the origin. In particular, for the translationally invariant system studied here

$$\rho_{\mathbf{0}} = \frac{1}{N_s^2}\sum_{\mathbf{j}}\left\langle \hat{b}_{\mathbf{0}}^{\dagger}\hat{b}_{\mathbf{j}}\right\rangle. \tag{8.32}$$

For the parameters mentioned above, with the chemical potential estimated using Eq. (8.31), the condensate density computed from Eq. (8.32) is shown in Fig. 8.3(a). Note that the maximum in $\rho_{\mathbf{0}}$ is due to the fact that the density is not kept constant when J/U is varied [Fig. 8.2]. The condensate depletion, which measures the fraction of atoms that are not in the ground state, is shown in Fig. 8.3(b). As expected, for larger values of J/U, the number of atoms not in the condensate decreases. The condensate depletion is defined as

$$\text{Condensate depletion} = \frac{n - \rho_{\mathbf{0}}}{n}. \tag{8.33}$$

8.3.4 Temperature dependence of the condensate density

One of the possible applications of non-resonant light scattering as a probe is thermometry [104, 31]. This possibility will be explored in Section 8.5. In this section, the system is characterised. To study the temperature dependence of the superfluid using QMC, two different cases have been studied. Both cases are in a square lattice with $N_s = 32$, $U = 1$, $J = U$, and NMax$= 15$. In the first case, the density has been kept constant† with

---

† By changing the input chemical potential [Table 8.1].

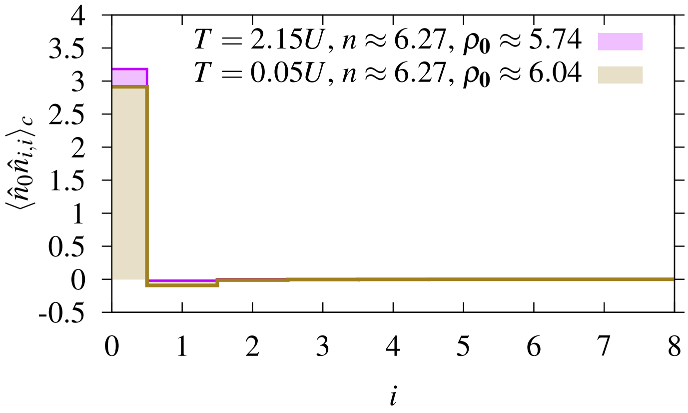

Figure 8.4: Connected density-density correlations at fixed total density and J for changing T. These results are computed from QMC for a 2D Bose-Hubbard model in a square lattice with $N_s = 32$, $U = 1$, $J = U$, and NMax= 15.

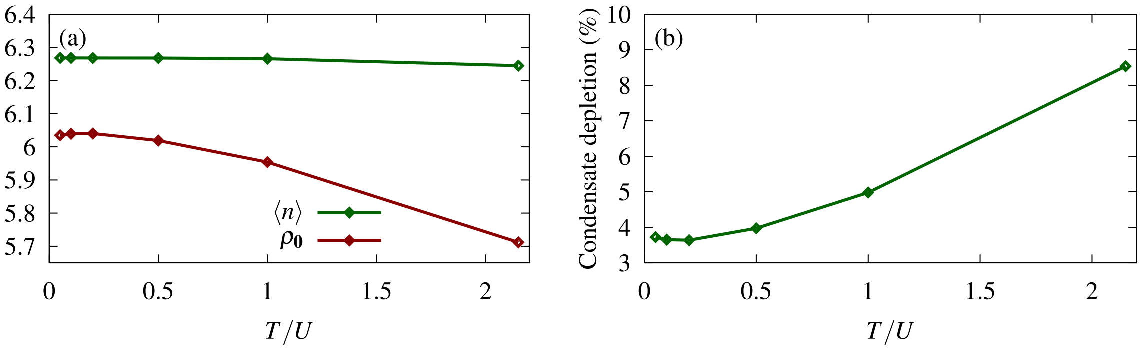

Figure 8.5: Temperature dependence of the total and condensate density of a superfluid at fixed chemical potential for changing T. These results are computed from QMC for a 2D Bose-Hubbard model in a square lattice with linear lattice size $N_s = 32$, $U = 1$, $\mu = 2U$, $J = U$, and NMax= 15.

a value ≈ 6.27 and the temperature has been changed from $T = 0.05U$, in which case the condensate depletion [Eq. (8.33)] is $\approx 3.5\%$ to $T = 2.15U$ for which the condensate depletion increases to $\approx 9\%$. The connected correlations along the diagonal are shown in Fig. 8.4. The second case is one in which the chemical potential is given a fixed value of $\mu = 2U$ and the temperature is increased from $T = 0.05U$ up to $T = 2.15U$. In this case, the density is not constant with increasing temperature. This is shown in Fig. 8.5. The changes in the correlations, not shown, are similar to those of Fig. 8.4.

8.3.5 System evolution across the first Mott lobe

The final case studied in this section is the Mott insulator to superfluid transition at finite T. At zero temperature and in the thermodynamic limit, there is a sharp quantum phase transition between the MI and the superfluid phase. This transition in optical lattices has

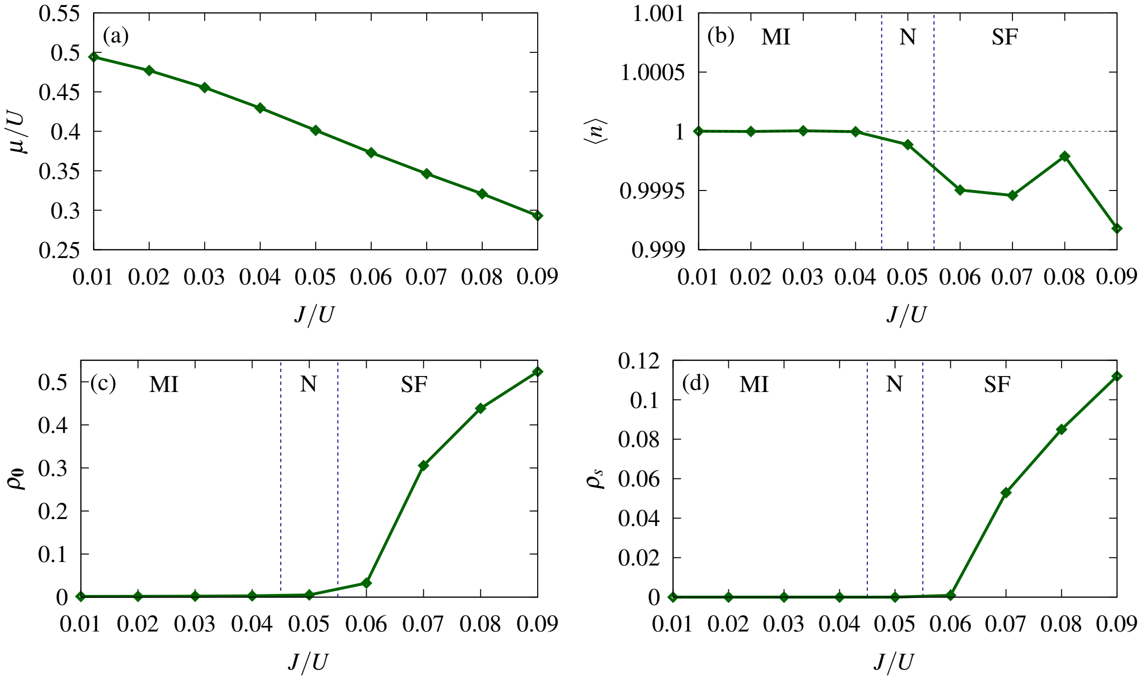

Figure 8.6: Total, condensate, and superfluid density, from the Mott insulator to a superfluid. These results have been computed using QMC for a 2D Bose-Hubbard model in a square lattice with linear lattice size $N_s = 32$,$U = 1$, $T = 0.05U$, and NMax= 10. (a) Shows the input chemical potential [Table 8.1], (b) total density, (c) condensate density computed using Eq. (8.32), and (d) superfluid density. The horizontal dashed line in (b) is a visual aid to show deviations from unit filling. The vertical dashed line are an indication as to which phase the different data points belong to. However, given the small number of data points, the position of the phase boundaries can only be indicated very roughly. Note that the error bars in (b) and (d) are not visible at this scale.

been studied in the literature both theoretically [39, 32, 72, 22] and experimentally [111]. In fact, at finite T, apart from the usual Mott insulator and superfluid phases [39], a third normal (N) liquid phase appears in between [72]. The normal phase is characterised by the fact that the superfluid density is zero and the filling is not integer [72]. The transition between the MI and the N phases is not sharp but a crossover [72]. For the purposes of this Chapter, the details of the transition are not as important as whether the transition leads to any observable change in the scattered light. This change will happen if the density-density correlations show any notable change when going through the transition. To study this, the evolution of the system from the Mott insulating phase $J/U = 0.01$ to the superfluid $J/U = 0.09$ has been studied in a square lattice with linear lattice size $N_s = 32$, $U = 1$ at $T = 0.05U$, and NMax= 10. The total density has been kept as close to 1 as possible by modifying the chemical potential. The total, condensate, and superfluid densities for this case are shown, along with the chemical potential, in

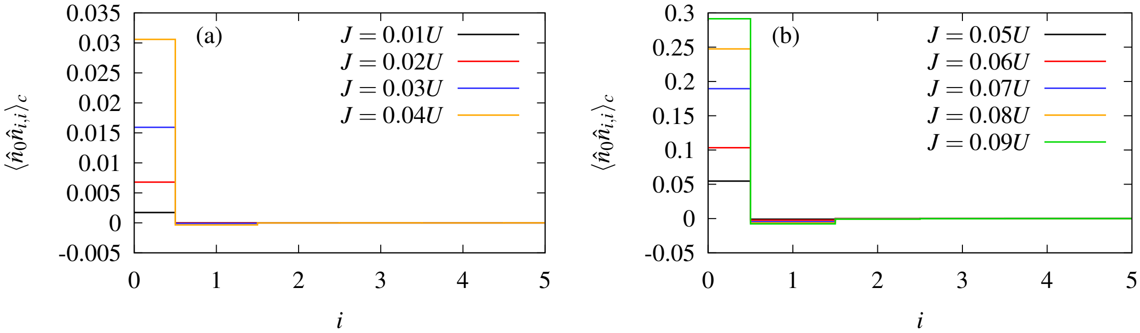

Figure 8.7: Evolution of the density-density correlations from the Mott insulator to the superfluid regime, at constant unit total density. The shown results are computed using QMC for a 2D Bose-Hubbard model in a square lattice with linear lattice size $N_s = 32$,$U = 1$, $T = 0.05U$, and NMax$= 10$. Note that there is an order of magnitude between (a) and (b). The chemical potential, total density, and condensate density are shown in Fig. 8.6.

Fig. 8.6. The phase boundary between the MI and the N phases and the N and SF phases are indicated by vertical dashed lines. The boundary between the MI and the N phases has been determined by the point at which the total density at a site changes from 1 [Fig. 8.6(b)]. Note that the QMC numerical error bars are not visible at the corresponding scale of Figs. 8.6(b) and (c). The boundary between the N and SF phases is determined by the point at which the superfluid density ρ_s reaches a finite value. Note that given the sparseness of the data, the position of the phase boundaries cannot be determined accurately. Hence, the position of the vertical lines is only a very rough estimate as to where the phase boundaries lie. In particular, the error bars associated with the location of the phase boundaries are at least $\pm 0.005U$. The density-density correlations for this case are shown in Fig. 8.7. The main changes are at the origin, $\langle \hat{n}_\mathbf{0} \hat{n}_\mathbf{0} \rangle_c$. In particular, from the MI to the SF, the magnitude of this point increases by two orders of magnitude [Compare Figs. 8.7(a) and (b)].

8.4 Comparison between the Bogoliubov approximation and QMC

For all the comparisons between QMC and the Bogoliubov approximation presented in this chapter, first the QMC simulation is run with a given set of input parameters [Table 8.1]. The QMC total density n is obtained as an output from the simulation [Table 8.2]. In order to compare with the Bogoliubov approximation, this value for the total density obtained from the QMC is used in Eq. (8.21) to obtain the condensate density in the Bogoliubov approximation. The rest of the parameters are identical in both calculations. In particular, these parameters are the system size N_s, the temperature T, the hopping amplitude J, and the on-site interaction U.

For instance, Fig. 8.2 shows the total density obtained from QMC for a square lattice with linear lattice size $N_s = 16$, $U = 1$, $T = 0.05U$, μ given by Eq. (8.31), and NMAX= 20. Fig. 8.3 compares the condensate density computed from QMC with that obtained from the Bogoliubov approximation by solving Eq. (8.21). Eq. (8.21) is solved with the same parameters, that is, for a square lattice with $N_s = 16$, $U = 1$, $T = 0.05U$, and the total density n shown in Fig. 8.2. As expected, the agreement between the QMC numerical results and the Bogoliubov approximation is better for large values of J/U. Figure 8.8 shows a comparison of the connected density-density correlations for some particular values of J/U. The difference between QMC and the Bogoliubov approximation is larger for the correlations than it is for the condensate density [Fig. 8.3(a)]. Only for the largest value of $J = 7U$ the correlations computed with the two different methods fall on top of each other. A comparison between QMC calculations and the Bogoliubov is interesting not only as a confirmation that the QMC calculation is working appropiately, but also as a numerical test of a technique that is used quite often to describe certain aspects of ultracold atoms in optical lattices. The results of Figures 8.3 and 8.8 should offer guidance as to how reliable the Bogoliubov approximation is. The excitation spectra of the Bose-Hubbard model was computed using QMC and the Bogoliubov approximation in [92] with similar results to the ones shown here. The Bogoliubov approximation qualitatively describes the behaviour of the system but fails quantitatively. In the particular case shown here, the Bogoliubov approximation overestimates the correlations between the particles [Fig. 8.8].

8.5 Scattered light intensity from the Bose-Hubbard model

The formalism presented in Chapter 4, in particular Section 4.2, can be directly applied to analyse the scattered intensity from a gas in an optical lattice.

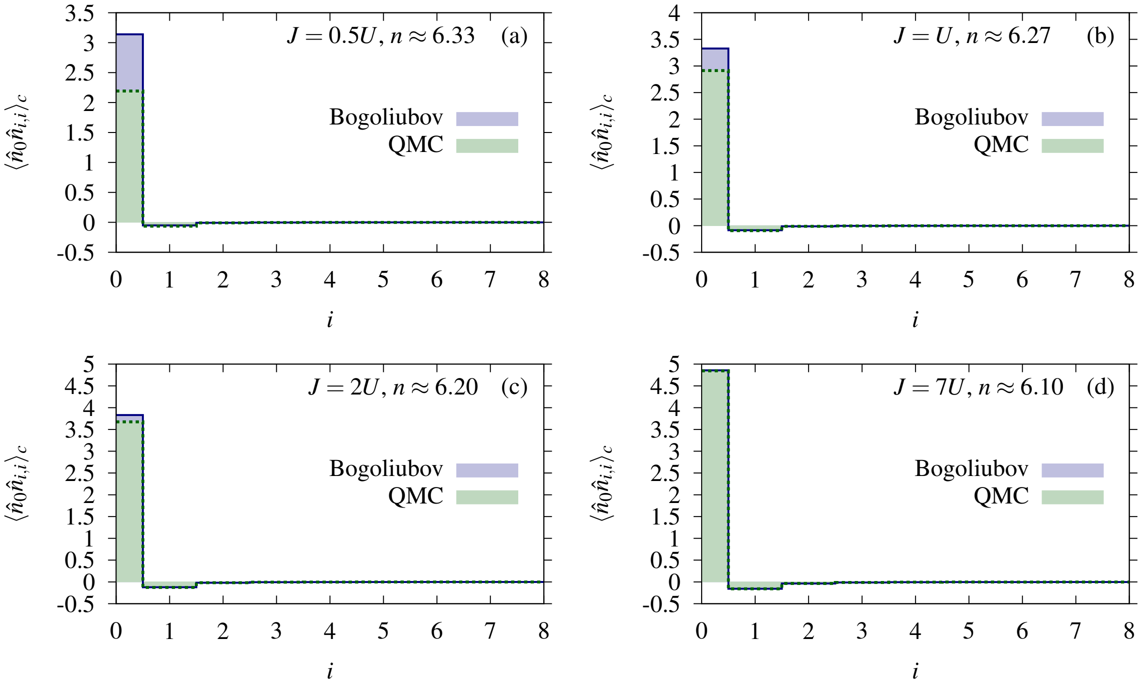

Figure 8.8: Connected density-density correlations at fixed T and changing J. Comparison between the Bogoliubov approximation and Quantum Monte Carlo for a 2D Bose-Hubbard model in a square lattice with linear lattice size $N_s = 16$, $U = 1$, $T = 0.05U$, and NMax= 20. The total density is listed in the figure and the condensate density, and condensate depletion are shown in Fig. 8.3. The density is used in the Bogoliubov approximation to compute the condensate density ρ_0 self-consistently from Eq. (8.21). The correlations in the Bogoliubov approximation are computed using Eq. (8.30). The correlations are shown along the diagonal in the lattice.

8.5.1 Single-species ^{87}Rb gas

As an example of the application of the optical diagnostics techniques presented in this thesis to the Bose-Hubbard model, the single-species ^{87}Rb gas is analysed. The lattice confinement along the z direction is taken as $\omega_z = 10\sqrt{2}E_R/\hbar$, and the lattice depth is fixed at $s = 25$. The parameter κ [Eq. (4.16)] is fixed to 1.05. In the single-species case, and using the same set of states and illuminating transition used by Douglas and Burnett [31], the ground-state is taken to be

$$|g\rangle = |5^2 S_{1/2}, F = 2, m_F = 2\rangle \tag{8.34}$$

and the excited state

$$|e\rangle = |5^2 P_{3/2}, F = 3, m_F = 3\rangle. \tag{8.35}$$

When illuminated with σ^+-polarised light, the resulting transition is cycling [Fig. 8.9]. The corresponding dipole matrix element can be computed from Eq. (4.20) taking into

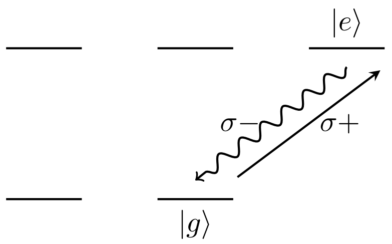

Figure 8.9: Transitions induced with σ^+ illumination in the particular case of ^{87}Rb studied in this chapter. This is a cycling transition: $|g\rangle \overset{\sigma^+}{\to} |e\rangle \overset{\sigma^-}{\to} |g\rangle$.

account that there is no sum over states g. The result is

$$\mathsf{M}_{gg}^{gg} = \frac{1}{4}\left(3 + \cos 2\theta\right) \tag{8.36}$$

Hence, the elastic component of the scattered light intensity is [Eq. (4.27)]

$$I_{\mathrm{e}}(\Delta\mathbf{k}) = \alpha_{\Delta\mathbf{k}} B \mathsf{M}_{gg}^{gg} |\mathfrak{u}_{\bar{\Delta}\mathbf{k}}|^2 n^2. \tag{8.37}$$

Here, n is the total atomic density at a site and the diffraction factor is defined in Eq. (4.36). The Debye-Waller factor $\alpha_{\Delta\mathbf{k}}$ is defined in Eq. (4.22). For the single-species bosonic gas, there is no broken translation symmetry, hence, the elastic component only has the trivial diffraction peak in the forward direction. Using Eq. (4.49), the losses to higher bands can be computed

$$I_{\mathrm{hb}}(\Delta\mathbf{k}) = BN\left[1 - \alpha_{\Delta\mathbf{k}}\right]\mathsf{M}_{gg}^{gg}, \tag{8.38}$$

where N is the number of atoms in the lattice.

The inelastic component of the scattered intensity for a homogeneous bosonic single-species gas in the Bogoliubov approximation can be written by combining Eqs. 8.30 and 4.23,

$$\begin{aligned} I_i^{\mathrm{B}}(\Delta\mathbf{k}) =& \frac{\rho_{\mathbf{0}} B \alpha_{\Delta\mathbf{k}} \mathsf{M}_{gg}^{gg}}{N_s^2} \sum_{\mathbf{q}\neq\mathbf{0}} \left(u_{\mathbf{q}} - v_{\mathbf{q}}\right)^2 \left[|\mathfrak{u}_{\bar{\Delta}\mathbf{k}-\mathbf{q}}|^2 n_{\mathbf{q}} + |\mathfrak{u}_{\bar{\Delta}\mathbf{k}+\mathbf{q}}|^2 (1 + n_{\mathbf{q}})\right] \\ &+ \frac{B \alpha_{\Delta\mathbf{k}} \mathsf{M}_{gg}^{gg}}{N_s^4} \sum_{\mathbf{q},\mathbf{q}'\neq\mathbf{0}} \left\{ \left(u_{\mathbf{q}} u_{\mathbf{q}'} + v_{\mathbf{q}} v_{\mathbf{q}'}\right)^2 |\mathfrak{u}_{\bar{\Delta}\mathbf{k}-\mathbf{q}+\mathbf{q}'}|^2 n_{\mathbf{q}} (1 + n_{\mathbf{q}'}) \right. \\ &\left. + \frac{\left(u_{\mathbf{q}} v_{\mathbf{q}'} + v_{\mathbf{q}} u_{\mathbf{q}'}\right)^2}{2} \left[|\mathfrak{u}_{\bar{\Delta}\mathbf{k}-\mathbf{q}-\mathbf{q}'}|^2 n_{\mathbf{q}} n_{\mathbf{q}'} + |\mathfrak{u}_{\bar{\Delta}\mathbf{k}+\mathbf{q}+\mathbf{q}'}|^2 (1 + n_{\mathbf{q}})(1 + n_{\mathbf{q}'})\right] \right\}. \end{aligned} \tag{8.39}$$

Equation (8.39) is equivalent to the results of [31, 103]. The Quantum Monte Carlo code outputs an estimate for the full density-density correlations $\langle \hat{n}_{\mathbf{j}} \hat{n}_{\mathbf{j}} \rangle$, that is, it does not

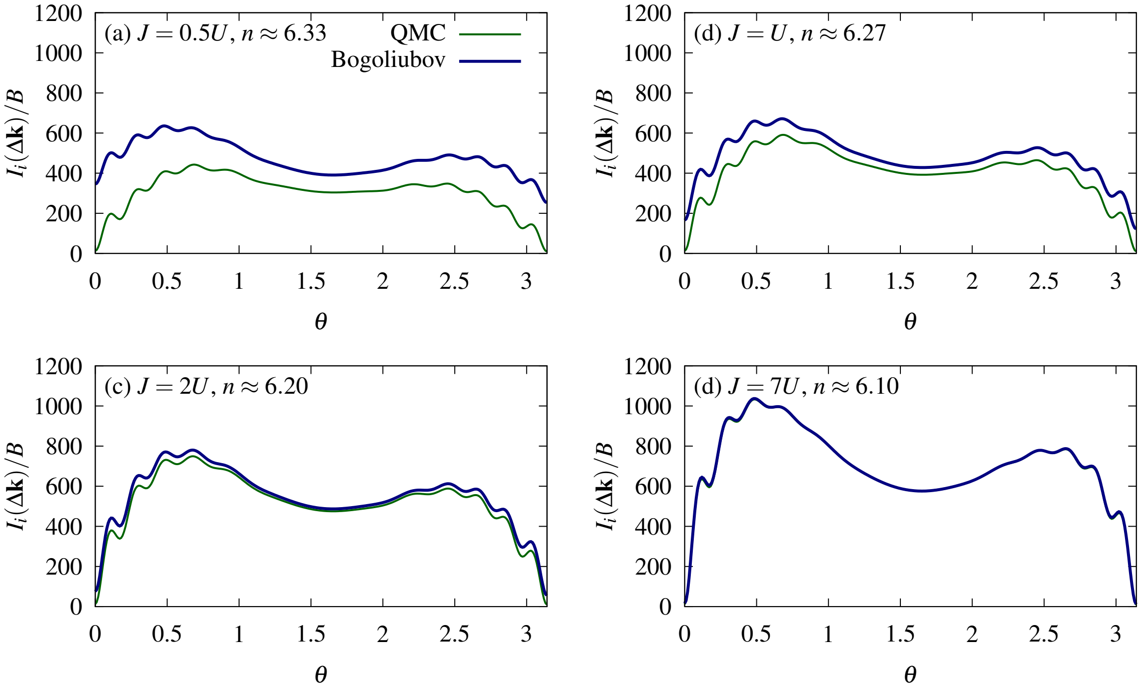

Figure 8.10: Angular dependence of the scattered light intensity for a small lattice in the Bogoliubov regime, at fixed T and changing J along the $\phi = \pi/4$ direction. This figure compares QMC results with the Bogoliubov approximation for a 2D Bose-Hubbard model in a square lattice with linear lattice size $N_s = 16$,$U = 1$, $T = 0.05U$, and NMax= 20. The curves in these figures are computed from the correlation functions shown in Fig. 8.8.

separate between connected and disconnected components. The elastic component of the scattered light can be computed directly using the total density in Eq. (4.27). The inelastic intraband component [Eq. (4.23)] is computed by subtracting the elastic component to the whole signal:

$$I_i^{\text{QMC}}(\Delta\mathbf{k}) = \alpha_{\Delta\mathbf{k}} B \mathsf{M}_{gg}^{gg} \sum_{i,j} e^{i\Delta\mathbf{k}\cdot(\mathbf{r}_i - \mathbf{r}_j)} \left\langle \hat{n}_{\mathbf{i}} \hat{n}_{\mathbf{j}} \right\rangle_c . \tag{8.40}$$

The angular dependence of the scattered light for the different cases studied in the previous section are analysed below.

8.5.2 Small lattices in the Bogoliubov regime

The results are shown in Fig. 8.10. The scattered light has been computed using the density-density correlation functions shown in Fig. 8.8. The scattered light is sensitive to differences in the density-density correlations [Fig. 8.8]. For $J \sim U$, the Bogoliubov approximation overestimates the number of inelastically scattered photons. This is due to the fact that the Bogoliubov approximation overestimates the connected density-density

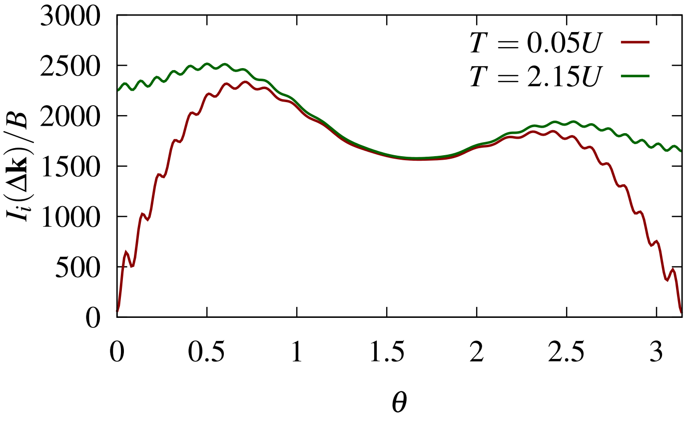

Figure 8.11: Angular dependence of the scattered light intensity at fixed total density and varying T along the $\phi = \pi/4$ direction. This figure shows QMC results for a 2D Bose-Hubbard model in a square lattice with linear lattice size $N_s = 32$, $U = 1$, $J = 1$ and NMAX= 15. The total density has been kept constant, $n \approx 6.27$, by changing the input chemical potential μ. $T = 0.05U$ corresponds to a condensate depletion $\approx 3.5\%$, and $T = 2.15U$ corresponds to a condensate depletion $\approx 9\%$.

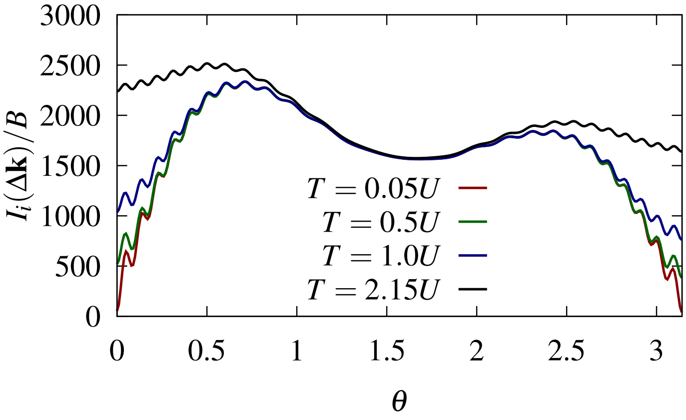

Figure 8.12: Angular dependence of the scattered light intensity for varying T with $J = U$ along the $\phi = \pi/4$ direction. This figure shows QMC results for a 2D Bose-Hubbard model in a square lattice with linear lattice size $N_s = 32$, $U = 1$, $J = 1$ and NMAX= 15. The total density is not constant. $T = 0.05U$ corresponds to a condensate depletion of $\approx 3.5\%$, and $T = 2.15U$ corresponds to a condensate depletion of $\approx 8.5\%$.

correlation functions, as shown in Fig. 8.8. For large values of J/U [Fig. 8.10(d)], the Bogoliubov approximation coincides with the QMC calculations, as is to be expected from Fig. 8.8(d).

8.5.3 Temperature dependence in a superfluid

The inelastic component of the scattered light off a superfluid is temperature sensitive. The changes occur around the forward direction Fig. 8.11. The angular dependence of the scattered light at constant density for different temperatures is shown in

Fig. 8.11. This agrees with the results obtained using the Bogoliubov approximation of Douglas and Burnett [31]. However, as demonstrated by Fig. 8.10, the Bogoliubov calculation overestimates the amount of scattered light in the regime $J \sim U$. Figure 8.12 shows the angular dependence of the scattered light for the temperature dependence at fixed chemical potential [Fig. 8.5]. The scattered light intensity is sensitive to temperature changes, which could be used for thermometry.

8.5.4 From a Mott insulator into a superfluid

Figure 8.13 shows the changes in the scattered light across the critical region starting in the Mott insulating phase into the superfluid [see Fig. 8.6]. Note that this is done at a temperature $T = 0.05U$ which is not low compared to J, even in the superfluid. The magnitude of the scattered light intensity in Fig. 8.13 increases by two orders of magnitude with increasing J/U. The results shown in Fig. 8.13 interpolate between the two limiting cases studied by Douglas and Burnett [31][‡]. They found that the inelastic component of the scattered intensity is not suitable as a probe in the Mott regime. This is due to the small number of inelastically scattered photons in the Mott lobe or close to it, which agrees with the results from numerical computations using QMC presented here [Fig. 8.13].

[‡] Using the $J = 0$ Mott ground state, and the Bogoliubov approximation, Douglas and Burnett [31] studied inelastic light scattering deep in the Mott insulator, and deep in the superfluid phase.

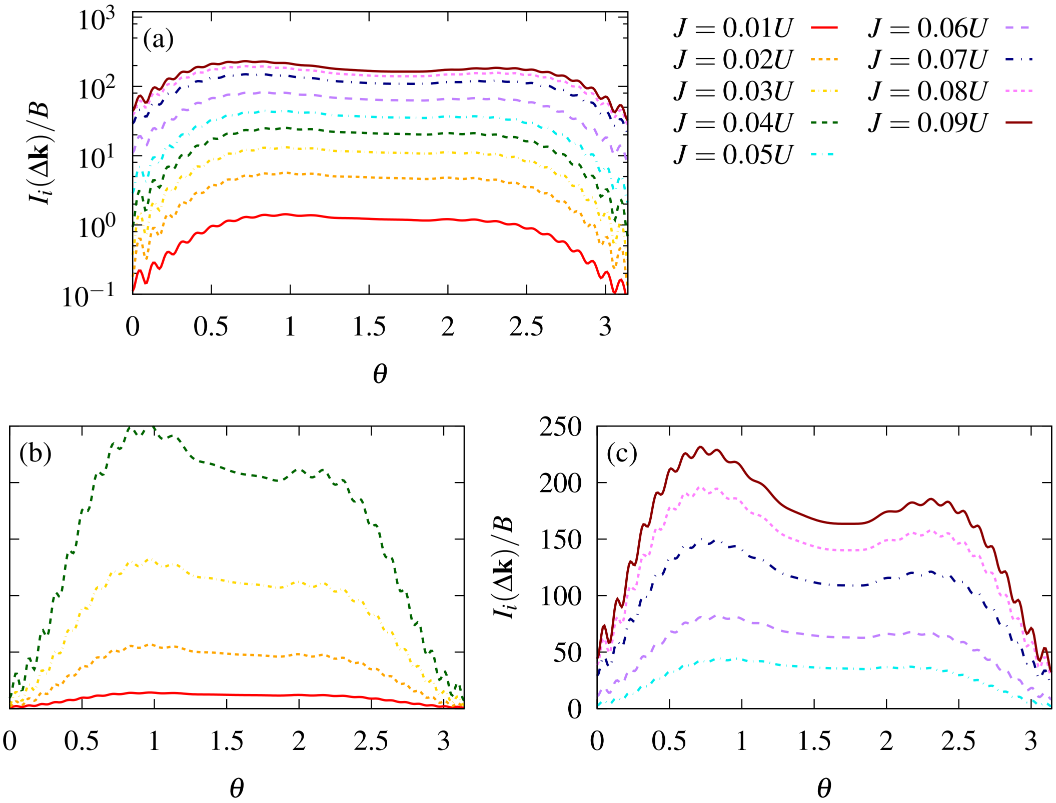

Figure 8.13: Angular dependence of the scattered light from the Mott insulator to a superfluid along the $\phi = \pi/4$ direction for a 2D Bose-Hubbard model in a square lattice with linear lattice size $N_s = 32$,$U = 1$, $T = 0.05U$, and NMAX= 10. (a) shows all the computed curves. Note the logarithmic scale due to the fact that the scattered light increases over an order of magnitude going from the Mott state into the superfluid regime. (b) shows the scattered light for the first four data points, in the Mott regime. (c) shows the scattered light for the rest of the data points, across the transition and into the superfluid.

Chapter 9

Conclusions

> So long, and thanks for all the fish
>
> The dolphins

> ¡Que inventen ellos!
>
> Miguel de Unamuno

9.1 Summary of key results

In this thesis, light scattering off atoms loaded in optical lattices has been analysed. The general formalism has been presented in Chapter 4. This formalism is general, and can be directly applied to any gas provided that the correlations of the system can be computed. Specifically, it has been shown how calculations from condensed matter can be directly used to compute experimental observables in the analogue systems realised with ultracold gases in optical lattices. This calculation can be in the form of a Dyson perturbation series, or the output of a Quantum Monte Carlo simulation. The computations presented in Chapters 5, 6 and 7 are for the particular case of the 2D repulsive Hubbard model at half-filling in the square lattice. However, the formalism presented in Chapter 4 can be applied to any other system for which the correlations can be computed. This was demonstrated in this thesis for the bosonic Hubbard model in Chapter 8. If other lattice configurations are realised, say, a hexagonal lattice, applying the methods presented in this thesis is quite straightforward. MFT or beyond MFT correlation functions can be computed, depending on the complexity of the calculation. In the case of the Hubbard model in the hexagonal lattice, the RPA calculation can be done too [87]. To apply the methods presented here to other atomic systems and lattice correlations can be done by: choosing an atom, choosing a level structure, computing the possible transitions [Eq. (4.20)], and use the necessary correlations functions in Eqs. (4.27), (4.28), and (4.49) for the intensity or Eqs. (4.39), and (4.40) for the spectrum.

One of the key results of this thesis is derived from applying the general formalism to an experimentally relevant case. It has been shown that the AFM ordering pattern in the system can be accurately detected by studying the elastic component of the scattered light. If the magnetic peaks are not accessible, it has also been proven that the inelastic component conveys information about the atomic correlations. This can be also used to probe the system. In particular, it has been shown that changes in the inelastic component of the scattered light can be used to detect changes in the different susceptibilities of the system, and that these susceptibilities can be geometrically separated. Apart from magnetic correlations, the scattered light can be used as a temperature probe. Also, if the scattered light spectrum is accessible, it has been shown to be a very powerful probe which is able to reveal the excitations of the system, both, single-particle and collective modes. Conversely, the formalism presented in Chapter 4 can be used to determine which correlations are being probed for systems for which there are no theoretical results available.

9.2 Future prospects

The work presented in this thesis can be extended in many directions. Here, some of the possible routes to be taken are listed. Starting with the specific case of modelling the AFM state of the two-species fermion gas in optical lattices, the natural step to be taken would be to extend the treatment to finite temperatures. This extension could be made principally in two different ways: the first way to approach the problem remains analytical. In particular, extending the RPA calculation to finite temperatures should offer a better quantitative way of analysing the temperature detection accuracy achievable. On the other hand, the different existing approaches to the finite-temperature 2D Hubbard model already published in the literature can be taken advantage of. For example, using the Non linear σ model calculation of [16], the finite-temperature scattered light intensity and spectrum could be computed. In a completely different approach, given that the Hubbard model reduces to the Heisenberg model in the large U limit, and given that the Heisenberg model can be efficiently simulated at finite temperatures using Quantum Monte Carlo methods, the finite temperature scattered light can be studied by means of QMC. This treatment does not take into account the effect of single-particle excitations. However, for large U, single-particle are gapped and clearly separated from the collective mode. The second way to improve the analysis presented in this thesis is to include inhomogeneity effects. In particular, taking into account the harmonic trap. In 1D, it has been demonstrated for the single-species non-interacting Fermi gas that the harmonic trap has a beneficial effect in the detection accuracy [104]. This can be done with relatively less technical difficulties in the bosonic case[*]

In the case of the bosonic Hubbard model, the next step to be carried out is clear. The results of Section 8.5, have to be analysed using the methods of Chapter 6, which would determine quantitatively the achievable detection accuracy. The spectrum of the Bose-Hubbard model can also be studied using QMC methods. For example, Pippan et al. [92] studied the excitation spectra of the one-dimensional case. The results of such simulations can be directly used to compute the scattered light spectrum.

---

[*] The current version of the ALPS codes [3] can easily be used to simulate a trapped ultracold gas. However, correlation measurements are not implemented by default for the inhomogeneous gas due to the lost of translation invariance. Without translation invariance, the number of values to be stored can easily become too large and it is switched off by default.

Appendix A

Hubbard model susceptibilities

In this Appendix, the calculation of the MFT and RPA susceptibilities presented in Secs. 3.2.1 and 3.3 is outlined. In particular, the RPA series is calculated for the charge $\hat{\rho}$ [Eq. (3.45)], longitudinal spin $\hat{S}^z$ [Eq. (3.46)] and transverse spin $\hat{S}^+, \hat{S}^-$ [Eqs. (3.48) and (3.49)]. The calculation is done via a diagrammatic expansion. As shown in Section 3.2.2, the MFT susceptibilities and structure factors [Eqs. (4.29) and (4.41)] can be calculated directly from the MFT Hamiltonian [Eq. (3.16)] and the Bogoliubov transformation [Eq. (3.13)]. Here, the susceptibilities are rederived to illustrate the diagrammatic method in the sim-

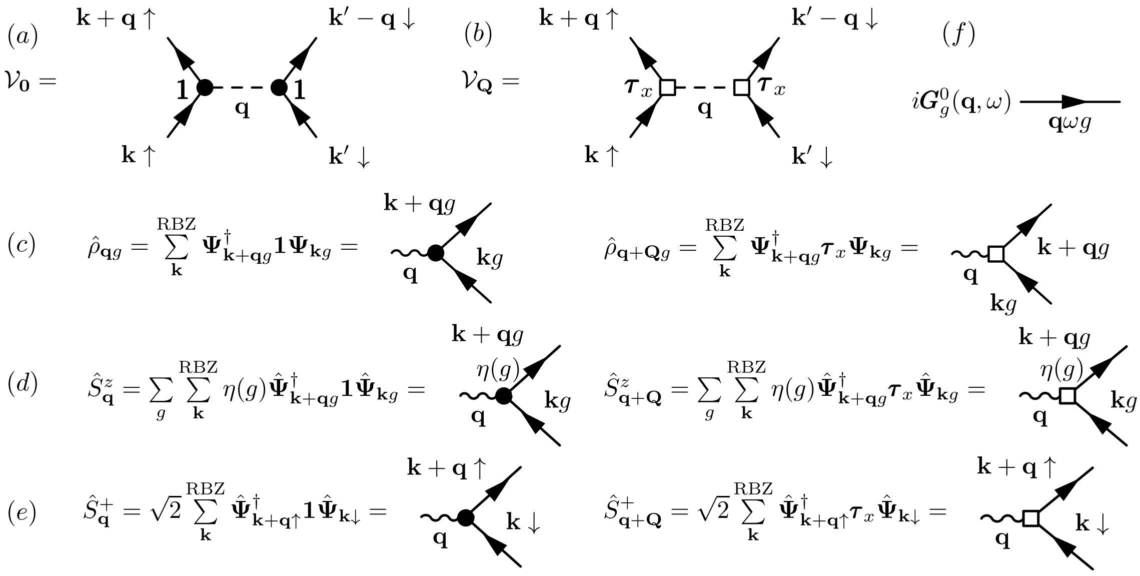

Figure A.1: Diagrammatic representation of the interaction vertices, spin densities, and Green's function needed for the RPA calculation of the susceptibilities. (a) and (b) interaction vertices [Eq. (A.1)], (c) density operator [Eq. (3.24)], (d) spin projection on the z direction [Eq. (3.20)], (e) spin raising operator [Eq. (3.23)] and (f) MFT Green's function [Eq. (A.6)].

plest case, and to be used in the RPA calculation. The perturbation expansion in the *sdw* AFM state is different from the usual RPA for the dielectric function, found in textbooks*. Instead of using the non-interacting ground state as a starting point, the perturbation expansion is done using the *sdw* MFT ground state of Eq. (3.16) [109].

In Section 3.2, the fluctuations were dropped to obtain the MFT Hamiltonian of Eq. (3.12). In this thesis, these fluctuations have been partially taken into account by using the RPA susceptibilities [Sec. 3.3] and RPA-corrected order parameter [Sec. 3.3].

The full Hamiltonian [Eq. (3.1)] can be written as sum of the MFT one $\mathcal{H}$ [Eq. (3.12)] and the fluctuations (the interaction part). Using the compact Nambu notation [Eq. (3.11)], this results in

$$\begin{aligned}\mathcal{H}_{\text{tot}} =& \mathcal{H} + \mathcal{V}_{\mathbf{0}} + \mathcal{V}_{\mathbf{Q}},\\ \mathcal{V}_{\mathbf{0}} =& \frac{U}{N_s^2}\sum_{\mathbf{q},\mathbf{k},\mathbf{k}'}^{\text{RBZ}} \hat{\mathbf{\Psi}}^{\dagger}_{\mathbf{k}+\mathbf{q},\uparrow}\mathbf{1}\hat{\mathbf{\Psi}}_{\mathbf{k},\uparrow}\hat{\mathbf{\Psi}}^{\dagger}_{\mathbf{k}'-\mathbf{q},\downarrow}\mathbf{1}\hat{\mathbf{\Psi}}_{\mathbf{k}',\downarrow},\\ \mathcal{V}_{\mathbf{Q}} =& \frac{U}{N_s^2}\sum_{\mathbf{q},\mathbf{k},\mathbf{k}'}^{\text{RBZ}} \hat{\mathbf{\Psi}}^{\dagger}_{\mathbf{k}+\mathbf{q},\uparrow}\boldsymbol{\tau}_x\hat{\mathbf{\Psi}}_{\mathbf{k},\uparrow}\hat{\mathbf{\Psi}}^{\dagger}_{\mathbf{k}'-\mathbf{q},\downarrow}\boldsymbol{\tau}_x\hat{\mathbf{\Psi}}_{\mathbf{k}',\downarrow}.\end{aligned} \tag{A.1}$$

In the previous equation, the two matrices $\mathbf{1}$ and $\boldsymbol{\tau}_x$ stand for a 2×2 unit matrix and a Pauli matrix, respectively. Their explicit expression is

$$\mathbf{1} = \begin{pmatrix} 1 & 0 \\ 0 & 1 \end{pmatrix}, \quad \boldsymbol{\tau}_x = \begin{pmatrix} 0 & 1 \\ 1 & 0 \end{pmatrix} \tag{A.2}$$

The unit matrix takes into account that the interaction term $\mathcal{V}_{\mathbf{0}}$ corresponds to a momentum transfer within the RBZ. On the other hand, the interaction term $\mathcal{V}_{\mathbf{Q}}$ contains the Pauli matrix $\boldsymbol{\tau}_x$ because it corresponds to a momentum transfer that connects the first and the second RBZ [Fig. 3.2].

The diagrammatic representation for the terms used in the calculation is presented in Fig. A.1. The basic components, the creation (annihilation) Nambu spinors $\hat{\mathbf{\Psi}}^{\dagger}_{\underset{\sim}{\mathbf{k}}g}$ $\left(\hat{\mathbf{\Psi}}_{\underset{\sim}{\mathbf{k}}g}\right)$ [Eq. (3.11)], are represented by a solid line with an outcoming (incoming) arrow and a momentum and spin label. A wavy line represents the momentum transfer. When the momentum transfer happens within the RBZ, the presence of a unit matrix $\mathbf{1}$ is denoted by a filled circle. Momentum transfers between two RBZ, which require a Pauli matrix $\boldsymbol{\tau}_x$ are denoted by an open square. The interaction vertices $\mathcal{V}_{\mathbf{0}}$ and $\mathcal{V}_{\mathbf{Q}}$ appear in Fig. A.1(a) and (b), respectively. Interactions are represented with a dashed line, and aside from the

---

*For example, [20, 35, 77].

corresponding matrix ($\mathbf{1}$ or $\boldsymbol{\tau}_x$), each interaction vertex carries a factor of $-iU/N_s^2$. The diagrammatic representation of the different operators (total density, longitudinal, and transverse spin) is shown in Figs. A.1(c)-(e).

As mentioned, the perturbation is performed around the spin density wave ground state $|\Psi_{\text{sdw}}\rangle$. For this ground state, the bare Green's function at zero temperature can also be written as a 2×2 matrix in terms of the Nambu spinors [Eq. (3.11)]

$$i\boldsymbol{G}_g^{(0)}(\underset{\sim}{\mathbf{k}},t'-t) = \langle\Phi_{\text{sdw}}|\mathcal{T}\hat{\boldsymbol{\Psi}}_{\underset{\sim}{\mathbf{k}},g}(t')\hat{\boldsymbol{\Psi}}^\dagger_{\underset{\sim}{\mathbf{k}},g}(t)|\Phi_{\text{sdw}}\rangle = \quad t \xrightarrow[\mathbf{q},g]{} t' \,. \tag{A.3}$$

The Feynman rules listed above can be derived from the full Green's function perturbation expansion. The formalism for the matrix perturbation expansion is similar to the BCS superconductivity case [77, 108]. The exact Green's function can be written as

$$\begin{aligned}
i\boldsymbol{G}_g(\underset{\sim}{\mathbf{k}},t'-t) &= \left\langle \Phi_{\text{sdw}} \left| \mathcal{T}\hat{\boldsymbol{\Psi}}_{\underset{\sim}{\mathbf{k}},g}(t')\exp\left\{-i\int\limits_{-\infty}^{\infty} d\bar{t}\,[\mathcal{V}_{\mathbf{0}}(\bar{t})+\mathcal{V}_{\mathbf{Q}}(\bar{t})]\right\}\hat{\boldsymbol{\Psi}}^\dagger_{\underset{\sim}{\mathbf{k}},g}(t)\right| \Phi_{\text{sdw}} \right\rangle_c \\
&= \sum_{n=0}^{\infty}\frac{(-i)^n}{n!}\left\langle \Phi_{\text{sdw}} \left| \mathcal{T}\hat{\boldsymbol{\Psi}}_{\underset{\sim}{\mathbf{k}},g}(t')\left\{-\int\limits_{-\infty}^{\infty} d\bar{t}\,[\mathcal{V}_{\mathbf{0}}(\bar{t})+\mathcal{V}_{\mathbf{Q}}(\bar{t})]\right\}^n\hat{\boldsymbol{\Psi}}^\dagger_{\underset{\sim}{\mathbf{k}},g}(t)\right| \Phi_{\text{sdw}} \right\rangle_c \\
&= \sum_{n=0}^{\infty} i\boldsymbol{G}_g^{(n)}(\underset{\sim}{\mathbf{k}},t'-t) = \quad t \xRightarrow[\mathbf{q},g]{} t' \,,
\end{aligned} \tag{A.4}$$

where the subscript c represents *only connected diagrams*. In the last equation, the n-th term in the Green's function perturbation expansion has been implicitly defined as

$$i\boldsymbol{G}_g^{(n)}(\underset{\sim}{\mathbf{k}},t'-t) = \frac{(-i)^n}{n!}\left\langle \Phi_{\text{sdw}} \left| \mathcal{T}\hat{\boldsymbol{\Psi}}_{\underset{\sim}{\mathbf{k}},g}(t')\left\{-\int\limits_{-\infty}^{\infty} d\bar{t}\,[\mathcal{V}_{\mathbf{0}}(\bar{t})+\mathcal{V}_{\mathbf{Q}}(\bar{t})]\right\}^n\hat{\boldsymbol{\Psi}}^\dagger_{\underset{\sim}{\mathbf{k}},g}(t)\right| \Phi_{\text{sdw}} \right\rangle_c \tag{A.5}$$

For notational convenience, the explicit ground state bras and kets will be dropped from now on. All the expectations values are for the spin density wave ground state Ψ_{sdw}. The Fourier transform of the MFT Green's function $i\boldsymbol{G}_g^{(0)}(\underset{\sim}{\mathbf{k}},t'-t)$ can be directly calculated from the MFT Hamiltonian [Eq. (3.16)] and the Bogoliubov transformation [Eq. (3.13)]. This results in

$$i\boldsymbol{G}_g^{(0)}(\underset{\sim}{\mathbf{k}},\omega) = \int_{-\infty}^{\infty} dt e^{i\omega t} i\boldsymbol{G}_g^{(0)}(\underset{\sim}{\mathbf{k}},t) = \frac{i}{(\hbar\omega)^2 - E_{\underset{\sim}{\mathbf{k}}}^2 + i\delta}\begin{pmatrix} \hbar\omega+\epsilon_{\underset{\sim}{\mathbf{k}}} & \Delta_g \\ \Delta_g & \hbar\omega-\epsilon_{\underset{\sim}{\mathbf{k}}} \end{pmatrix}. \tag{A.6}$$

The diagrammatic representation of $i\boldsymbol{G}_g^{(0)}(\underset{\sim}{\mathbf{k}},\omega)$, a solid line with momentum, frequency, and spin labels, is shown in Fig. A.1(f). In a similar manner, the Feynman rules for the susceptibilities can be derived from the general expression for the perturbation expansion. For the susceptibilities defined in Eq. (3.19), the general expression for one of the components of the matrix is given by

$$\begin{aligned}\chi^{ij}(\mathbf{q},\mathbf{q}';t) =& \frac{i}{2N_s^2}\left\langle \mathcal{T}\hat{\mathbf{O}}_i(\mathbf{q},t)\exp\left\{-i\int_{-\infty}^{\infty}d\bar{t}\,[\mathcal{V}_{\mathbf{0}}(\bar{t})+\mathcal{V}_{\mathbf{Q}}(\bar{t})]\right\}\hat{\mathbf{O}}_j(\mathbf{q}',0)\right\rangle_c \\ =& \frac{i}{2N_s^2}\sum_{n=0}^{\infty}\frac{(-i)^n}{n!}\left\langle \mathcal{T}\hat{\mathbf{O}}_i(\mathbf{q},t)\left\{\int_{-\infty}^{\infty}d\bar{t}\,[\mathcal{V}_{\mathbf{0}}(\bar{t})+\mathcal{V}_{\mathbf{Q}}(\bar{t})]\right\}^n\hat{\mathbf{O}}_j(\mathbf{q}',0)\right\rangle_c \qquad \text{(A.7)} \\ =& \sum_{n=0}^{\infty}\chi^{ij}_{(n)}(\mathbf{q},\mathbf{q}';t) \qquad \text{(A.8)}\end{aligned}$$

The n-th order term for the perturbation series of the susceptibility has been defined implicitly as

$$\chi^{ij}_{(n)}(\mathbf{q},\mathbf{q}';t) = \frac{i}{2N_s^2}\frac{(-i)^n}{n!}\left\langle \mathcal{T}\hat{\mathbf{O}}_i(\mathbf{q},t)\left\{\int_{-\infty}^{\infty}d\bar{t}\,[\mathcal{V}_{\mathbf{0}}(\bar{t})+\mathcal{V}_{\mathbf{Q}}(\bar{t})]\right\}^n\hat{\mathbf{O}}_j(\mathbf{q}',0)\right\rangle_c . \qquad \text{(A.9)}$$

A.0.1 Mean-field susceptibilities

In this section, the calculation of the MFT susceptibilities listed in Section (3.2.1) is detailed. The calculation of only one susceptibility is shown in detail as the process is equivalent for the rest. Within the MFT approximation, the susceptibilities can be represented diagrammatically with the so-called *bubble diagrams* [Eqs. (A.10), and (A.13)]. For the transverse spin susceptibility [Eq.(3.35)] corresponds to the following diagrams,

$$\boldsymbol{\chi}^{+-}_{(0)}(\mathbf{q},t) = \begin{pmatrix} \chi^{+-}_{(0)}(\underset{\sim}{\mathbf{q}},\underset{\sim}{\mathbf{q}};t) & \chi^{+-}_{(0)}(\underset{\sim}{\mathbf{q}},\underset{\sim}{\mathbf{q}}+\mathbf{Q};t) \\ \chi^{+-}_{(0)}(\underset{\sim}{\mathbf{q}}+\mathbf{Q},\underset{\sim}{\mathbf{q}};t) & \chi^{+-}_{(0)}(\underset{\sim}{\mathbf{q}}+\mathbf{Q},\underset{\sim}{\mathbf{q}}+\mathbf{Q};t) \end{pmatrix}$$

$$=$$

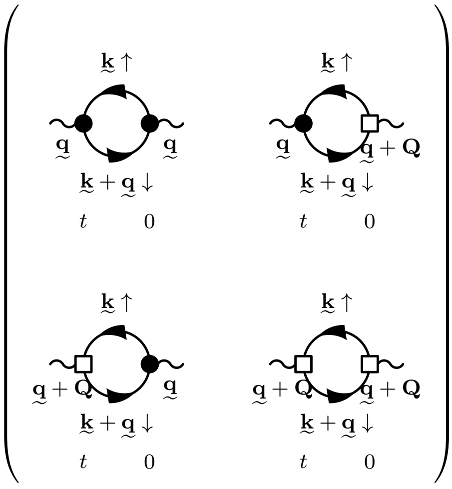

(A.10)

To illustrate the computational procedure, the detailed computation of the first diagonal element of the transverse spin susceptibility in the equation above [Eq. (A.10)] is shown below. The trick resides in expanding the matrix product in Nambu space before doing the contractions. Once the contractions have been made, the matrix structure is recovered again. Inserting the raising and lowering spin operators [Fig. A.1](e) into Eq. (A.9) with $n = 0$, the first diagonal element of the MFT transverse spin susceptibility [Eq .(A.10)] is computed as follows

$$\begin{aligned}
\chi^{+-}_{(0)}(\underset{\sim}{\mathbf{q}}, \underset{\sim}{\mathbf{q}}'; t) =& \frac{2i}{2N_s^2} \sum_{\mathbf{k},\mathbf{k}'}^{\text{RBZ}} \left\langle \mathcal{T} \hat{\mathbf{\Psi}}^{\dagger}_{\mathbf{k}+\underset{\sim}{\mathbf{q}},\uparrow}(t) \mathbf{1} \hat{\mathbf{\Psi}}_{\mathbf{k},\downarrow}(t) \hat{\mathbf{\Psi}}^{\dagger}_{\mathbf{k}'-\underset{\sim}{\mathbf{q}}',\downarrow}(0) \mathbf{1} \hat{\mathbf{\Psi}}_{\mathbf{k}',\uparrow}(0) \right\rangle_c \\
=& \frac{i}{N_s^2} \sum_{\mathbf{k}}^{\text{RBZ}} \sum_{\substack{a,b\\c,d}} \left\langle \mathcal{T} \hat{\mathbf{\Psi}}^{\dagger}_{\mathbf{k}+\underset{\sim}{\mathbf{q}},\uparrow}(t)_a \mathbf{1}_{ab} \hat{\mathbf{\Psi}}_{\mathbf{k},\downarrow}(t)_b \hat{\mathbf{\Psi}}^{\dagger}_{\mathbf{k}'-\underset{\sim}{\mathbf{q}}',\downarrow}(0)_c \mathbf{1}_{cd} \hat{\mathbf{\Psi}}_{\mathbf{k}',\uparrow}(0)_d \right\rangle_c \\
=& \delta_{\underset{\sim}{\mathbf{q}},\underset{\sim}{\mathbf{q}}'} \frac{-i}{N_s^2} \sum_{\mathbf{k},\mathbf{k}'}^{\text{RBZ}} \sum_{\substack{a,b\\c,d}} i\boldsymbol{G}^{(0)}_{\downarrow}(\mathbf{k}, t)_{da} \mathbf{1}_{ab} i\boldsymbol{G}^{(0)}_{\uparrow}(\mathbf{k}+\underset{\sim}{\mathbf{q}}, -t)_{bc} \mathbf{1}_{cd} \\
=& \delta_{\underset{\sim}{\mathbf{q}},\underset{\sim}{\mathbf{q}}'} \frac{-i}{N_s^2} \sum_{\mathbf{k}}^{\text{RBZ}} \mathbf{Tr} \left[\mathbf{1} i\boldsymbol{G}^{(0)}_{\downarrow}(\mathbf{k}, t) \mathbf{1} i\boldsymbol{G}^{(0)}_{\uparrow}(\mathbf{k}+\underset{\sim}{\mathbf{q}}, -t) \right]. \\
=& \delta_{\underset{\sim}{\mathbf{q}},\underset{\sim}{\mathbf{q}}'} \chi^{+-}_{(0)}(\underset{\sim}{\mathbf{q}}, \underset{\sim}{\mathbf{q}}; t)
\end{aligned} \tag{A.11}$$

The trace is over the Nambu matrices. The minus sign appears because of the anticommutation operator needed to write $i\boldsymbol{G}^{(0)}_{\downarrow}(\mathbf{k}, t)$. This is an example of the Feynman rule that assigns a factor of (-1) to each fermion closed loop. In frequency space,

$$\chi^{+-}_{(0)}(\underset{\sim}{\mathbf{q}}, \underset{\sim}{\mathbf{q}}'; \omega) = \delta_{\underset{\sim}{\mathbf{q}},\underset{\sim}{\mathbf{q}}'} \frac{i}{N_s^2} \sum_{\mathbf{k}}^{\text{RBZ}} \int \frac{d\nu}{2\pi} \mathbf{Tr} \boldsymbol{G}^{(0)}_{\downarrow}(\mathbf{k}, \nu) \boldsymbol{G}^{(0)}_{\uparrow}(\mathbf{k}+\underset{\sim}{\mathbf{q}}, \omega+\nu). \tag{A.12}$$

For the density and the longitudinal spin operators, the MFT diagrams are given by

$$\boldsymbol{\chi}^{\rho\rho}_{(0)}(\underset{\sim}{\mathbf{q}}, t) = \begin{pmatrix} \chi^{\rho\rho}_{(0)}(\underset{\sim}{\mathbf{q}}, \underset{\sim}{\mathbf{q}}, t) & \chi^{\rho\rho}_{(0)}(\underset{\sim}{\mathbf{q}}, \underset{\sim}{\mathbf{q}}+\mathbf{Q}, t) \\ \chi^{\rho\rho}_{(0)}(\underset{\sim}{\mathbf{q}}+\mathbf{Q}, \underset{\sim}{\mathbf{q}}, t) & \chi^{\rho\rho}_{(0)}(\underset{\sim}{\mathbf{q}}+\mathbf{Q}, \underset{\sim}{\mathbf{q}}+\mathbf{Q}, t) \end{pmatrix}$$

$=$ 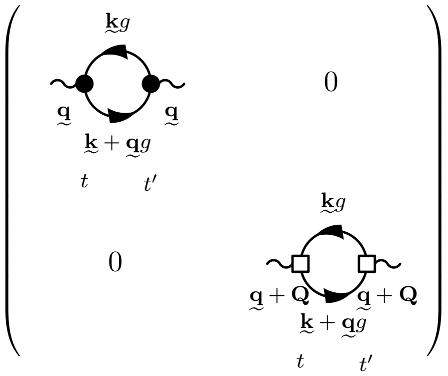 . (A.13)

In the previous equation, the sums over momentum $\underset{\sim}{\mathbf{k}}$ and spin g are not written explicitly. In the second line, the fact that the diagonal terms are zero has been taken into account

$$\boldsymbol{\chi}^{\rho\rho}_{(0)}(\utilde{\mathbf{q}}, t) =$$

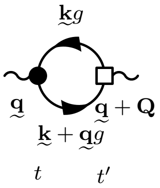

$$= \chi^{\rho\rho}_{(0)}(\utilde{\mathbf{q}}, \utilde{\mathbf{q}}, t) =$$

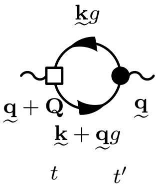

$$= 0. \tag{A.14}$$

At the MFT level, the longitudinal spin susceptibility coincides with the density susceptibility [Eq. (3.34)],

$$\boldsymbol{\chi}^{\rho\rho}_{(0)}(\utilde{\mathbf{q}}, t) = \boldsymbol{\chi}^{zz}_{(0)}(\utilde{\mathbf{q}}, t). \tag{A.15}$$

Hence, $\boldsymbol{\chi}^{zz}_{(0)}(\utilde{\mathbf{q}}, t)$ has the same diagrammatic form as $\boldsymbol{\chi}^{zz}_{(0)}(\utilde{\mathbf{q}}, t)$.

A.0.2 RPA susceptibilities

The RPA results from a partial summation of Eq. (A.8) in which only terms that can be written as products of bubble diagrams are considered. The RPA series can be summed to infinite order analytically because it is a geometric series. The first few terms of the RPA series for the density and transverse spin susceptibility are shown in Figs. A.2 and A.3. The second term in Fig. A.2 corresponds to the first order correction to the density-density susceptibility. It can be computed inserting the Nambu total density operator [Fig. A.1(c)] into Eq. (A.9) with $n = 1$. The result is

$$\begin{aligned}\chi^{\rho\rho}_{(1)}(\utilde{\mathbf{q}}, \utilde{\mathbf{q}}; t) =& 2\left(\tfrac{i}{2N_s^2}\right)\left(\tfrac{-iU}{N_s^2}\right)\sum_{\mathbf{k},\mathbf{k}'}^{\mathrm{RBZ}}\int_{-\infty}^{\infty} dt' \Big[\mathbf{Tr}\boldsymbol{G}^{(0)}_{\uparrow}(\mathbf{k},t-t')\boldsymbol{G}^{(0)}_{\uparrow}(\mathbf{k}+\utilde{\mathbf{q}},t'-t)\mathbf{Tr}\boldsymbol{G}^{(0)}_{\downarrow}(\mathbf{k}',t')\boldsymbol{G}^{(0)}_{\downarrow}(\mathbf{k}'+\utilde{\mathbf{q}},-t') \\ &+\mathbf{Tr}\boldsymbol{G}^{(0)}_{\uparrow}(\mathbf{k},t-t')\boldsymbol{\tau}_x\boldsymbol{G}^{(0)}_{\uparrow}(\mathbf{k}+\utilde{\mathbf{q}},t'-t)\mathbf{Tr}\boldsymbol{G}^{(0)}_{\downarrow}(\mathbf{k}',t')\boldsymbol{G}^{(0)}_{\downarrow}(\mathbf{k}'+\utilde{\mathbf{q}},-t')\boldsymbol{\tau}_x\Big]\end{aligned} \tag{A.16}$$

$$= -U\int_{-\infty}^{\infty} dt' \chi^{\rho\rho}_{(0)}(\utilde{\mathbf{q}}, \utilde{\mathbf{q}}; t-t')\chi^{\rho\rho}_{(0)}(\utilde{\mathbf{q}}, \utilde{\mathbf{q}}; t'). \tag{A.17}$$

Note that the factor of 2 in Eq. (A.16) results from the sum over spins in the density operator [Figs. A.1(c) and A.2], and the fact that the bubbles are spin independent. The second line in Eq. (A.16) is zero because it is proportional to $\int dt' \chi^{\rho\rho}_{(0)}(\utilde{\mathbf{q}}, \utilde{\mathbf{q}}+\mathbf{Q}; t-t')\chi^{\rho\rho}_{(0)}(\utilde{\mathbf{q}}, \utilde{\mathbf{q}}+\mathbf{Q}; t')$, which is zero by Eq. (A.14). $\boldsymbol{\chi}^{\rho\rho}_{(0)}$ is a diagonal matrix in Nambu space. If only bubble contributions are considered in Eq. (A.8), the resulting frequency space

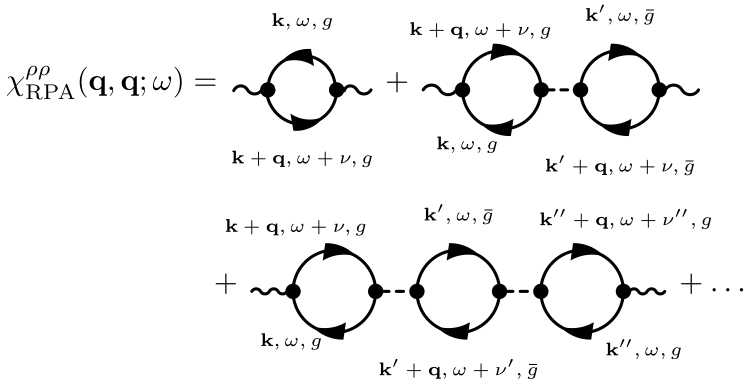

Figure A.2: Diagrammatic representation of the RPA series for the density susceptibility. The first order term is the MFT bubble. The sums over internal momenta $\mathbf{k},\mathbf{k}',\mathbf{k}''$, and frequencies ν,ν',ν'' have not been written explicitly. $\bar{g}$ stands for the opposite spin of g.

RPA series factorises and can be summed as a geometric series,

$$\begin{aligned}
\boldsymbol{\chi}^{\rho\rho}_{\mathrm{RPA}}(\underset{\sim}{\mathbf{q}},\omega) =&\boldsymbol{\chi}^{\rho\rho}_{(0)}(\underset{\sim}{\mathbf{q}},\omega) + \boldsymbol{\chi}^{\rho\rho}_{(0)}(\underset{\sim}{\mathbf{q}},\omega)(-U)\boldsymbol{\chi}^{\rho\rho}_{(0)}(\underset{\sim}{\mathbf{q}},\omega) \\
&+ \boldsymbol{\chi}^{\rho\rho}_{(0)}(\underset{\sim}{\mathbf{q}},\omega)(-U)\boldsymbol{\chi}^{\rho\rho}_{(0)}(\underset{\sim}{\mathbf{q}},\omega)(-U)\boldsymbol{\chi}^{\rho\rho}_{(0)}(\underset{\sim}{\mathbf{q}},\omega) + \dots \\
=&\boldsymbol{\chi}^{\rho\rho}_{(0)}(\underset{\sim}{\mathbf{q}},\omega) - \boldsymbol{\chi}^{\rho\rho}_{(0)}(\underset{\sim}{\mathbf{q}},\omega)U\boldsymbol{\chi}^{\rho\rho}_{(0)}(\underset{\sim}{\mathbf{q}},\omega) + \boldsymbol{\chi}^{\rho\rho}_{(0)}(\underset{\sim}{\mathbf{q}},\omega)U\boldsymbol{\chi}^{\rho\rho}_{(0)}(\underset{\sim}{\mathbf{q}},\omega)U\boldsymbol{\chi}^{\rho\rho}_{(0)}(\underset{\sim}{\mathbf{q}},\omega) + \dots \\
=&\boldsymbol{\chi}^{\rho\rho}_{(0)}(\underset{\sim}{\mathbf{q}},\omega)\left[1 + U\boldsymbol{\chi}^{\rho\rho}_{(0)}(\underset{\sim}{\mathbf{q}},\omega)\right]^{-1}. \qquad \text{(A.18)}
\end{aligned}$$

This corresponds to Eq. (3.45). The same type of calculation for the longitudinal spin operator $\hat{S}^z$ leads to a similar result. At the RPA level, the density and longitudinal spin susceptibilities do not coincide. For the longitudinal spin susceptibility, the RPA series is equivalent to the one shown in Fig. A.2, except that each of the spin operators [Eq. (3.20) and Fig. A.1(d)] has a spin dependent factor $\eta(g)$ [Eq. (3.5)], which in terms where the number of bubbles is odd leads to an extra factor of (-1). Thus,

$$\begin{aligned}
\boldsymbol{\chi}^{zz}_{\mathrm{RPA}}(\underset{\sim}{\mathbf{q}},\omega) =&\boldsymbol{\chi}^{zz}_{(0)}(\underset{\sim}{\mathbf{q}},\omega) + (-1)\boldsymbol{\chi}^{zz}_{(0)}(\underset{\sim}{\mathbf{q}},\omega)(-U)\boldsymbol{\chi}^{zz}_{(0)}(\underset{\sim}{\mathbf{q}},\omega) \\
&+ \boldsymbol{\chi}^{zz}_{(0)}(\underset{\sim}{\mathbf{q}},\omega)(-U)\boldsymbol{\chi}^{zz}_{(0)}(\underset{\sim}{\mathbf{q}},\omega)(-U)\boldsymbol{\chi}^{zz}_{(0)}(\underset{\sim}{\mathbf{q}},\omega) + \dots \\
=&\boldsymbol{\chi}^{zz}_{(0)}(\underset{\sim}{\mathbf{q}},\omega) + \boldsymbol{\chi}^{zz}_{(0)}(\underset{\sim}{\mathbf{q}},\omega)U\boldsymbol{\chi}^{zz}_{(0)}(\underset{\sim}{\mathbf{q}},\omega) + \boldsymbol{\chi}^{zz}_{(0)}(\underset{\sim}{\mathbf{q}},\omega)U\boldsymbol{\chi}^{zz}_{(0)}(\underset{\sim}{\mathbf{q}},\omega)U\boldsymbol{\chi}^{zz}_{(0)}(\underset{\sim}{\mathbf{q}},\omega) + \dots \\
=&\boldsymbol{\chi}^{zz}_{(0)}(\underset{\sim}{\mathbf{q}},\omega)\left[1 + U\boldsymbol{\chi}^{zz}_{(0)}(\underset{\sim}{\mathbf{q}},\omega)\right]^{-1}. \qquad \text{(A.19)}
\end{aligned}$$

This corresponds to Eq. (3.46).

The RPA series for the transverse susceptibility is depicted in Fig. A.3(c). To derive this series, the interaction term has to be rewritten in a different form to $\sim U\hat{\rho}_{\uparrow}\hat{\rho}_{\downarrow}$ as for Eq. (A.1). The computation can be simplified if the interaction term is written $\sim$

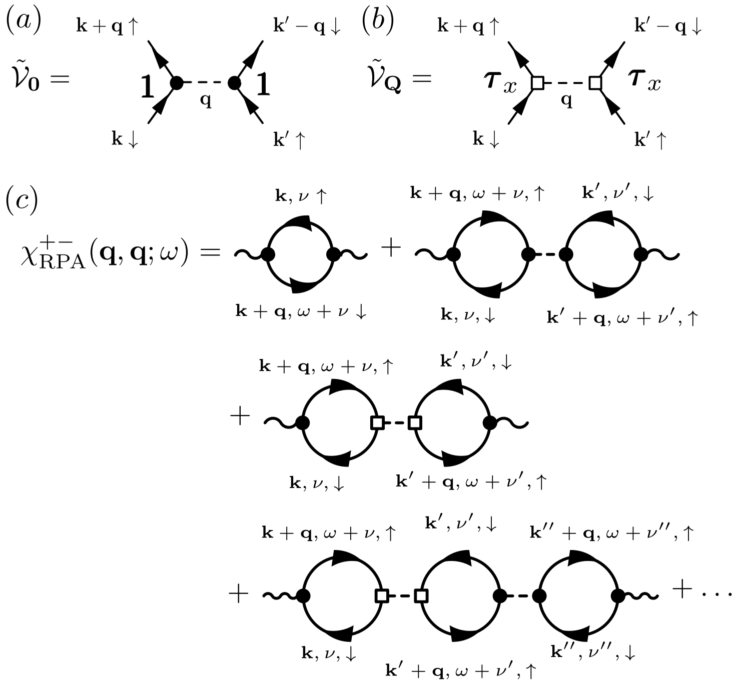

Figure A.3: Diagrammatic representation of the alternative form of the interaction vertices suited to computing the transverse spin susceptibility for (a) Eq. (A.20); (b) Eq. (A.21). In (c), we show the RPA series for the transverse spin susceptibility. The sums over internal momenta $\mathbf{k}, \mathbf{k}', \mathbf{k}''$, and frequencies ν, ν', ν'' have not been written explicitly.

$-U\hat{S}^{+}\hat{S}^{-}$ [45]. In particular, the interaction can be rewritten as

$$\tilde{\mathcal{V}}_{\mathbf{0}} = -\frac{U}{N_s^2}\sum_{\mathbf{q},\mathbf{k},\mathbf{k}'}^{\mathrm{RBZ}} \hat{\mathbf{\Psi}}^{\dagger}_{\mathbf{k}+\mathbf{q},\uparrow}\mathbf{1}\hat{\mathbf{\Psi}}_{\mathbf{k},\downarrow}\hat{\mathbf{\Psi}}^{\dagger}_{\mathbf{k}'-\mathbf{q},\downarrow}\mathbf{1}\hat{\mathbf{\Psi}}_{\mathbf{k}',\uparrow}, \tag{A.20}$$

$$\tilde{\mathcal{V}}_{\mathbf{Q}} = -\frac{U}{N_s^2}\sum_{\mathbf{q},\mathbf{k},\mathbf{k}'}^{\mathrm{RBZ}} \hat{\mathbf{\Psi}}^{\dagger}_{\mathbf{k}+\mathbf{q},\uparrow}\boldsymbol{\tau}_x\hat{\mathbf{\Psi}}_{\mathbf{k},\downarrow}\hat{\mathbf{\Psi}}^{\dagger}_{\mathbf{k}'-\mathbf{q},\downarrow}\boldsymbol{\tau}_x\hat{\mathbf{\Psi}}_{\mathbf{k}',\uparrow}. \tag{A.21}$$

The rewritten interaction vertices are shown in Fig. A.3(a), (b). Using these *tilded* interaction vertices, the RPA series has an equivalent structure to that of the density [Eq. (A.18)] and the longitudinal spin [Eq. (A.19)]. For example, the second and third diagrams in Fig. A.3(c) can be computed using the tilded interaction vertices [Eqs. (A.20) and (A.21)] in Eq. (A.8). This results in

$$\chi^{+-}_{(1)}(\utilde{\mathbf{q}},\utilde{\mathbf{q}};t) = 2\left(\tfrac{i}{2N_s^2}\right)\left(\tfrac{+iU}{N_s^2}\right)\sum_{\mathbf{k},\mathbf{k}'}^{\mathrm{RBZ}}\int_{-\infty}^{\infty}dt'\Big[\mathbf{Tr}\boldsymbol{G}^{(0)}_{\downarrow}(\mathbf{k},t-t')\boldsymbol{G}^{(0)}_{\uparrow}(\mathbf{k}+\utilde{\mathbf{q}},t'-t)\mathbf{Tr}\boldsymbol{G}^{(0)}_{\downarrow}(\mathbf{k}',t')\boldsymbol{G}^{(0)}_{\uparrow}(\mathbf{k}'+\utilde{\mathbf{q}},-t')$$
$$+\mathbf{Tr}\boldsymbol{\tau}_x\boldsymbol{G}^{(0)}_{\downarrow}(\mathbf{k}',t')\boldsymbol{G}^{(0)}_{\uparrow}(\mathbf{k}'+\utilde{\mathbf{q}},-t')\mathbf{Tr}\boldsymbol{G}^{(0)}_{\uparrow}(\mathbf{k}+\utilde{\mathbf{q}},t'-t)\boldsymbol{G}^{(0)}_{\downarrow}(\mathbf{k},t-t')\boldsymbol{\tau}_x\Big] \tag{A.22}$$

$$= U\int_{-\infty}^{\infty}dt'\Big[\chi^{+-}_{(0)}(\utilde{\mathbf{q}},\utilde{\mathbf{q}};t-t')\chi^{+-}_{(0)}(\utilde{\mathbf{q}},\utilde{\mathbf{q}};t')$$
$$+\chi^{+-}_{(0)}(\utilde{\mathbf{q}},\utilde{\mathbf{q}}+\mathbf{Q};t-t')\chi^{+-}_{(0)}(\utilde{\mathbf{q}}+\mathbf{Q},\utilde{\mathbf{q}};t')\Big]. \tag{A.23}$$

The factor of 2 in the first line of the right-hand side of Eq. (A.23) is due to the definition of the raising and lowering spin operators [Eq. (3.23) and Fig. A.1(e)].

The remaining components of $\boldsymbol{\chi}^{+-}_{(1)}(\mathbf{q},\omega)$ can be evaluated in a similar manner. The time dependent full matrix first order term takes the following form:

$$\boldsymbol{\chi}^{+-}_{(1)}(\utilde{\mathbf{q}},t) = U\int_{-\infty}^{\infty}dt'\boldsymbol{\chi}^{+-}_{(0)}(\utilde{\mathbf{q}},t-t')\boldsymbol{\chi}^{+-}_{(0)}(\utilde{\mathbf{q}},t'). \tag{A.24}$$

Fourier transforming the previous equation, the susceptibilities factorise and the series takes a similar form as Eq. (A.18) and (A.19), but in this case, the matrices are not diagonal. Hence, for the transverse susceptibility, the RPA series can also be summed as a geometric series, which results in

$$\boldsymbol{\chi}^{+-}_{\mathrm{RPA}}(\utilde{\mathbf{q}},\omega) = \boldsymbol{\chi}^{+-}_{(0)}(\utilde{\mathbf{q}},\omega)\left[\mathbf{1}-U\boldsymbol{\chi}^{+-}_{(0)}(\utilde{\mathbf{q}},\omega)\right]^{-1}. \tag{A.25}$$

This corresponds to Eq. (3.47).

Bibliography

[1] Al-Assam, S., Williams, R. A., and Foot, C. J. (2010). Ultracold atoms in an optical lattice with dynamically variable periodicity. *Phys. Rev. A*, 82:021604.

[2] Albuquerque, A., Alet, F., Corboz, P., Dayal, P., Feiguin, A., Fuchs, S., Gamper, L., Gull, E., Gurtler, S., Honecker, A., Igarashi, R., Korner, M., Kozhevnikov, A., Lauchli, A., Manmana, S., Matsumoto, M., McCulloch, I., Michel, F., Noack, R., Pawlowski, G., Pollet, L., Pruschke, T., Schollwock, U., Todo, S., Trebst, S., Troyer, M., Werner, P., and Wessel, S. (2007a). The alps project release 1.3: Open-source software for strongly correlated systems. *Journal of Magnetism and Magnetic Materials*, 310(2, Part 2):1187 – 1193. Proceedings of the 17th International Conference on Magnetism.

[3] Albuquerque, A., Alet, F., Corboz, P., Dayal, P., Feiguin, A., Fuchs, S., Gamper, L., Gull, E., Gürtler, S., Honecker, A., Igarashi, R., Körner, M., Kozhevnikov, A., Läuchli, A., Manmana, S., Matsumoto, M., McCulloch, I., Michel, F., Noack, R., Pawłowski, G., Pollet, L., Pruschke, T., Schollwöck, U., Todo, S., Trebst, S., Troyer, M., Werner, P., and Wessel, S. (2007b). The alps project release 1.3: Open-source software for strongly correlated systems. *Journal of Magnetism and Magnetic Materials*, 310(2, Part 2):1187 – 1193. Proceedings of the 17th International Conference on Magnetism.

[4] Alet, F., Wessel, S., and Troyer, M. (2005). Generalized directed loop method for quantum monte carlo simulations. *Phys. Rev. E*, 71:036706.

[5] Ambegaokar, V. and Troyer, M. (2010). Estimating errors reliably in monte carlo simulations of the ehrenfest model. *American Journal of Physics*, 78(2):150–157.

[6] Amico, L. and Penna, V. (1998). Dynamical mean field theory of the bose-hubbard model. *Phys. Rev. Lett.*, 80:2189–2192.

[7] Amico, L. and Penna, V. (2000). Time-dependent mean-field theory of the superfluid-insulator phase transition. *Phys. Rev. B*, 62:1224–1237.

[8] Anderson, M., Ensher, J., Matthews, M., Wieman, C., and Cornell, E. (1995). Observation of bose-einstein condensation in a dilute atomic vapor. *Science*, 269(5221):198–201.

[9] Ashcroft, N. W. and Mermin, N. D. (1976). *Solid State Physics*. Holt, Rinehart and Winston, New York.

[10] Auerbach, A. (1998). *Interacting Electrons and Quantum Magnetism*. Graduate Texts in Contemporary Physics. Springer, Berlin, 2 edition.

[11] Barnett, S. and Radmore, P. (2002). *Methods in Theoretical Quantum Optics*. Oxford Series in Optical and Imaging Sciences. Oxford University Press, Incorporated.

[12] Bauer, B., Carr, L. D., Evertz, H. G., Feiguin, A., Freire, J., Fuchs, S., Gamper, L., Gukelberger, J., Gull, E., Guertler, S., Hehn, A., Igarashi, R., Isakov, S. V., Koop, D., Ma, P. N., Mates, P., Matsuo, H., Parcollet, O., Pawłowski, G., Picon, J. D., Pollet, L., Santos, E., Scarola, V. W., Schollwöck, U., Silva, C., Surer, B., Todo, S., Trebst, S., Troyer, M., Wall, M. L., Werner, P., and Wessel, S. (2011). The alps project release 2.0: open source software for strongly correlated systems. *Journal of Statistical Mechanics: Theory and Experiment*, 2011(05):P05001.

[13] Bednorz, J. G. and Müller, K. A. (1986). Possible high T_c superconductivity in the Ba-La-Cu-O system. *Zeitschrift fur Physik B Condensed Matter*, 64:189–193.

[14] Bloch, I., Dalibard, J., and Zwerger, W. (2008). Many-body physics with ultracold gases. *Reviews of modern physics*, 80(3):885–964.

[15] Borejsza, K. and Dupuis, N. (2003). Antiferromagnetism and single-particle properties in the two-dimensional half-filled hubbard model: Slater vs. mott-heisenberg. *EPL (Europhysics Letters)*, 63(5):722.

[16] Borejsza, K. and Dupuis, N. (2004). Antiferromagnetism and single-particle properties in the two-dimensional half-filled hubbard model: A nonlinear sigma model approach. *Phys. Rev. B*, 69:085119.

[17] Bransden, B. and Joachain, C. (2003). *Physics of Atoms and Molecules*. Pearson Education. Prentice Hall.

[18] Brinkman, W. F. and Rice, T. M. (1970). Single-Particle Excitations in Magnetic Insulators. *Phys. Rev. B*, 2:1324–1338.

[19] Bruun, G. M., Syljuåsen, O. F., Pedersen, K. G. L., Andersen, B. M., Demler, E., and Sørensen, A. S. (2009). Antiferromagnetic noise correlations in optical lattices. *Phys. Rev. A*, 80:033622.

[20] Bruus, H. and Flensberg, K. (2004). *Many-Body Quantum Theory in Condensed Matter Physics: An Introduction*. Oxford graduate texts in mathematics. OUP Oxford.

[21] Burnett, K., Edwards, M., Clark, C. W., and Shotter, M. (2002). The bogoliubov approach to number squeezing of atoms in an optical lattice. *Journal of Physics B: Atomic, Molecular and Optical Physics*, 35(7):1671.

[22] Capogrosso-Sansone, B., Söyler, i. m. c. G. m. c., Prokof'ev, N., and Svistunov, B. (2008). Monte carlo study of the two-dimensional bose-hubbard model. *Phys. Rev. A*, 77(1):015602.

[23] Carmichael, H. (1998). *Statistical Methods in Quantum Optics 1: Master Equations and Fokker-Planck Equations*. Physics and Astronomy Online Library. Springer.

[24] Carrasquilla, J. and Rigol, M. (2012). Superfluid to normal phase transition in strongly correlated bosons in two and three dimensions. *Phys. Rev. A*, 86:043629.

[25] Chakravarty, S., Halperin, B. I., and Nelson, D. R. (1989). Two-dimensional quantum heisenberg antiferromagnet at low temperatures. *Phys. Rev. B*, 39:2344–2371.

[26] Chin, C., Grimm, R., Julienne, P., and Tiesinga, E. (2010). Feshbach resonances in ultracold gases. *Rev. Mod. Phys.*, 82:1225–1286.

[27] Chubukov, A. V. and Frenkel, D. M. (1992). Renormalized perturbation theory of magnetic instabilities in the two-dimensional hubbard model at small doping. *Phys. Rev. B*, 46(18):11884–11901.

[28] Cohen-Tannoudji, C., Dupont-Roc, J., and Grynberg, G. (1992). *Atom-photon interactions: basic processes and applications*. Wiley-Interscience publication. J. Wiley.

[29] Corcovilos, T. A., Baur, S. K., Hitchcock, J. M., Mueller, E. J., and Hulet, R. G. (2010). Detecting antiferromagnetism of atoms in an optical lattice via optical bragg scattering. *Phys. Rev. A*, 81(1):013415.

[30] Dingle, R. and Müller, H. (1962). Asymptotic expansions of mathieu functions and their characteristic numbers. *Journal für die reine und angewandte Mathematik*, 211:11–32.

[31] Douglas, J. S. and Burnett, K. (2011). Light scattering from ultracold atomic gases in optical lattices at finite temperature. *Phys. Rev. A*, 84:033637.

[32] Elstner, N. and Monien, H. (1999). Dynamics and thermodynamics of the bose-hubbard model. *Phys. Rev. B*, 59:12184–12187.

[33] Esslinger, T. (2010). Fermi-hubbard physics with atoms in an optical lattice. *Annu. Rev. Cond. Mat. Phys*, 1(1):129–152.

[34] Fazekas, P. (1999). *Lecture Notes on Electron Correlation and Magnetism*. Series in Modern Condensed Matter Physics. World Scientific, Singapore.

[35] Fetter, A. and Walecka, J. (2003). *Quantum theory of many-particle systems*. Dover Books on Physics. Dover Publications.

[36] Feynman, R. (1982). Simulating physics with computers. *International journal of theoretical physics*, 21(6-7):467–488.

[37] Feynman, R. P. (1985). Quantum mechanical computers. *Optics News*, 11(2):11–20.

[38] Fisher, M. E. and Ferdinand, A. E. (1967). Interfacial, boundary, and size effects at critical points. *Phys. Rev. Lett.*, 19:169–172.

[39] Fisher, M. P. A., Weichman, P. B., Grinstein, G., and Fisher, D. S. (1989). Boson localization and the superfluid-insulator transition. *Phys. Rev. B*, 40:546–570.

[40] Gaunt, A. L., Schmidutz, T. F., Gotlibovych, I., Smith, R. P., and Hadzibabic, Z. (2013). Bose-einstein condensation of atoms in a uniform potential. *Phys. Rev. Lett.*, 110:200406.

[41] Greif, D., Uehlinger, T., Jotzu, G., Tarruell, L., and Esslinger, T. (2013). Short-range quantum magnetism of ultracold fermions in an optical lattice. *Science*, 340(6138):1307–1310.

[42] Greiner, M. (2003). *PhD Thesis: Ultracold quantum gases in three-dimensional optical lattice potentials*. Ludwig-Maximilians-Universität München.

[43] Greiner, M., Mandel, O., Esslinger, T., Hansch, T., and Bloch, I. (2002). Quantum phase transition from a superfluid to a mott insulator in a gas of ultracold atoms. *Nature*, 415(6867):39–44.

[44] Grimm, R., Weidemüller, M., and Ovchinnikov, Y. B. (2000). Optical Dipole Traps for Neutral Atoms. *Advances in Atomic Molecular and Optical Physics*, 42:95–170.

[45] Ho, A. F. (2013). *Private communication*.

[46] Ho, A. F., Cazalilla, M. A., and Giamarchi, T. (2009). Quantum simulation of the hubbard model: The attractive route. *Phys. Rev. A*, 79(3):033620.

[47] Hofstetter, W., Cirac, J. I., Zoller, P., Demler, E., and Lukin, M. D. (2002). High-temperature superfluidity of fermionic atoms in optical lattices. *Phys. Rev. Lett.*, 89:220407.

[48] Hubbard, J. (1963). Electron correlations in narrow energy bands. *Proc. Roy. Soc. Lond. A*, 276(1365):238–257.

[49] Imada, M., Fujimori, A., and Tokura, Y. (1998). Metal-insulator transitions. *Rev. Mod. Phys.*, 70:1039–1263.

[50] Jaksch, D., Bruder, C., Cirac, J. I., Gardiner, C. W., and Zoller, P. (1998). Cold bosonic atoms in optical lattices. *Phys. Rev. Lett.*, 81(15):3108–3111.

[51] Javanainen, J. and Ruostekoski, J. (1995). Off-resonance light scattering from low-temperature bose and fermi gases. *Phys. Rev. A*, 52(4):3033–3046.

[52] Javanainen, J. and Ruostekoski, J. (2003). Optical detection of fractional particle number in an atomic fermi-dirac gas. *Phys. Rev. Lett.*, 91:150404.

[53] Jimenez-Garcia, K., Compton, R. L., Lin, Y.-J., Phillips, W. D., Porto, J. V., and Spielman, I. B. (2010). Phases of a two-dimensional bose gas in an optical lattice. *Phys. Rev. Lett.*, 105:110401.

[54] Joerdens, R., Strohmaier, N., Guenther, K., Moritz, H., and Esslinger, T. (2008). A mott insulator of fermionic atoms in an optical lattice. *Nature*, 455(7210):204–U34.

[55] Ketterle, W., Durfee, D., and D.M., S.-K. (1999a). Making, probing and understanding Bose-Einstein condensates. In *Bose-Einstein condensation in atomic gases, Proceedings of the International School of Physics "Enrico Fermi", Course CXL*, volume 35, pages 1079–1072. IEEE.

[56] Ketterle, W., Durfee, D., and Stamper-Kurn, D. (1999b). Making, probing and understanding bose-einstein condensates. In Inguscio, M., Stringari, S., and Wieman, C., editors, *Bose-Einstein Condensation in atomic gases*, volume 140 of *Proceedings of the international school of physics Enrico Fermi*, pages 67–176, Nieuwe Hemweg 6B, 1013 BG Amsterdam, Netherlands. Inst Sch Phys Enrico Fermi, I O S Press. International School of Physics Enrico Fermi on Bose-Einstein Condensation in Atomic Gases, Varenna Lake Como, Italy, Jul 07-17, 1998.

[57] Ketterle, W. and Zwierlein, M. W. (2008). Making, probing and understanding ultracold fermi gases (reprinted from rivista del nuovo cimento, pg 95-287, 2008). *Rivista del nuovo cimento*, 31(5-6):247–422.

[58] Köhl, M., Moritz, H., Stöferle, T., Günter, K., and Esslinger, T. (2005). Fermionic atoms in a three dimensional optical lattice: Observing fermi surfaces, dynamics, and interactions. *Phys. Rev. Lett.*, 94:080403.

[59] Kohn, W. (1959). Analytic properties of bloch waves and wannier functions. *Phys. Rev.*, 115:809–821.

[60] Krauth, W. (2006). *Statistical Mechanics, Algorithms and Computations*. Oxford Master Series in Statistical, Computational and Theoretical Physics. Oxford University Press, Oxford, 1 edition.

[61] Köhl, M., Moritz, H., Stöferle, T., Schori, C., and Esslinger, T. (2005). Superfluid to mott insulator transition in one, two, and three dimensions. *Journal of Low Temperature Physics*, 138(3-4):635–644.

[62] L. Taylor, P. and Heinonen, O., editors (2004). *A Quantum Approach to Condensed Matter Physics*. Cambridge University Press, Cambridge.

[63] Łakomy, K., Idziaszek, Z., and Trippenbach, M. (2009). Thermal effects in light scattering from ultracold bosons in an optical lattice. *Phys. Rev. A*, 80:043404.

[64] Landau, D. P. (1976). Finite-size behavior of the ising square lattice. *Phys. Rev. B*, 13:2997–3011.

[65] Leblanc, L. J. (2006). The hyperfine structure of potassium-40. Technical report.

[66] Lewandowski, H., Harber, D., Whitaker, D., and Cornell, E. (2003). Simplified system for creating a bose–einstein condensate. *Journal of Low Temperature Physics*, 132(5-6):309–367.

[67] Li, T. C., Kelkar, H., Medellin, D., and Raizen, M. G. (2008). Real-time control of the periodicity of a standing wave: an optical accordion. *Opt. Express*, 16(8):5465–5470.

[68] Liang, J.-Q. and Müller-Kirsten, H. J. W. (1995). Quantum tunneling for the sine-gordon potential: Energy band structure and bogomolny-fateyev relation. *Phys. Rev. D*, 51:718–725.

[69] Lieb, E. H. and Wu, F. Y. (1968). Absence of mott transition in an exact solution of the short-range, one-band model in one dimension. *Phys. Rev. Lett.*, 20(25):1445–1448.

[70] Loudon, R. (1983). *The quantum theory of light*. Oxford science publications. Oxford University Press, Oxford, 2 edition.

[71] Mahan, G. D. (2000). *Many-particle Physics*. Physics of Solids and Liquids. Springer, Berlin, 3 edition.

[72] Mahmud, K. W., Duchon, E. N., Kato, Y., Kawashima, N., Scalettar, R. T., and Trivedi, N. (2011). Finite-temperature study of bosons in a two-dimensional optical lattice. *Phys. Rev. B*, 84:054302.

[73] Majlis, N. (2007). *The Quantum Theory of Magnetism*. World Scientific Publishing Company Incorporated (NJ).

[74] Manousakis, E. (1991). The spin-heisenberg antiferromagnet on a square lattice and its application to the cuprous oxides. *Rev. Mod. Phys.*, 63(1):1–62.

[75] Mathy, C. J. M., Huse, D. A., and Hulet, R. G. (2012). Enlarging and cooling the néel state in an optical lattice. *Phys. Rev. A*, 86:023606.

[76] Mattis, D. (2006). *The theory of magnetism made simple: an introduction to physical concepts and to some useful mathematical methods*. World Scientific.

[77] Mattuck, R. (1976). *A Guide to Feynman Diagrams in the Many-body Problem*. Dover Books on Physics Series. Dover Publications, Incorporated.

[78] Mekhov, I. B., Maschler, C., and Ritsch, H. (2007). Light scattering from ultracold atoms in optical lattices as an optical probe of quantum statistics. *Phys. Rev. A*, 76:053618.

[79] Mermin, N. D. and Wagner, H. (1966). Absence of ferromagnetism or antiferromagnetism in one- or two-dimensional isotropic heisenberg models. *Phys. Rev. Lett.*, 17:1133–1136.

[80] Metcalf, H. and Van Der Straten, P. (1999). *Laser Cooling and Trapping*. Graduate Texts in Contemporary Physics. Springer-Verlag GmbH.

[81] Metzner, W. and Vollhardt, D. (1989). Correlated lattice fermions in $d = \infty$ dimensions. *Phys. Rev. Lett.*, 62(3):324–327.

[82] Mueller-Kirsten, H., zu Zhang, J., and Zhang, Y. (2001). Once again: instanton method vs. wkb. *Journal of High Energy Physics*, 2001(11):011.

[83] Nang Ma, P. (2013). *PhD Thesis: Numerical simulations of bosons and fermions in three dimensional optical lattices*. ETH Zurich.

[84] Negele, J. and Orland, H. (1988). *Quantum Many-Particle Systems*. Advanced Book Program. Westview Press, United States of America.

[85] Onsager, L. (1944). Crystal statistics. i. a two-dimensional model with an order-disorder transition. *Phys. Rev.*, 65:117–149.

[86] Pathria, R. and Beale, P. (2011). *Statistical Mechanics*. Elsevier Science.

[87] Peres, N. M. R., Araujo, M. A. N., and Bozi, D. (2004). Phase diagram and magnetic collective excitations of the hubbard model for graphene sheets and layers. *Phys. Rev. B*, 70:195122.

[88] Pethick, C. and Smith, H. (2002). *Bose-Einstein Condensation in dilute gases*. CUP Press, Cambridge.

[89] Pethick, C. and Smith, H. (2008). *Bose-Einstein Condensation in dilute gases*. CUP Press, Cambridge, second edition.

[90] Phillips, W. D. and Metcalf, H. (1982). Laser deceleration of an atomic beam. *Phys. Rev. Lett.*, 48:596–599.

[91] Pines, D. and Nozières, P. (1966). *The Theory of Quantum Liquids: Normal Fermi liquids*. Theory of quantum liquids. W. A. Benjamin.

[92] Pippan, P., Evertz, H. G., and Hohenadler, M. (2009). Excitation spectra of strongly correlated lattice bosons and polaritons. *Phys. Rev. A*, 80:033612.

[93] Pollet, L. (2012). Recent developments in quantum monte carlo simulations with applications for cold gases. *Reports on Progress in Physics*, 75(9):094501.

[94] Pollet, L., Houcke, K. V., and Rombouts, S. M. (2007). Engineering local optimality in quantum monte carlo algorithms. *Journal of Computational Physics*, 225(2):2249 – 2266.

[95] Pollet, L., Kollath, C., Houcke, K. V., and Troyer, M. (2008). Temperature changes when adiabatically ramping up an optical lattice. *New Journal of Physics*, 10(6):065001.

[96] Pollet, L., Rombouts, S. M. A., Van Houcke, K., and Heyde, K. (2004). Optimal monte carlo updating. *Phys. Rev. E*, 70:056705.

[97] Pollock, E. L. and Ceperley, D. M. (1987). Path-integral computation of superfluid densities. *Phys. Rev. B*, 36:8343–8352.

[98] Prokofev, N. V., Svistunov, B. V., and Tupitsyn, I. S. (1998). Worm algorithm in quantum Monte Carlo simulations. *Physics Letters A*, 238(4-5):253 – 257.

[99] Prokof'ev, N., Svistunov, B., and Tupitsyn, I. (1998). Exact, complete, and universal continuous-time worldline monte carlo approach to the statistics of discrete quantum systems. *Journal of Experimental and Theoretical Physics*, 87:310–321.

[100] Rey, A. M., Burnett, K., Roth, R., Edwards, M., Williams, C. J., and Clark, C. W. (2003). Bogoliubov approach to superfluidity of atoms in an optical lattice. *Journal of Physics B: Atomic, Molecular and Optical Physics*, 36(5):825.

[101] Rigol, M., Batrouni, G. G., Rousseau, V. G., and Scalettar, R. T. (2009). State diagrams for harmonically trapped bosons in optical lattices. *Phys. Rev. A*, 79:053605.

[102] Rist, S., Menotti, C., and Morigi, G. (2010). Light scattering by ultracold atoms in an optical lattice. *Phys. Rev. A*, 81:013404.

[103] Ruostekoski, J. (2013). *Private communication*.

[104] Ruostekoski, J., Foot, C. J., and Deb, A. B. (2009). Light scattering for thermometry of fermionic atoms in an optical lattice. *Physical Review Letters*, 103(17):170404.

[105] Sakurai, J. (2006). *Modern Quantum Mechanics*. Pearson Education.

[106] Sandvik, A. W. (1999). Stochastic series expansion method with operator-loop update. *Phys. Rev. B*, 59:R14157–R14160.

[107] Schneider, U., Hackermuller, L., Will, S., Best, T., Bloch, I., Costi, T. A., Helmes, R. W., Rasch, D., and Rosch, A. (2008). Metallic and insulating phases of repulsively interacting fermions in a 3d optical lattice. *Science*, 322(5907):1520–1525.

[108] Schrieffer, J. (1999). *Theory of superconductivity*. Advanced Book Program Series. Advanced Book Program, Perseus Books.

[109] Schrieffer, J. R., Wen, X. G., and Zhang, S. C. (1989). Dynamic spin fluctuations and the bag mechanism of high-t_c superconductivity. *Phys. Rev. B*, 39(16):11663–11679.

[110] Sherson, J. F., Weitenberg, C., Endres, M., Cheneau, M., Bloch, I., and Kuhr, S. (2010). Single-atom-resolved fluorescence imaging of an atomic mott insulator. *Nature*, 467(7311):68–72.

[111] Spielman, I. B., Phillips, W. D., and Porto, J. V. (2007). Mott-insulator transition in a two-dimensional atomic bose gas. *Phys. Rev. Lett.*, 98:080404.

[112] Squires, G. (2012). *Introduction to the Theory of Thermal Neutron Scattering*. Cambridge University Press.

[113] Tammuz, N., Smith, R. P., Campbell, R. L. D., Beattie, S., Moulder, S., Dalibard, J., and Hadzibabic, Z. (2011). Can a bose gas be saturated? *Phys. Rev. Lett.*, 106:230401.

[114] Thijssen, J. (2007). *Computational Physics*. Cambridge University Press.

[115] Tiecke, T. (2011). Properties of Potassium. Technical report.

[116] Trotzky, S., Pollet, L., Gerbier, F., Schnorrberger, U., Bloch, I., Prokof'Ev, N. V., Svistunov, B., and Troyer, M. (2010). Suppression of the critical temperature for superfluidity near the Mott transition. *Nature Physics*, 6:998–1004.

[117] Troyer, M., Alet, F., Trebst, S., and Wessel, S. (2003). Non-local updates for quantum monte carlo simulations. *AIP Conference Proceedings*, 690(1):156–169.

[118] Troyer, M. and Werner, P. (2009). Quantum monte carlo simulations. *AIP Conference Proceedings*, 1162(1):98–173.

[119] Troyer, M. and Wiese, U.-J. (2005). Computational complexity and fundamental limitations to fermionic quantum monte carlo simulations. *Phys. Rev. Lett.*, 94:170201.

[120] Valiente, M. (2010). Lattice two-body problem with arbitrary finite-range interactions. *Phys. Rev. A*, 81(4):042102.

[121] van Oosten, D., van der Straten, P., and Stoof, H. T. C. (2001). Quantum phases in an optical lattice. *Phys. Rev. A*, 63:053601.

[122] Weitenberg, C., Schauß, P., Fukuhara, T., Cheneau, M., Endres, M., Bloch, I., and Kuhr, S. (2011). Coherent light scattering from a two-dimensional mott insulator. *Phys. Rev. Lett.*, 106(21):215301.

[123] Wessel, S., Alet, F., Troyer, M., and Batrouni, G. G. (2004). Quantum monte carlo simulations of confined bosonic atoms in optical lattices. *Phys. Rev. A*, 70:053615.

[124] Will, S., Best, T., Braun, S., Schneider, U., and Bloch, I. (2011). Coherent interaction of a single fermion with a small bosonic field. *Phys. Rev. Lett.*, 106(11):115305.

[125] Williams, R. A., Pillet, J. D., Al-Assam, S., Fletcher, B., Shotter, M., and Foot, C. J. (2008). Dynamic optical lattices: two-dimensional rotating and accordion lattices for ultracold atoms. *Opt. Express*, 16(21):16977–16983.

[126] Wolff, U. (1989). Collective monte carlo updating for spin systems. *Phys. Rev. Lett.*, 62:361–364.

[127] Wolfram Research, Inc (2013). *Mathematica Edition: Version 9.0*. Wolfram Research, Inc., Champaign, Illinois.

[128] Wunsch, D. (2009). *Complex Variables With Applications, 3/E*. Pearson Education.

[129] Wyld, H. (2008). *Mathematical Methods For Physics*. Westview Press.

[130] Zhou, Q., Kato, Y., Kawashima, N., and Trivedi, N. (2009). Direct mapping of the finite temperature phase diagram of strongly correlated quantum models. *Phys. Rev. Lett.*, 103:085701.

Index

Acknowledgements

> Don't be alone,
>
> Amelia Williams

This thesis would have not been possible without the constant support and encouragement from my parents. It is entirely due to them that I ended up doing a PhD in Physics. Merely because they have always had the odd idea that children should have access to as many books as they want. And I could not be more grateful for that. I also want to thank my wonderful brother and sister, who are the best brother and sister one could hope for, respectively. No matter how busy this thesis has made my life at times (and by that I mean at all times), my grandfather Paco has reminded me very often that I was *nearly there*. I am also very lucky that my grandmas have been there, trying to make me fat. María del Carmen and Amparo have both done a great job continuing the initial task that my late grandfather Juan Manuel started back when I was a (fat) kid, giving me bread straight out of the oven and a bowl of olive oil to dip it in. Of course, when my mother was not looking. I also would like to thank my cousin Juanfri, because he has read a lot about this book.

Of all the people whom I have met during my years as a physicist in the making (which I still am), I could not let this occasion without acknowledging their company and friendship. My years in Granada (and after) would have not been the same without Pedro Escalante[†], Marina Quintero, Javier Carrillo, Laura *Voz Bonita*, Pedro Parra, Ricardo Garzón, James Aaron Christopher Key, Juan Venegas, Carmen Ruiz, Mikael Chala, Jordi Hidalgo, Juanpe Araque, Laura Mompeán, and all those whom I have forgotten with the years. Likewise, my Egham years would have not been the same without the company of great people I've been lucky enought to meet in the Physics department, James Wells, Niclas Wennerdal, Roland Grein, Simon Schmidlin, Chris Harrison, Richard Marsh, Connor Shelly, Rob Cantrill, Chris Kent, Dave Voneshen, Terence Giles, Aya Shibahara, Lev Levitin, Eugene Balkind, and Gabriele Sala. Special thanks to George Nichols, for inviting me to have a different look at gravity. Outside the Physics department, my life would have been very boring hadn't it been because of the great people I met on campus, in MACS and in the RHUL Swimming Club. Thank you guys!. Specially Dave, Gaby, Christos, Patricia Lexie, Emily, Ali Z, and Sarah-Jane. In Southampton, I would really like to thank the Department of Applied Mathematics for the warm welcome during my year there. Also there, I found great people with whom I shared many pints: Joe Tait, Ana Khukhro, Justin Lovegrove, Yago Antolín, Rubén Sánchez, David Torres, and those whom I may have forgotten, because I have a terrible memory for names. My third year would have been a complete omnishambles without Jenni, Lorena and María. I would also like to specially thank Andrea Velasco for proofreading this thesis and pointing out my comma shyness. Thank you, Manuel Valiente, for all these years of advice and friendship.

I would like to thank Ping Nang Ma for answering my many questions and for all the help he provided me for running the QMC simulations.

Last but not least, I would like to acknowledge the help of my supervisors Dr. Andrew Ho and Prof. Janne Ruostekoski. Without the many discussions that I have had with them over the last four years, this thesis would not be what it is.

The first three years during which I worked on the material presented in this thesis were funded by SepNET. The author acknowledges the use of the IRIDIS High Performance Computing Facility, and associated support services at the University of Southampton, in the completion of this work.

[†] *Ergo sum la polla!*